Federal University of Uberlândia
SCHOOL OF MECHANICAL ENGINEERING

Bruno Silva de Lima

PHYSICAL EXPERIMENTATION AND NUMERICAL SIMULATION OF LIQUID FILM:
COMPARISON OF EULERIAN METHODS

Uberlândia
2022

Bruno Silva de Lima

PHYSICAL EXPERIMENTATION AND NUMERICAL SIMULATION OF LIQUID FILM:
COMPARISON OF EULERIAN METHODS

Thesis submitted to the Graduate Program in Mechanical Engineering at the Federal University of Uberlândia, in partial fulfillment of the requirements to obtain the degree of **DOCTOR IN MECHANICAL ENGINEERING**.
Concentration area: Heat transfer and Fluid Mechanics.
Advisor: Prof. Dr. Francisco José de Souza

Uberlândia
2022

Dados Internacionais de Catalogação na Publicação (CIP)
Sistema de Bibliotecas da UFU, MG, Brasil.

L732p
2022

Lima, Bruno Silva de, 1992-
Physical experimentation and numerical simulation of liquid film [recurso eletrônico] : comparison of eulerian methods / Bruno Silva de Lima. - 2022.

Orientador: Francisco José de Souza.
Tese (Doutorado) - Universidade Federal de Uberlândia, Programa de Pós-Graduação em Engenharia Mecânica.
Modo de acesso: Internet.
Disponível em: http://doi.org/10.14393/ufu.te.2022.5028
Inclui bibliografia.

1. Engenharia Mecânica. I. Souza, Francisco José de, 1973-, (Orient.). II. Universidade Federal de Uberlândia. Programa de Pós-Graduação em Engenharia Mecânica. III. Título.

CDU: 621.01

André Carlos Francisco
Bibliotecário – CRB-6/3408

UNIVERSIDADE FEDERAL DE UBERLÂNDIA
Coordenação do Programa de Pós-Graduação em Engenharia Mecânica
Av. João Naves de Ávila, nº 2121, Bloco 1M, Sala 212 - Bairro Santa Mônica, Uberlândia-MG, CEP 38400-902
Telefone: (34) 3239-4282 - www.posgrad.mecanica.ufu.br - secposmec@mecanica.ufu.br

ATA DE DEFESA - PÓS-GRADUAÇÃO

Programa de Pós-Graduação em:	Engenharia Mecânica				
Defesa de:	Tese de Doutorado Acadêmico, nº 329, COPEM				
Data:	28/07/2022	Hora de início:	08:00	Hora de encerramento:	10:18
Matrícula do Discente:	11823EMC002				
Nome do Discente:	Bruno Silva de Lima				
Título do Trabalho:	PHYSICAL EXPERIMENTATION AND NUMERICAL SIMULATION OF LIQUID FILM: COMPARISON OF EULERIAN METHODS				
Área de concentração:	Transferência de Calor e Mecânica dos Fluidos				
Linha de pesquisa:	Dinâmica dos Fluidos e Transferência de Calor				
Projeto de Pesquisa de vinculação:					

Reuniu-se por meio de videoconferência a Banca Examinadora, designada pelo Colegiado do Programa de Pós-graduação em Engenharia Mecânica, assim composta: Professores Doutores: João Marcelo Vedovotto - FEMEC/UFU; Daniel Dall'Onder dos Santos - FEMEC/UFU; Rudolf Huebner - UFMG; Martin Sommerfeld - Otto-von-Guericke-Universität Magdeburg e Francisco José de Souza - FEMEC/UFU, orientador do candidato.

Iniciando os trabalhos, o presidente da mesa, Dr. Francisco José de Souza, apresentou a Comissão Examinadora e o candidato, agradeceu a presença do público, e concedeu ao Discente a palavra para a exposição do seu trabalho. A duração da apresentação do Discente e o tempo de arguição e resposta foram conforme as normas do Programa.

A seguir o senhor(a) presidente concedeu a palavra, pela ordem sucessivamente, aos(às) examinadores(as), que passaram a arguir o(a) candidato(a). Ultimada a arguição, que se desenvolveu dentro dos termos regimentais, a Banca, em sessão secreta, atribuiu o resultado final, considerando o(a) candidato(a):

Aprovado.

Esta defesa faz parte dos requisitos necessários à obtenção do título de Doutor.

O competente diploma será expedido após cumprimento dos demais requisitos, conforme as normas do Programa, a legislação pertinente e a regulamentação interna da UFU.

Nada mais havendo a tratar foram encerrados os trabalhos. Foi lavrada a presente ata que após lida e achada conforme foi assinada pela Banca Examinadora.

Documento assinado eletronicamente por **Francisco José de Souza**, **Professor(a) do Magistério**

Superior, em 28/07/2022, às 10:19, conforme horário oficial de Brasília, com fundamento no art. 6º, § 1º, do Decreto nº 8.539, de 8 de outubro de 2015.

Documento assinado eletronicamente por **Daniel Dall'Onder dos Santos**, **Professor(a) do Magistério Superior**, em 28/07/2022, às 10:24, conforme horário oficial de Brasília, com fundamento no art. 6º, § 1º, do Decreto nº 8.539, de 8 de outubro de 2015.

Documento assinado eletronicamente por **João Marcelo Vedovotto**, **Professor(a) do Magistério Superior**, em 28/07/2022, às 10:24, conforme horário oficial de Brasília, com fundamento no art. 6º, § 1º, do Decreto nº 8.539, de 8 de outubro de 2015.

Documento assinado eletronicamente por **Rudolf Huebner**, **Usuário Externo**, em 28/07/2022, às 10:25, conforme horário oficial de Brasília, com fundamento no art. 6º, § 1º, do Decreto nº 8.539, de 8 de outubro de 2015.

Documento assinado eletronicamente por **Martin Josef Sommerfeld**, **Usuário Externo**, em 28/07/2022, às 10:26, conforme horário oficial de Brasília, com fundamento no art. 6º, § 1º, do Decreto nº 8.539, de 8 de outubro de 2015.

A autenticidade deste documento pode ser conferida no site https://www.sei.ufu.br/sei/controlador_externo.php?acao=documento_conferir&id_orgao_acesso_externo=0, informando o código verificador **3772083** e o código CRC **AB02BDC4**.

"Dream until your dreams come true" (Steven Tyler)

Acknowledgements

First of all I thank the two people who were able to make this dream possible, without them this work would not have even started and it is because of them that now it becomes true, my parents Kleverson and Jusenia. I also thank my brothers Gabriel and Rafael for their support, understanding and companionship. To my family members who always supported me and cheered for this achievement.

I thank all the masters who keep us dreaming; a special thanks to professor Francisco, who is the best example I have ever seen.

Thanks for the examination committee, that helped me improve the quality of this work.

Strange not to thank those who, however much time passes and the distance only seems to increase, our friendship remains strong and makes us look more and more like brothers; to my friends from my hometown, thank you so much for making my days so much happier.

Thank you for the worst room mechanical engineering has ever seen pass by UFMG that I could have the privilege of being part of. Our hours of reviews together were instrumental in giving me the strength to keep fighting for this dream. Thanks for all "Resenhas" for the companionship.

I thank the Milhagem-UFMG team who contributed a lot to my training as an engineer by showing me in practice the knowledge acquired in the classroom. Thanks to the other teams that contributed to our success, Baja, Formula and Uai-So-fly. During this period I also met amazing people who made me grow a lot.

I thank everyone who was part of the history of my shared apartment, which has had several names, Humble Residence, Uncle Allans Nursery, Masters House, but all just wanted to tell me that there, I and all who were part, were invited to understand the true meaning of the word 'welcome'. Many thanks to those who welcomed me.

Thanks to the Handsome guys and those with the last name WK and Halle, who on the other side of the world made me feel at home. Special thanks to the friends of LCFD, especially for the beautiful friendship built during all these years and for the great times we have lived together.

I thank everyone who welcomed me in Uberlândia, who received me in this new journey. I also like to express a huge gratitude to the friends of MFLab, who made this task much easier.

Thanks to Chai for the support, the understanding, the affection, the long conversations, and many more things that kept me believing.

Thanks God for always blessing me by putting all these people to guide me in this journey of so many joys.

I would like to express gratitude to Convergent Science Inc. for their assistance and for the use of the CONVERGE™ software. Acknowledgement is given to Universidade Federal de Uberlândia for providing the computational resources used for the CFD simulation presented and for Programa de Pós-graduação em Engenharia Mecânica – FEMEC/UFU for fostering research activities. This study was financed in part by the Coordenação de Aperfeiçoamento de Pessoal de Nível Superior - Brasil (CAPES) - Finance Code 001. Acknowledgements is also given to Otto-von-Guericke-Universität Magdeburg for providing the necessary physical experimentation resources.

DE LIMA, B. S., **EXPERIMENTAÇÃO FÍSICA E SIMULAÇÃO NUMÉRICA DE FILME LÍQUIDO: COMPARAÇÃO DE MÉTODOS EULERIANOS**, 2021. 243 p. Tese de doutorado, Universidade Federal de Uberlândia, Uberlândia-MG, Brasil.

Resumo

O presente trabalho baseia-se em modelos e resultados atuais publicados na literatura para implementar e avaliar diferentes metodologias com o objetivo de simular o comportamento de um filme líquido. O objetivo principal do trabalho é comparar as metodologias para solução numérica da formação de filme liquido, apresentando as principais vantagens de cada uma delas. Duas diferentes abordagens são utilizadas, o método Volume de Fluido (VOF) e o método Eulerian Wall Film (EWF). Para cumprir o objetivo da tese, o programa comercial Convergent Science Inc.'s CONVERGE ^{TM} CFD foi utilizado para modelagem pelo método VOF. Este software adota técnicas de refinamento de malha adaptativa (AMR),que foram utilizadas para realizar as simulações. Outra técnica utilizada foi a de passo de tempo adaptativo. As variações foram dependentes do número de Courant–Friedrichs–Lewy (CFL) e tiveram uma grande diferença para simulações com o modelo High-Resolution Interface Capturing (HRIC) e o modelo Piece-wise Linear Interface Calculation (PLIC). Para o esquema HRIC, as simulações foram executadas com um passo de tempo de aproximadamente $5{,}10^{-6}$, enquanto as simulações usando o esquema PLIC foram executadas com um passo de tempo mínimo predefinido de $1{,}10^{-7}$, o que significa que passos de tempo ainda menores seriam necessários. Essas observações se opõem aos resultados observados para escoamentos alinhados com a malha apresentadados em trabalhos passados. O escoamento de gás foi considerado incompressível. O número máximo de iterações PISO por etapa de tempo é definido como 20 com tolerância de 10^{-5}. Para a modelagem do fechamento de turbulência, foi utilizado o modelo $RNG\ k-\epsilon$. Já os modelos utilizados neste trabalho para modelagem EWF foram implementados no codigo Unsteady Cyclone Flow - 3D (Unscyfl3D), código que está em constante desenvolvimento no laboratório de mecânica dos fluidos da Universidade Federal de Uberlândia. Este código se caracteriza por simular escoamentos multifásicos laminares e turbulentos. Para tal, as Equações de Navier-Stokes são resolvidas na forma incompressível por meio do método dos volumes finitos em malhas não estruturadas e arranjo colocalizado. Para o acoplamento pressão velocidade o algoritmo SIMPLE foi implementado. Esse código já foi amplamente validado com resultados relevantes na literatura para escoamentos com partículas. Na primeira etapa do trabalho, experimentos físicos foram realizados no laboratório da Otto-von-Guericke-Universität Magdeburg. Para a experimentação física, um injetor foi usado para gerar uma cadeia de gotas de água que colidem com a parede oposta, formando um filme líquido. As imagens das gotas foram obtidas usando duas câmeras de gravação de alta velocidade. Os resultados para diferentes tamanhos de gotas e ângulos de impacto são apresentados e uma relação entre o parâmetro de momentum e o tamanho adimensional da poça foi estabelecida. Esses resultados também são usados para comparação com os resultados numéricos. Na segunda parte do trabalho os resultados dos experimentos físicos foram comparados com os resultados das simulações numéricas com o método VOF. Concluiu-se que o esquema HRIC pode lidar melhor com o não alinhamento do escoamento do fluido com a malha, pois o esquema PLIC distorceu a forma das gotas redondas. Entretanto, o esquema PLIC mantém uma interface mais nítida que o esquema HRIC. Por outro lado, o esquema HRIC é mais eficiente computacionalmente que o esquema PLIC. Na terceira etapa do trabalho dois casos teste foram analisados. O primeiro caso é referente ao espalhamento de uma gota em uma superfície plana. Este caso foi resolvido analiticamente em um trabalho encontrado na literatura e comparado a testes físicos experimentais. Esse caso é mais simples e logo pode ser usado para validação do esquema numérico e os efeitos da pressão capilar. O segundo experimento consiste em um jato que interage com um escoamento cruzado muito semelhante a injeção de combustível em atomizadores por jato de ar, cujos experimentos foram realizados por outros pesquisadores e foram publicados em formato de artigo. Nesse caso o modelo Eulerian Wall Film (EWF) foi validado para diferentes modelos de turbulência. Avaliações da estabilidade do modelo perante suas principais variáveis foram realizadas. Os resultados da formação de filme líquido se mostraram satisfatórios perante a comparação com testes de experimentos físicos. As principais observações são de que o modelo SST pode prever melhor o comportamento do filme líquido, já que o k-ϵ e o k-ϵ otimizado subestimam a formação do filme líquido. Um extenso estudo de diferentes metodologias foi apresentado. Cada uma das técnicas avaliadas tem sua importância em problemas de engenharia. Como as metodologias VOF consomem mais tempo computacional do que as abordagens EWF, elas são utilizadas para resolver problemas que envolvem domínios computacionais menores, bem como aprofundar o conhecimento em fenômenos envolvendo escoamentos multifásicos. Os resultados numéricos deste tipo de simulações podem ser usados para desenvolver ferramentas numéricas que consomem menos tempo computacional, como o método EWF. Como o método EWF consome menos tempo computacional quando comparado ao método VOF, ele pode ser usado para otimizar processos de engenharia mais realistas. Como exemplo, o escoameno dentro de uma câmara de combustão de turbina pode ser previsto por essas modelagens, auxiliando na otimização mais rápida do projeto. Embora ainda seja necessária uma avaliação mais aprofundada para abranger uma gama mais ampla de casos e uma maior variedade de abordagens numéricas, um passo importante foi dado no presente trabalho para um melhor entendimento da dinâmica do filme líquido e aprimoramento das técnicas numéricas.

Palavras-chave: Formação de filme líquido fino, jato liquido em escoamento cruzado, Eulerian Wall Film (EWF), Câmera de alta velocidade, Colisão de gotas, Volume de fluido (VOF), PLIC, HRIC.

DE LIMA, B. S., **PHYSICAL EXPERIMENTATION AND NUMERICAL SIMULATION OF LIQUID FILM: COMPARISON OF EULERIAN METHODS**, 2021. 243 p. Ph.D. thesis, Federal University of Uberlândia, Uberlândia-MG, Brazil.

Abstract

The present work is based on current models and results published in the literature to implement and evaluate different methodologies in order to simulate the behaviour of a liquid film. The main objective of this work was to compare the methodologies for numerical solution of liquid film formation, presenting the main advantages of each one of them. Two different approaches were used, the Volume of Fluid (VOF) method and the Eulerian Wall Film (EWF) method. To fulfil the objective of the thesis, the commercial software Convergent Science Inc.'s CONVERGE ^{TM} CFD was used to run the simulations with the VOF method. This software adopts adaptive mesh refinement (AMR) techniques, which were used to perform the simulations. Another technique used was the adaptive time step. The variations were dependent on the Courant–Friedrichs–Lewy (CFL) number and had a big difference for High-Resolution Interface Capturing (HRIC) and Piece-wise Linear Interface Calculation (PLIC) simulations. For the HRIC scheme, the simulations were run with a time step of approximately 5.10^{-6}, while the simulations using the PLIC scheme were run with a predefined minimum time step of 1.10^{-7}, which means it would require even smaller time steps. These observations were contrary to the results observed for flows aligned with the mesh presented in previous works. The gas flow was considered incompressible. The maximum number of PISO iterations per time step was set to 20 with a tolerance of 10^{-5}. To model the turbulence closure model, the $RNG\ k-\epsilon$ model was used. The models used in this work for EWF modelling were implemented in the code Unsteady Cyclone Flow - 3D (Unscyfl3D), code that is under constant development in the fluid mechanics laboratory of the Federal University of Uberlândia. This code is characterised by simulating laminar and turbulent multi-phase flows. For this, the Navier-Stokes equations are solved in incompressible form by means of the finite volume method in unstructured meshes and co-localised array. For pressure-velocity coupling the SIMPLE algorithm was implemented. This code has already been widely validated with relevant results in the literature for particle flows. In the first stage of the work, physical experiments were carried out in the laboratory of Otto-von-Guericke-Universität Magdeburg. For physical experimentation, an injector was used to generate a chain of water droplets that collide with the opposite wall, forming a liquid film. Droplet images were obtained using two high-speed recording cameras. The results for different droplet sizes and impact angles are presented and a relation between the momentum parameter and the dimensionless pool size was established. These results are also used for comparison with numerical results. In the second part of the work the results of the physical experiments were compared with the results of the numerical simulations with the VOF method. It was concluded that the HRIC scheme can better deal with the non-alignment of the fluid flow with the mesh, as the PLIC scheme distorted the shape of the round drops. However, the PLIC scheme maintained a sharper interface than the HRIC scheme. On the other hand, the HRIC scheme was more computationally efficient than the PLIC scheme. In the third part of the work, two test cases were analysed. The first case refers to the spreading of a drop on a flat surface. This case was solved analytically and is found on the literature and compared to physical experimentation tests. This case is simpler and therefore can be used to validate the numerical scheme and the effects of capillary pressure. The second experiment consists of a jet that interacts with a cross flow, which is very similar to fuel injection in air jet atomisers, whose experiments were performed another author and was published as a paper. In this case, the Eulerian Wall Film (EWF) model was validated for different turbulence models. Assessments of the stability of the model against the main variables that consists the same were carried out. The results of the formation of liquid film were satisfactory when compared with tests of physical experiments. The main observation was that the SST model can better predict the liquid film behaviour, since the optimised k-ϵ and k-ϵ underestimate the liquid film formation. An extensive study of different methodologies was presented. Each of the evaluated techniques has its importance in engineering problems. As VOF methodologies are more time consuming than EWF approaches, they are used to solve problems involving smaller computational domains, as well as to deepen the knowledge on phenomena involving multi-phase flows. The numerical results of this type of simulation can be used to develop less time consuming numerical tools, such as the EWF method. As the EWF method is less time consuming than the VOF method, it can be used to optimise more realistic engineering process. As an example, the flow within a turbine combustion chamber can be predicted by these models, aiding in faster design optimisation. Although further evaluation is still needed to cover a wider range of cases and a greater variety of numerical approaches, an important step has been taken in the present work towards a better understanding of liquid film dynamics and improvement of numerical techniques.

Keywords: Thin liquid film formation, liquid jet in cross flow, Eulerian Wall Film (EWF), High Speed Camera, Droplet Collision, Fluid Volume (VOF), PLIC, HRIC.

DE LIMA, B. S., **PHYSIKALISCHE EXPERIMENTATION UND NUMERISCHE SIMULATION VON FLÜSSIGFILM: VERGLEICH DER EULERIANISCHEN METHODEN**, 2021. 243 s. Doktorarbeit, Bundesuniversität Uberlândia, Uberlândia-MG, Brasilien.

Zusammenfassung

Die vorliegende Arbeit basiert sich auf aktuellen Modellen und Ergebnissen, die in der Literatur veröffentlicht wurden, um verschiedene Methoden zu implementieren und zu evaluieren, um das Verhalten eines Flüssigkeitsfilms zu simulieren. Das Hauptziel dieser Arbeit war es, die Methodologien zur numerischen Lösung der Flüssigkeitsfilmbildung zu vergleichen und die Hauptvorteile jeder von ihnen darzustellen. Dafür wurden es zwei unterschiedliche Ansätze verwendet, die Volume of Fluid (VOF)-Methode und die Eulerian Wall Film (EWF)-Methode. Um das Ziel der Diplomarbeit zu erreichen, wurde die kommerzielle Software CONVERGE ^{TM} CFD von Convergent Science Inc. für die Modellierung mit der VOF-Methode verwendet. Diese Software verwendet Techniken zur adaptiven Netzverfeinerung (AMR), die zur Durchführung der Simulationen verwendet wurden. Eine zusätzliche verwendete Technik war der adaptive Zeitschritt. Die Variationen waren abhängig von der Courant–Friedrichs–Lewy (CFL) Zahl und führten zu bedeutenden Unterschiede für High-Resolution Interface Capturing (HRIC) und Piece-wise Linear Interface Calculation (PLIC) Simulationen. Für das HRIC-Schema wurden die Simulationen mit einem Zeitschritt von etwa $5{,}10^{-6}$ ausgeführt, während die Simulationen, die das PLIC-Schema verwenden, mit einem vordefinierten minimalen Zeitschritt von $1{,}10^{-7}$ ausgeführt wurden. Das heißt, dass es noch kleinere Zeitschritte erfordert würden. Diese Beobachtungen stehen im Gegensatz zu einander wenn verglichen mit den Ergebnissen, die für Strömungen beobachtet wurden, ausgerichtet auf das Netz, wie es durch frühere Arbeiten dargestellt wird. Der Gasstrom wurde für inkompressibel gehalten. Die maximale Anzahl von PISO-Iterationen pro Zeitschritt war auf 20 mit einer Toleranz von 10^{-5} eingestellt. Zur Modellierung des Turbulenzschlusses wurde das $RNG\ k-\epsilon$-Modell verwendet. Die verwendeten Modelle in dieser Arbeit für die EWF-Modellierung wurden im Code Unsteady Cyclone Flow - 3D (Unscyfl3D) implementiert. Dieser Code wird ständig im Strömungsmechaniklabor der Federal University of Uberlândia weiterentwickelt. Dieser Code zeichnet sich durch die Simulation laminarer und turbulenter Mehrphasenströmungen aus. Dazu werden die Navier-Stokes-Gleichungen in inkompressibler Form durch die Finite-Volumen-Methode in unstrukturierten Netzen und kolokalisierten Arrays gelöst. Für die Druck-Geschwindigkeits-Kopplung wurde der SIMPLE-Algorithmus implementiert. Dieser Code wurde bereits umfassend mit relevanten Ergebnissen in der Literatur für Partikelströmungen validiert. Im ersten Arbeitsschritt wurden physikalische Experimente im Labor der Otto-von-Guericke-Universität Magdeburg durchgeführt. Für physikalische Experimente wird ein Injektor verwendet, um eine Kette von Wassertropfen zu erzeugen, die mit der

gegenüberliegenden Wand kollidieren und einen Flüssigkeitsfilm bilden. Tröpfchenbilder wurden unter Verwendung von zwei Hochgeschwindigkeits-Aufzeichnungskameras erhalten. Die Ergebnisse für verschiedene Tröpfchengrößen und Aufprallwinkel wurden präsentiert und es wurde eine Beziehung zwischen dem Momentenparameter und der dimensionslosen Pfützengröße hergestellt. Diese Ergebnisse wurden auch zum Vergleich mit numerischen Ergebnissen verwendet. Im zweiten Teil der Arbeit wurden die Ergebnisse der physikalischen Experimente mit den Ergebnissen der numerischen Simulationen mit der VOF-Methode verglichen. Es wurde geschlossen, dass das HRIC-Schema besser mit der Nichtausrichtung des Flüssigkeitsflusses mit dem Netz umgehen kann, da das PLIC-Schema die Form der runden Tropfen verzerrte. Darüber hinaus behält das PLIC-Schema eine schärfere Schnittstelle als das HRIC-Schema bei. Andererseits ist das HRIC-Schema rechnerisch effizienter als das PLIC-Schema. In der dritten Phase der Arbeit wurden zwei Testfälle analysiert. Der erste Fall bezieht sich auf die Streuung eines Tropfens auf einer ebenen Fläche. Dieser Fall wurde von anderen Autoren analytisch gelöst und mit experimentellen Tests verglichen. Dieser Fall ist einfacher und kann daher verwendet werden, um das numerische Schema und die Auswirkungen des Kapillardrucks zu validieren. Das zweite Experiment besteht aus einem Strahl, der mit einer Querströmung interagiert, sehr ähnlich der Kraftstoffeinspritzung in Luftstrahlzerstäubern, deren Experimente von anderen Autoren durchgeführt und als Aufsätze veröffentlicht wurden. In diesem Fall wurde das Eulerian Wall Film (EWF)-Modell für verschiedene Turbulenzmodelle validiert. Bewertungen der Stabilität des Modells gegenüber den Hauptvariablen des Modelles wurden durchgeführt. Die Ergebnisse der Flüssigkeitsfilmbildung waren im Vergleich zu physikalischen Experimenten zufriedenstellend. Die Hauptbeobachtungen sind, dass das SST-Modell das Flüssigkeitsfilmverhalten besser vorhersagen kann, da die optimierten k-ϵ und k-ϵ die Flüssigkeitsfilmbildung unterschätzen. Es wurde umfassende Untersuchung verschiedener Methoden vorgestellt. Jeder bewertete Techniken hat ihre Wichtigkeit für technische Probleme. Da VOF-Methoden rechenintensiver als EWF-Ansätze sind, werden sie verwendet, um Prozesse zu optimieren, die kleinere Rechendomänen betreffen, sowie um das Wissen über Phänomene zu vertiefen, die Mehrphasenströmungen betreffen. Die numerischen Ergebnisse dieser Art von Simulation können sogar verwendet werden, um weniger rechenintensiv numerische Werkzeuge wie die EWF-Methode zu entwickeln. Da die EWF-Methode weniger rechenintensiv ist als die VOF-Methode, kann sie verwendet werden, um realistischere technische Probleme zu lösen. Beispielsweise kann die Strömung innerhalb einer Turbinenbrennkammer durch diese Modelle vorhergesagt werden, was zu einer schnelleren Konstruktionsoptimierung beiträgt. Obwohl noch weitere Auswertungen erforderlich sind, um ein breiteres Spektrum von Fällen und eine größere Vielfalt numerischer Ansätze abzudecken, es wurde in der vorliegenden Arbeit ein wichtiger Schritt in Richtung eines besseren Verständnisses der Dynamik von Flüssigkeitsfilmen und der Verbesserung numerischer Techniken unternommen.

Schlüsselwörter: Bildung eines dünnen Flüssigkeitsfilms, Flüssigkeitsstrahl im Querstrom, Eulerian wall film (EWF), Hochgeschwindigkeitskamera, Tröpfchenkollision, Flüssigkeitsvolumen (VOF), PLIC, HRIC.

Figures

Tables

Abbreviations and Acronyms

Latin letters

A - amplitude or area
a - weight-buyoancy force divided by the mass
A_f - area vector outward the face or surface area of the impacted face
ap_L - coefficient used for the approximation scheme of momentum interpolation method
ap_R - coefficient used for the approximation scheme of momentum interpolation method
b - distance between the center of the reference drop and the line that passes in the center of the second drop that contains the relative speed or impact parameter
b_{crit} - critical impact parameter
B - impact number
C - constant to evaluate the non-dimensional velocity parallel to the wall
c - damping coefficient
Ca - Capillary number
C_μ - adjustable parameter for the turbulence modelling
C_σ - constant
$C_{1\epsilon}$ - adjustable parameters for the turbulence modelling
$C_{2\epsilon}$ - adjustable parameters for the turbulence modelling
c_{iD} - droplet velocity
C_B - dimensionless constants for the TAB model
C_d - drag coefficient
C_f - dimensionless constants for the TAB model or Courant number
C_k - dimensionless constants for the TAB model
C_o - Courant number
D - diameter or distance between the cell centers
d - distance between the considered faces or plane equation constant
d_{edge} - size of the edge
D_{iD} - droplet diameter
d_{jet} - jet diameter
d_0 - average diameter

d_f - position of the center of the face
d_{face} - distance between the considered faces
d_l - diameter of the other drop involved in the collision process
d_s - diameter of a droplet
d_w - distance to the nearest wall
ds - the distance of the elements center
$\vec{e}_s$ - unit vector from the centroid of the left element to the right element
f - values at the cell face
F - external force or working angle constant (also found in calibration certificate)
$F_{w,b}$ - combined buoyancy-weight force
F_d - drag force
g - gravity
g_τ - gravity component parallel to the surface
h - film height or thickness across the interface between fluids
$\bar{h}_F$ - mean film height
$\dot{h}$ - flux of film height
h^* - normalized film height
h_0 - non dimensional film height
i - x direction or level of refinement of the mesh
ij - suffix notation
j - y direction
J - liquid to jet momentum ratio
k - interface curvature or z direction or model constant on TAB set to $10/3$ or spring stiffness
K - average kinetic energy or ball constant according to test certificate or mean kinetic energy or parameter to evaluate liquid deposition or turbulent kinetic energy per unit mass or combination of Ca and La non dimensional numbers
$\overline{\nabla k}$ - average gradient calculated from adjacent finite volumes
$k(t)$ - instantaneous kinetic energy
k_f^* - first approximation of the curvature at the face between the two cells
k_s - film roughness parameter
l - length scale
l_e - edge vector pointing outwards of the cell, whose modulus is the edge length.
l_{LR} - distance between both cell centres
La - Laplace number

m - mass or interface normal vector
$\dot{m}_p$ - flow rate of the droplet impinging on the wall surface or mass source term per unit wall area
N - number of elements in the mesh
n - unit normal to the interface or wall
$\vec{n}$ - vector pointing out the face
n_{ij} - unit vector normal to the considered face
n_{wi} - unit vector normal to the wall
n_i - surface normal at the cell next to the wall
nf - represents the number of faces
Oh - Ohnesorg number
P - for the pressure
∇p_f - gradient evaluated between the considered faces
P_σ - pressure due to surface tension
P_{gas} - gas flow pressure
P_h - pressure due to film height
P_L - liquid film pressure
q - momentum of the droplet
$\dot{q}$ - momentum source term due to droplet collection or separation
R - ratio that can represent a monotonic convergence if less than unity in GCI
r - radius
r_1 - radius of the biggest droplet
r_2 - radius of the smallest droplet
r_0 - e undisturbed droplet radius
r_fc - position of the center of the finite volumes faces cell
r_p - new position of the cell
r_r - droplet size ratio (r_1/r_2)
Re_{k_s} - roughness Reynolds number
s - curvature
∇_s - surface gradient operator
S_{ij} - average rate of deformation
S_{Mi} - source term for momentum in the i direction
s_{cd} - momentum parameter
S_{ij} - average ratio of deformation
s_{ij} - ratio of deformation
t - time or travelling time of the ball
t_d - turbulence correlation time
t_l - film thickness

$t_w i$ - unit vectors tangential to the wall
ts - current time step
Δt - represents the time step
T^* - non dimension temperature
T_{sat} - saturation temperature
T_w - wall temperature
U - average velocity on the x direction or relative velocity
u - average velocity
u - velocity in x direction
u_i - velocity in i direction
$u(t)$ - instantaneous velocity
u^+ - non-dimensional velocity parallel to the wall
u_τ - friction velocity
$u_{i,t}$ - instantaneous fluid velocity
u^*_{if} - first approximation of the velocity on the considered face
u_i - velocity and the subscript stands for the current direction
$\vec{U}^2_{rel}$ - relative velocity
$\vec{U}_g$ - average vector velocity over cells neighboring the injection point for the gas phase
$\vec{U}_l$ - average vector velocity over cells neighboring the injection point for the liquid phase
v - velocity in y direction
v_d - average velocity
V - average velocity on the y direction or general vector velocity or volume
v_∞ - air velocity or droplet velocity or jet velocity
V_f - liquid film velocity
V_g - velocity of the gas
V_m - velocity modulus of the droplet
V_n - normal velocity of the droplet
V_S - source term for liquid film velocity
V_d - volume of the droplets in the impacting parcel
$\vec{V}_l$ - liquid film velocity
$\vec{V}_P$ - particle velocity
W - average velocity on the z direction
w - oscillation frequency or pool size or velocity in z direction
w_0 - non dimensional pool size
We - Weber number
We_c - Weber number of the collision

x - displacement of the drop from its undisturbed position or distance from the light source to the furthest light reflection or distance from the nozzle in the downstream direction at the jet or nozzle center line or particle position or general position

x_{dry} - distance from the light source to the furthest light reflection in the absence of liquid film

x_b - x distance where breakup occur

X - distance

Δx - represents the cell base size.

y - distance (along the jet) of the liquid jet from the exit

Y - random number between 0 and 1

$y(t)$ - non dimensional distance

y^+ - non-dimensional wall distance

y_b - y direction distance where breakup occur

Greek letters

α - VOF transport variable or the parameter that evaluates if the solution is in the asymptotic range in GCI

α_{iD} - impingement angle

α_{imp} - impingement angle

α_{impact} - impact angle

α_{sd} - secondary droplet angle

$\tilde{\alpha}(x)$ - modified void fraction

$\tilde{\beta}$ - intermediate parameter used in HRIC scheme for variable approximation

δ - liquid film thickness

δ_{ij} - Kronecker Delta

δ_S - Dirac distribution concentrated on the interface S

Δt - time step

ϵ - rate of dissipation of turbulent kinetic energy per unit mass or tiny number in the order of zero machine

η - deposit mass fraction or dynamic viscosity

γ_f - represents the blending factor

γ_{LG} - surface tension of the liquid

γ_{SG} - surface free energy of the solid

γ_{SL} - solid/liquid interfacial tension

κ - is the Von Kármán constant or local curvature in the VOF method
λ_b - dimensionless wave length
λ_c - column wave length
μ_{lq} - liquid viscosity
μ_t - turbulent viscosity
μ_g - dynamic gas viscosity
μ_l - liquid dynamic viscosity
μ_t - eddy viscosity
ν - kinematic viscosity.
Φ - convective velocity parameter
ϕ - Gaussian filter interpolation function or general variable or a chosen variable
ϕ_e - variable evaluated at the cell edge
ρ_f^* - first approximation of density
ρ_g - gas density
ρ - density of the fluid
ρ_1 - density of the ball
ρ_2 - density of the liquid
ρ_l - liquid density
σ - surface tension coefficient
σ_ϵ - Prandtl numbers that connects the diffusivity of ϵ to the eddy viscosity
σ_k - Prandtl number that connects the diffusivity of k to the eddy viscosity
σ_τ - surface tension coefficient
τ - stress tensor
τ_{fs} - wall shear stress
τ_p - relaxation time
θ - contact angle
θ_{cvl} - reflection angle of the liquid
θ_f - the angle between the vector normal to the fluid interface and the vector connecting the center of the fluid interface cell to the center of acceptor cell
θ_w - contact angle on the wall
ϑ - velocity scale

Acronyms

AtoMIST	Atomization Model Interfaced with Surface Tracking
AMR	Algebraic Multigrid
CAP	Contribution of the ap coefficients
CDS	Central difference scheme
CFD	Computational Fluid Dynamics
CICSAM	Compressive Interface Capturing Scheme for Arbitrary Meshes
CLSVOF	Coupled Level-Set and Volume of Fluid
CSF	Continuum Surface Force model
DNS	Direct Numerical Simulation
DPM	Discrete Particle Model
EWF	Eulerian Wall Film
FVM	Finite Volume Method
GCI	Grid Convergence Index
HRIC	High Resolution Interface Capturing
KH − RT	Kelvin-Helmholtz Rayleigh-Taylor
LDA	Laser-Doppler anemometry
LED	Light-emitting diode
LIF	Laser Induced Fluorescent
LJIC	Liquid Jet in Cross Flow
LWENO	Linear Weighted Essentially Non-Oscillatory
MFLab	Fluid Mechanics Laboratory
MWI	Momentum Weighted Interpolation
NAG	Node-Averaged-Gauss
PDA	Phase Doppler Anemometry
PDPA	Phase Doppler Particle Analyzer
PISO	Pressure Implicit with Splitting of Operator
PLIC	Piecewise-Linear Interface Calculation
RIM	Refractive Index Matching
SAMR	Structured Adaptive Mesh Refinement
SIMPLE	Semi-Implicit Method for Pressure-Linked Equations
SST	Shear Stress Transport
TAB	Taylor analogy break-up
URANS	Unsteady Reynolds Average Navier-Stokes equations
UFU	Federal University of Uberlândia
UNSCYFL3D	Unsteady Cyclone Flow 3D
VOF	Volume of Fluid

Subscripts

A - represents the acceptor cell
d - droplet parameters
D - represents the Donor cell
e - face at the east or cell edge

E - represents the cell at the east
f - denotes value at the face
g - denotes generated which stands for secondary droplets
L - denotes the cell on the left side
P - the current cell
p - indicates that it is related to a particle or droplet
R - denotes the cell on the right side
s - source
$t+1$ - denotes an advance in time step
U - denotes upwind cells

Superscripts

$'$ - represents the fluctuation
$*$ - denotes a first approximation in the velocity-pressure coupling algorithm or value correction to avoid alignment
$**$ - represents the variable correction considering Courant number in HRIC scheme
$\bar{}$ - denotes an averaged quantity or normalized variable
$\tilde{}$ - represents normalized variable
$\vec{}$ - vector quantity
n - indicates the current time step
$n+1$ - future time step
$n-1$ - previous time step

SUMMARY

1 Introduction

The study of multi-phase flows is of great importance for engineering, since there is a wide range of phenomena described by the interaction between fluids and between fluids and solid walls. Among them there are natural processes such as the rain drop, which can cause soil erosion and is also a medium to transport bacteria and spores, as quoted by Morton et al. (2000). The impact of rain drops also influences in the air-sea gas exchange as well as in the damping of wave motion, as in the work of Morton et al. (2000).

There are also industrial processes involving multi-phase flows such as coating, painting, fuel injection, and irrigation. To effective achieve the desired results in each of these processes, the instruments must be correctly characterised and applied. For example, the jet spray used in painting and coating process, has to be accurately applied onto the surface of the subject to obtain the best quality of the finishing as cited in the works of Li et al. (2010a) and Li et al. (2010b). In the case of fuel injection in internal combustion engines, the spray has to be correctly characterised. This is done to achieve improvements in the combustion process reducing fuel consumption and engine emission, as stated in the works of Baumgarten (2006), Shim et al. (2008), and Heywood (1988).

The correct usage of irrigation instruments leads to a decrease of water consumption as well as avoid soil erosion. Noticing that sprinkler irrigation is responsible for half of annual consumption of water, the optimisation of this process is extremely important, as in the work of Stevenin et al. (2016).

The interaction between fluids and solid walls might form liquid films. These liquid films are often found in engineering applications with thicknesses ranging from micrometer scales to meter scales. To model such phenomenon, different approaches are found on the literature.

The liquid film flow modelling and characterisation is important for many applications, including steam power generation, crude oil supply and refining, chemical processing, and refrigeration systems. For instance, the injection of fuel in an internal combustion engine is subjected to wall impingement, which directly affects the outcome of the combustion process. Many methods for measuring and predicting these phenomena have been developed including physical experiments as well as numerical-computational techniques. The improvement in the characteristics of this process makes them more efficient and less environmentally degrading, as presented in the work of Shedd and Newell (1997).

The understanding of the physics involving the multi-phase flow phenomena as well as the wall film formation is a fundamental step in order to improve these processes. For that purpose, numerical methods have been increasingly used in complex engineering tasks, providing results in scenarios where experiments may not be feasible. The Computational Fluid Dynamics (CFD) approach has proven to be a powerful and valuable tool to reach the state-of-art in engineering, reducing costs and development time, as mentioned in the work of Fontes et al. (2018a).

One of the major difficulties in simulating these phenomena is to correctly predict the interaction between the fluids and the surface. For that, different approaches have been used, such as Eulerian, Eulerian-Lagrangian, and Hybrid methods. For the Eulerian approach several methodologies can be used to track the interface between fluids, which include the front-tracking, level-set and volume of fluid (VOF) methods. Among them, the VOF is an attractive option as it is locally and globally mass conservative as stated by Fontes et al. (2018a) and Morton et al. (2000).

Unlike the mentioned approaches, which are solved in a three dimensional system, the EWF model, is a numerical tool to simulate liquid films. This type of model is solved in specific surfaces and no linear systems are involved. On the other hand, this model has some limitations and only holds when the liquid film is thin when compared to the surface curvature. More details of the models are presented in the next chapter.

In this thesis, the evaluation of different methodologies to numerically solve a liquid film are presented. The objective is to advance the research on the formation of liquid film on walls by testing different approaches, highlighting the main advantages, limitations, and the influence of the main parameters on the results.

1.1 Objectives

This thesis aims to evaluate numerical models capable of describing the phenomenon of formation of liquid film on a surface by means of different approaches. The numerical methods used to address such tasks are the VOF and EWF models. These methods were painstakingly evaluated in this work in order to ponder the impact of the main parameters on the governing equations. To better evaluate the influence of different parameters in the VOF model, a physical experimentation was designed.

The following may be listed as specific objectives of this project:

- Perform physical experimentation to acquire data for VOF liquid film simulations validation. The experiments presented data that were not yet available on the literature, with details that are challenging to reproduce with the VOF approach.

- Validate the VOF numerical method by comparing with physical experimental results. This step is also carried out to evaluate the influence of several parameters on the numerical methods.

- Implement computational models verifying the most suitable for unstructured meshes in Eulerian-Lagrangian approaches, assessing the main parameters. This implementation improves the quality of UNSCYFL3D (Unsteady Cyclone Flow - 3D) code, which is under constant development in the fluid mechanics laboratory of the Federal University of Uberlândia.

The novelty of this work consists of the evaluation of the limits of each approach within its framework of modelling, assessing parameters in liquid film formation for the VOF approach as well as the EWF approach.

1.2 Thesis structure

This thesis follows a structure composed by seven chapters. In the current chapter, an introduction of the work is presented, covering the motivation to study wall formation and the objectives of the thesis.

In Chapter 2, the studied cases are illustrated as well as a bibliographic review about liquid cross flow and wall film formation, highlighting the main findings in this field. The physical and numerical results found in the literature are presented in order to introduce the studied case.

In Chapter 3, the models are presented. The physical, mathematical and numerical models used to run the simulations are presented in this chapter.

In Chapter 4, the experimental procedure is presented. The experimental rig is presented with its sketches and main equipment. The logic for the image analysing is detailed using FIJI software. The main results are presented and discussed.

In Chapter 5, the methodology for the numerical simulations is presented. The computational domain used and its features as well as boundary and initial conditions are described in this chapter.

In Chapter 6, the numerical results are presented and discussed. The used models are validated using data found in the literature for the case described in Chapter 2. The results are then discussed highlighting the main findings.

In Chapter 7, the main conclusions and suggestions for future works are presented.

2 Literature review

This chapter presents the necessary foundation for a better understanding of the physics of droplet impact and liquid film formation. The main works related to the objectives of this thesis are analysed, and used as basis for the creation of the methodology of this work. The chapter is divided in physical experimentation findings, numerical simulation findings, and comments summarising the importance of this chapter. The section containing numerical simulation findings is divided in the VOF findings and the EWF findings.

2.1 Physical experimentation findings

Several researchers are making effort to better describe the physics of droplet collision and liquid film formation. For that, numerical simulations and physical experimentation are being used. A briefly overview of works concerning physical experimentation in liquid film formation is presented in the current section.

Diez et al. (1994) developed an analytical solution for the spreading of a viscous droplet on a smooth rigid horizontal surface. The droplet has a positive value of spreading parameter, which means that it spreads spontaneously. The results were validated against physical experimentation. The results were normalised and the main observation was that the results for this non dimensional variables were independent of time.

Mundo et al. (1995) performed physical experimentation of liquid spray impingement on a flat surface. The main objective was to formulate an empirical model to describe the outcomes of the droplet collision, whether it is absorption or splashing. Droplets of ethanol, water, and a mixture of water-sucrose-ethanol were forced to impinge on a rotating disc. To correctly characterise the secondary droplets generated, a two-component phase Doppler anemometer was used. A correlation of deposition or splashing was achieved in terms of Reynolds and Ohnesorge numbers by means of the visualisation of the phenomena. For the calculation of the non dimensional number only the normal component of the impact velocity was considered.

Al-Roub et al. (1996) investigated the interactions between droplets and between droplet and liquid film on a heated wall by means of high speed imaging. Single droplets and multiple droplets collision were tested. This was done to provide insight on how to extrapolate data from one droplet collision to multiple droplets collision. Concerning the break-up of liquid film by droplet impingement, some observations were of great importance. One droplet might not be enough to break-up the liquid film, but if two droplets impinge over the liquid film and their energy interfere constructively for surface waviness, the film can break-up. This observation was captured for cases with Weber number of around 200 and time ratio of 0.5. Another observation was that thicker films behave like pool impingement, thus generate less secondary droplets as just a small portion of the energy is used for radial wave growth. As the number of impinging droplets grows, the number of ejected droplets also grows. On the other hand, the size and the velocity of the droplets are inversely proportional to the frequency of droplets impacting on the liquid surface.

Mao et al. (1997) studied the impact of droplets on flat surfaces at room temperatures. Using a high speed camera, different impact angles, impact velocities, wall roughness, and liquid viscosities were tested. It was observed that the liquid viscosity and the impact velocity have a high influence on the maximum spread of the droplet. A correlation for the maximum spread was achieved in terms of Reynolds number, Weber number, and contact angle. The outcomes for the collision are closely linked to the liquid viscosity and the static contact angle. A model for the rebound was proposed as a function of maximum spread and static contact angle.

Thoroddsen and Sakakibara (1998) also studied the impingement of a droplet on a solid surface. The study of the fingering pattern at the edge of the droplet expansion was studied. For that, imaging techniques were used to analyse the frontal face of the droplet. The splitting and merging process of the droplet was studied as well as the undulation. The images generated illustrates that the undulations starts in the moment of the impact, and the disturbances remains during the expansion of the droplet on the wall, evolving during spreading.

Rioboo et al. (2001) conducted experiments to qualitative verify the outcomes of droplet impacts upon wet wall. Different wall roughness and liquids were tested. The velocity impact was changed by moving the droplet generator up and down, getting further or closer to the wall surface. The results were summarised in outcomes such as splash, rebound, partial rebound, and deposition.

Mathews et al. (2003) used a pintle injector to inject iso-octane upon a flat Plexiglas plate. A Phase Doppler Particle Analyser (PDPA) was used to characterise the fuel spray droplets as well as the secondary droplets generated by the droplet impingement on the wall. Images of the fuel cloud were also generated using an unintensified CCD camera. To determine the thickness of the liquid film formed on the wall an optical technique was used. A comprehensive study was conducted to acquire data for spray impingement. Size and velocity of both the incoming and secondary droplets were measured. The shape and thickness of the liquid film could also be measured. The main objective was to generate data for different impingement angles. It was observed that the liquid film becomes closer to an elliptical shape when the injection angle is increased.

Panão and Moreira (2005) studied an intermittent gasoline spray impingement on the surface of a flat wall by means of a PDA technique. The spray was submitted to a cross flow of air. The experiments captured droplet size and velocity. Concerning the liquid film formation on the wall, a vortical structure was observed in the vicinity of wall. This structure captures droplets with small Reynolds numbers and make them impinge on the wall, causing the liquid film thickness to grow in such regions.

Moita and Moreira (2007) studied single droplet impact on heated walls. Images of the impact were generated by means of a high speed camera to characterise the droplet impact phenomena. The main objective was to quantify the outcomes of the secondary droplets generated. The results evidenced that the liquid dynamic is a complex combination of wettability, liquid properties, wall temperature and surface topography. The main objective was to describe the disintegration of the droplet during impact. Analysing the results, it was concluded that the liquid fuels could penetrate the roughness grooves of metallic surfaces, forming a homogeneous wetting system. The surface roughness did not considerably changed the results concerning crown growth rate, however, this growth was strongly influenced by the surface tension.

Okawa et al. (2008) conducted experiments of single water droplet impact on a planar water surface. To visualise the droplet, a high speed camera was used. The main objective was to investigate the effects of impinging angle on the outcomes of secondary droplets, specially the mass. For impingement angles less than 50°, an increase in the impingement angle causes a great increase in the mass of secondary droplets. When the impingement angle exceed 70° no secondary droplet was observed.

Samenfink et al. (1999) investigated the interaction of droplet with a shear-driven liquid film. The main focus was on the droplet splashing and the characteristics of the deposit mass and also the characteristics of the secondary droplets. In his work, a relation of the deposit mass fraction and the composition of the secondary droplet was found based on the droplet impact angle and film height. For the measurements, a Phase-Doppler-Anemometer (PDA) technique was used. In order to generalize the results as well as reduce the number of variables that are handled during the physical experiments, Samenfink et al. (1999) introduced some dimensionless numbers. The first of them is the momentum of the primary droplet (s_{cd}). This parameter is directly connected to the outcomes of the droplet collision on the wall surface. For low s_{cd} the droplet is absorbed by the liquid film. As s_{cd} grows there is a trend for formation of secondary droplets. The second dimensionless number is the Laplace number (La) that influences on the mean size and velocity of secondary droplets. The dimensionless height and impinging angle were used to generalise the results as well. To take the waviness of the liquid film in account, Samenfink et al. (1999) developed a system to characterise the waves and verify its influence on the outcomes of droplet impingement. The results were summarised in models for CFD implementation. The physical experiment consisted of the absorption of laser light to determine film height with a high temporal and spatial resolution. With his results, Samenfink et al. (1999) was then able to model the main variables for wet wall conditions. His models are the basis for a complete 2D simulation of the droplet impingement on a wall surface and film formation.

Shedd et al. (2009a) studied the impingement of a liquid jet on a solid wall surface. His experiment consisted in a planar representation of more complex and realistic fuel injector geometries. The reason for this simplification is to retain only the main relevant physics of the studied case, allowing easier diagnose for optical techniques. The development of a shear-driven film characterisation was carried out and was represented by two important dimensionless numbers, the Weber number and the momentum-flux ratios. For the visualisation of the liquid film formation by the impinging droplets, a high-speed digital imaging system was used. An important observation from his work is that the liquid film height grows in stream-wise direction and decreases in span-wise direction.

Moreira et al. (2010) conducted a painstaking overview of the droplet wall interaction. With his studies he concluded that for a deep understanding of complex spray-wall interaction, an important step is the foundation of the knowledge in simpler cases, such as the simple single droplet wall interaction.

Akop et al. (2013b) performed a physical experimentation to better understand the behaviour of the liquid film formed by the impact of droplets on wall. The main objective was to optimise the spray dispersion inside a Diesel engine, avoiding liquid film formation. In his work, different variables were analysed in order to asses their influence on the dynamics of the liquid film, such as impingement distance, injection pressure, and chamber pressure. For the experiments, a high-speed camera was used to record the spray and liquid film adhesion in a cold condition high pressure chamber. In conclusion, with an increase in the impingement distance the mass ratio also increases. The opposite behaviour was observed for the injection pressure. Continuing their work, Akop et al. (2013a) tested the influence of the disk size and angle on the spray adhesion. The disk diameter had low influence on the results, meanwhile the adhesion was decreased for an increase in the disk angle. In another work, Akop et al. (2014a) investigated the influence of the Weber number and concluded that an increase in the Weber number causes a strong decrease on the adhered mass ratio. An empirical correlation for adhered mass ratio, the adhered fuel thickness and the Weber number was achieved. In a separated work, Akop et al. (2014b) investigated the effect of the chamber pressure and the injection pressure on the adhered fuel mass. It was possible to conclude that for both the pressure of the chamber and the injection pressure, an increase in the pressure causes a decrease in the adhered mass fuel.

Luo et al. (2017) investigated the impingement of fuel sprays on a wall under engine conditions. In this work the spray impingement dynamic and liquid mass adhered to the wall were measured by means of Mie scattering and refractive index matching methods. The mass, area, and thickness were evaluated against different parameters, including wall roughness, injection pressure, and ambient pressure. Analysing the results, it was possible to conclude that an increase in the wall roughness decreased the spray tip penetration, and decrease the liquid film uniformity. Increasing the ambient pressure results in a more uniform distribution.

Ferrão et al. (2019) carried out physical experimentation in order to study the impingement of droplets on a dry sloped wall. The droplet is falling and its velocity is parallel to the gravitational force. Different fluids and different angles were tested. It was observed that splashing decreases with the decrease of the incident angle. With an increase in the Weber number the splashing is more likely to occur for the same angle of impact. The lamella development becomes different in longitudinal and transverse directions for low Weber numbers.

Xiao et al. (2019) claimed that the behaviour of impinging spray and corresponding film liquid were not yet thoroughly studied. To better analyse such phenomena, the macroscopic shape of the spray and the corresponding liquid film generated by the droplets impingement were measured simultaneously. MATLAB software was used for image analyses. A high speed camera was used to capture the shape of the spray, meanwhile for the liquid film measurement a Laser Induced Fluorescent (LIF) technique was used. To capture the film characteristics another high speed camera was used. The authors concluded that the radial penetration of the spray is wider than the generated liquid film formed by the impingement; the spray penetration is more sensitive to chamber pressure than the liquid film; the liquid film area increases with chamber pressure and injection pressure; and the liquid film thickness follows a different trend depending on the chamber pressure, i.e. for low chamber pressure an increase in injection pressure increases the liquid film thickness, however, in high chamber pressures an increase in injection pressure decreases the liquid film thickness.

Luo (2021) characterise the fuel spray and impingement under engine like conditions by means of a Mie scattering technique. The liquid film adhered to the wall was measured using a Refractive Index Matching (RIM). Different injection pressures, chamber pressures and temperatures were used. It was observed from the results that the injection pressure increases the liquid film mass and area in almost all cases. Specifically for the chamber temperature of 433 K, the injection pressure decreases the liquid film mass and area. This behaviour was observed due to a better atomization and easy evaporation of the spray. It was also observed that high ambient pressure increases the fuel film mass and area.

2.2 Numerical simulation findings

Among the approaches found in the literature to simulate droplet impingement and liquid film formation, there are Eulerian approaches, that consider both the gas phase and the liquid phase of the case as continuous fluids, as in the Volume of Fluid (VOF) method. This method is used to simulate multiphase flows. It consists of tracking the interface between fluids, in which they share the momentum and energy. In the first step, the void fraction of each cell is computed across the computational domain. This void fraction is the ratio of the volume of gas to the volume of liquid in each element. The value of the void fraction can be found in three different situations. The value can be zero representing only a first fluid in the cell. The value can be one, representing another fluid. In the last case the value can be between zero and one representing both fluids. In this work, the value 0 represents water and the value 1 represents air. The next paragraphs are dedicated to an overview of works concerning this approach.

Many authors cite the VOF methodology as being "Eulerian-Eulerian". In the present work the "Eulerian" nomenclature was adopted because it is considered more correct, since only one equation is solved for the fluids simultaneously. To differentiate the phases and the interface, the value of the volume fraction is considered in the equations.

Rider and Kothe (1995) used four different test cases to validate interface tracking schemes. The test cases included the translation of a solid body, rotation of a solid body, a single vortex, and a complex deformation field. The main findings are that the level set presented good agreement on the cases that the body being tracked does not deform, however, conservation of mass was not achieved.

Pasandideh-Fard et al. (1998) conduct physical experimentation and numerical simulations to study the impact and solidification of tin droplets upon a wall of stainless steel. High speed imaging was used to obtain images and the dynamic of the droplet spreading. The liquid solid contact angle was also measured from the images. By means of the SOLA-VOF program, the numerical simulations were run. The model computes the droplet deformation, solidification and heat transfer to the substrate. The values of contact angle were used as boundary condition for the numerical model. An analytical model was developed to predict the maximum spread of the droplet

Bussmann et al. (2000) investigated the fingering and splashing of a droplet impact on a wall by means of numerical simulations. Different liquids were used for the simulations: molten tin, water, and heptane. The numerical results are compared to experimental images for validation, presenting good agreement. The results suggest that there is a strong dependency of water and heptane results on the contact angle. The formulated expressions are valid only for low Ohnesorge number.

Morton et al. (2000) carried out numerical simulations for the impingement of a droplet on a pool. For the simulations carried out in his work, the Piecewise Linear Interface Calculation (PLIC) scheme was used for the advection term of the VOF method. Considering the huge difference of density of the gas and the liquid phases, the gas phase density was neglected. The main findings are that the absence of the gas phase did not affect the representation of the physics involved in some cases. The numerical simulation was capable of predicting with good agreement the crater formation. However, the bubble formation due to the droplet impact is not represented correctly as the gas phase is assumed as vacuum, the trapped bubble disappears after crater closure.

Nourgaliev et al. (2005) used the Structured Adaptive Mesh Refinement (SAMR) technique along with the Linear Weighted Essentially Non-Oscillatory (LWENO) scheme to minimise the errors caused by spatial discretisation on the level set method. The main objective of his work was to minimise these errors to improve the mass conservation. The main finding is that the combination of these techniques on the simulations reduced mass conservation errors. The authors also highlighted that this code is easy implemented in parallel coding in comparison to the hybridisation of VOF and level set methods.

Nikolopoulos et al. (2005) studied the flow generated by a droplet normal impingement on a wall. For the numerical simulations, the VOF method was used to track the interface. An axis-symmetric simulation was run, and its accuracy was considered good up until crown formation. At this point, three dimensional effects are predominant as the lamella rim is formed and spill off occurs. Results illustrate the fact that viscosity does not strongly affects the simulation at the beginning stages, but it has great influence on the ejected sheet in later stages. The numerical simulation was accurate in predicting the behaviour of the lamella rim flow. The VOF method was able to predict specific characteristics of the flow, such as bubble entrapment, capillary waves and jets of air and liquid.

Nikolopoulos et al. (2007) conducted three dimensional numerical simulations to investigate a droplet impinging normally onto a liquid film. The VOF method was applied to reconstruct the interface between fluids, along an adaptive mesh refinement technique. The results were validated against physical experimentation, presenting good agreement. Two mechanisms were identified that leads to secondary break-up. The first one was the Rayleigh instability in the first stages of the impact. The second one were the effects of surface tension, which are important for later stages. A correlation for the Weber number, size of secondary droplets, and number of secondary droplets was achieved. The VOF method was capable of predicting details of the flow field, like bubble entrapment, capillary waves, and liquid jets.

Yokoi et al. (2009) studied the behaviour of liquid droplet impact onto a dry wall surface. The simulations considered axis-symmetry and were carried out to test a dynamic contact angle model. The numerical method applied was the level set coupled with a VOF method. The work highlighted the dependency of good results for both the spreading and receding phases of the droplet impact on the dynamic contact angle. For the simplified dynamic contact angle model the results deviated from physical experimentation data.

Li et al. (2011) investigated a droplet collision on the wall using the VOF method. The main objective was to numerically investigate the erosion caused by the droplet impact. An important observation was that the compressibility of the fluid affected the numerical results presented. A model for the liquid droplet impingement erosion was developed as a function of impact angle.

Keshavarzi et al. (2013) by means of the VOF method and a coupling of level Set and VOF methods, studied the shape of rising bubbles. This work was carried out to compare these methods. The test case consisted of bubbles rising in a two dimensional channel. The models accounted for breaking up, coalescence, and deformation of the bubble. The main findings were that the coupled level set and VOF method required a higher computational time. The VOF method required a finer mesh to capture the interface between the bubble and the liquid accurately. The coupled method proved to be accurate on capturing complex topological changes. Nevertheless, this method is not mass conservative. On the other hand, the VOF method solves a scalar convective equation through the computational domain, being locally and globally mass conservative.

Malgarinos et al. (2014) used numerical simulations to evaluate a new numerical implementation for the adhesion force. For that, the source term of the momentum equation of the VOF method was changed to account for the adhesion forces. The setup consisted of a droplet impinging normally on the surface of a wall. With this model the dynamic contact angle was not imposed as a boundary condition, but rather calculated at run time. The adaptive mesh refinement technique was used to refine the regions of interest making the mesh finer on the triple point regions. The numerical simulations were validated against physical experimentation data. The results were compared to other models found on the literature, presenting similar results. The new adhesion force model presented an over prediction smaller than 15% of droplet maximum spread. The improvement in droplet maximum spreading in comparison to the models found on the literature was considered promising by the author.

Pivello et al. (2014) used variable mesh and time step to simulate a rising bubble. The results were validated against physical experimentation and numerical simulations found on the literature. For that the Front-Tracking method was used along with an implicit–explicit pressure correction scheme. A Lagrangian interface was modelled using the GNU Triangulated Surface (GTS) library. The results yielded a preserved geometry shape and dimension and could also preserve volume. The interpolation for the velocity field was non-conservative, thus, an additional volume recovery was used. Sensitivity analysis presented non-physical undulations of the bubbles. To solve this issue, the TSUR-3D algorithm was used, and could preserve the volume of the bubble.

Malgarinos et al. (2015) conducted numerical simulations using the VOF method along with an adaptive mesh refinement. The study presented an interface sharpening scheme. This model is capable of decrease the numerical diffusion maintaining a smooth velocity field around the interface. The sharpening equation is solved after the volume fraction advection equation. A method was proposed to couple the sharpening equation with the momentum conservation equation, saving computational time. One important observation came from the results, the suppression of numerical diffusion was grid independent. The numerical simulation was validate against theoretical cases and physical experimentation of a falling droplet. The results illustrate the fact that the sharpening equations with the High Resolution Interface Capturing (HRIC) scheme decreased the interface numerical diffusion.

Yu et al. (2015) used high sped imaging to capture the spreading of a silicon droplet over a substrate. Numerical simulations were carried out in order to simulate the spreading. For that, the VOF method was used. The time evolution of the dynamic radius and dynamic contact angle were validated against physical experimentation data. However, at the beginning stages of the simulations the numerical results presented a droplet velocity slower than the presented by the physical experimentation. In later stages, the velocity for the droplet was higher on the numerical simulations when compared to physical experimentation.

Fontes et al. (2018a) compared the effect of four different interpolation schemes for density interpolation for the CICSAM method. The numerical simulations presented in his work consisted of a droplet falling onto a deep pool. The analyses of the results consisted on the comparison with the numerical results and the physical experimentation of Morton et al. (2000). The author compared the crater and the ascending jet height formed by the impact of the impinging droplet on the pool. The results presented a better agreement for the volume fraction weighted scheme over the central difference, first-order upwind and second order upwind when compared with experimental data. It is commented that algebraic discretisation schemes for the advection term of the VOF equation, such as HRIC and CICSAM, required less simulation time when compared to geometrically schemes such as the PLIC scheme. On the other hand, the geometrical schemes yields better results.

Zhao et al. (2018) investigated the impact of a single fuel droplet on a wall by means of numerical simulations and physical experimentation. For these tests, different wall conditions were used to further understand the dynamics of the impinging process. Different liquids were tested, for example, water, diesel, n-dodecane, and n-heptane. For the physical experimentation, a high speed camera was used. The droplets were injected from a precision syringe pump for different Weber numbers. Many outcomes were observed on this test, such as stick, spread, rebound, and splash. The outcomes of droplet impact are dependent on Weber number, Reynolds number, Ohnesorge number, liquid properties, surface properties, among others. The data acquired on the physical experimentation was used to aid in the development of a dynamic contact angle model for a VOF method. The VOF method was used to run simulations using Convergent Science Inc.'s CONVERGE TM CFD. The simulation results presented good agreement with the physical experimentation. According to the author, more studies are going to be carried out using CFD modelling for predicting droplet wall interactions.

Chen et al. (2019) used the CLSVOF method to simulate a single droplet impacting on a wet wall. A two dimensional mathematical model was used to analyse the influence of droplet diameter and initial velocity on the droplet impact behaviour. Analysing the results, it was possible to verify that the motion could be divided in three different patterns, namely crown motion, wave motion, and splashing. These three patterns are determined by impinging droplet diameter and velocity, being high velocities and diameters more likely to present splashing outcomes.

de Lima et al. (2020) studied the effects of the schemes for the VOF transport equation. For that, numerical simulations were run with PLIC and HRIC schemes using Convergent Science Inc.'s CONVERGE TM CFD. The software uses Adaptive Mesh Refinement (AMR) in a cut cell Cartesian mesh. The numerical results were compared to the physical experimentation data presented by (MORTON ET AL., 2000). It was concluded from the numerical results that the PLIC scheme maintained a sharper interface and was computationally more efficient than HRIC. PLIC scheme was also capable of predicting droplet entrapment, meanwhile the HRIC scheme was not capable of predicting the same behaviour. One disadvantage of the PLIC scheme is that it can only be used for incompressible flow simulations.

Mawarsih et al. (2020) studied the impact of liquid droplets in horizontal solid surfaces. For that, numerical simulation were run using Finite-difference and front-tracking methods.

The numerical modelling considered incompressible two-dimensional unsteady flow. The fluids were considered as immiscible. The density ratio was changed in the simulations. The presented results were validated against experimental data, and highlight the importance of gravity on the equations, which was dominant to the maximum deformation diameter and maximum spreading velocity.

Sotoudeh et al. (2021) numerically investigated Newtonian and non-Newtonian fluids impacting on different surfaces. For the simulations a two-phase finite volume method was employed. The hybrid surfaces were defined as surfaces whose behaviour vary from hydrophilic to hydrophobic and super-hydrophobic. The maximum spreading factor was larger for both the Newtonian and non-Newtonian fluids in comparison to the other tested surfaces. It was observed that the shear stress at the edge of the droplets was higher for the non-Newtonian fluid in comparison to the Newtonian fluid. This study highlighted the importance of the surface in manipulating the behaviour of the impinging droplet.

To analyse the liquid film formation behaviour, there are also the Eulerian-Lagrangian approaches. In this approach one of the phases is considered continuous and the other is considered a discrete phase. In the case of this thesis, the gas was considered continuous and the liquid was considered as discrete droplets. The discrete fluid drops share the equation of momentum and energy with the Eulerian phase. The advantage of the Eulerian-Lagrangian approach is that it has a lower computational cost while the Eulerian approach has a better representation of the physics involved. In the Eulerian-Lagrangian approach, fluid drops have their trajectories calculated considering them as clusters, with each cluster representing a set of drops with the same diameter and velocity. A wide range of models can be found on the literature to describe the droplet impingement on walls and consequently liquid film formation. In the current work, the Eulerian Wall Film (EWF) was employed. In this approach, after the droplets collide with a wall they can form film liquid. The numerical models for this approach are discussed in Chapter 3. The next paragraphs are dedicated to cover a brief review of works using this approach for liquid film simulation.

Bai and Gosman (1995) studied a spray impingement model. The model consisted of mass, momentum and energy conservation equations. This model evaluates the droplet impingement characteristics in order to predict the outcomes of the collision, which also involves random functions to reproduce the stochastic nature of the outcomes. Good agreement with experimental data was achieved. The developed model was able to distinguish different regimes for dry and wet wall. The model was also tested in engine conditions with high pressure and temperature. However, the model was not able to accurate predict all the outcomes, and as the author commented in his text, there is a need for an improvement in the droplets impingement model.

Bai and Gosman (1996) developed a mathematical model to simulate the dynamics of liquid films on wall. The model considered the pressure due to impinging droplets, tangential momentum transfer due to oblique impact of droplets, and the gas shear force on the liquid film surface. The model was tested against simplified cases with analytical solution. Afterwards, the model was validated against physical experimentation presenting satisfactory agreement. The authors comment that a promising first step was made and the main objective is to develop a model to predict the liquid film dynamic under engine conditions.

O'rourke and Amsden (1996) developed a numerical model for a Lagrangian approach to solve the liquid film development on wall, with the main objective of predicting hydrocarbon emission during engine cold start. To run the numerical simulations the KIVA-3 code was used. The developed model considers the influence of impinging spray, and the gas flow near the wall in the dynamics of the liquid film, meanwhile splash was not considered.

Stanton and Rutland (1996) developed a numerical model to simulate liquid film formation in diesel engines. The model considers the interaction of the spray with the wall as well as with the liquid film surface. The empirical model was developed to solve liquid film in two dimensions over a three dimensional surface. The considered droplet outcomes after collision were stick, rebound, spread, and splash. The model was implemented in KIVA-II code. The simulations presented good agreement with physical experimentation data concerning secondary droplet velocity, spray radius, spray height, film thickness, and percentage of fuel stick to the wall. As the model cannot predict evaporation processes, the recommendation is to use this model only for cold starts.

Foucart et al. (1998) run simulations to predict the mixture of air and fuel in the intake ports of a internal combustion engine. For that, models for film formation by the impingement of droplets and film transport were implemented. To run the simulation KIVA-II was used. Preliminary tests were carried out with cases that have analytical solution. The results were then validated against experimental data. The model did not significantly increase the computation costs. For a more realistic engine simulations, the authors commented that a film separation model was needed to describe the striping of the liquid film generated in the valves.

Meingast et al. (2000) conducted a experimental investigation of the interaction of fuel spray with walls. This experiment was carried out to investigate the spray tip penetration in small diesel engines and improve the CFD models concerning spray break-up and evaporation. In his experiments, Phase-DopplerAnemometry (PDA) was used to visualise the spray and surface thermocouples were used to check the interaction between spray and wall. Using FLUENT, numerical simulations were conducted and a correct prediction of the spray tip penetration was achieved. The modelling of break-up due to the droplets impingement on the wall was not investigated, and according to the author this phenomena needs further analyses.

Maroteaux et al. (2002) studied the striping of the liquid film by means of aerodynamic forces. A model for film separation at the edges was also implemented and the numerical simulations were run using a modified version of KIVA-II code called KMB code. The main objective was to reproduce the condition at an intake manifold of an internal combustion engine. The simulations presented good agreement when compared to experimental data concerning the images of film separation and droplet size distribution. Based on the results obtained, a scheme for film striping based on the step angle of the geometry was proposed.

Ebner et al. (2004) studied the influences of the cross flow of air in the liquid film on walls. As the acceleration of the cross flow of air generates an additional pressure gradient as well as an increase in the shear forces at the liquid gas interface, a new model was developed to predict the interaction between the liquid and the gas phases. With an improvement in the boundary layer approach, the results were validated against physical experimentation data. This model was capable of achieve good results in distinct pressure gradients of the cross flow of air.

Arienti et al. (2006) studied the influence of the blockage of the liquid jet in the cross flow of air. The main objective was to analyse the role of the wake generated by the liquid jet on the spray characteristics, specially on the droplets formed by the striping of the liquid jet. To track the interface between fluids, the VOF method was used. For the turbulence closure model a standard RANS model was used. Sub models were used for break-up mechanisms and were coupled to the surface tracking algorithm. The main finding was that the vortices generated by the liquid jet persists for several orifice diameters in the flow direction. Physical experimentation data was missing to validate his model.

Andreassi et al. (2007) conducted physical experimentation and numerical simulations to observe the impingement of diesel spray under engine conditions. The experimental setup used was able to capture the radial spray penetration as well as the thickness growth of the impacted fuel. By varying the pressure used to inject the fuel, the back pressure inside the transparent vessel, and the wall temperature of the steel sheet in which the droplets impinge, an empirical correlation was achieved. For the numerical simulations a numerical tool based on KIVA-3 code was used. Testing a model developed for low pressure, the authors concluded that the model was unable to predict the correct behaviour of the spray. A new model was proposed for engine conditions pressure. This new method was validated against the acquired experimental data for different back-pressures and injection pressures. The main changes concerning the new model were on the empirical correlations for secondary droplets ejection angle and the Weber number, and correlations for velocity of the secondary droplets and the back pressure inside the pressure vessel.

Kiura et al. (2009) studied the liquid film formation in a wall under the influence of a cross-flow of air. This study was carried out to develop a more efficient port fuel injection for internal combustion engines. The main objective was to develop a technique for usage in port fuel injections to predict liquid film formation. For that, the spray and the liquid film were characterised. The film thickness was measured by means of optical techniques, which is similar to the technique used by Shedd et al. (2009a). For the numerical simulation, ANSYS, Inc.'s FLUENT 6.3 was used. For the numerical setup, the Discrete Particle Modelling (DPM) model was used. The droplet distribution considered the Rosin-Rammler droplet size distribution function. The Taylor Analogy Break-up (TAB) model proposed by O'rourke and Amsden (1996) was used for secondary break-up model. The results presented good agreement with physical experimentation concerning droplet size distribution and liquid film thickness.

Arienti et al. (2011), in continuity of his work in Arienti and Soteriou (2007) based his model in the refined level set grid method data presented by Herrmann (2008) and experiments from Shedd et al. (2009a) to conduct his work. In his work, the Atomization Model Interfaced with Surface Tracking (AtoMIST) was used. Different sub models are combined in this code to simulate the dynamics of the liquid fluid, such as column breakup, film breakup, shear stripping, and splashing. The numerical results presented good agreement concerning the physical experimentation results for liquid film thickness measurements. The main objective was to develop affordable calculations to be applied on combustor simulations.

Chaussonnet et al. (2013) studied the liquid film formation by means of numerical simulation using Large Eddy Simulation (LES) turbulence model. Both liquid film and droplets were described in a Lagrangian approach. The tested configuration was a planar pre filming atomiser. The numerical simulations were validated against experimental data for air velocity profile, film thickness, droplet size distribution, and spray angle. The differences on the results of liquid film thickness were attributed to the poor prediction of the turbulence model concerning the accuracy of wall shear stress and pressure loss.

Ingle et al. (2014) studied a cross-flow injection and liquid film atomisation in a system close to air-blast atomisers. The Eulerian Wall Film (EWF) model was used to simulate the liquid film formation on the wall. Simulations presented good agreement with experimental data. The result of film height is illustrated in Figure 2.1 for the studied case. The film looks as expected except by the peaks on the corners, where high film thickness is observed. Also, it is observed that there is a peak near the edge. This is caused by the back flow of air, which slows down the liquid film and forces it to go sideways. The liquid film reaches the symmetry boundary condition and accumulates in that region, causing this non expected behaviour.

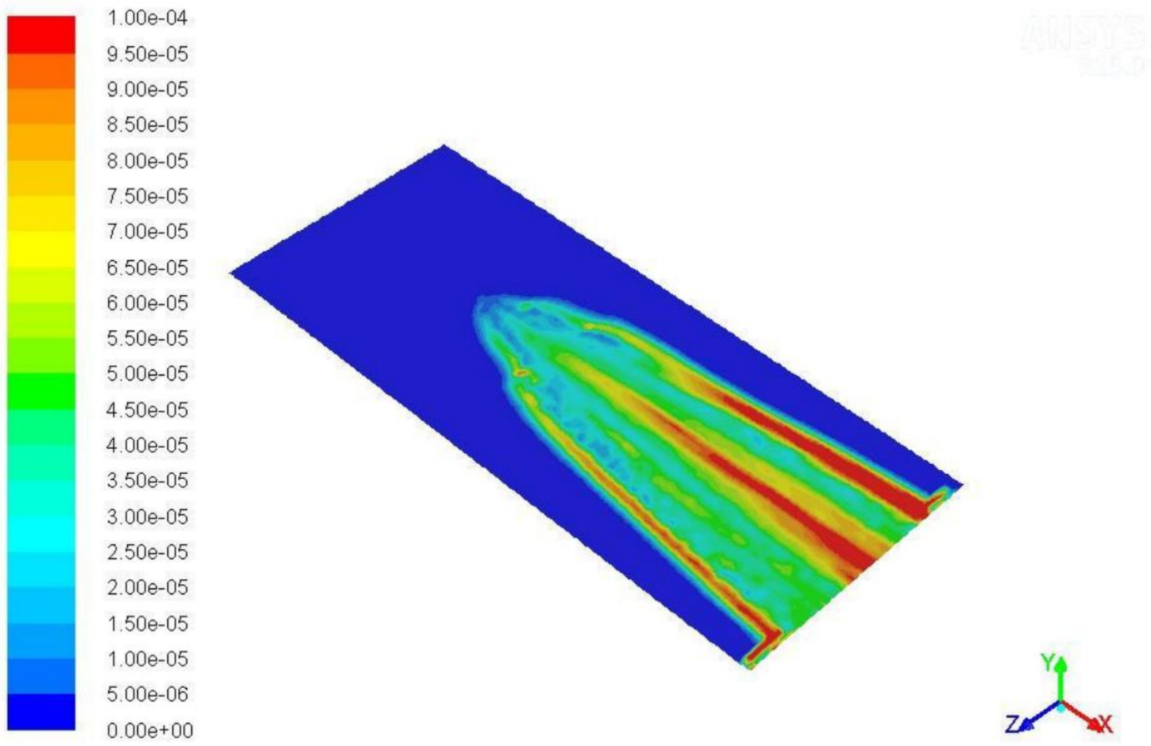

Figure 2.1: Liquid film thickness represented in meters as in the work of (Ingle et al., 2014). Note that peaks near the centre and sides of the computational domain are observed.

Zhang et al. (2016) developed a new liquid film model based on the work of O'rourke and Amsden (1996). Based on a Lagrangian method the new method was developed under engine conditions. The main modifications of the method concerns the source term for the momentum of the impinging droplet. By considering the gas compressibility, the authors concluded that the model could predict the heat flux of the liquid film on the wall under different temperatures, pressures, and impingement distances.

Drennan et al. (2019) used an autonomous meshing software to perform predictions of the pre film documented by Shedd et al. (2009a). The software used is the Convergent Science Inc.'s CONVERGE^{TM} CFD software. A surface mesh was created in this software and this surface mesh was used to generate a volumetric structured mesh every time step. An Adaptive Mesh Refinement (AMR) was used. For the spray model, the DPM model was used coupled with TAB break-up model for secondary breakup modelling to compare with Kelvin-Helmholtz Rayleigh-Taylor (KH-RT) break-up model. For these cases, a cross flow velocity of 82 m/s was simulated for two different cases, Case 1 with jet velocity of 12.7 m/s and Case 2 with 17.0 m/s. Both models were quite accurate when compared to the physical experimentation results.

It is observed that for case two none of the models captured the behaviour of the dip on the film height observed in Case 2. The contour of film height on the wall surface for Drennan et al. (2019) simulations is represented on Figure 2.2 for the TAB model. It is observed that in Case 2, peaks near the centre and sides of the computational domain can be observed. The peaks away from the centre are not expected, and it was formed by droplets that have sheared from the edges of the jet.

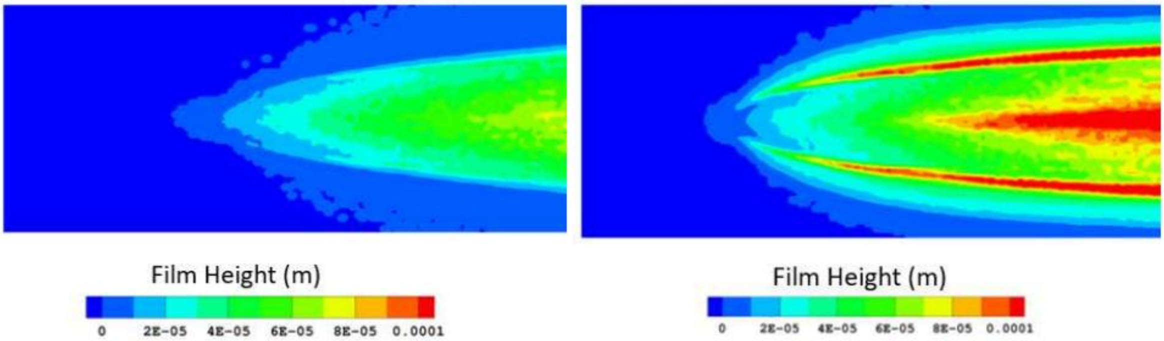

Figure 2.2: Two dimensional representation of film height for Case 1 on the left and Case 2 on the right. The image presents the results of TAB break-up model as presented by (Drennan et al., 2019). Note that for Case 2 peaks near the centre and sides of the computational domain can be observed.

Asgari and Amani (2021) developed a spray wall interaction in an Eulerian-Lagrangian framework. The model was compared to widely used numerical simulation softwares as OpenFOAM, Ansys Fluent, and KIVA. The results of spray tip penetration height and radius were compared to five different physical experimentation databases, presenting good agreement. The new model proved to be superior to the other tested in predicting detailed spray, gas, and droplet statistics.

Si et al. (2021) used the EWF method to numerically simulate nasal spray delivering to nasal olfactory region. The study was conducted to overcome the lack of quantitative dosimetry in the target region. It was concluded that the droplet deposition in the region of interest is highly dependent on the plume angle. By adjusting the plume angle and the head position it was possible to enhance the system delivering by 6.2%, reducing drug losses.

2.2.1 Literature review implications

This chapter presented a brief overview of different approaches to study the liquid film behaviour. Throughout the literature review, it was possible to certify that there is a wide range of applications of this phenomena in engineering, and so, the importance of further the knowledge in this field is clear.

As the time passes, the researches feel the need for more models and a further understanding of them. By reading the overview, it was also possible to realise that as one reads in chronological order, the first authors complain about the lack of information in some phenomena, missing models, phenomena that was not completely described by the existing models, and errors detected in the results. Later researchers create physical experiments, creates new models, verify and change existing models, to fill the gaps of information, better describing the phenomena and optimising its applications. To create and validate either empirical or theoretical models, great part of the researchers start from the analysis of physical experimentation or analytical solutions.

Some unanswered questions emerged from the literature review, and as described before, need further analyses for a better comprehension. These questions are treated in later chapters of this thesis, and a few of them are quoted below.

Most of the physical experimentation found on the literature for single droplet impingement are for droplets impinging on horizontal plates, such as the work of Ferrão et al. (2019). Many engineering applications do not follow this configuration. The physics of this type of phenomena must be addressed to further the knowledge in such phenomena. Thus, it was one of the objectives of the author to build a test rig and run numerical simulations to validate the acquired data and asses the influence of the main parameters, highlighting the advantages and limitations of the VOF method.

In the work of de Lima et al. (2020), the PLIC scheme behaved better in all the analysed variables. The advantages and disadvantages of this model should be analysed to light the shade in VOF simulations.

In the work of Drennan et al. (2019), there is a strange behaviour of the results presented in Figure 2.2 for Case 2 in the EWF model. In the work presented by Shedd et al. (2009a) it was clear that the peaks of liquid film height in spam wise direction deviate from experimental data. A complete analyses of the modelling should be assessed to verify the possible causes of such behaviour.

Some works, such as the work of Zhang et al. (2016), presented a changing in the EWF method. More specific the author chose the source term to be changed. The question that arises from this type of work concerns the influence of each parameter on the final results, and why the source term was chosen to be changed.

The methodology of this work was created based on the literature review, and ideas to overcome the problems found. Different approaches are going to be used to bridge the gaps of knowledge in the liquid film formation and transport. It was the author's intention to propose a new physical experimentation to challenge the numerical models in solving the physics involved. As mentioned before, the setup will be for droplets impinging on a vertical surface. The VOF scheme will be used to analyse the phenomena and further the knowledge in both the physical experimentation and numerical simulation. To complement the cited method, and analyse a more affordable methodology as mentioned by Arienti et al. (2011), the EWF model will be painstaking analysed to make it more reliable and answer open questions as the generated in the work of Drennan et al. (2019).

3 Modelling

In this chapter the physical, mathematical and numerical modelling for the liquid injection and wall film formation are described in three separated sections.

The subsequent chapters will cover the models validation by means of comparison of the numerical simulations against physical experimental data. The physical experiments used for VOF simulations validations were carried out by the author and presented in Chapter 4. Concerning the EWF method, two cases were found on the literature and used for validation. They are presented with its main features in Chapter 5 and its results in Chapter 6.

To run the Eulerian simulations, the CFD software Convergent Science Inc.'s CONVERGE ^{TM} CFD was used with the VOF method. This code is based on the Finite Volume Methods (FVM). To couple the velocity with pressure the Pressure Implicit with Splitting of Operator (PISO) algorithm is used. A collocated arrangement is used for the variables. For turbulence closure modelling, the $RNG\ k - \epsilon$ model was used. The convective flux scheme used was the flux blending, which is a blend of second-order upwind and reconstructed central difference spatial discretisation schemes. The automatic grid generation uses a modified cut-cell Cartesian grid generation method.

To run the Eulerian-Lagrangian simulations the UNSCYFL3D code was used. This Computational Fluid Dynamics (CFD) code is in constant development at the Fluid Mechanics Laboratory (MFLab) from the Federal University of Uberlândia (UFU) and it was already extensively validated. This code is based on the FVM in unstructured three-dimensional grids. To couple the velocity with pressure the Semi-Implicit Method for Pressure-Linked Equations (SIMPLE) is used. A collocated arrangement is used for the variables. The Momentum Weighted Interpolation (MWI) scheme is used to compute mass flow rate through each face in the domain. The Algebraic Multigrid (AMR) is used to solve the linear system generated in this code.

3.1 Physical modelling

In this thesis the classical fluid mechanics concept was adopted, therefore, Newton's laws were adopted. Conservation of mass was taken in account. The fluid was considered a continuum medium, meaning that the non-continuous effects are represented as mean properties.

The main studied cases of this thesis are multi-phase flows of liquid injection and liquid film formation. The fluids were considered Newtonian. To model both the gas and liquid phases, immiscibility was considered as well as no evaporation. However, they can interpenetrate each other and interact at the interface, where surface tension is modelled.

Concerning the flow both gas and liquid were considered incompressible. The equation of energy is not solved, meaning that temperature remains constant and mean properties are not dependent on temperature.

In the Eulerian-Lagrangian modelling the interaction between the Lagrangian droplets should also be modelled. This phenomenon is more important in locations that the concentration of droplets is high. The collision outcomes were modelled for grazing and coalescence. For coalescence the droplets join in one bigger droplet, conserving mass and momentum. For grazing collisions the droplets sizes are kept the same, but the velocities change, also conserving momentum. The outcome of the collision is strong dependent of the surface tension force and liquid inertia forces. Models for the break-up of the droplets and its outcomes were also considered.

The studied case was modelled considering the effects of turbulence in the mean flow, meaning that turbulence is also modelled in the Unsteady Reynolds Average Navier-Stokes equations (URANS).

Concerning the boundary conditions, for symmetry boundary condition the values of all properties are reflected. For the inlet boundary condition, Dirichlet conditions for volume fraction and velocity were used, the last considered perpendicular to the entrance and pressure gradient is set to zero. For the outlet boundary condition, Dirichlet condition for pressure and other values being calculated were used, for the Lagrangian droplets escape conditions were used. For wall boundary conditions, no slip velocity and no mass flux were considered. Also, for wall boundary liquid film formation models were implemented and validated using physical experimentation data.

3.2 Mathematical modelling

The mathematical model follows different parts: Eulerian referential, Lagrangian referential, and wall film formation models.

3.2.1 Eulerian referential

The equations presented in this section were adapted to follow the index notation. The basic equations for fluid flow are mainly conservation of mass and momentum. Equation 3.1 represents the conservation of mass in its three-dimensional form for incompressible flows as in the book of White (1962).

$$\frac{\partial u_i}{\partial x_i} = 0, \tag{3.1}$$

in which u is the fluid velocity and i is the direction of the velocity.

According to Versteeg and Malalasekera (2007), to define conservation of momentum, Newton's second law is applied in a control volume. This law defines that the rate of change in the amount of fluid momentum is equal to the sum of the forces on the fluid particle.

For Newtonian fluids it is assumed that the viscous stresses are proportional to the rate of deformation of fluid elements. The dynamic viscosity μ is used to relate these two variables. The equations for conservation of momentum for Newtonian incompressible fluid flows, can be summarised in index notation as in Equation 3.2. This equation was adapted from Versteeg and Malalasekera (2007).

$$\rho\frac{\partial u_i}{\partial t} + \rho\frac{\partial}{\partial x_j}(u_i u_j) = -\frac{\partial P}{\partial x_i} + \frac{\partial}{\partial x_j}(\mu(\frac{\partial u_i}{\partial x_j} + \frac{\partial u_j}{\partial x_i})) + S_{Mi}, \tag{3.2}$$

in which S_{Mi} is the source term for momentum in the i direction (x, y and z). The subscript j also stands for the different directions (x, y and z). P is the cell pressure, ρ is the density of the fluid, and μ is dynamic viscosity.

Several authors also add the equation of energy conservation, but this equation is not considered in this thesis.

A flow becomes unstable after reaching a certain Reynolds number value, which is the ratio between inertial forces and viscous forces. If instabilities keep on rising, the fluid flow can become turbulent. This flow regime generates fluid vortices, which are responsible for more efficient energy and mass exchanges, as in the work of Versteeg and Malalasekera (2007).

To numerically solve this phenomena using Equation 3.2, time consuming numerical-computational methods and mesh refinement are necessary, i.e. solution by Direct Numerical Simulation (DNS). Therefore, the usage of different methodologies is necessary to simulate turbulent flows in an affordable manner.

Among the methods to solve this type of cases there is the RANS method. In this method, attention is focused on the average flow and the effects that turbulence generates on its properties, as stated by Versteeg and Malalasekera (2007).

As the RANS method has a lower computational cost when compared to LES and DNS, this method was chosen for the simulations performed in this work. The following paragraphs will briefly describe the modelling of turbulence in such flows using RANS method.

The properties of turbulent fluid flows vary as illustrated for velocity in Figure 3.1. This is an example of a point measurement of velocity in a turbulent flow, as quoted by Versteeg and Malalasekera (2007).

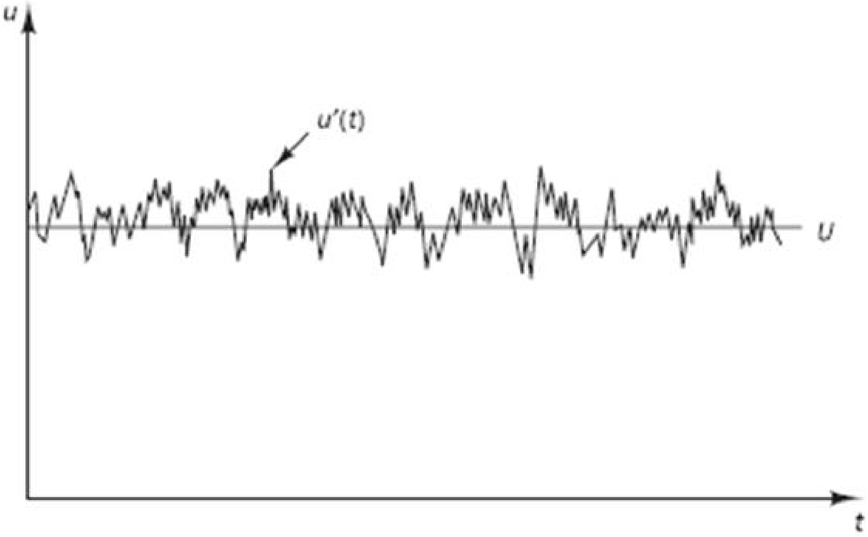

Figure 3.1: Representation of velocity fluctuation, u' is the fluctuation and U the mean velocity as presented by Versteeg and Malalasekera (2007).

The instantaneous velocity $u_i(t)$ is decomposed in the average velocity U_i and a fluctuation of velocity $u_i'(t)$, this type of decomposition is called Reynolds decomposition. Turbulent flows are then characterised by the average values of their properties and by fluctuations of these statistically determined values, as represented in Equation 3.3, as presented in Versteeg and Malalasekera (2007)

$$u_i(t) = U_i + u_i'(t), \tag{3.3}$$

in which the superscript ' represents the fluctuation, and U the average velocity. The equation for pressure is also similar to Equation 3.3, just changing u for p and U for P.

Considering that $\overline{\nabla \cdot u_i} = \nabla \cdot U_i$ then the continuity equation for the mean flow is represented by Equation 3.4, as presented by Versteeg and Malalasekera (2007).

$$\tfrac{\partial U_i}{\partial x_i} = 0, \tag{3.4}$$

Applying time averages on Equation 3.2, gives Equation 3.5. This Equation is called Reynolds-averaged Navier–Stokes equations and describe the behaviour of time-average turbulent flow systems. This equation was adapted from Versteeg and Malalasekera (2007).

$$\tfrac{\partial U_i}{\partial t} + \tfrac{\partial}{\partial x_j}(U_i U_j) = -\tfrac{1}{\rho}\tfrac{\partial P}{\partial x_i} + \nu \tfrac{\partial}{\partial x_j}((\tfrac{\partial U_i}{\partial x_j} + \tfrac{\partial U_j}{\partial x_i})) - \tfrac{1}{\rho}\sum_k(\tfrac{\partial \rho \overline{u'_i u'_k}}{\partial x_k}) \tag{3.5}$$

in which $\sum_k$ is the summation in each of the directions.

3.2.1.1 Turbulence closure modelling

According to Lesieur (2008), when the prediction of the average quantities of a turbulent flow is the concern, the main difficulty comes from the so-called closure problem, which arises from the non-linearity of the Navier-Stokes equations.

In order to simulate turbulent flows with the Reynolds-Averaged Navier-Stokes equations, it is necessary to add turbulence viscosity models to predict Reynolds stresses as well as the scalar transport terms and close the equation system. Among the most widely used and validated methods today are the $k - \epsilon$ models. They are based on the assumption that there is an analogy between the viscous stresses and the Reynolds stress tensor in the mean flow, as in the work of Versteeg and Malalasekera (2007).

According to FREIRE et al. (2006), the first model used to describe the terms of turbulent stresses was presented by Boussinesq (1877), proposing the formulation of Equation 3.6 for the Reynolds stresses. This equation presents the fact that Reynolds stresses are proportional to mean rates of deformation, as in the work of Versteeg and Malalasekera (2007).

$$\tau_{ij} = -\rho\overline{u'_i u'_j} = \mu_t(\tfrac{\partial U_i}{\partial x_j} + \tfrac{\partial U_j}{\partial x_i}) - \tfrac{2}{3}\rho k \delta_{ij} \tag{3.6}$$

in which k is the turbulent kinetic energy, μ_t is the turbulent viscosity, δ_{ij} is the Kronecker delta, and ij is the suffix notation that represents the directions.

In the $k - \epsilon$ model the instantaneous turbulent kinetic energy is also separated in a mean kinetic energy K, as in Equation 3.7, and the turbulent kinetic energy k, as in Equation 3.8. The instantaneous turbulent kinetic energy is represented in Equation 3.9 as in Versteeg and Malalasekera (2007).

$$K = \tfrac{1}{2}(\textstyle\sum_i U_i^2), \tag{3.7}$$

$$k = \tfrac{1}{2}(\textstyle\sum_i \overline{u_i'^2}), \tag{3.8}$$

$$k(t) = K + k', \tag{3.9}$$

in which i stands for the velocity directions (x, y, and z), K is the average kinetic energy, and k(t) is the instantaneous kinetic energy.

In turbulence closure models such as the $k - \epsilon$, equations for the turbulent kinetic energy are used to determine the velocity scale as represented in Equation 3.10, as stated by Ferziger and Perić (2002).

$$\tfrac{\partial(\rho k)}{\partial t} + \tfrac{\partial(\rho \bar{u}_j k)}{\partial x_j} = \tfrac{\partial}{\partial x_j}\left(\mu \tfrac{\partial k}{\partial x_j}\right) - \tfrac{\partial}{\partial x_j}\left(\tfrac{\rho}{2}\overline{u_j' u_i' u_i'} + \overline{p' u_j'}\right) - \rho \overline{u_i' u_j'}\tfrac{\partial \bar{u}_i}{\partial x_j} - \mu \overline{\tfrac{\partial u_i'}{\partial x_k}\tfrac{\partial u_i'}{\partial x_k}}, \tag{3.10}$$

A few terms in Equation 3.10 need extra modelling, and they are explained in the following paragraphs. The second term on the right hand side of the equation represents the turbulent diffusion and it is modelled by the usage of gradient diffusion assumption as represented in Equation 3.11, as quoted by Ferziger and Perić (2002).

$$-\left(\tfrac{\rho}{2}\overline{u_j' u_i' u_i'} + \overline{p' u_j'}\right) \approx \tfrac{\mu_t}{\sigma_k}\tfrac{\partial k}{\partial x_j}, \tag{3.11}$$

in which σ_k is a turbulent Prandtl number.

The third term on the right hand side represents the transformation rate of kinetic energy from the mean flow into turbulent kinetic energy. Using the eddy-viscosity hypothesis from Equation 3.6 the third term can be approximated as in Equation 3.12, as in the work of Ferziger and Perić (2002).

$$-\rho \overline{u_i' u_j'}\tfrac{\partial \bar{u}_i}{\partial x_j} \approx \mu_{\mathrm{t}}\left(\tfrac{\partial \bar{u}_i}{\partial x_j} + \tfrac{\partial \bar{u}_j}{\partial x_i}\right)\tfrac{\partial \bar{u}_i}{\partial x_j}, \tag{3.12}$$

According to Ferziger and Perić (2002), all the terms of the right hand side of the transport equation for k can be calculated with equations 3.10 - 3.12 using quantities that are computed during numerical simulations.

To complete the $k - \epsilon$ model, an equation to describe the length scale is needed. For that purpose, a variable that describes the equilibrium in turbulent flows was chosen and represents the rate of transformation of turbulence, and it is represented by ϵ. The rate of transformation of turbulence, the turbulent kinetic energy, and the length scale are related as presented in Equation 3.13, as stated by Ferziger and Perić (2002).

$$\epsilon \approx \frac{k^{3/2}}{L}, \tag{3.13}$$

in which L is the length scale, and ϵ is the rate at which turbulence kinetic energy is converted into internal energy.

Equation 3.13 is used to obtain ε and L. According to Ferziger and Perić (2002) the equation to transport ϵ can be represented by Equation 3.14 .

$$\frac{\partial(\rho\varepsilon)}{\partial t} + \frac{\partial(\rho u_j \varepsilon)}{\partial x_j} = C_{\varepsilon 1} P_k \frac{\varepsilon}{k} - \rho C_{\varepsilon 2} \frac{\varepsilon^2}{k} + \frac{\partial}{\partial x_j}\left(\frac{\mu_\mathrm{t}}{\sigma_\varepsilon}\frac{\partial \varepsilon}{\partial x_j}\right), \tag{3.14}$$

in which $C_{\epsilon 1}$, and $C_{\epsilon 2}$ are adjustable parameters for the turbulence modelling. σ_ϵ is the Prandtl number that connects the diffusivity ϵ to the eddy viscosity.

The eddy viscosity μ_t is represented as in Equation 3.15, as stated by Ferziger and Perić (2002).

$$\mu_\mathrm{t} = \rho C_\mu \sqrt{k} L = \rho C_\mu \frac{k^2}{\epsilon}, \tag{3.15}$$

in which C_μ is an adjustable constant in the eddy viscosity model.

The model constants were defined using data fitting in physical experiments and are summarised in Table table:modelconstants, as in Ferziger and Perić (2002).

C_μ	σ_k	σ_ϵ	$C_{1\epsilon}$	$C_{2\epsilon}$
0.09	1.00	1.30	1.44	1.92

Table 3.1: $k - \epsilon$ model constants

Several works are available on the literature in which the authors calibrate the model constants for specific cases. For example, (Ray et al., 2014) tuned the constants for the case of a Liquid Jet in Cross Flow (LJIC) using optimisation techniques. The constants are summarised on Table 3.2. This set of constants was tested for the LJIC case and improved the overall results when compared to experimental results. This new tuned constants were also tested for bluff bodies in the work of Duarte et al. (2020a) and presented improvements on the prediction of velocity profile.

C_μ	σ_k	σ_ϵ	$C_{1\epsilon}$	$C_{2\epsilon}$
0.117	1.00	1.30	1.262	1.936

Table 3.2: Tuned $k - \epsilon$ model constants

According to Versteeg and Malalasekera (2007) many other turbulence closure models are found on the literature. Each of these models was developed to predict better results under different conditions. As an example, the $k-\omega$ turbulence model proposed by Wilcox (1988) was first develop to predict boundary layers with adverse pressure gradients, as the $k-\epsilon$ did not predict good results.

The difference of the $k-\epsilon$ model and the $k-\omega$ model starts on the expression of the kinematic eddy viscosity. In the former the kinematic eddy viscosity is expressed as the product of the length scale and the velocity scale. On the later the turbulence frequency is used as the second variable, and it is expressed as in Equation 3.16.

$$\omega = \epsilon/k, \tag{3.16}$$

(Menter et al., 2003) went further and proposed a hybrid model to take the advantages of both $k-\epsilon$ and $k-\omega$ models. In the near wall regions the equations of the $k-\omega$ model are used and regions further from the wall the $k-\epsilon$ model equations are used. To achieve a smooth transition between models, blending functions are used.

There are several different models for the closure of the turbulence equations, but presenting them is not the objective of this thesis. More information concerning this topic is found in Versteeg and Malalasekera (2007), and Ferziger and Perić (2002)

3.2.1.2 Volume of fluid method

The Volume of Fluid (VOF) method is used to simulate multi-phase flows of gases and liquids. This technique is used to track the interface between the fluids, in which the immiscible fluids share momentum and energy. To track the interface, the volume fraction (α) of each cell is calculated throughout the computational domain. The value of the volume fraction can be found in three different situations: 0 representing only one fluid in the cell, 1 representing only another fluid, or the value can be in between 0 and 1 representing both fluids, as illustrated in Figure 3.2. The third situation can indicate the existence of the interface between fluids, as presented by Richards et al. (2016).

In the current work the value of α will be set to 0 for the liquid phase and 1 for the gas phase.

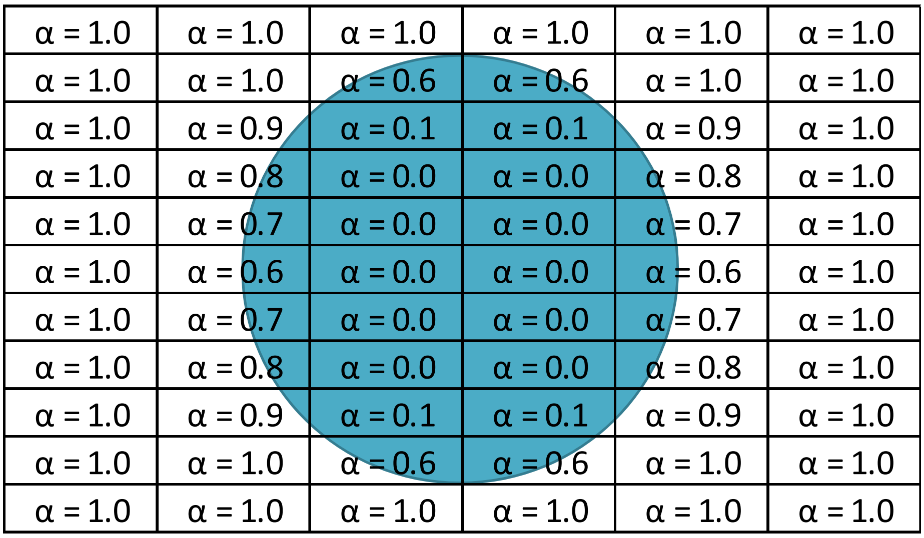

α = 1.0	α = 1.0	α = 1.0	α = 1.0	α = 1.0	α = 1.0
α = 1.0	α = 1.0	α = 0.6	α = 0.6	α = 1.0	α = 1.0
α = 1.0	α = 0.9	α = 0.1	α = 0.1	α = 0.9	α = 1.0
α = 1.0	α = 0.8	α = 0.0	α = 0.0	α = 0.8	α = 1.0
α = 1.0	α = 0.7	α = 0.0	α = 0.0	α = 0.7	α = 1.0
α = 1.0	α = 0.6	α = 0.0	α = 0.0	α = 0.6	α = 1.0
α = 1.0	α = 0.7	α = 0.0	α = 0.0	α = 0.7	α = 1.0
α = 1.0	α = 0.8	α = 0.0	α = 0.0	α = 0.8	α = 1.0
α = 1.0	α = 0.9	α = 0.1	α = 0.1	α = 0.9	α = 1.0
α = 1.0	α = 1.0	α = 0.6	α = 0.6	α = 1.0	α = 1.0
α = 1.0	α = 1.0	α = 1.0	α = 1.0	α = 1.0	α = 1.0

Figure 3.2: Volume of Fluid method. Values of α equal 0 represents one of the fluids, values of 1 represents another fluid, and any value in between represents an interface between fluids. The image was adapted from (Richards et al., 2016)

Regarding the mathematical modeling, the main equations are presented by Equations 3.17-3.21. The mass conservation equation in the VOF method for incompressible two-phase systems is presented in Equation 3.17. The momentum conservation is presented in Equation 3.18. The transport equation of the volume fraction (α) is presented in Equation 3.19. The density and the dynamic viscosity are calculated in Equations 3.20 and 3.21, respectively, as a function weighted by the volume fraction (α) contained in the cell, as in the work of (Richards et al., 2016).

$$\frac{\partial u_i}{\partial x_i} = 0, \tag{3.17}$$

$$\rho\frac{\partial u_i}{\partial t} + \rho\frac{\partial}{\partial x_j}(u_i u_j) = -\frac{\partial P}{\partial x_i} + \frac{\partial}{\partial x_j}(\mu(\frac{\partial u_i}{\partial x_j} + \frac{\partial u_j}{\partial x_i})) + \sigma k \delta_s n, \tag{3.18}$$

$$\frac{\partial \alpha}{\partial t} + \frac{\partial}{\partial x_i}(u_i \alpha) = 0, \tag{3.19}$$

$$\rho = (1-\alpha)\rho_g + \alpha\rho_l, \tag{3.20}$$

$$\mu = (1-\alpha)\mu_g + \alpha\mu_l, \tag{3.21}$$

in which α is the volume fraction, t is time, k is the local curvature of the interface, δ_S is the Dirac distribution concentrated on the interface S, n is the unit normal to the interface, ρ_g

is the gas density, ρ_l is the liquid density, μ_g is the gas dynamic viscosity, and μ_l is the liquid dynamic viscosity.

The last term in Equation 3.18 represents the contribution of the surface tension to the momentum, which in turn requires the evaluation of local curvature. The surface curvature is calculated at the interface according to Equation 3.22.

$$n_i = \frac{\frac{\partial \alpha}{\partial x_i}}{\left|\frac{\partial \alpha}{\partial x_i}\right|}, \tag{3.22}$$

The curvature in then calculated as in Equation 3.23.

$$\kappa = -\frac{\partial n_i}{\partial x_i}, \tag{3.23}$$

in which κ stands for local curvature.

3.2.2 Lagrangian referential modeling

As mentioned in Subsection 3.1, small droplets follow a Lagrangian methodology, being represented as discrete phase. To calculate their velocity and position, the equations of motion are used, represented by Equation 3.24 and Equation 3.25 respectively, as stated by Fontes et al. (2018b).

$$m_p \frac{du_{pi}}{dt} = F_d + F_{w,b}, \tag{3.24}$$

$$\frac{dx_{pi}}{dt} = u_{pi}, \tag{3.25}$$

in which the subscript p indicates that it is related to a particle or droplet, x is the position m is the mass, F_d is the drag force, and $F_{w,b}$ is the combined buoyancy-weight force.

As represented in Equation 3.24 only two forces are considered. The drag force F_d, represented in Equation 3.26 and the combined buoyancy-weight force $F_{w,b}$ represented in Equation 3.27, as in the work of Fontes et al. (2018b).

$$F_d = m_p \frac{3\rho C_d}{4\rho_p d_p}(u_{i,t} - u_{pi}), \tag{3.26}$$

$$F_{w,b} = (1 - \frac{\rho}{\rho_p}) m_p g_i, \tag{3.27}$$

in which g_i is the gravity component in the i direction, $u_{i,t}$ is the instantaneous fluid velocity, calculated as the mean velocity plus a fluctuating component, as in the Langevin dispersion model proposed by Sommerfeld (2001). In this model C_d is the drag coefficient and it is calculated according to Equation 3.28, which represents empirical correlations considering rigid spherical droplets, as presented by Fontes et al. (2018b).

$$C_d = \begin{cases} \frac{24}{Re_p}(1 + 0.15Re_p^{0.687}) : Re_p < 1000 \\ 0.424 : Re_p > 1000 \end{cases}, \tag{3.28}$$

in which Re is the Reynolds number and it is calculated as Equation 3.29, as in Fontes et al. (2018b).

$$Re_p = \frac{\rho|u_i - u_{pi}|d_p}{\mu}, \tag{3.29}$$

As the Eulerian phase is solved in a different framework of the Lagrangian phase, the coupling of these phases are taken in account by means of the interaction forces, in the so called two-way coupling. In the Eulerian framework, the force exerted by the droplet is accounted in the source term of the momentum equation. In the Lagrangian framework, the force is added in the equation of motion as represented in Equation 3.24. Generally in very low mass loading, the influence of the Lagrangian phase on the Eulerian phase is neglected in the so called one-way coupling.

3.2.2.1 Droplet interaction

For droplets interaction the droplet collision models are defined in collision regimes. These regimes can be described as coalescence, bounce and separation. These effects have a direct connection with the dimensionless number named Ohnesorge number, represented by Equation 3.30. This dimensionless number represents the ratio of viscous forces and forces of inertia and surface tension. For Ohnesorge numbers larger than the unit there is a tendency for the droplets to coalesce. For values of Ohnesorge number smaller than the unit the cited phenomena compete with each other. More details will be given in this text.

$$Oh^2 = \frac{\mu_d^2}{D_d \rho_d \sigma_d}, \tag{3.30}$$

in which Oh is the Ohnesorg number, D is the diameter, σ is the surface tension, and the subscript d stands for droplet parameters.

In addition to Ohnesorge number, some other factors have a great influence on the result of the collision, as example: the velocity, the ratio between the diameter of the drops, and the angle of impact. Due to the vast number of properties that influence this process, a unique solution for collision models has not yet been presented on the literature. The different possible scenarios for collision are usually expressed on maps in a relation of two dimensionless numbers, represented in Equation 3.31, in Equation 3.32, and in Figure 3.3. On the diagram on Figure 3.3, the dots are the results of the experiments and the lines are the models for the droplets collision outcomes.

$$We = \frac{\rho_l d_s \vec{U}^2_{rel}}{\sigma_1}, \tag{3.31}$$

$$B = \frac{2b}{d_s+d_l}, \tag{3.32}$$

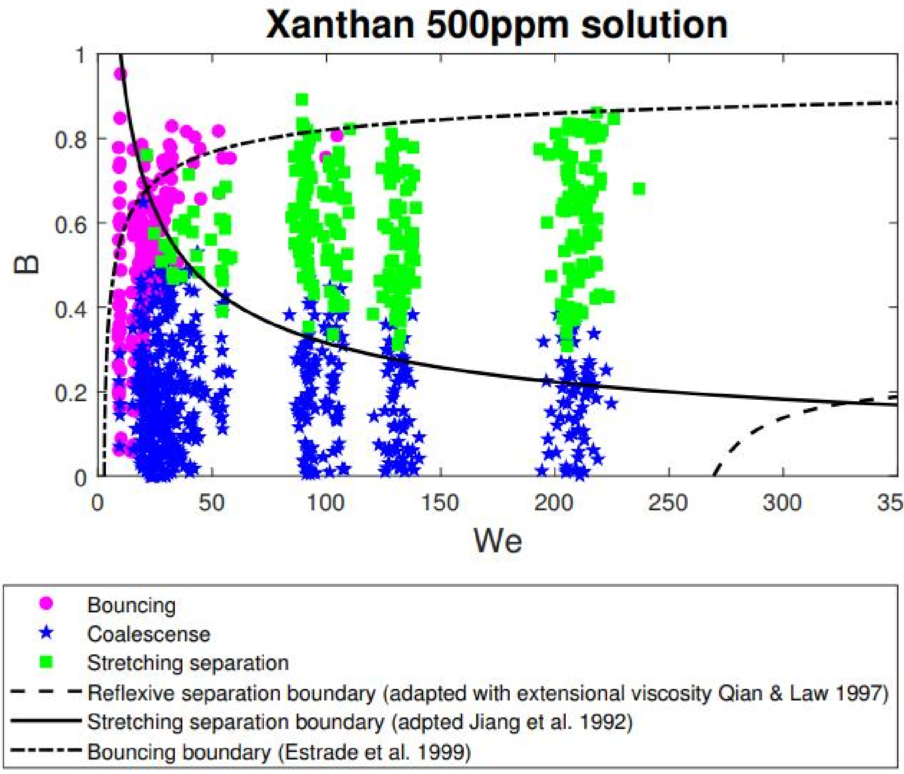

Figure 3.3: Collision effects dependent on Weber's number and impact number (represented as B). The diagram presented by (Finotello, 2019) illustrates 3 different regions, which presents different outcomes for droplet collisions. In purple the region that presents bouncing, in blue coalescence, and in green stretching separation.

in which We is the Weber number, B is the impact number, d_s is the diameter of a droplet and d_l is the diameter of the other drop involved in the collision process. $\vec{U}^2_{rel}$ is the relative velocity. b is the distance between the centre of the reference drop and the line that passes in the centre of the second drop that contains the relative speed.

In the current work only two outcomes were considered for droplets interaction: grazing collision and coalescence as represented in Figure 3.4.

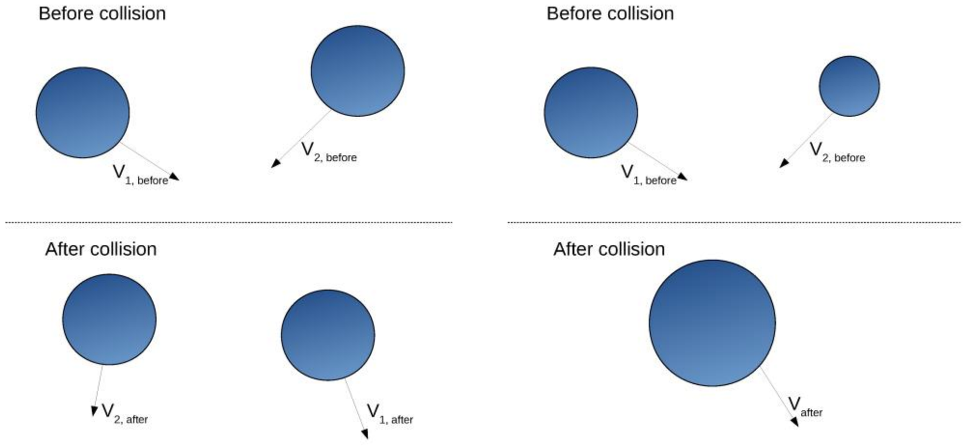

(a) Grazing collision.

(b) Coalescence.

Figure 3.4: Illustration of the considered droplet collision outcomes as presented by (Fontes et al., 2018a). On the left the grazing collision is illustrated, on the right the coalescence is illustrated.

The collision occurrence and its outcomes were modelled according to the method developed by Reitz (1987). In this model the parcels, which are a group of droplets with same volume and velocity, can collide only inside the same finite volume element. When collision occurs, the collision outcome depends on the collision impact parameter (b), represented in Equation 3.33. This parameter is compared to a critical impact parameter (b_{crit}), represented in Equation 3.34, as quoted by Fontes et al. (2018b).

$$b = (r_1 + r_2)\sqrt{Y}, \tag{3.33}$$

$$b_{crit} = (r_1 + r_2)\sqrt{min\left(1.0, \left(\frac{2.4(r_r^3 - 2.4r_r^2 + 2.7r_r)}{We_c}\right)\right)}, \tag{3.34}$$

in which b is the impact parameter, b_{crit} is the critical impact parameter, Y is a random number between 0 and 1, r_1 is the radius of the biggest droplet, r_2 is the radius of the smallest droplet, r_r is the droplet size ratio (r_1/r_2), and We_c is the Weber number of the collision as represented in Equation 3.35. For values of b above b_{crit} grazing collisions occur, as in the work of Fontes et al. (2018b).

$$We_c = \frac{\rho U_{rel}^2 \overline{D}}{\sigma}, \tag{3.35}$$

in which U_{rel} is the relative velocity between the droplets and $\overline{D}$ is the average between the diameter of the droplets.

3.2.2.2 Break-up models

The secondary breakup model used in the code is the Taylor analogy breakup (TAB) model. In this model the droplet is compared to a spring damping system. In this comparison, the surface tension acts as the spring and the viscosity as the damping system, as represented in Figure 3.5, as presented by Fontes et al. (2018b).

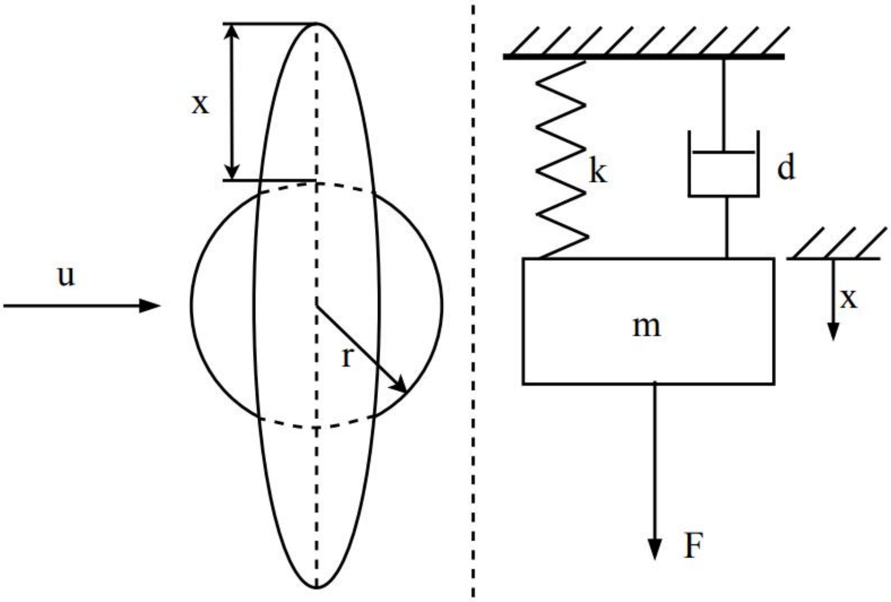

Figure 3.5: Comparison of a droplet with a spring-damping system as presented by Fontes et al. (2018b). In this comparison, the surface tension acts as a spring and the viscosity as a damping system.

For the described system the equation of motion is represented by Equation 3.36, as in the work of Fontes et al. (2018b).

$$\frac{d^2x}{dt^2} + \frac{c}{m}\frac{dx}{dt} + \frac{k}{m}x = \frac{F}{m}, \tag{3.36}$$

in which x is the displacement of the drop from its undisturbed position, k is the spring stiffness, and c is the damping coefficient.

Using the analogy of Taylor, the similarity between the coefficients are presented in Equation 3.37 - 3.39, as stated by Richards et al. (2016).

$$\frac{F}{m} = C_f \frac{\rho_g |U_i|^2}{\rho_l r_0}, \tag{3.37}$$

$$\frac{k}{m} = C_k \frac{\sigma}{\rho_l r_0^3}, \tag{3.38}$$

$$\frac{d}{m} = C_d \frac{\mu_l}{\rho_l r_0^2}, \tag{3.39}$$

in which F is the external force, m is the object mass, U is the relative velocity, r_0 is the undisturbed droplet radius, and the dimensionless constants C_f, C_k and C_B are summarised in Table 3.3.

C_k	C_d	C_F	C_m
8	5	1/3	1/2

Table 3.3: TAB breakup model constants

Setting $y = x/C_b r_0$ in which r_0 is the undisturbed droplet radius and C_b is a dimensionless constant defined as 0.5, the droplet oscillation frequency w and the dimensionless variable y can be expressed in Equation 3.40 and 3.41 respectively, as in Fontes et al. (2018b).

$$w^2 = C_k \frac{\sigma}{\rho_l r_0^3} + \frac{1}{t_d^2}, \tag{3.40}$$

$$y(t) = We_c + e^{(-\frac{t}{t_d})}[(y - We_c)cos(wt) + 1/w(dy/dt(0) + (y(0) - We_c)/t_d)sin(wt), \tag{3.41}$$

in which t_d is the turbulence correlation time, w is the oscillation frequency, and $y(t)$ a non dimensional distance.

If w^2 is greater than zero then the amplitude A is calculated by Equation 3.42, as presented by Richards et al. (2016).

$$A = \sqrt{(y - We_c)^2 + (\dot{y}/w)^2}, \tag{3.42}$$

If $A + We_c \leq 1$ the phenomenon is not observed. Otherwise, if $A + We_c > 1$ and $y \geq 1$, breakup is predicted to occur, as in the work of Richards et al. (2016).

The outcomes of the breakup are represented in Equation 3.43-3.44 for velocity and radius respectively. The direction of the droplet velocity is randomly chosen in a plane normal to the droplet relative velocity. The normal velocity component calculated in Equation 3.42 is added to the droplet velocity, as presented by Richards et al. (2016).

$$V_n = 0.5 r_0 \dot{y}, \tag{3.43}$$

$$r = \frac{r_0}{1 + \frac{8k}{20} y^2 + \frac{\rho_l r_0^3}{\sigma} \dot{y}^2 \left(\frac{6k-5}{120} \right)}, \tag{3.44}$$

in which k is a model constant set to $10/3$, and r_0 is the droplet radius prior to break-up.

A more recent work published by Dahms and Oefelein (2016) presented an improvement on the TAB method by considering droplet distortion in the equations. The new method is called Accurate Balance Taylor Analogy Breakup (AB-TAB) and it is mass, momentum, and energy conservative. This model is more consistent to describe the droplet break-up as it has less empirical correlations and proved to better predict the diameter of the generated droplets. This model also proved to better predict spray angles. Several other models are found on the literature which are based on the TAB method as the ETAB proposed by Tanner (1997), and other models with different methodologies such as the KH-RT model proposed by Reitz (1987), which is a combination of the Kelvin-Helmholtz analogy and the Rayleigh-Taylor analogy. The Kelvin-Helmholtz analogy is based on a liquid jet stability analysis, in which a liquid jet enters a quiescent chamber. The Rayleigh-Taylor analogy is based on the instability generated from rapid drop deceleration due to aerodynamic forces.

3.2.3 Film formation models

This subsection describes the formulation of the equations for the Eulerian Wall Film (EWF) model.

3.2.3.1 Eulerian Wall Formation

The EWF model was developed to simulate the behaviour of thin liquid film formation and propagation after droplet collection. Using the consideration of thin film, lubrication approximation is used and solved in local coordinates parallel to the surface. According to Ingle et al. (2014) the process of film formation can be described by five phenomena starting from the droplet impingement as presented in Figure 3.6. The first is droplet collection and film formation, in which droplets collide on the wall surface and may form liquid film. The second is film transport, in which the formed liquid film moves due to shear forces between the film and the Eulerian gas phase. The third is the splashing of new droplets on the liquid film surface, in which the impinging droplets instead of forming film liquid can remove liquid from the liquid film. The fourth is the striping, in which droplets can separate from the film liquid due to shear forces between the liquid film and the Eulerian gas phase. The fifth is the separation, in which the liquid reaches a geometry degree, sometimes the end of a filmer wall, may forming new droplets and ligaments.

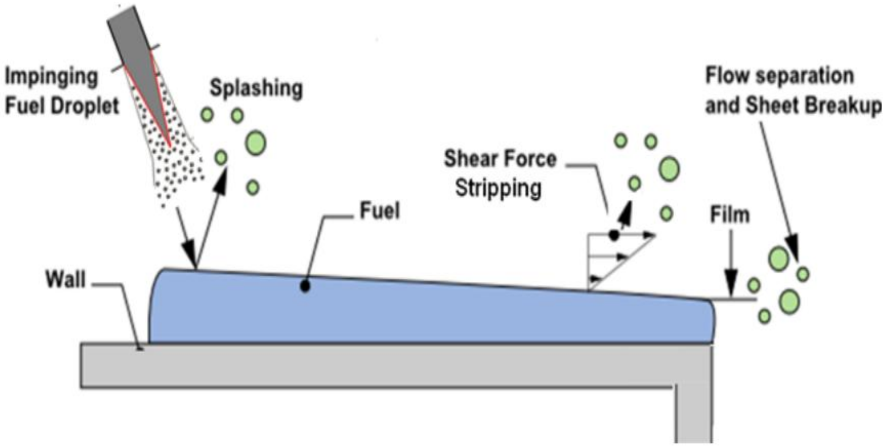

Figure 3.6: Representation of the sub-grid processes in the EWF model as presented by (Ingle et al., 2014). The process is divided in film formation, film transport, splashing, striping, and flow separation.

A few assumptions of the EWF model are as follows: the EWF model considers flow of liquid film only parallel to the surface, meaning that the normal component is zero. The velocity profile have a parabolic shape. The overall mass is conserved. In the case of the EWF model, this conservation of mass is carried out in a two dimensional model in a three dimensional domain. For that, a transient explicit formulation is used, as represented in Equation 3.45, as in the work of Ingle et al. (2014).

$$\left(\frac{\partial h}{\partial t}\right) + \nabla_s \cdot \left[h\vec{V_l}\right] = \left(\frac{\dot{m}_s}{\rho_l}\right), \tag{3.45}$$

in which $\vec{V_l}$ is the mean film velocity, h is the film height, ∇_s is the surface gradient operator, and $\dot{m}_s$ is the mass source term per unit wall area due to the phenomena described before.

The overall momentum conservation is represented by Equation 3.46. The first term on the left hand side of Equation 3.46 represents the transient effect and the second term represents the advection effects. On the right hand side the first term represents three effects, the gas-flow pressure, the normal gravity component and surface tension. The second term represents the effect of gravity parallel to the surface. The third term is the viscous shear force at the interface between the gas phase and the liquid film. The fourth term represents the viscous force in the liquid film. The fifth term is the source term, as presented by Ingle et al. (2014).

$$\left(\frac{\partial h\vec{V_l}}{\partial t}\right) + \nabla_s \cdot \left[h\vec{V_l}\vec{V_l}\right] = -\left(\frac{h\nabla_s P_L}{\rho_l}\right) + \left(\vec{g}_\tau\right) h + \frac{3}{2\rho_l}\vec{\tau}_{fs} - \frac{3\nu_l}{h}\vec{V_l} + \frac{\dot{q}}{\rho_l}, \tag{3.46}$$

in which

$$P_L = P_{gas} + P_h + P_\sigma, \tag{3.47}$$

$$P_h = -\rho h \left(\vec{n} \cdot \vec{g}\right), \tag{3.48}$$

$$P_\sigma = \sigma \nabla_s \cdot \left(\nabla_s h\right), \tag{3.49}$$

in which $\dot{q}$ is the momentum source term due to droplet collection or separation, g_τ is the gravity component parallel to the surface, τ_{fs} is the shear stress, P_L is the liquid film pressure, P_{gas} is the gas flow pressure, P_h is the pressure due to film height, and P_σ is the pressure due to surface tension.

The source terms account for the modelling of the interaction between the EWF model with the Lagrangian phase. For that the above mentioned droplet collection, splashing, stripping and separation phenomena are modelled by means of sub models.

Discrete droplets (Lagrangian phase) after impinging on the wall can be absorbed by the liquid film. The mass of the discrete phase is then added to the liquid film as represented by Equation 3.50 and its momentum as represented by Equation 3.51, as in Ingle et al. (2014).

$$\dot{m}_s = \dot{m}_p, \tag{3.50}$$

$$\vec{q}_s = \dot{m}_p \cdot \left(\vec{V}_P - \vec{V}_l\right), \tag{3.51}$$

in which q is the momentum of the droplet, $\dot{m}_p$ is the flow rate of the droplet impinging on the wall surface, $\vec{V}_P$ is the droplet velocity, and $\vec{V}_l$ is the liquid film velocity. The subscript s stands for source.

To predict the outcomes of the droplets after impingement the model presented by Kuhnke (2004b) was used. The main outcomes are summarised in Figure 3.7. The graph was plotted for the K number and the non dimensional temperature T^*, as presented in Equation 3.52 and Equation 3.53 respectively. The outcomes are summarised as rebound, splash, absorption or thermal breakup.

$$T^* = T_w/T_{sat}, \tag{3.52}$$

in which T^* is the non dimension temperature, T_w is the wall temperature, and T_{sat} is the saturation temperature of the liquid.

$$K = Ca^{5/4} La^{3/4}, \tag{3.53}$$

in which K is a non dimensional number that combines the effects of Ca and La as in the work of Mundo et al. (1995), Ca is the Capillary non dimensional number, and La is the Laplace number.

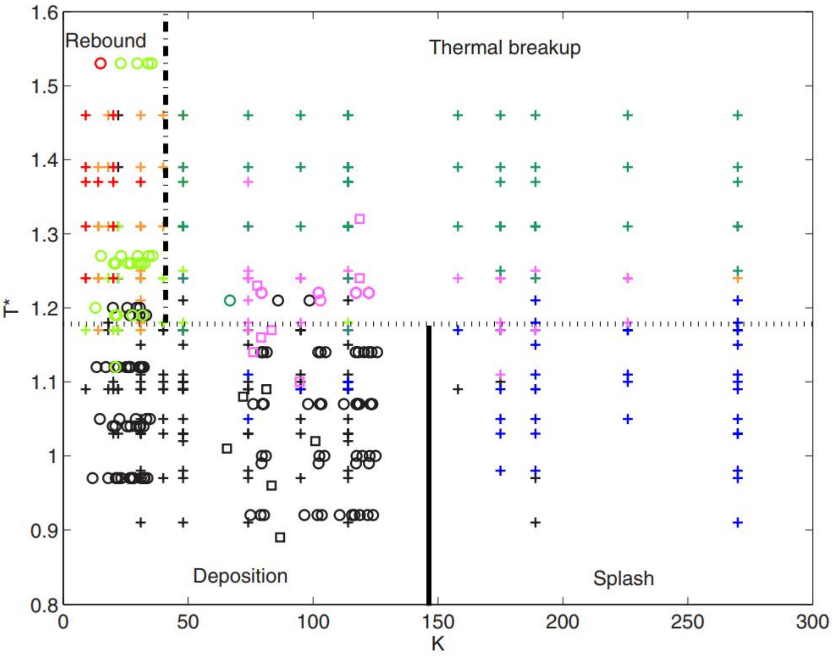

Figure 3.7: Regime map for the outcomes of the interaction of the spray with the wall according to Kuhnke (2004a). The regime map contains physical experimentation data of chain impingement droplet. The symbols coloured by red represent rebound, coloured by orange represent large droplets, coloured by dark green immediate break-up, light green huge droplets, magenta wet break-up, black deposition, and blue kinetic splash.

The outcomes of droplet impingement are based on criteria regarding the liquid properties, local liquid film height, and droplet impact angle. The surface of impact can be solid or liquid. In the case of impacting in a liquid film, according to the EWF approximations, the liquid covering a solid surface must be thin.

The model used to simulate the collision outcomes of the interaction of single droplets with liquid films follows the equations defined in the work of Samenfink et al. (1999). His model was developed for a complete 2D model simulation based on the droplet impact angle and liquid film height. His experiment is illustrated in Figure 3.8. It is observed that the droplets that come from the droplet generator impinge over a liquid film. This liquid film is fed trough small holes in the bottom of the test rig. Downstream of the droplet impingement, the remaining liquid film is sucked through a small hole. To generate the gas flow a fan is coupled to the test rig. A conductivity probe was installed downstream of the droplet impingement to detect the secondary droplets.

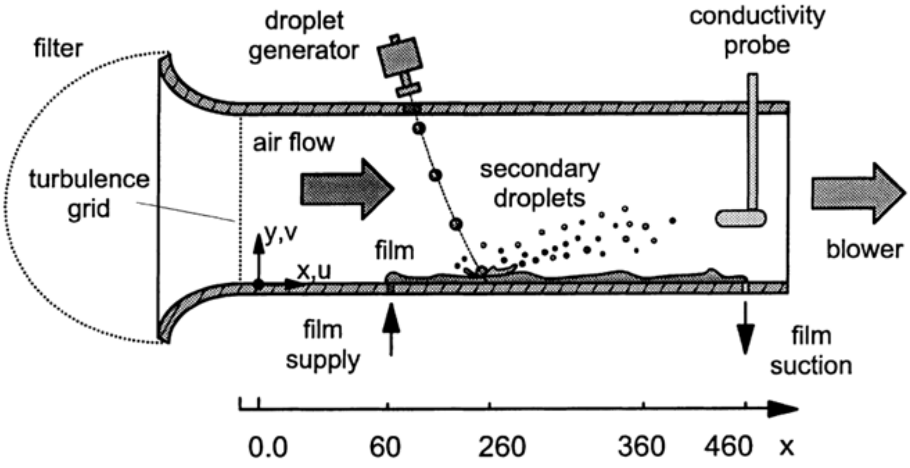

Figure 3.8: Physical experimentation used in the work of (Samenfink et al., 1999). This test section was used to acquire data for the droplets outcomes after impingement over a liquid film.

The distributions of droplet diameter, velocity and angle were summarised in a series of equations as follows: Equation 3.54 represents the deposit mass fraction in liquid film, Equation 3.55 represents the diameter ratio of the secondary droplets, Equation 3.56 represents the velocity ratio of the secondary droplets, Equation 3.57 represents the secondary droplet angle. The diameter and the velocity of secondary droplets are normalised by the corresponding values for the primary droplets.

$$\eta = 1.0 - 0.0866(s_{cd} - 1.0)^{0.3188}\alpha_{iD}^{0.1223}h^{*-0.9585}, \tag{3.54}$$

$$\frac{D_g}{D_{iD}} = 1.0 - 0.03454 s_{cd}^{0.175}\alpha_{iD}^{0.1239}La^{0.265}, \tag{3.55}$$

$$\frac{V_g}{V_{iD}} = 0.08214 s_{cd}^{-0.3384}\alpha_{iD}^{0.2938}h^{*-0.03113}La^{0.1157}, \tag{3.56}$$

$$\alpha_{sd} = 2.154 s_{cd}^{1.0946}\alpha_{iD}^{0.03389}h^{*-0.1589}, \tag{3.57}$$

in which η is the deposit mass fraction, s_{cd} is the momentum parameter, h^* is the normalised film height, La is the Laplace number, V_{iD} stands for droplet velocity, D_{iD} for droplet diameter, α_{iD} for impingement angle, μ_{lq} for liquid viscosity, and α_{sd} is the secondary droplet angle. The subscript g denotes generated which stands for secondary droplets.

This set of equations are valid for the range represented in Equation 3.58.

$$
\begin{aligned}
&1.0 < s_{cd} < 5.0,\\
&0.3 < h^{*} < 3.0,\\
&5000 < La < 20000,\\
&5^{o} < \alpha_{iD} < 90^{o},
\end{aligned}
\tag{3.58}
$$

in equations 3.54 - 3.58 the dimensionless parameters are represented in Equation 3.59 for the momentum parameter, in Equation 3.60 for Laplace number and Equation 3.61 for normalised film height. For momentum parameters less than 1 it is considered completely coalescence.

$$s_{cd} = \frac{1}{24} Re La^{-0.4189} = \frac{1}{24} \frac{\rho_{lq}^{0.581}}{\mu_{lq}^{0.162} \sigma_{lq}^{0.4189}} D_{iD}^{0.581} c_{iD} sin^{0.63}(\alpha_{imp}), \tag{3.59}$$

$$La = \frac{\rho_{lq} \sigma_{lq} D_{iD}}{\mu_{lq}^{2}}, \tag{3.60}$$

$$h^{*} = \bar{h}_{F} / D_{iD}, \tag{3.61}$$

in which c_{iD} is the droplet velocity, $\bar{h}_F$ is the mean film height, and α_{imp} is the impingement angle.

The conditions at the phase interface can be modelled as follows. A film roughness approach is used as in Equation 3.62 - 3.66. This set of equations were adapted from Stanton and Rutland (1998), bearing in mind that in his case the evaporation was considered and in the current work the equation of energy is not solved. The approach to couple the liquid film with the gas phase is equivalent to the sand-grain roughness approach, as presented in Equation 3.62. The sketch presented in Figure 3.9 represents the dynamics of the current model. On the left side of the image, it is observed that the gas phase flows above a wavy liquid phase. The liquid phase significantly influences the velocity and temperature profiles of the gas phase, as illustrated by u(y) and T(y). Therefore, as an approximation of the real physics, modified wall functions based on the logarithmic law of the wall are used at the film surface.

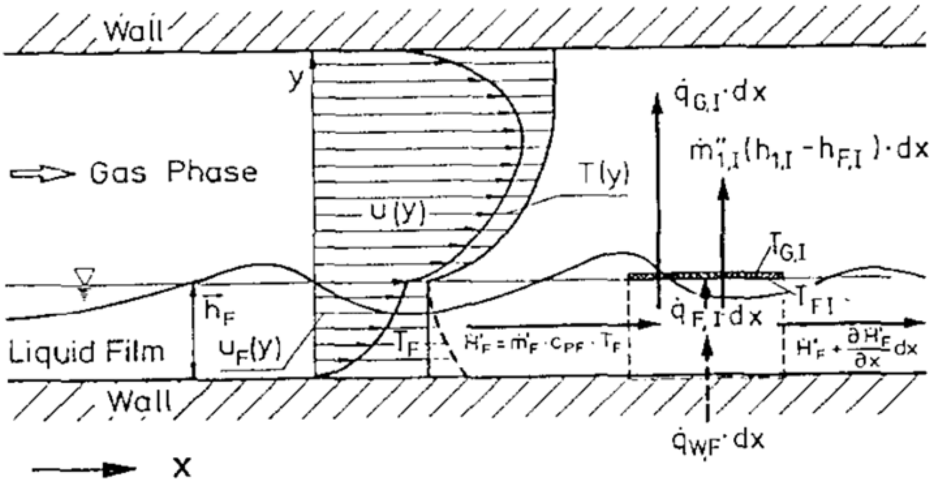

Figure 3.9: Two phase flow with evaporating wavy liquid film(Himmelsbach et al., 1994) The influence of the wavy liquid film on the gas phase is illustrated with its main parameters.

$$k_s = 2\Phi\delta, \tag{3.62}$$

in which k_s is the film roughness parameter, δ is the liquid film thickness, and Φ is the convective velocity parameter and can be estimated as in Equation 3.63.

$$\Phi = 0.735 + 0.009255\bar{\tau}, \tag{3.63}$$

in which $\bar{\tau}$ is the average inter-facial shear stress.

The influence of the liquid film roughness on the air flow can be estimated using the logarithmic law of the wall as in Equation 3.64.

$$u^+ = \frac{1}{\kappa} ln(y^+) + C, \tag{3.64}$$

in which u^+ is the non-dimensional velocity parallel to the wall, κ is the is the Von Kármán constant, y^+ is the non-dimensional wall distance, the constant C is a function of Reynolds number, defined as in Equation 3.65.

$$Re_{k_s} = \frac{k_s u_\tau}{\nu}, \tag{3.65}$$

in which Re_{k_s} is the roughness Reynolds number, and u_τ is the friction velocity.

And C can then be estimated as in Equation 3.66.

$$C = \begin{cases} 5.15 : Re_{k_s} < 5 \\ \\ 1.5497 + 19.1 log(Re_{k_s}) - 14.43[log(Re_{k_s})]^2 + 3.31[log(Re_{k_s})]^3 \\ -\frac{1}{\kappa} ln(Re_{k_s}) : 5 \leq Re_{k_s} \leq 70 \\ \\ 8.5 - \frac{1}{\kappa} ln(Re_{k_s}) : 70 < Re_{k_s} \end{cases}, \tag{3.66}$$

3.3 Numerical modelling

This section covers the numerical modelling of the mathematical models in Section 3.2. This chapter follows the same order of Section 3.2 explaining the numerical modelling of the mathematical models. A subsection presents the Eulerian referential with its subsections for the approximations of its terms. Another subsection presents the Lagrangian referential with its subsections for numerical approximation. A third subsection covers the film formation for the VOF and the EWF methods.

The numerical methodology here presented follows the FVM method. For the purpose of exemplification, the nomenclature for the elements discretisation is illustrated in Figure 3.10. The capital letters represent the centre of a volume of fluid and the lowercase letters represent the surface.

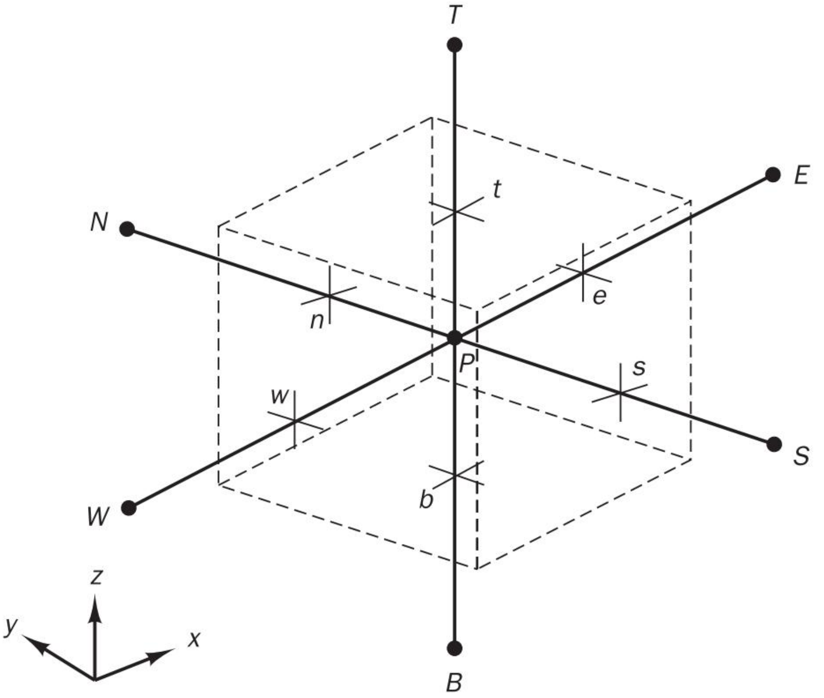

Figure 3.10: Example of structured elements discretisation as presented by Versteeg and Malalasekera (2007). The capital letters represent the centre of a volume of fluid and the small letters represent the surface.

For the purpose of exemplification, one of the differentiation schemes will be illustrated for a one-dimensional uniform mesh in the x direction.

The basis for the discretisation of the equations presented in the Subsection 3.2 comes from the Taylor series expansion as presented in Equation 3.67. For Equation 3.67, ϕ is a chosen variable and the subscripts represent the location where the variable is evaluated. It is possible to obtain the value of ϕ_E using values of ϕ_e and its derivatives.

$$\phi_E = \phi_e + \tfrac{d\phi}{dx}|_e(X_E - X_e) + \tfrac{d^2\phi}{dx^2}|_e(X_E - X_e)^2/2 + ..., \tag{3.67}$$

in which ϕ is a general variable, and X is the distance. The subscript e is the face at the east, and the subscript E represents the cell at the east.

A similar equation to evaluate the value in point P using Taylor series is represented in Equation 3.68.

$$\phi_P = \phi_e + \tfrac{d\phi}{dx}|_e(X_e - X_P) + \tfrac{d^2\phi}{dx^2}|_e(X_e - X_P)^2/2 + ..., \tag{3.68}$$

in which the subscript P stands for the current cell.

Combining Equation 3.67 - 3.68, neglecting higher order derivatives and using some algebra, Equation 3.69 is developed. This equation represents the Central Difference Scheme (CDS) in a uniform mesh.

$$\frac{d\phi}{dx} = \frac{\phi_E - \phi_P}{dx}, \tag{3.69}$$

In the following subsection of this chapter, similar methodologies are applied to different mathematical models to obtain the numerical models.

3.3.1 Eulerian referential

For the Eulerian phase two considerations are important to apply the FVM method. The variables inside the control volume are constants and the values at the surface are located at the centre of each face, as presented by Fontes et al. (2018b).

A general cell is represented in Figure 3.11. Two elements are presented, the left (L) and the right (R) elements. $\vec{A_f}$ represents the area vector outward the face. $|\vec{d_s}|$ stands for the distance of the elements centre, $d\vec{r}_L$ is the vector from the centre of the left element to the centre of the surface, and $d\vec{r}_R$ is the vector from the centre of the right element to the centre of the surface, as in the work of Fontes et al. (2018b).

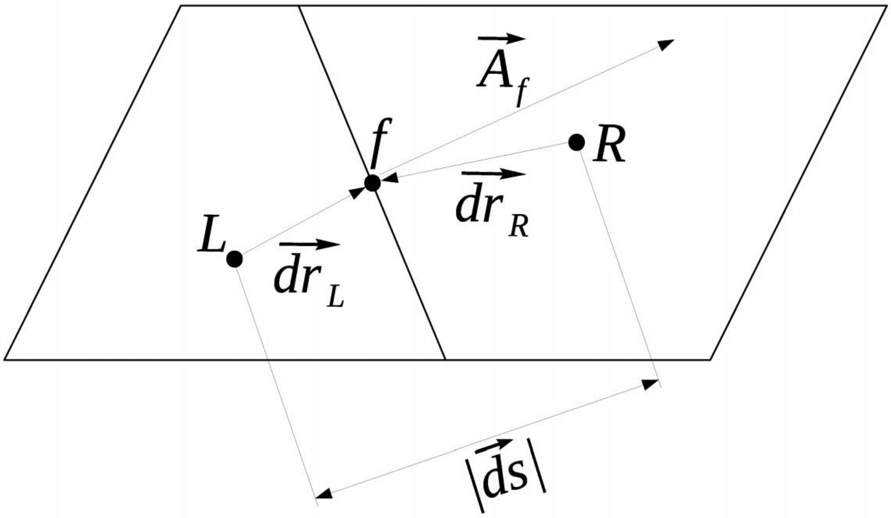

Figure 3.11: Representation of elements discretisation as in the work of Fontes et al. (2018b). The main parameters of two cells are represented (L stands for the left cell and R for the right)

The following subsection presents the discretisation of the Eulerian phase for each of the main terms based on the nomenclature of Figure 3.11.

3.3.1.1 Temporal term

Considering the left volume element of Figure 3.11, the temporal term was discretise using a second-order three level method as represented in Equation 3.70, as presented by Fontes et al. (2018b).

$$(\tfrac{\partial}{\partial t}\textstyle\int_{CV}\rho u_i dv)_L = \tfrac{3(\rho_L u_{iL})^{n+1}-4(\rho_L u_{iL})^{n}+(\rho_L u_{iL})^{n-1}}{2\Delta t}, \tag{3.70}$$

in which the superscript n indicates the current time step, n+1 the future time step, n-1 the previous time step. The subscript L denotes the cell on the left side. Δt is the time step.

In the following subsections the superscript n+1 will be neglected to simplify the equations, thus, unless is mentioned, the variables are calculated implicitly.

3.3.1.2 Advection term

The advection term can be numerically approximated as represented in Equation 3.71, as in Fontes et al. (2018b).

$$(\textstyle\int_{CS}\rho u_i u_j \cdot n_j ds)_L = \sum_{m=1}^{nf}\rho_f^n u_i|_f u_j^n|_f \cdot A_{fj}, \tag{3.71}$$

in which nf represents the number of faces of the considered finite volume. The subscript f stands for face. ds stands for the distance of the elements centre, and A_f is the area vector outward the face. The face value is calculated using different methods such as the first order upwind, second order upwind or central differences schemes.

3.3.1.3 Diffusion term

The diffusion term is calculated using Equation 3.72, as in the work of Fontes et al. (2018b).

$$(\textstyle\int_{CS}[(\mu + \frac{\mu_t}{\sigma_k})\frac{\partial k}{\partial x_j}] \cdot n_j ds)_L = \sum_{m=1}^{nf}(\mu + \frac{\mu_t}{\sigma_k})\frac{\partial k}{\partial x_j}|_f \cdot A_{fj}, \tag{3.72}$$

The gradient inside a diffusion term of transport equations is represented in Equation 3.73. This equation represents the diffusion term of the turbulent kinetic energy equation. The primary diffusion is represented as the first term on the right hand side inside the parenthesis in Equation 3.73, and the secondary diffusion is represented as the second term on the right hand side inside the parenthesis in Equation 3.73, as in Fontes et al. (2018b).

$$D_f = \frac{\partial k}{\partial x_j}|_f \cdot A_{fj} = \frac{k_R - k_L}{|\vec{d_s}|}\frac{\vec{A_f}\cdot\vec{A_f}}{\vec{A_f}\cdot\vec{e_s}} + \left(\overline{\nabla k}\cdot\vec{A_f} - \overline{\nabla k}\cdot\vec{e_s}\frac{\vec{A_f}\cdot\vec{A_f}}{\vec{A_f}\cdot\vec{e_s}}\right), \tag{3.73}$$

in which $\vec{e_s} = \frac{\vec{d_s}}{|\vec{d_s}|}$ is the unit vector from the centroid of the left element to the right element and $\overline{\nabla k}$ is the average gradient calculated from adjacent finite volumes.

3.3.1.4 VOF advection scheme

There are special schemes for the numerical modelling of the Volume of Fluid (VOF) advection term. This is related to the fact that usual interpolation schemes, such as the central difference scheme leads to an oscillating behaviour or a very diffuse interface. This behaviour is due to the fact that there is an abrupt change on fluid properties. For example, the difference on density for air water interface can be on the order of 10^3.

Among the available advection schemes found on the literature for VOF advection term, there are geometric schemes, which usually require more computational simulation time such as the Piecewise-Linear Interface Calculation (PLIC) scheme, and the algebraic schemes such as the Compressive Interface Capturing Scheme for Arbitrary Meshes (CICSAM) and the High-Resolution Interface Capturing (HRIC).

Among the different schemes available for interface tracking in the literature, the HRIC and PLIC were chosen and outlined in this work. Both schemes were already implemented on Convergent Science Inc.'s CONVERGE ^{TM} CFD.

According to (Richards et al., 2016) the HRIC scheme is based on a criterion which states that a variable distribution between the centres of two adjacent cells should be smooth when $\phi_D \leq \phi_f \ \leq \phi_A$ as illustrated in Figure 3.12. In this figure U stands for upwind cells, D for donor cells, and A for acceptor cells.

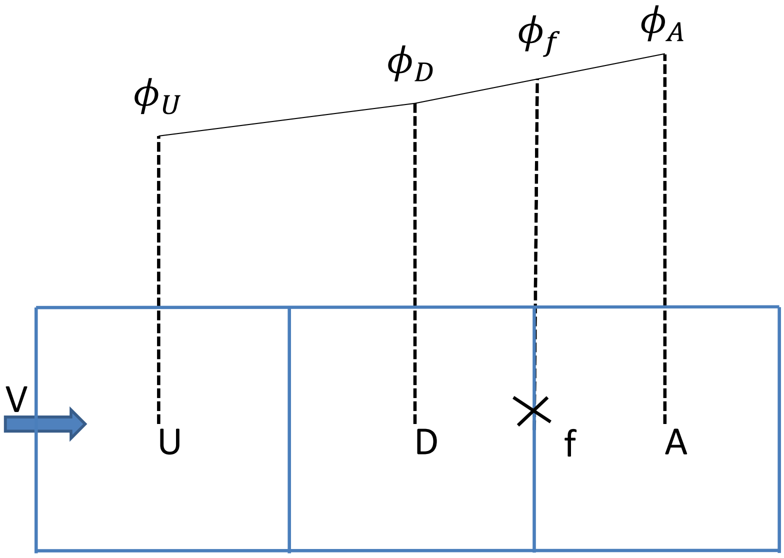

Figure 3.12: Schematic representing the convective boundedness criterion for HRIC Scheme, as adapted from (Richards et al., 2016).

To solve the HRIC scheme, normalised variables are introduced as represented in Equations 3.74 and 3.75.

$$\tilde{\phi_f} = \frac{\phi_f - \phi_U}{\phi_A - \phi_U}, \tag{3.74}$$

$$\tilde{\phi_D} = \frac{\phi_D - \phi_U}{\phi_A - \phi_U}, \tag{3.75}$$

in which ϕ is a chosen variable, U denotes upwind cells, D denotes donor cells, f denotes face, and A denotes acceptor cells. The superscript ˜ stands for normalised variable.

The volume fraction for each cell face can be calculated using Equation 3.76.

$$\phi_f = (1 - \tilde{\beta})\phi_D + \tilde{\beta}\phi_A, \tag{3.76}$$

in which $\tilde{\beta}$ is calculated as Equation 3.77.

$$\tilde{\beta} = \frac{\tilde{\phi_f} - \tilde{\phi_D}}{1 - \tilde{\phi_D}}, \tag{3.77}$$

A mixture of upwind and downwind schemes is then used to estimate the normalised cell face value as in Equation 3.78.

$$\tilde{\phi_f} = \begin{cases} \tilde{\phi_D} : \tilde{\phi_D} < 0, \tilde{\phi_D} > 1 \\ 2\tilde{\phi_D} : 0 \leq \tilde{\phi_D} \leq 0.5 \\ 1 : 0.5 \leq \tilde{\phi_D} \leq 1 \end{cases}, \tag{3.78}$$

To avoid alignment of the interface with the mesh the upwind scheme is used. The blending factor γ_f is used to smooth the transition between schemes as Equation 3.79 and Figure 3.13 present. In Figure 3.13, n stands for the vector normal to the fluid interface and d is the vector connecting the centre of the fluid interface cell to the centre of acceptor cell. The normalised cell face value is then recalculated by Equation 3.80.

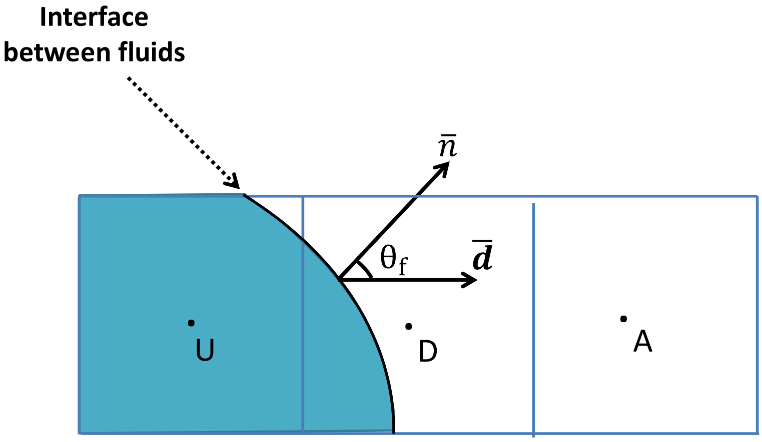

Figure 3.13: Schematic illustrating vectors used to define the angle θ_f in order to obtain the blending factor (γ_f), as adapted from (Richards et al., 2016).

$$\gamma_f = \sqrt{cos(\theta_f)}, \tag{3.79}$$

$$\tilde{\phi}^*_f = \gamma_f \tilde{\phi_f} + (1 - \gamma_f)\tilde{\phi_D}, \tag{3.80}$$

in which γ_f is the blending factor, θ_f is the angle between the vector normal to the fluid interface and the vector connecting the centre of the fluid interface cell to the centre of acceptor cell. The superscript $*$ stands for the value correction to avoid alignment.

In case of the CFL condition not being satisfied, the HRIC scheme can cause instability. Thus, the value of $\tilde{\phi}^*_f$ is corrected using the Courant number C_f as presented in Equation 3.81 and Equation 3.82.

$$C_f = u\tfrac{\Delta t}{\Delta x}, \tag{3.81}$$

$$\tilde{\phi}_f^{**} = \begin{cases} \tilde{\phi}_f^{*} : C_f < 0.3 \\ \tilde{\phi}_D : C_f > 0.7 \\ \tilde{\phi}_D + (\tilde{\phi}_f^{*} - \tilde{\phi}_D)\frac{0.7-C_f}{0.7-0.3} : 0.3 < C_f < 0.7 \end{cases} , \tag{3.82}$$

in which C_f is the Courant number, u is the local fluid velocity, Δt is the time step and Δx is the cell base size. The superscript $**$ represents the variable correction considering Courant number.

In the PLIC scheme, the interface between the fluids is geometrically reconstructed, maintaining a sharper interface as compared to the HRIC scheme. To calculate the interface normal vector m, illustrated in Figure 3.14, Equation 3.83 and the plane equation 3.84, are employed. The red dashed line in Figure 3.15 represents the interface obtained as an approximation. The volume fraction and the normal orientation m are used to define the parameter d, then the interface is advected, as stated by (Richards et al., 2016).

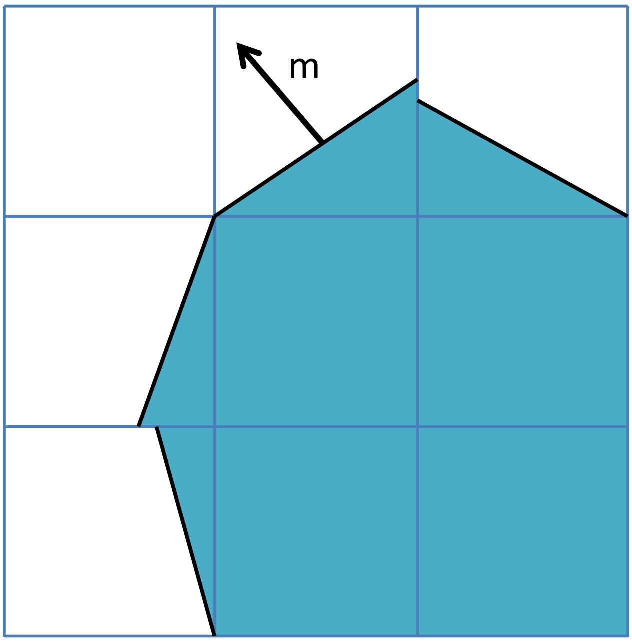

Figure 3.14: Illustration of planar shapes for PLIC scheme with normal orientation m, as adapted from (Richards et al., 2016).

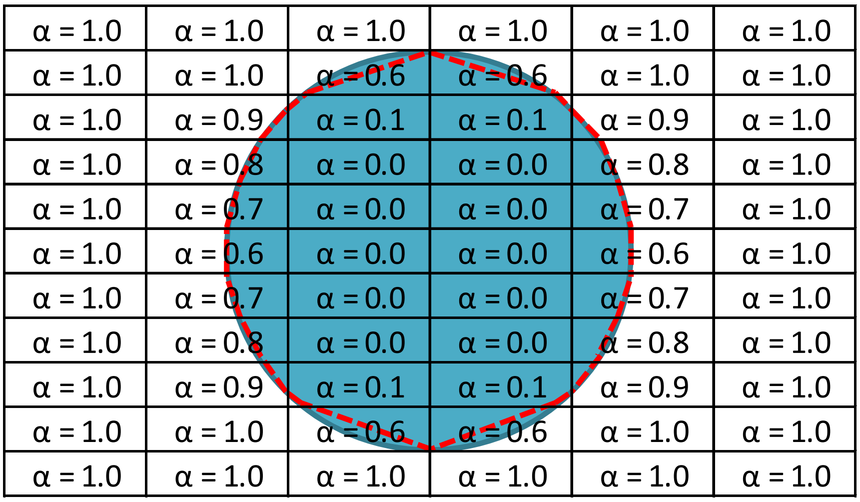

α = 1.0	α = 1.0	α = 1.0	α = 1.0	α = 1.0	α = 1.0
α = 1.0	α = 1.0	α = 0.6	α = 0.6	α = 1.0	α = 1.0
α = 1.0	α = 0.9	α = 0.1	α = 0.1	α = 0.9	α = 1.0
α = 1.0	α = 0.8	α = 0.0	α = 0.0	α = 0.8	α = 1.0
α = 1.0	α = 0.7	α = 0.0	α = 0.0	α = 0.7	α = 1.0
α = 1.0	α = 0.6	α = 0.0	α = 0.0	α = 0.6	α = 1.0
α = 1.0	α = 0.7	α = 0.0	α = 0.0	α = 0.7	α = 1.0
α = 1.0	α = 0.8	α = 0.0	α = 0.0	α = 0.8	α = 1.0
α = 1.0	α = 0.9	α = 0.1	α = 0.1	α = 0.9	α = 1.0
α = 1.0	α = 1.0	α = 0.6	α = 0.6	α = 1.0	α = 1.0
α = 1.0	α = 1.0	α = 1.0	α = 1.0	α = 1.0	α = 1.0

Figure 3.15: Representation of Volume of Fluid method for a droplet with planar shape equation in red dotted line, as adapted from (Richards et al., 2016).

$$m = \frac{\partial \alpha}{\partial x_i}, \tag{3.83}$$

$$m_x x + m_y y + m_z z = d, \tag{3.84}$$

in which m is the interface normal vector, and d stands for the plane equation constant.

3.3.1.5 Pressure-velocity coupling

As the equations for velocity and pressure are solved separately they must be linked to guarantee that the velocity field is linked to the pressure gradient in the pressure-velocity coupling. Among the available methods found on the literature the Semi-Implicit Method for Pressure Linked Equations (SIMPLE) is a well validated method. This method is well documented by Versteeg and Malalasekera (2007) and summarised in Figure 3.16

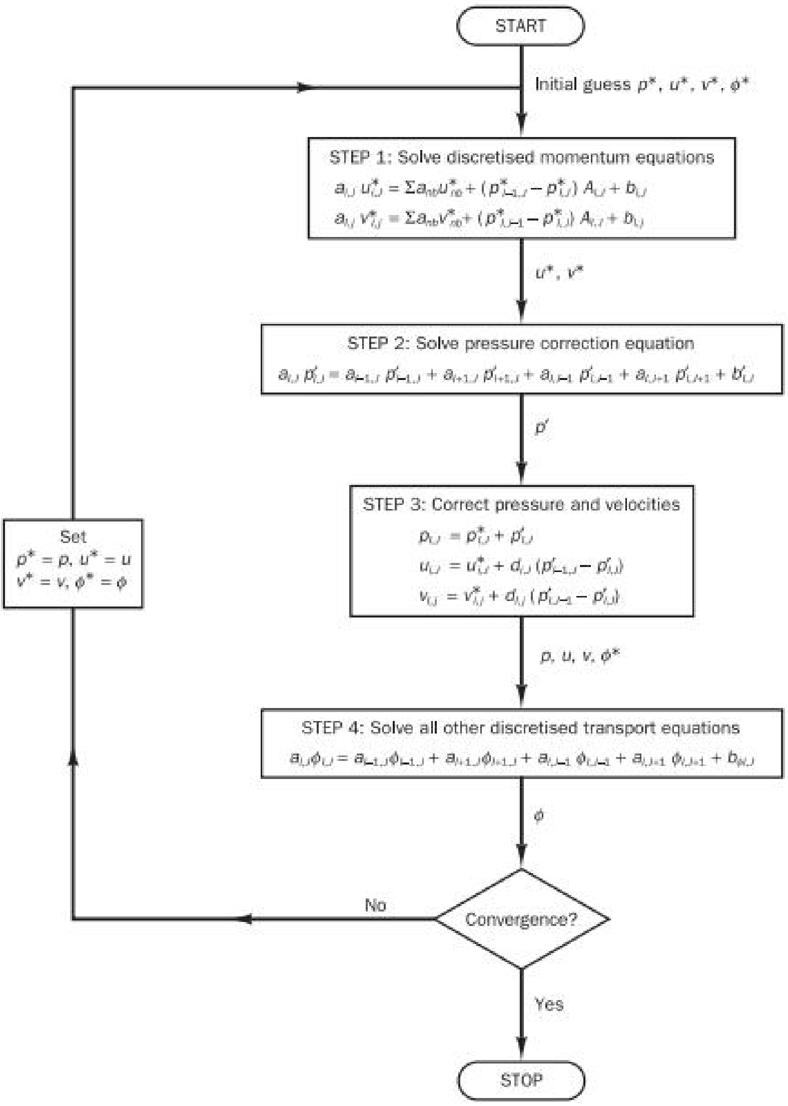

Figure 3.16: SIMPLE method as presented by (Versteeg and Malalasekera, 2007). The image illustrates the block diagram containing the logic of the algorithm used to couple velocity and pressure.

in which the superscript $t+1$ denotes an advance in time step.

The algorithm can be interpreted as follows. An initial guess of the variables are needed to solve the discretised equations for momentum. The second step consists of solving the pressure correction equation. The pressure calculated in the second step is used to correct the variables in the third step. In the fourth step other discretised variables are solved. After all this steps residual is evaluated. If residual is below a chosen value, then the algorithm goes to the next time step, otherwise it will repeat the algorithm.

Following a similar methodology, Issa (1986) created the Pressure Implicit with Splitting of Operators (PISO) method. Figure 3.17 represents the diagram of the method. The PISO method was developed for non-iterative computation of unsteady compressible flows, but the method was further developed and was adapted for iterative computations. As presented by Versteeg and Malalasekera (2007), the PISO method can be interpreted as an extension of the SIMPLE method. The first three steps of SIMPLE are repeated in the PISO algorithm as presented in Figure 3.17. The difference starts on Step 4, in which a second pressure correction takes place. The pressures and velocities are corrected in Step 5. In Step 6, the convergence is checked and the time step is advanced or the algorithm is repeated for the current time step, depending on the convergence criteria used.

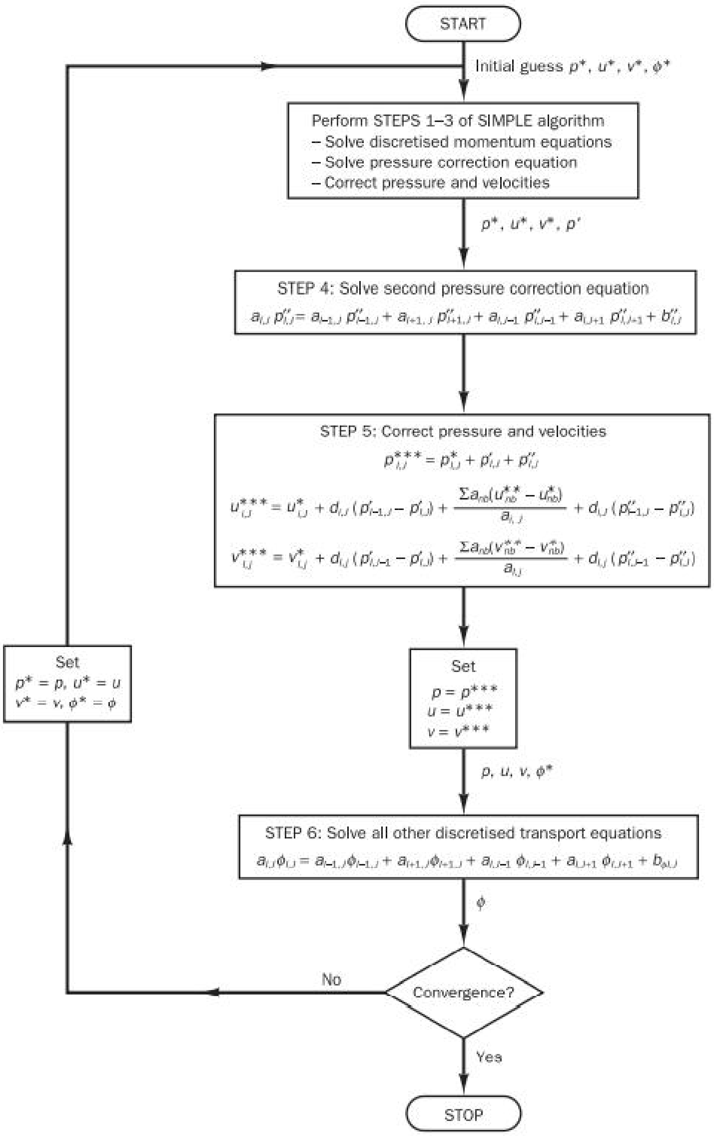

Figure 3.17: PISO method as presented by (Versteeg and Malalasekera, 2007). The image illustrates the block diagram containing the logic of the algorithm used to couple velocity and pressure.

A bench-marking of the methods presented good results for PISO algorithm for a case of laminar backward-facing step case presented by Issa (1986). The computational cost was reduced by its half when compared to SIMPLE. Many other methods based on SIMPLE are available on the literature, such as SIMPLER and SIMPLEC. More details are found in the work of Versteeg and Malalasekera (2007).

3.3.1.6 Momentum interpolation method

In a code that uses a collocated grid the variables are stored in the centroid of the control volume. To evaluate the variable at the centre of the surface an interpolation scheme is needed. The velocity is calculated at the face centre as presented in Equation 3.85, as documented by Fontes et al. (2018b).

$$\begin{gathered}u_{if} = u^*_{if} \cdot n_{if} + CAP\left(p_R - p_L - \nabla p_f \cdot \vec{ds}\right) - \\ \tfrac{2CAP\sigma}{\rho_g+\rho_l}\left(\rho^*_f k^*_f(\alpha_R - \alpha_L) - \tfrac{2(k_R\nabla\alpha_R + k_L\nabla\alpha_L)}{\rho^*_f} \cdot \vec{ds}\right) + \\ \tfrac{V_L\rho_L^{n-1}+V_R\rho_R^{n-1}}{\delta t(ap_L+ap_R)}\left(u_{if}^{n-1} - u_{if}^{*n-1} \cdot n_{if}\right),\end{gathered} \tag{3.85}$$

in which u^*_{if} is a first approximation of the velocity on the considered face, ap_L and ap_R are coefficients used for the approximation scheme, n_{ij} is the unit vector normal to the considered face, ∇p_f is a gradient evaluated between the considered faces, ρ^*_f is a first approximation of density, k^*_f is a first approximation of the curvature at the face between the two cells, CAP is the contribution of the cell volumes as represented in Equation 3.86.

$$CAP = -\left(\tfrac{1}{\vec{ds}\cdot n_{if}}\right)\left(\tfrac{V_L+V_R}{\alpha p_L+\alpha p_R}\right), \tag{3.86}$$

3.3.2 Lagrangian referential

As mentioned in Section 3.1, the small droplets are considered Lagrangian phase and their mathematical model is presented in Subsection 3.2.2. In the current section the numerical scheme to locate and evaluate the Lagrangian phase is presented.

3.3.2.1 Integration scheme for Lagrangian referential

Equations for droplet motion were integrated and the results are represent in Equation 3.87 and Equation 3.88 respectively for velocity and position of the parcels, as quoted by Fontes et al. (2018b).

$$u_p^{n+1} = u^n + e^{\frac{-\Delta t}{\tau_p}} \left(u_p^n - u^n\right) - a\tau_p \left(e^{\frac{-\Delta t}{\tau_p}} - 1\right), \tag{3.87}$$

$$x_p^{n+1} = x_p^n + u^n \Delta t + a\tau_p \Delta t + \left(u_p^n - u^n - a\tau_p\right) \tau_p \left(1 - e^{\frac{-(\Delta t)}{\tau_p}}\right), \tag{3.88}$$

in which x is the droplet position, τ_p is the relaxation time, and a is the weight-buoyancy force divided by the mass.

3.3.2.2 Interpolation at droplet position

The velocity of the Eulerian phase is required at the centre of the droplet in some equations. Regarding the fact that inside the control volume the velocity is considered constant, using the velocity of the containing element is not a good approximation. It is more precise to approximate the velocity at the droplet location also using the velocity of the surrounded volumes. To evaluate the required velocity the Shepard scheme was used. The main variables are represented in Figure 3.18. Equation 3.89 represents the numerical scheme to approximate a variable at the droplet position. This equation uses a weighted average of the inverse of the distances between the centroid of each cell and the droplet position to calculate the desired variable, as in the work of Fontes et al. (2018b).

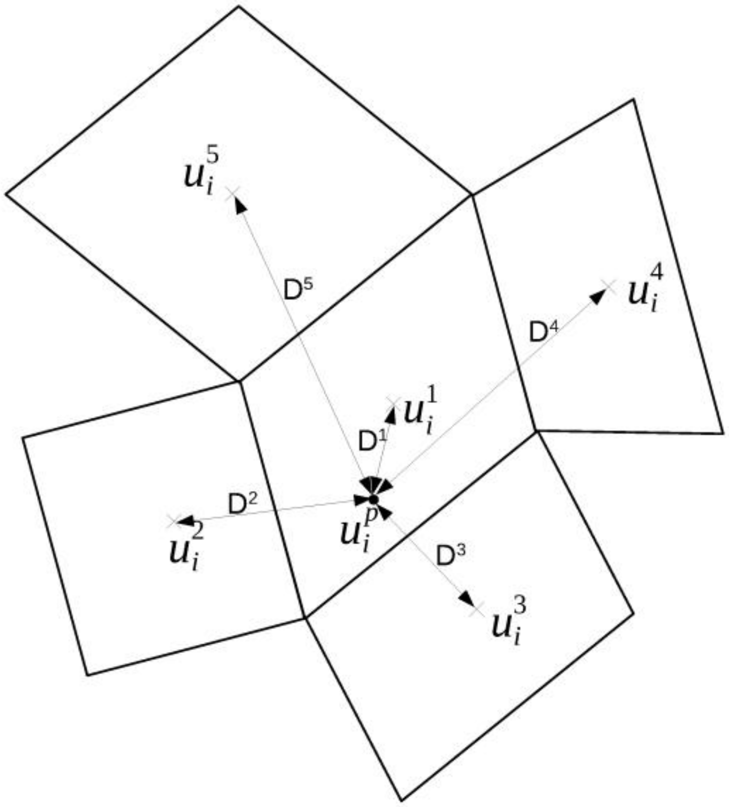

Figure 3.18: Representation of droplet position and Eulerian velocity approximation scheme at the droplet centre as in the work of (Fontes et al., 2018b). The velocity (u) of the surrounding cells are taken into account in order to accurately predict the velocity at the Lagrangian droplet.

$$u_{j_p} = \frac{\sum_{i=1}^{N}\left(\frac{u_j^i}{D^i}\right)}{\sum_{i=1}^{N}\left(\frac{1}{D^i}\right)}, \tag{3.89}$$

in which D is the distance between the cell centres.

3.3.2.3 Algorithm of droplet tracking

The droplet tracking algorithm is based on the computing of the intersections of the droplets trajectory. The first step is solving the flow for the Eulerian phase. In the second step the initial position and velocity of the droplets are known, and they are used to calculate the new velocity and position. To track the droplet, the new position is compared to the face centre of the control volume as expressed by Equation 3.90. It is important to highlight that the droplets in this algorithm can cross more than one control volume in a single step, making it more efficient than others found on the literature. The droplet will be inside the cell in analyses if the droplet location satisfies Equation 3.90 in the ‘in-cell test’ for all the cell faces, as in the work of Haselbacher et al. (2007).

$$(r_c - r_p) .\vec{n}{\geq}0, \tag{3.90}$$

in which r_c is the position of the centre of the finite volumes faces cell, r_p is the new position of the cell, and $\vec{n}$ is the vector pointing out the face.

3.3.3 Film formation numerical modelling

This section briefly describes the numerical modelling of the wall film formation. It is divided in two sections, the first one for the VOF method and the second section for the EWF method.

3.3.3.1 VOF film formation numerical modelling

For modelling the fluid interaction with the wall, the contact angle adjusts the normal vectors of the cells close to the wall. The curvature of the surface near the wall is adjusted to the boundary condition. The surface normal at the cell next to the wall is calculated as in Equation 3.91.

$$n_i = n_{wi} cos(\theta_w) + t_{wi} sin(\theta_w), \tag{3.91}$$

in which n_i is the surface normal at the cell next to the wall, θ_w is the contact angle on the wall, n_{wi} and $t_w i$ are the unit vectors normal and tangential to the wall, respectively.

The local curvature of the surface is determined by the combination of this contact angle and the calculated normal vector. This curvature is used to adjust the body force in the surface tension equation.

The force is modelled using a Continuum Surface Force Model (CSF). A modified void fraction is defined as in Equation 3.92. This modified void fraction is used to compute the force.

$$\tilde{\alpha}(x) = \frac{1}{h^3} \int_{CV} \alpha(x')\phi(x'-x)d^3x', \tag{3.92}$$

in which $\tilde{\alpha}(x)$ is the modified void fraction, ϕ is the Gaussian filter interpolation function, $\phi = 0$ for $|x| \geq h/2$, and h is the thickness across the interface between fluids.

The force is then calculated as in Equation 3.93.

$$F_{sfi} = \sigma\kappa(x)\frac{\partial\tilde{\alpha}(x)}{\partial x_i}, \tag{3.93}$$

3.3.3.2 EWF numerical modelling

In this section, the discretisation scheme for the surface gradient ∇_s and the surface Laplacian operator are presented. The surface gradient is found in Equation 3.45, which is the conservation equation for the film mass, and in Equation 3.46, which is the momentum conservation for the liquid film. The Laplacian operator is found in Equation 3.49, which is the term that accounts for the pressure generated by the surface tension.

By means of the Green-Gauss theorem applied to a two-dimensional cell, the surface gradient ∇_s can be represented as in Equation 3.94. In this equation, ϕ is a chosen variable.

$$\nabla_s\phi = \frac{1}{A}\sum \phi_e \vec{l_e} \tag{3.94}$$

in which ϕ_e is interpolated as the arithmetic average of the ϕ at the two neighbouring cells sharing the edge e. l_e is the edge vector pointing outwards of the cell, whose modulus is the edge length. A is the area of the cell. The summation runs over all cell edges.

The surface Laplacian operator is calculated as proposed by Baleta et al. (2015) and presented in Equation 3.95.

$$\nabla_s \cdot (\nabla_s\phi) = \frac{1}{A}\sum \frac{\phi_R - \phi_L}{l_{LR}}\vec{l_e} \tag{3.95}$$

in which the subscripts L and R indicate the cells at the left and right-hand-side of the edge, respectively. l_{LR} is the distance between both cell centres.

For the edge boundary condition steady Neumann-like boundary conditions are prescribed. This is equivalent as a sink, as it breaks-up the liquid film but no droplets are generated. This is mainly due to the absence of correlations for the resulting secondary droplets. Future works will further investigate this phenomena.

4 Physical experimentation procedure

This chapter presents the procedure used to conduct the physical experimentation. The experiments were carried out to generate data for the VOF simulations, whose results are presented in Chapter 5 and compared with the physical experiments of the current chapter. For that, images of droplets colliding with a wall were captured.

Throughout this chapter the test rig is presented, then three subsection explain the experimental procedure and the algorithm for image analyses and results. The first subsection explains the experimental test rig assembly and the measurement of the main parameters. The second subsection explains the image processing. The third subsection presents the main results.

The sketch for the experiment is illustrated on Figure 4.1. An injector generates a chain of droplets that collides on the opposite wall. This droplet impingement causes the formation of liquid film on the wall.

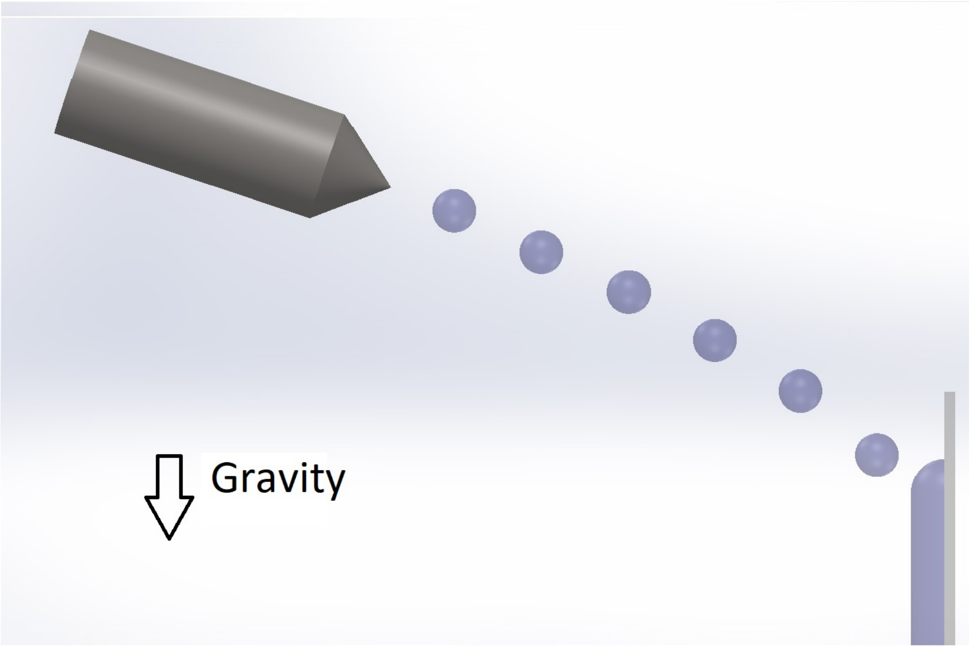

Figure 4.1: Illustration of test rig. The sketch for the experiment illustrates the injector in grey, the liquid in blue and the plate in light grey. The injector generates a droplet chain that hits the opposing wall forming a liquid film.

To help on the analysis of the impinging droplets and wall film formation, dimensionless numbers are used. The first one regarding the droplets is the Weber number, represented in Equation 4.1. This number measures the relative importance of the inertia of the fluid compared to its surface tension.

$$We = \frac{u^2 d_0 \rho_l}{\sigma}, \tag{4.1}$$

in which We is the Weber number, u is the average droplet velocity, d_0 is the average diameter of the droplet, ρ_l is the liquid density, and σ is the surface tension coefficient.

The Reynolds number is calculated for the droplet as represented in Equation 4.2. This number measures the relative importance of the inertia of the fluid compared to its viscous forces.

$$Re = \frac{\rho_l u d_0}{\mu_l}, \tag{4.2}$$

in which Re is the Reynolds number, and μ_l is the liquid dynamic viscosity.

The Laplace number is calculated for the droplet as represented in Equation 4.3. This number measures the relative importance of surface tension to the momentum-transport, and it is a combination of Reynolds and Weber number.

$$La = \frac{\rho_l \sigma d_0}{\mu_l^2} = \frac{Re^2}{We}, \tag{4.3}$$

in which La is the Laplace number.

The momentum parameter for the primary droplets S_{cd} is represented in Equation 4.4. This parameter is used to predict the outcomes of the droplet impact. Depending on this number the droplet can coalesce or splash after hitting a wall, as stated by Arienti et al. (2011).

$$S_{cd} = \frac{1}{24} \frac{\rho_l^{0.581}}{\mu_l^{0.162} \sigma^{0.4189}} d_0^{0.581} v_d \sin^{0.63}(\alpha_{impact}), \tag{4.4}$$

in which S_{cd} is the momentum parameter, v_d is the average velocity, α_{impact} is the impact angle.

As stated by Arienti et al. (2011), the momentum parameter is a combination of the Reynolds and the Laplace number as presented in Equation 4.5.

$$S_{cd} = \frac{1}{24} Re La^{-0.4189}, \tag{4.5}$$

Another important dimensionless number dependent on Weber and Reynolds is represented in Equation 4.6. This parameter is used to evaluate liquid deposition, as in the work of Kuhnke (2004a).

$$K = We^{0.5} Re^{0.25}, \tag{4.6}$$

in which K is the deposition coefficient.

The results for liquid film are represented in a non dimensional formulation for the liquid film height, as represented in Equation 4.7.

$$h_0 = \frac{h}{d_0}, \tag{4.7}$$

in which h_0 is the non dimensional film height, and h is the film height,

The results for pool size are represented in a non dimensional formulation similar to the liquid film height, as represented in Equation 4.8.

$$w_0 = \frac{w}{d_0}, \tag{4.8}$$

in which w_0 is the non dimensional pool size, and w is the pool size.

4.1 Experimental test rig

The experimental test rig is illustrated in Figure 4.2. It consists of a droplet generator with an oscillating membrane (Encap BioSystems, model IE-0010H-P) which is responsible for generating an water droplet chain. This droplet chain hits the opposite wall, where a liquid film is formed. For the experiment, two PHOTRON FASTCAM SA4 cameras were equipped with a Nikon lens PC-E Micro Nikkor 85mm 1:2. The first camera is used to record the impinging droplets and the film from the side. The second camera is used to record the film shape.

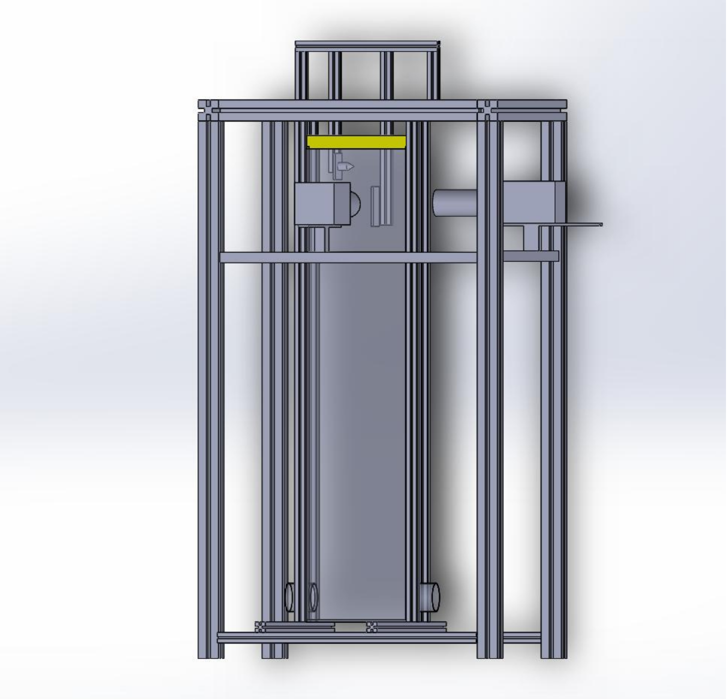

Figure 4.2: Illustration of test rig. The sketch represents the honey comb in yellow, the structure that holds the facility and the cameras in grey. The injector and the plate are illustrated inside the facility below the honey comb.

The injection system is pressurised by an Air Compressor Werther Model P 50/24 AL Black Panther, which is illustrated in Figure 4.3.

Figure 4.3: Air compressor used to pressurise the vessel.

The compressed air is used to pressurise a Impexron GmbH vessel Krautzberger 200-0278, which contains the water and the pressurised air, as illustrated in Figure 4.4. A valve is then used to regulate the flow rate of the nozzle.

Figure 4.4: Pressurized vessel containing the liquid to be injected and pressurised air.

The power amplifier (Thoman TA1050 MK-X) was used to generate the amplitude of the oscillation signal for the actuator. It is illustrated in Figure 4.5. The generated signal is used to control an actuator, which is illustrated in Figure 4.6. This set of equipment is used to control the first break-up of the liquid jet, generating a controlled droplet chain.

Figure 4.5: Tune generator used to tune the frequency to break-up the liquid jet in a liquid chain.

Figure 4.6: Signal actuator that receives the signal from the tune generator and vibrates the injector to generate a droplet chain.

The injector is illustrated on Figure 4.7. The water supply is represented by the pink hose. The actuator is assembled on the left side of the injector.

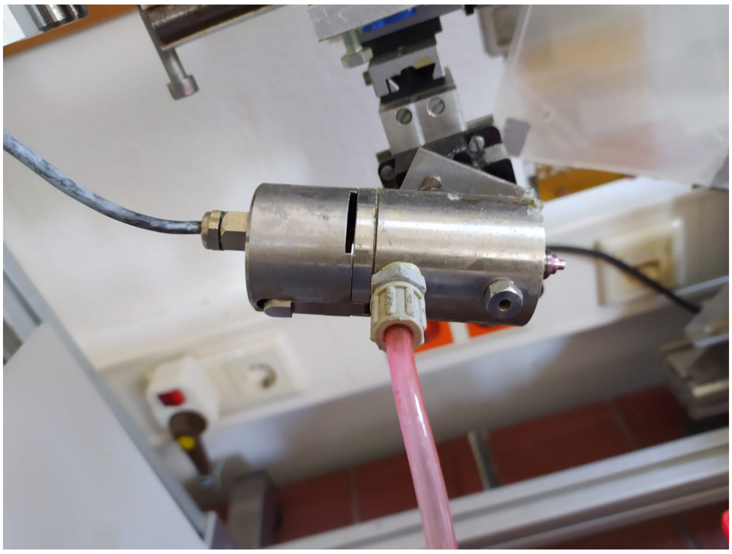

Figure 4.7: Injector assembled with the signal actuator and the pressurised liquid. This assembly generates the droplet chain.

A set of LED lights is assembled behind an opaque screen to diffuse the light as illustrated in Figure 4.8. The LEDs are powered with 12 volts by a programmable power supply Hameg Instruments HMP4030384 Watt as illustrated on Figure 4.9.

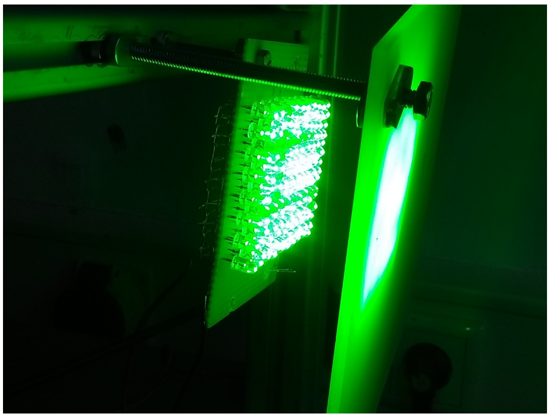

Figure 4.8: LED set used as back light for the high speed cameras.

Figure 4.9: Oscilloscope used to power the LED set.

The droplet chain is then aligned to hit the opposite wall as illustrated in Figure 4.10. The image illustrates a closer look to the general assembly of the experiment illustrating different components. The pressurised liquid comes from the right side and it is coupled with the injector. The signal actuator can be seen in the back side of the injector. The camera is on the left and the green LED set is assembled on the other side of the experiment so that the light travels to the camera lens after passing through the droplet chain. The injector is on the upper side with a droplet chain issuing out of the nozzle and hitting the transparent plate forming the liquid film.

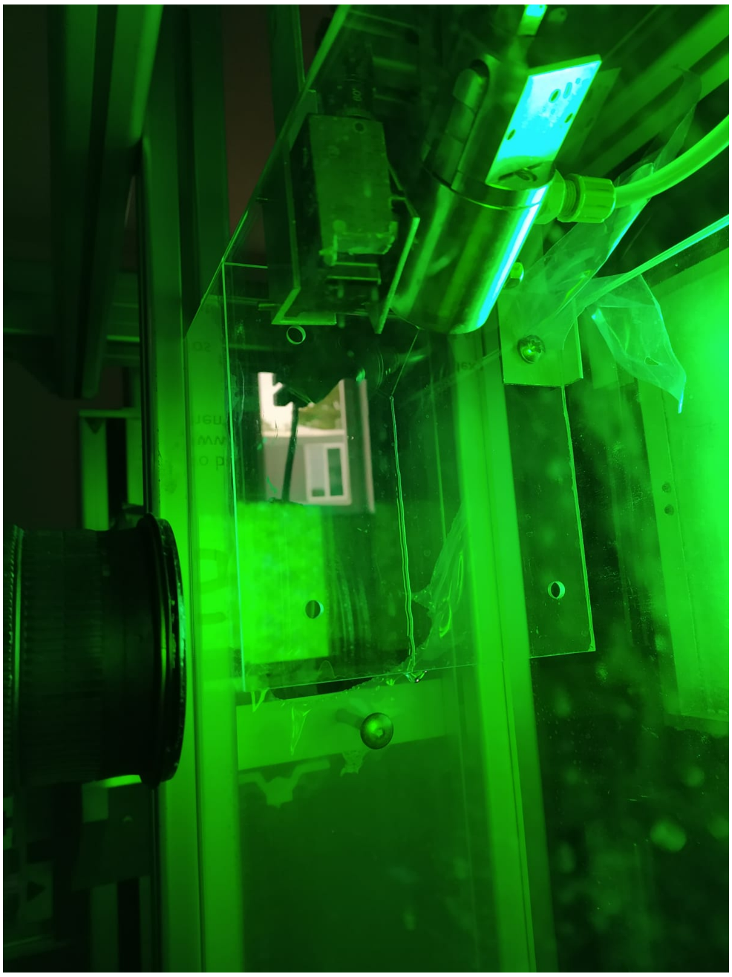

Figure 4.10: Impinging droplet chain. The image illustrates a closer look to the general assembly of the experiment illustrating different components. The pressurised liquid comes from the right side and it is coupled with the injector. The signal actuator can be seen in the back side of the injector. The camera is on the left and the green LED set is assembled on the other side of the experiment so that the light travels to the camera lens after passing through the droplet chain. The injector is on the upper side with a droplet chain issuing out of the nozzle and hitting the transparent plate forming the liquid film.

A traverse system ISEL automation CNC kontroller C 116 is used to align the camera as illustrated on Figure 4.11. To control the traverse system a control system is used and it is represented in Figure 4.12.

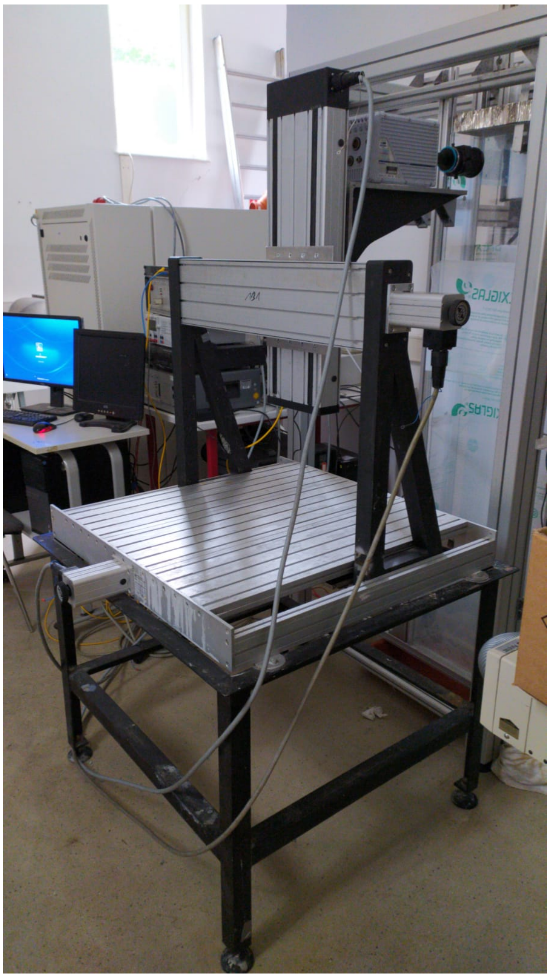

Figure 4.11: Traverse system used to position the camera. The system can position the camera in three different directions. Up, down left and right are used to align the camera with the droplet chain. The backward and forward movement is used to focus the camera.

Figure 4.12: Traverse control system. This system is connected to the computer to control the traverse system.

To measure the density of the liquid both a volume and mass measurements were necessary. To measure the volume a volumetric flask (DIN 12797) of 50 ml was used as represented in Figure 4.13 and 4.14. The empty volumetric flask was placed on a Sartorios electronic precision balance as illustrated in Figure 4.14. After that, it was filled with liquid as represented in Figure 4.13. The difference in mass is the liquid mass. Using the measured volume and the calculated mass it was possible to obtain the liquid density.

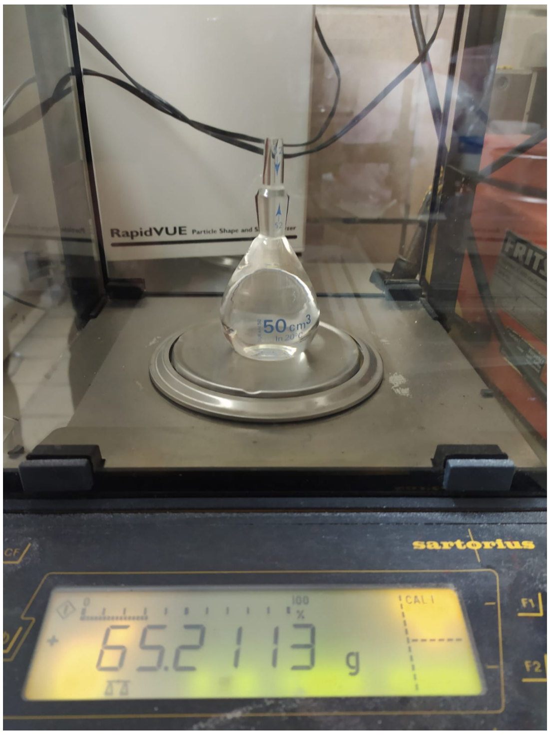

Figure 4.13: Volumetric flask containing liquid. The mass of the liquid and the flask are measured.

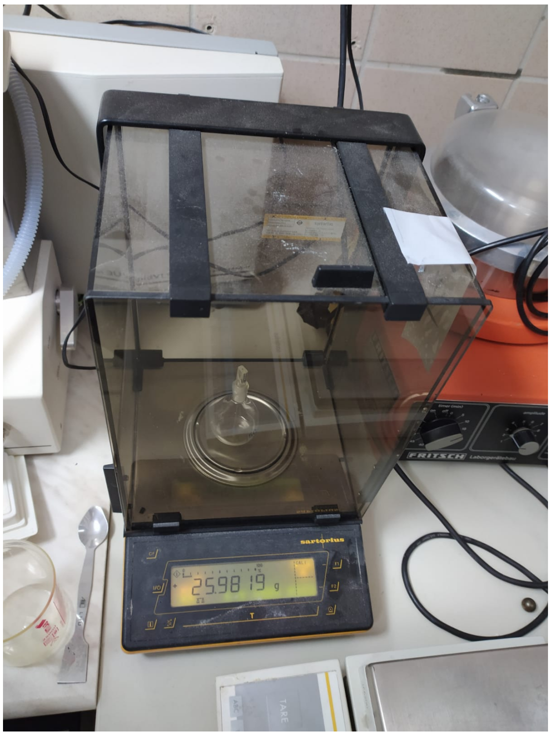

Figure 4.14: Empty volumetric flask. The mass of the flask is measured. The difference of the empty and the full volumetric flask are used to measure the fluid mass.

To measure the viscosity of the liquids a Brookfield KF10 falling ball viscometer was used. The viscometer is illustrated on Figure 4.15. The inside tube was filled with the liquid and a glass sphere was placed on the top side. By measuring the time spent for the ball to reach the bottom Equation 4.9 is used to calculate the viscosity.

Figure 4.15: Falling ball viscometer. This equipment is used to measure the viscosity of the liquids used in the physical experimentation.

$$\eta = t(\rho_1\rho_2)KF, \tag{4.9}$$

in which, η stands for dynamic viscosity, t for the travelling time of the ball, ρ_1 for density of the ball, ρ_2 for density of the liquid, K for ball constant according to calibration certificate and F for working angle constant, also found in calibration certificate.

To measure the surface tension of the liquid a ring tear-off method was used and the apparatus is illustrated on Figure 4.16. The ring is immersed in the liquid pool. Then, by moving the screw below the table, the ring goes in the direction of the surface between the liquid and air. To make sure it is levelled, a lens system is placed to check the lever balance as represented in Figure 4.17. By moving the screw below the table and the screw of the ring tear-off equipment while maintaining the balance of the lever, the ring is slightly pushed away from the surface. After the ring goes out from the pool the surface tension can be directed read from the scale.

Figure 4.16: Ring tear-off equipment to measure liquid surface tension.

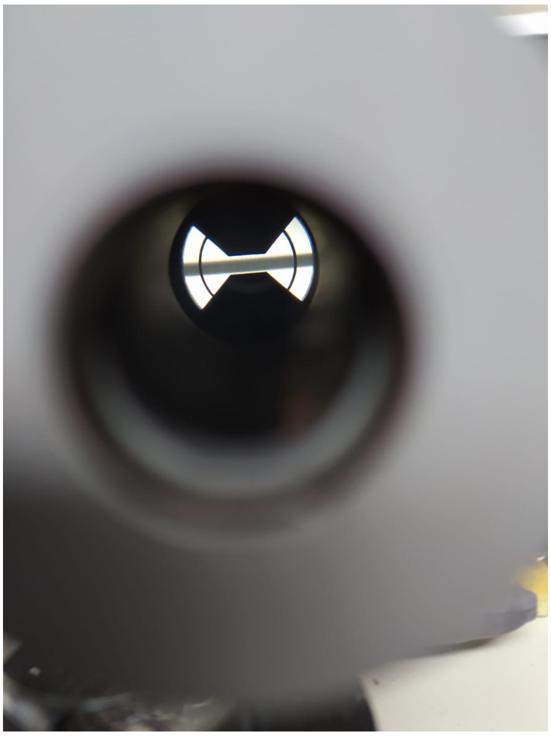

Figure 4.17: Lever balance using lens. This lever must be aligned in the middle of the lenss during the experiments to correct measure the surface tension.

The properties of the fluids are then presented as follows: The air is considered with density of $\rho_g = 1.427\ kg/m^3$, and dynamic viscosity of $\mu_g = 1.79 \cdot 10^{-5}\ kg/m \cdot s$, at 300 K. Water has density $\rho_l = 994\ kg/m^3$, and dynamic viscosity $\mu_l = 7.35 \cdot 10^{-4}\ kg/m \cdot s$, at 300 K. The surface tension between these phases is $\sigma = 0.0688\ N/m$. Ethanol has density $\rho_l = 783$ kg/m^3, and dynamic viscosity $\mu_l = 9.05 \cdot 10^{-4}\ kg/m \cdot s$, at 300 K. The surface tension between these phases is $\sigma = 0.0268\ N/m$. Fluid properties are summarised in Table 4.1.

	Density (kg/m^3)	Dynamic viscosity ($kg/m \cdot s$)	Surface tension coefficient (N/m)
Air	1.427	$1.79 \cdot 10^{-5}$	-
Water	994	$7.35 \cdot 10^{-4}$	0.0688
Ethanol	783	$9.05 \cdot 10^{-4}$	0.0268

Table 4.1: Fluids properties at $300\ K$. These fluid properties were measured for water and ethanol.

4.2 Image processing

For image processing the open source package Fiji was used. This package is based on ImageJ software. For the side images the script presented on Appendix A was used and it is explained in this section. It is important to note that in ImageJ the y direction is downwards.

The first step is to obtain an image of the system without the nozzle generating droplets which is called background. This image is illustrated in Figure 4.18. It is used to compare with the image generated during the experiment and filter its values. A Fiji package called "Difference" was used to combine these images. An image generated during the experiment is represented on Figure 4.19. The filtered image generated by combining them is illustrated on Figure 4.20.

Figure 4.18: Background image. This image is captured in the absence of droplet chain and it is used to combine with the image generated with the droplet chain to accurately capture the droplets and the liquid film.

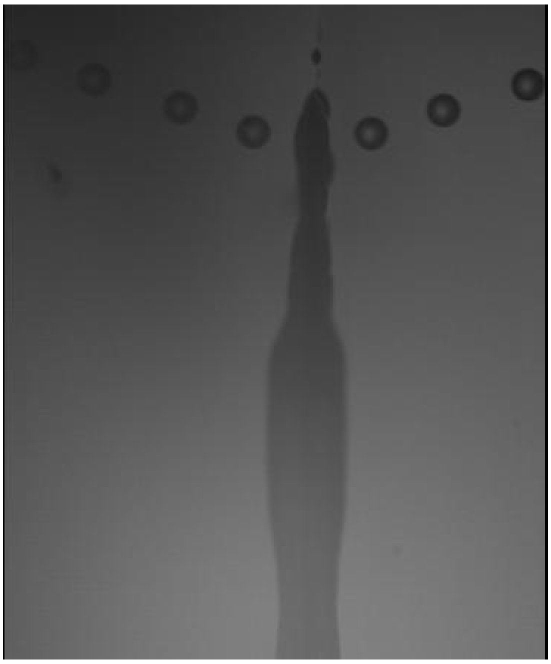

Figure 4.19: Image capturing the film liquid and the droplet chain. As the centre of this image received more light than in the corners it must be combined with the background image to accurately capture liquid locations.

Figure 4.20: Combination of the background image and the image capturing the liquid. The image cannot clearly present liquid location and needs further processing to generate binary locations of liquid.

After this process it is necessary to convert the resulting image into a binary image as well as filling the holes inside the droplets. The resulting image is illustrated in Figure 4.21 before filling holes and Figure 4.22 after filling the holes.

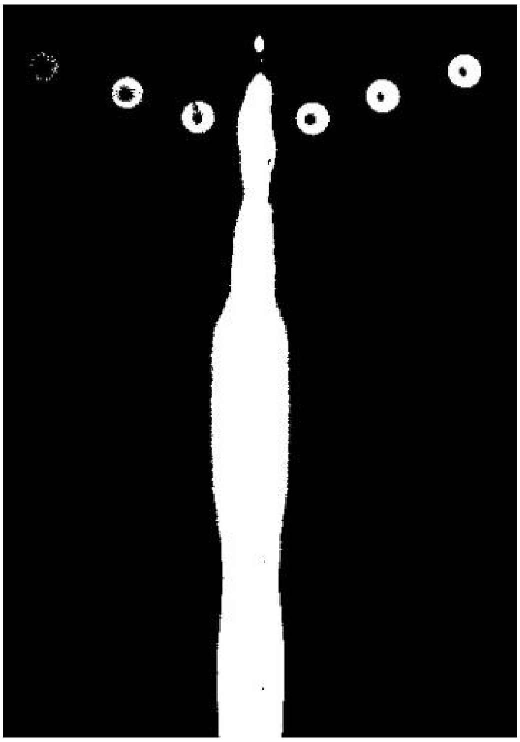

Figure 4.21: Binary image presenting liquid locations in white regions.

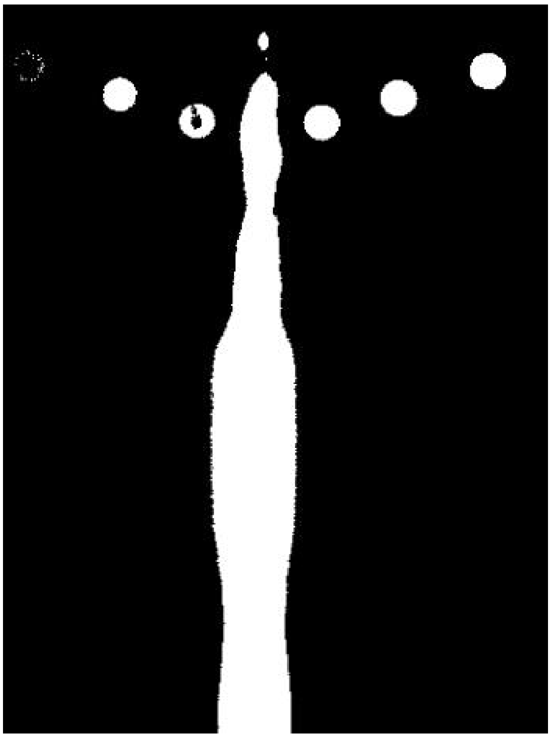

Figure 4.22: Binary image presenting liquid locations in white regions. After the liquid is identified, holes inside the liquid are filled in white.

The droplets are generated on the right side of the wall and hit on the same side. As can be observed on the images above, a reflection is observed on the left side. To remove the reflection the closest droplet to the right side of the wall as well as the closest droplet to the left side of the wall were used. A line was drawn connecting the centre of the two droplets. A line perpendicular to this line and crossing the middle point of the first line was generated and used to crop the image as represented on Figure 4.23. The image was also rotated by the angle of the last line and again transformed in binary, the resulting image is represented on Figure 4.24. This process is used to align the image and get a more precise impact angle. The rotations of the images were smaller than 1°.

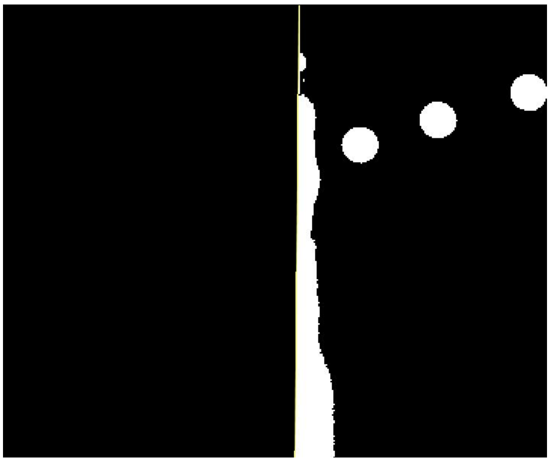

Figure 4.23: Cutting process of the image. As the image presented a mirror of liquid around the plate only half of the image is considered in the calculations.

Figure 4.24: Image presenting the final editing process with the droplet chain and the liquid film in white.

To analyse each droplet a Fiji package called Analyze particles was used. This package returns the values of circularity and centroid position of each droplet as represented in Figure 4.26. The analysed image is represented in Figure 4.25. Using values of the centroid position in subsequent frames the droplet velocity is calculated.

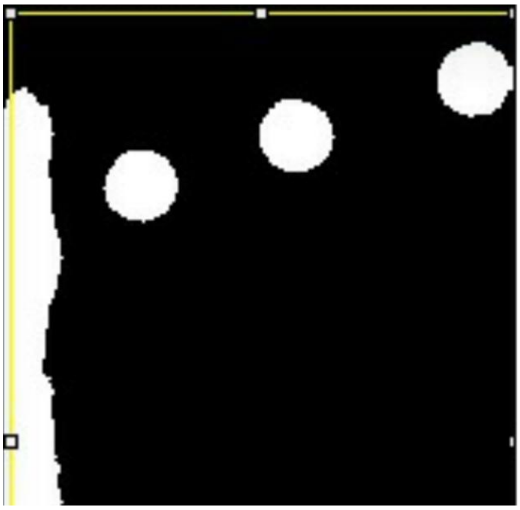

Figure 4.25: Block chosen to run the algorithm to detect droplet. The considered region is presented in the yellow box.

Figure 4.26: Droplets detected by the algorithm. After droplet identification the main parameters of the droplet can be measured such as radius and velocity.

To get the size of each pixel, a ruler was assembled on the experiment and an image was obtained. By counting the pixels on the ruler, the pixel size was obtained. The assembly is represented in Figure 4.27 and the image obtained in Figure 4.28.

Figure 4.27: Ruler assembly inside the test rig. The ruler is used to verify the dimension of each pixel recorded by the camera.

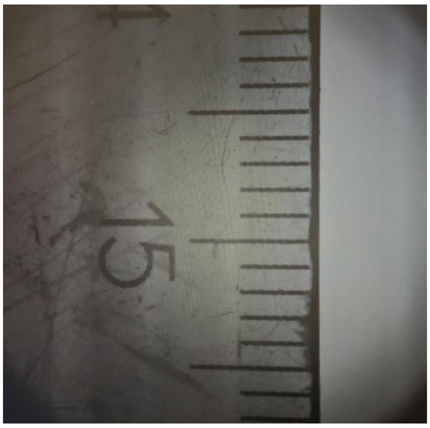

Figure 4.28: Image of the ruler used to verify the dimension of each pixel recorded by the camera.

This process was then repeated for all images. To calculate the velocity of each droplet the centroid of the droplet is compared to the centroid of the same droplet on the last image. The time was calculated by knowing the camera ratio of capturing images in frames per second.

To calculate the impact angle the velocity vector is used. The angle between the velocity line and the wall is considered as the impact angle of the droplet.

The script presented on Appendix A also stores the average of the film liquid height along the wall.

The second camera was used to capture images of the pool formation, and the image processing follows the script presented in Appendix B. This camera was also used to align the droplets as represented in Figure 4.29 for the not aligned droplets and Figure 4.30 for the aligned droplets.

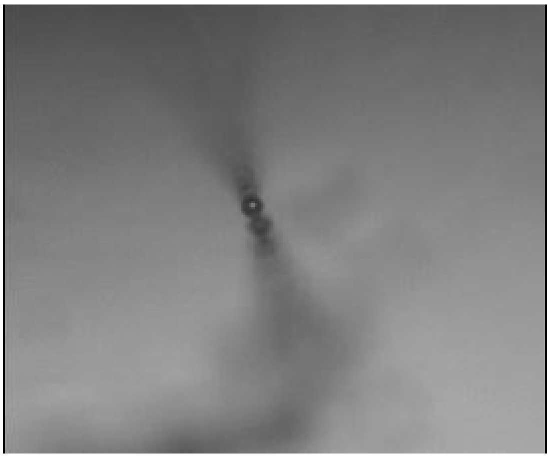

Figure 4.29: Droplets to be aligned. The image illustrates that the droplet chain is not yet aligned with the camera.

Figure 4.30: Droplets after alignment with camera.

For the images of side camera a similar procedure was conducted. Figure 4.31 presents the background image, Figure 4.32 the standard image and Figure 4.33 the difference of the images.

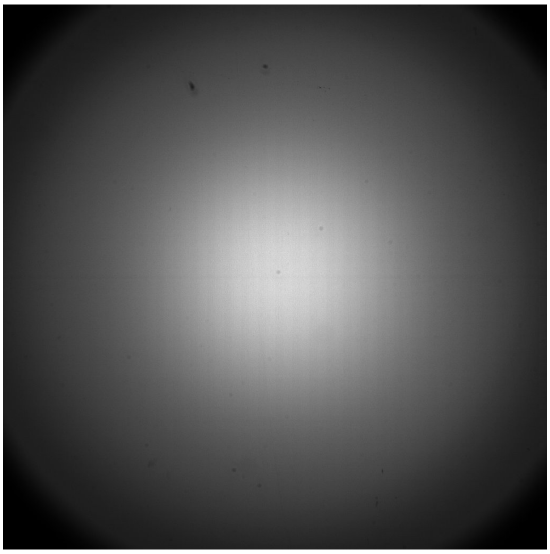

Figure 4.31: Background for side images. This image is captured in the absence of droplet chain and it is used to combine with the image generated with the droplet chain to accurately capture the liquid pool generated after droplet collision.

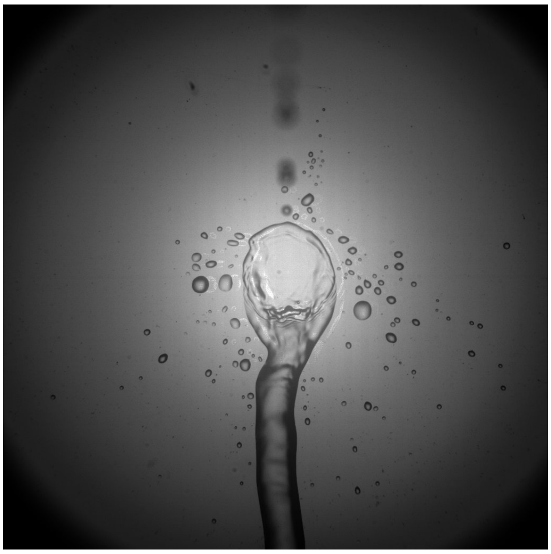

Figure 4.32: Image capturing the liquid pool formation after droplet collision. As the centre of this image received more light than in the corners it must be combined with the background image to accurately capture liquid locations.

Figure 4.33: Combination of the background image and the image capturing the liquid pool. The image needs further processing to generate binary locations of liquid.

From Figure 4.33 the binary image represented in Figure 4.34 could be obtained. From Figure 4.34 the droplets on the wall can be filtered as represented in Figure 4.35. After that, Figure 4.34 can be filtered as represented in Figure 4.36, and have its empty spaces filled as in Figure 4.37. The algorithm presented on Appendix B is able to calculate the average of the images and present a similar result to 4.37.

Figure 4.34: Image converted to binary. Liquid is presented in the white region.

Figure 4.35: Droplets detected outside the main vein. These droplets are not going to be considered in the calculations. Further processing excluded this droplets from the image.

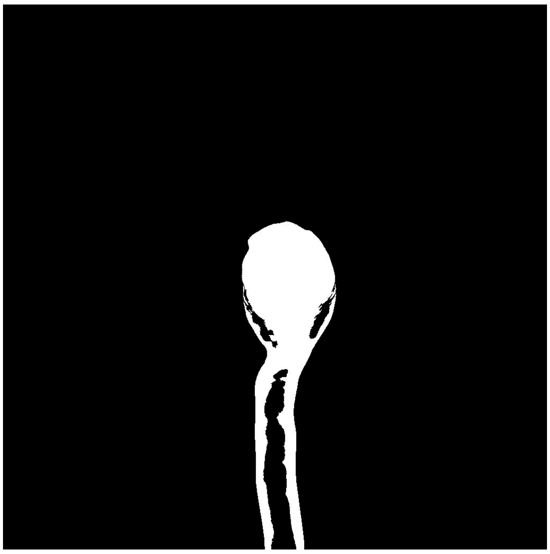

Figure 4.36: Filtered image excluding droplets outside vein. Liquid is present in white regions.

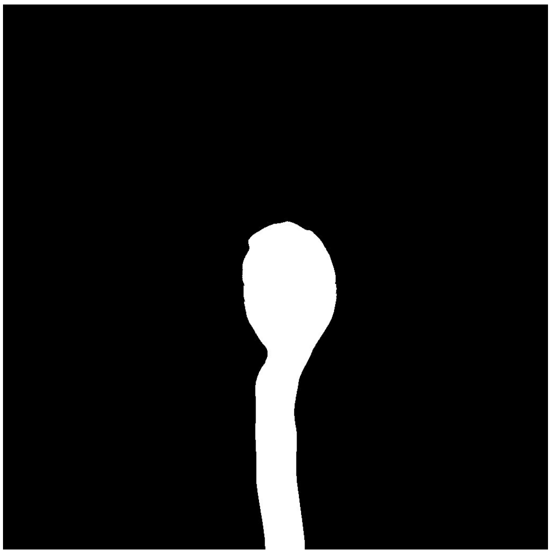

Figure 4.37: Image with filled empty spaces presenting the liquid in white.

The test rig was assembled in a different manner to measure the contact angle of the droplet with the wall. The transparent plate was positioned parallel to the floor as represented in Figure 4.38 and a droplet was placed above the plate as in Figure 4.39. The plate was positioned so that the drop did not flow out of it.

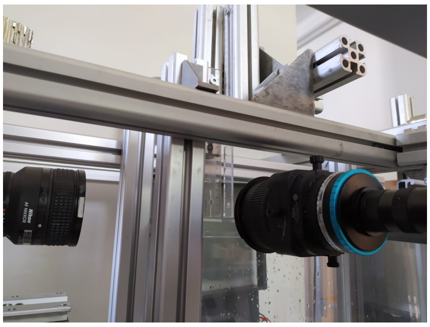

Figure 4.38: Camera and plate displacement for droplet contact angle experiment. The new assembly presents two rules in order to measure the pixel size as well as the droplet. The plate is assembled parallel to the ground to contain a droplet and measure contact angle.

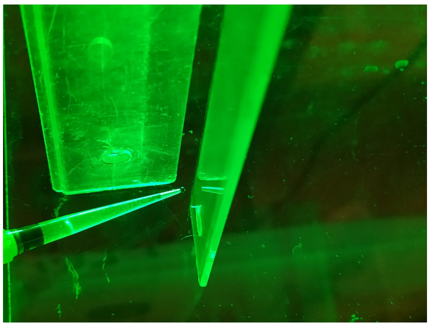

Figure 4.39: Small droplet being placed on plate for contact angle calculation.

The obtained images are represented in Figure 4.40 for the front camera and Figure 4.41 for the side camera.

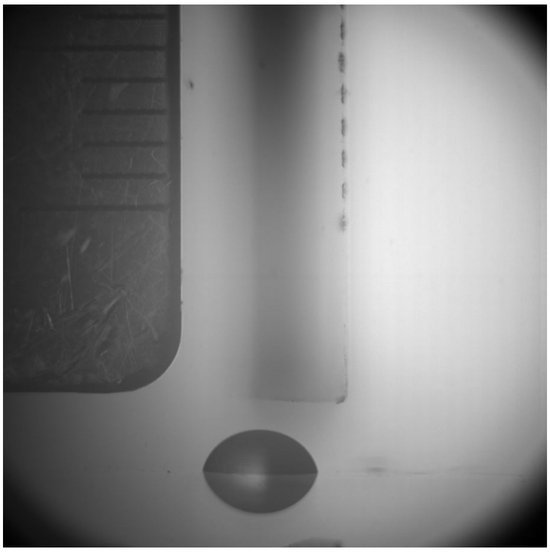

Figure 4.40: Droplet captured in front camera for contact angle calculation.

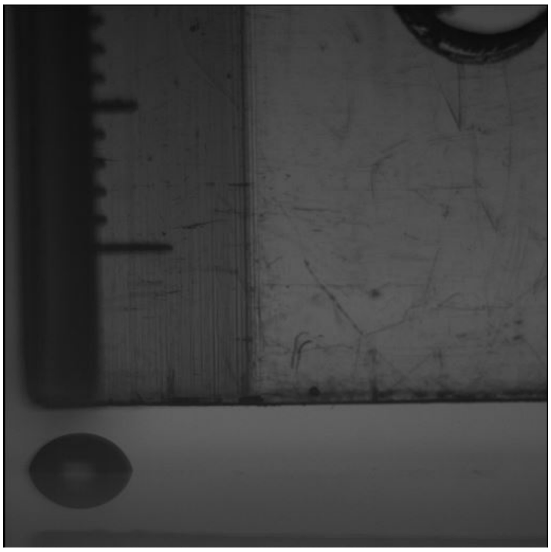

Figure 4.41: Droplet captured in side camera for contact angle calculation.

4.3 Experimental results

In this section the main results are presented and discussed. First the results are qualitatively discussed. Afterwards, the quantitative results are illustrated and discussed.

By means of Figure 4.40 and using the algorithm created by Stalder et al. (2006) for Fiji as represented in Figure 4.42 and Figure 4.43 a contact angle of 101.5 degrees was measured.

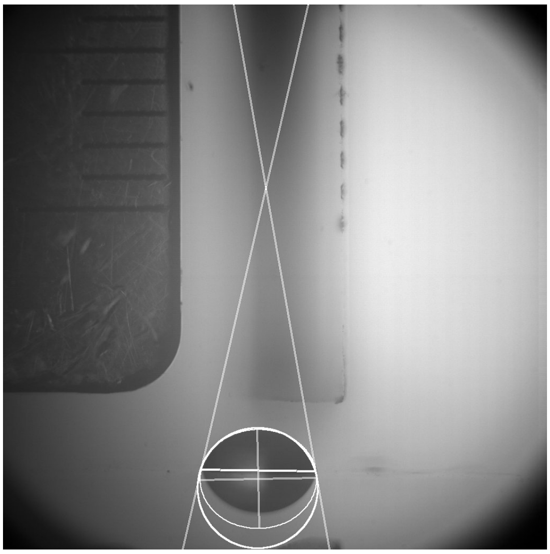

Figure 4.42: Representative lines for contact angle calculation on full image. The measured angle was 101.5 degrees.

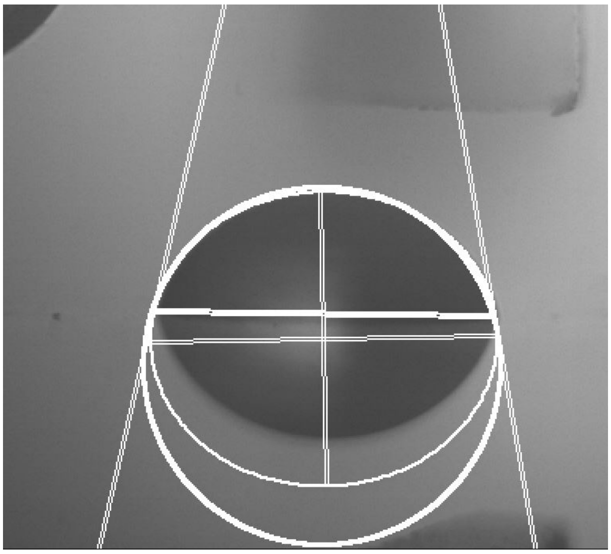

Figure 4.43: Representative lines for contact angle calculation near droplet and its reflex. The measured angle was 101.5 degrees.

For the physical tests of liquid film formation three different nozzles were used. Their difference is on the hole diameter, having 0.4, 0.3 and 0.2 mm. The tests were carried out in a quiescent environment.

Considering cases of complete absorption of the droplet on the liquid film some important observation are illustrated on the images that represents the pool formation. Taking for instance the example of droplets generated by the 0.3 mm nozzle, droplets with average diameter of 0.85 mm and velocity magnitude of 3.6 m/s were generated (Reynolds = 3428 and Weber = 151). For this case, the impact angle was set to 70°. The impact is represented in the sequence of images on Figure 4.44. Figure 4.44 a) represents the incoming droplet just before the impact. After the impact the droplet spreads radially as represented in Figure 4.44 b) spreading the liquid film. Gravity acts downwards meanwhile surface tension acts to regroup the liquid, resulting in the pool formation illustrated on Figure 4.44 c), in which the droplet spreading reaches the sides of the pool where the liquid height is maximum. Then this added mass is carried downwards as represented in Figure 4.44 d), forming a thinner and higher fluid.

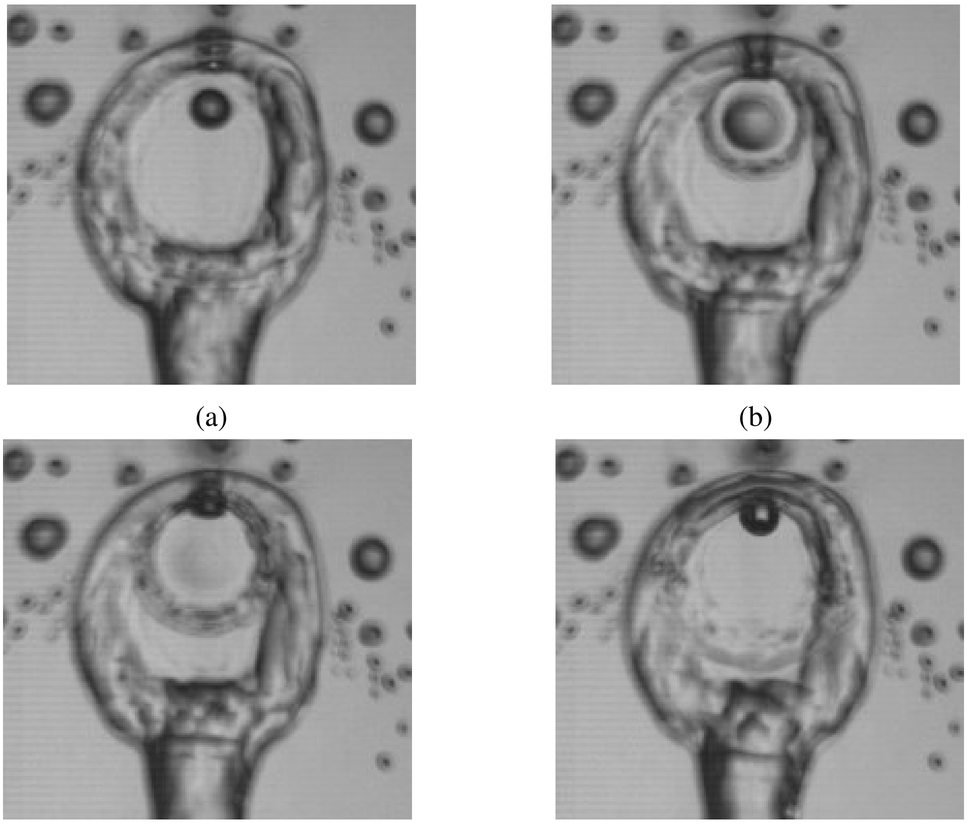

(a) (b)

(c) (d)

Figure 4.44: Droplet collision on wall. Figure (a) presents a moment just before the droplet collision with the wall. Figure (b) represents the droplet after collision and the start of the spread. Figure (c) represents the droplet already absorbed by the pool and the spreading of the liquid. Figure (d) represents the final stage of the droplet spreading and a new droplet going towards the plate.

Using the traverse system for the camera, different impact angles could be analysed. Figure 4.45 represents different pool shapes depending on impact angle. Figure 4.45a represents the impact generate by droplets with average diameter of 0.38 mm and velocity magnitude of 2.05 m/s (Reynolds = 873 and Weber = 22) in an impact angle of 56° and Figure 4.45b by droplets with average diameter of 0.33 mm and velocity magnitude of 2.25 m/s (Reynolds = 832 and Weber = 23) in an impact angle of 46°. Even though the Reynolds number and the Weber number are very similar, it is observed that the increasing impact angle generates a pool with an smaller aspect ratio. This behaviour was expected bearing in mind that the impact angle is related to the velocity components. Considering two equal droplets with the same velocity magnitude but different impact angles, the one with higher impact angle has a smaller velocity perpendicular to the wall. With that, less energy is used on the spreading of the droplet.

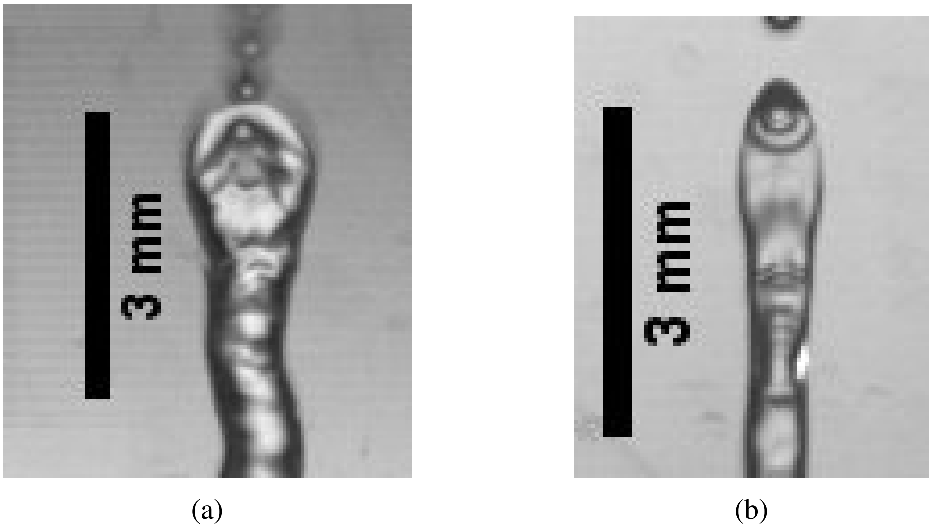
(a) (b)

Figure 4.45: Pool shape dependence on impact angle. Figure (a) presents the pool shape format for an in coming droplet at an angle of 56 °. Figure (b) presents the pool shape format for an in coming droplet at an angle of 46 °

By changing the flow rate in the valves and adjusting the cutting frequency it was possible to change the velocity of the impinging droplets. Taking the example of the impact generate by droplets with average diameter of 0.62 mm and velocity 2.1 m/s (Reynolds = 1459 and Weber = 37) in an impact angle of 60°, the pool is illustrated in Figure 4.46a. For an average diameter of 0.81 mm and velocity 2.71 m/s (Reynolds = 2459 and Weber = 82) in an impact angle of 66°, the pool is represented in Figure 4.46b. For an average diameter of 0.85 mm and velocity 3.36 m/s (Reynolds = 3199 and Weber = 132) in an impact angle of 69°, the pool is represented in Figure 4.46c. It is observed from the images that by increasing the velocity the aspect ratio of the pool also increases. This behaviour was also expected, bearing in mind that the velocity perpendicular to the wall was increased, then more energy is used to spread the droplet.

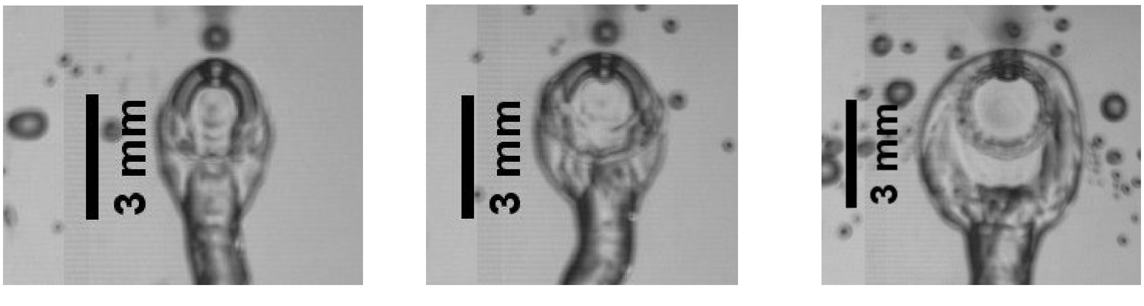
(a) (b) (c)

Figure 4.46: Pool shape dependence on droplet velocity. Figure (a) represents the pool shape formed for a droplet with velocity of 2.1 m/s, Figure (b) with 2.71 m/s, and Figure (c) with 3.36 m/s.

Three outcomes of the droplet impingement on the wall were observed and are illustrated in Figures 4.47, 4.48 and 4.49. Figure 4.47 represents a condition in which the incoming droplets hit the wall and start the film formation, part of the droplet mass is separated from the liquid film and part of the droplet attaches to the film liquid. Figure 4.48 represents the bouncing, in which the impinging droplets touches the wall but the film liquid is not formed and the droplets are bounced in the opposite direction of the impingement. Figure 4.49 presents the case in which the impinging droplets are completed absorbed by the liquid film. These behaviours are strongly affected by the impact angle and the non dimensional numbers presented in Equations 4.1, 4.2, 4.7, which are respectively the Weber number, the Reynolds number and the non-dimensional height.

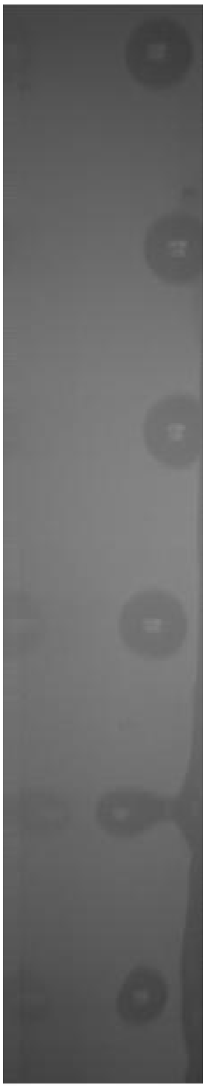

Figure 4.47: Droplet outcome after collision: Striping

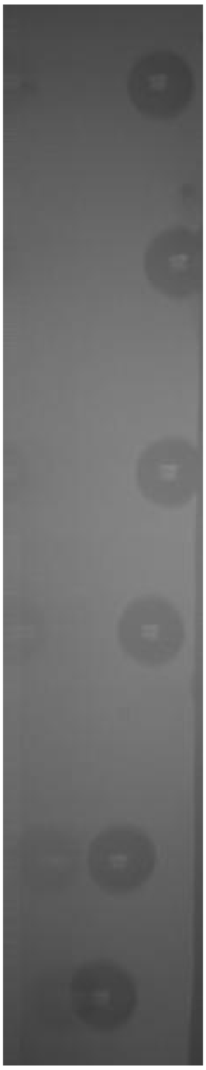

Figure 4.48: Droplet outcome after collision: Bouncing

Figure 4.49: Droplet outcome after collision: Absorption

As the velocity of the droplets was increased, the phenomenon of splashing was observed as in Figure 4.50. As the secondary droplets got out of focus of the camera, the measurements were not possible with this technique. To measure the secondary droplets, a technique similar to Samenfink et al. (1999) should be used. For that, the Laser-Doppler anemometry (LDA) technique is recommended.

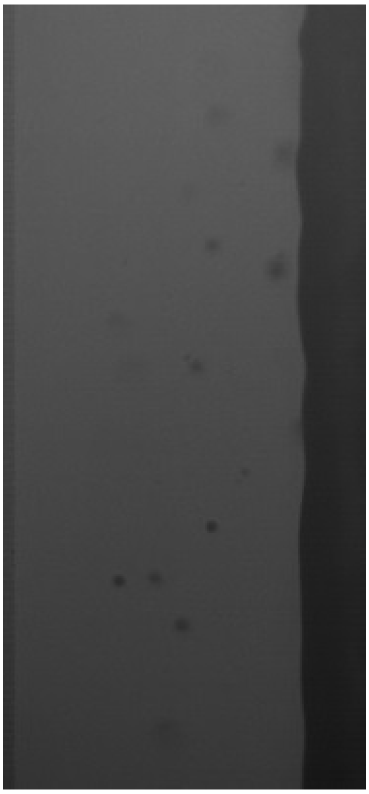

Figure 4.50: Image of splashing. The droplets for this case had a high velocity, which caused instabilities on the droplets. The small droplets generated by the splash went out of focus and could not be measured.

A sequence of images representing the absorption of a droplet and advection of the liquid film is presented in Figure 4.51. This sequence is illustrated for a case of complete absorption. Figure 4.51a represents a droplet being absorbed by the liquid pool, which is later spread radially on the liquid pool. After spreading, the droplet rejoins downstream of the impact point, forming the liquid tail, as represented in Figure 4.51b. The rejoining of the liquid forms a local increase in the liquid film height. This local height is later transported downwards as represented in Figure 4.51c. In the meanwhile, another droplet is coming from the chain of droplets and impinge on the pool, repeating the process.

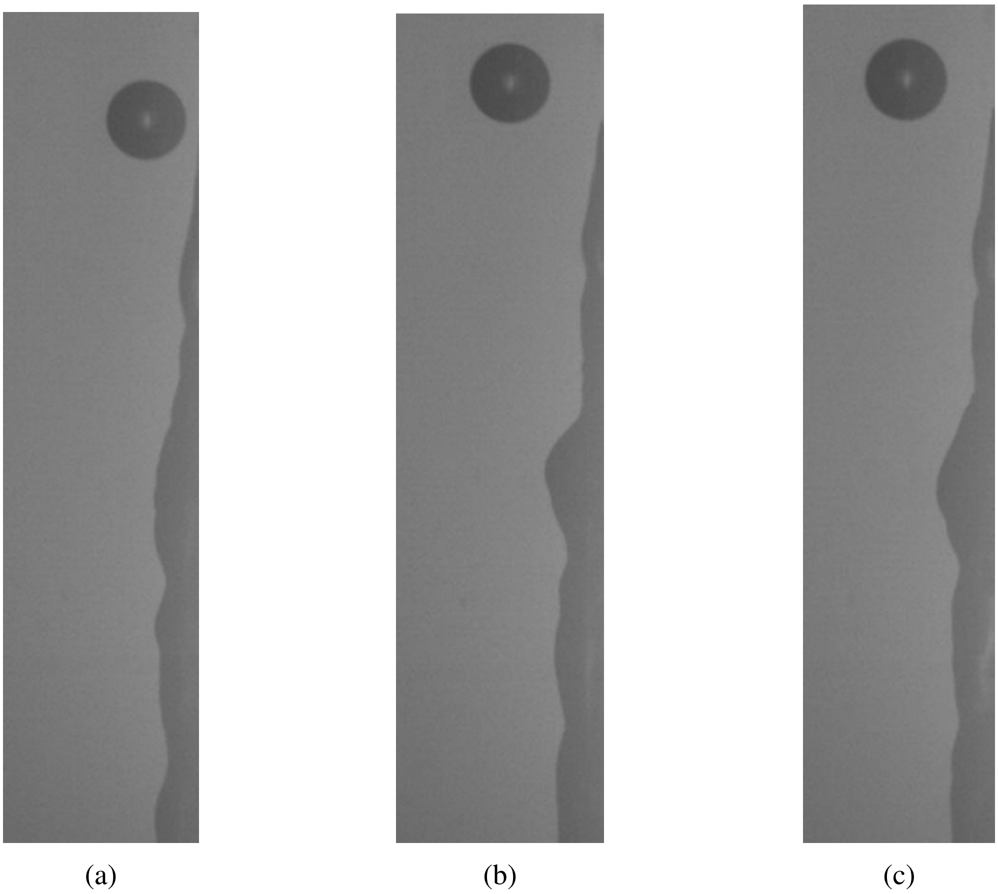
(a) (b) (c)

Figure 4.51: Sequence of images illustrating the side view of the droplet impingement. The images illustrates the droplet being absorbed by the pool, spreading radially, rejoining below the impact point, forming the tail with a greater height, and transporting this accumulated liquid downwards.

The tests for the quantitative results were carried out as follows. The droplets were generated in a certain angle, and then varied to obtain different impact angles. By varying the impact angle it was possible to check the maximum impact angle before partial deposition occurs. The flow ratio is then varied and again the impact angle is checked in order to obtain the maximum impact angle before partial deposition occurs. This procedure is also applied for different nozzle sizes, generating droplets with different diameters.

The case in which splashing was obtained is represented by 4.52. For this case the constant K, as represented in Equation 4.6, had a value of 125. According to Kuhnke (2004b) expectations were that splashing case would happen above K = 150, but considering that the droplets were not stable and had vibration energy, the value being below 150 was comprehensible.

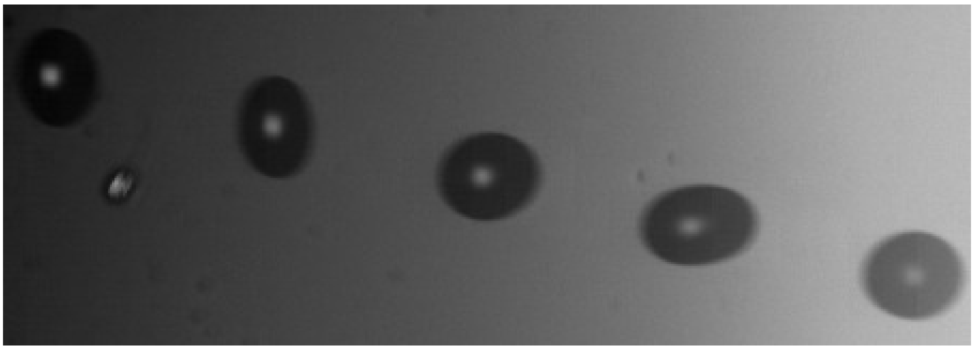

Figure 4.52: Droplets generated for splashing case. The spherical shape could not be maintained for the set flow ratio.

The main results of the experiments can be summarized in Figure 4.53, which is a plot of Equation 4.8 and Equation 4.4. By analysing this data, it is possible to conclude that the results follows a logarithmic trend and as the non dimensional pool size approaches the value of one, meaning that the pool size is approximately the same size of the droplet diameter, partial deposition is more likely to occur.

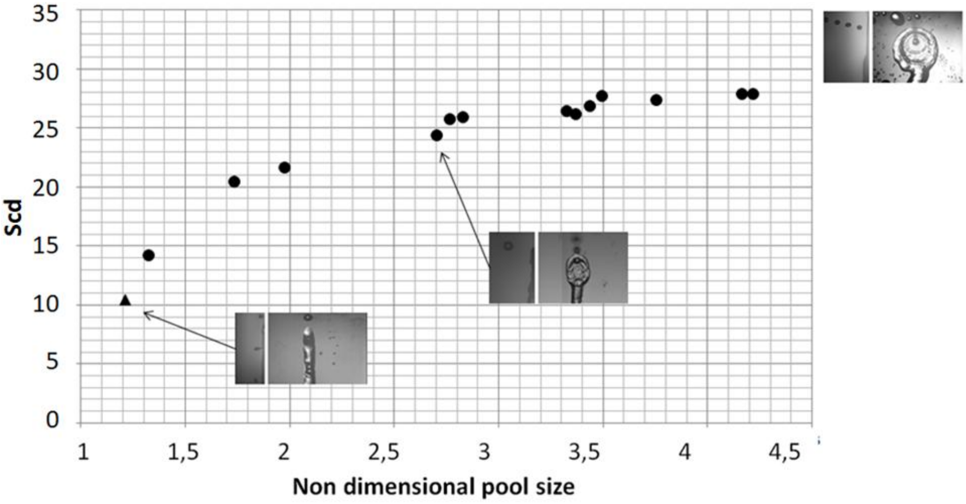

Figure 4.53: Scd x non dimensional pool size. The triangle represents the case in which striping is more likely to occur. The cases represented by circles are for the cases in which complete absorption of the droplet occurred.

For ethanol a different behaviour was observed. The droplets spreads in a much wider pool after collision, as can be observed in Figure 4.55. Observing Figure 4.54 it is also noted that this spread is greater for ethanol, as the film liquid cannot be observed. As the pool size was not measured a correlation for Scd and pool size could not be achieved for this case.

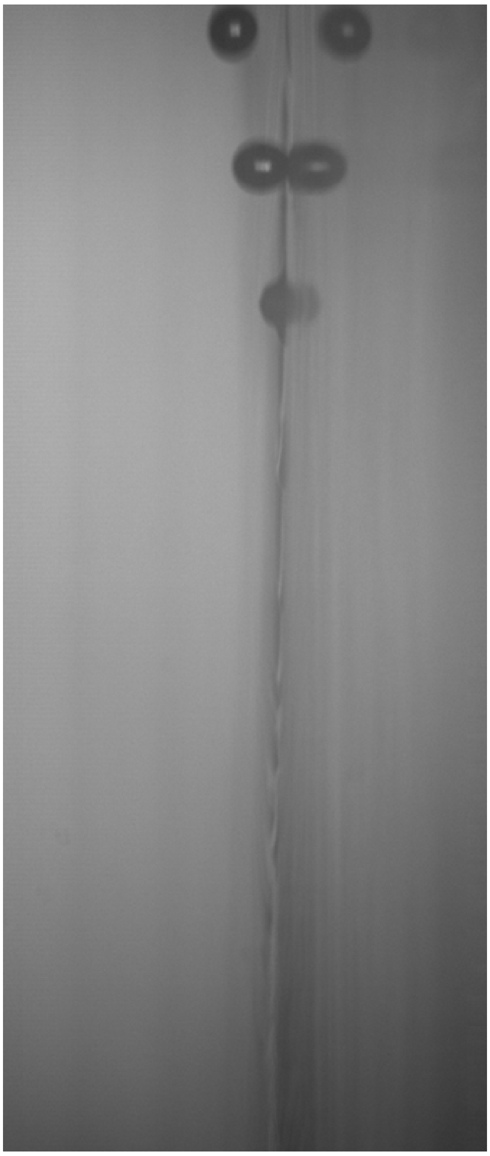

Figure 4.54: Ethanol droplets (side view). The formed liquid film was too thin for the camera to capture.

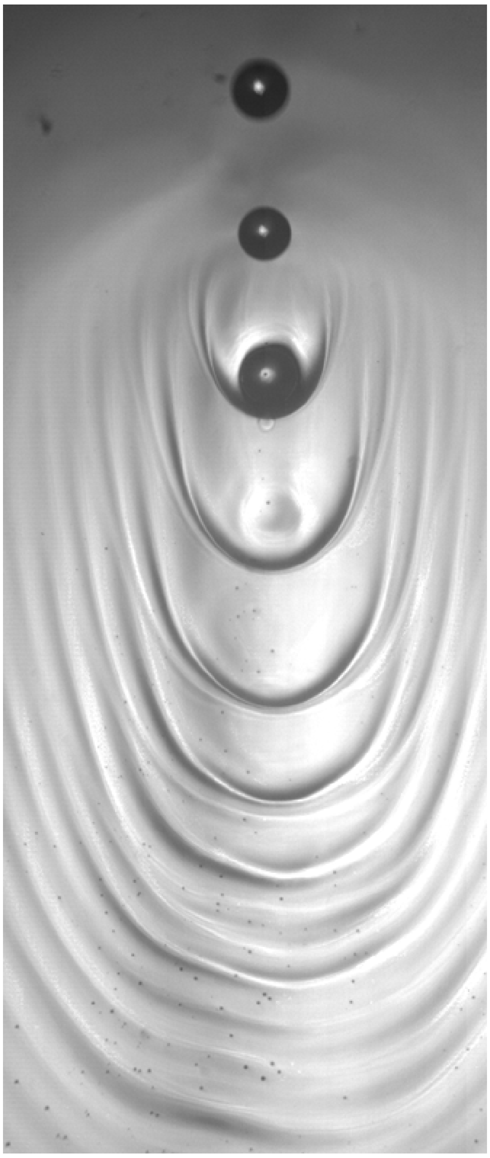

Figure 4.55: Ethanol droplets (front view). The droplets spread on the plate and did not form a pool shape as observed in the water experiments.

The outcomes of droplet impingement can be summarised in Table 4.2. Observing the behaviour of water droplets, the highest value found for a partial deposition condition was 13.73 meanwhile the smallest for complete absorption was 15.06.

Regarding the outcomes for deposition a similar behaviour was observed for ethanol. Critical values for partial deposition cases were in the range of interference between 15 and 18, in which both partial and total deposition were observed. For both water and ethanol it was observed that for values around 15 there is a chance of partial deposition to occur.

Water		Ethanol	
Scd	Outcome	Scd	Outcome
29.44	Absorption	22.35	Absorption
25.76	Absorption	15.23	Absorption
21.58	Absorption	17.73	Partial deposition
15.06	Absorption	16.89	Partial deposition
13.74	Partial deposition	16.13	Partial deposition
11.26	Partial deposition	15.04	Partial deposition

Table 4.2: Outcome of droplets

The results presented in this chapter are used for the setup of the VOF numerical simulations. The numerical results are presented in Chapter 6, along with a comparison and a discussion concerning the main findings.

5 Numerical Simulations Methodology

This chapter describes the methodology to run the numerical simulations. The simulations were run using CONVERGE CFD software for the simulation with VOF method and UNSCYFL3D code for the simulations with EWF method. To analyse the three-dimensional results ParaView software was used.

For the simulations an Intel®Core^{TM} i7-9700 CPU 3.00 GHz with 16 GiB system memory and eight physical cores was used.

The CONVERGE CFD software was created initially to run internal combustion engine simulations. With the development of the software, it is now able to numerically simulate a wide variety of engineering machinery. As example, the software is able to handle gas turbines, exhaust after-treatment, compressors, fun, blowers, pumps, valves, wind turbines, among others.

The UNSCYFL3D code was initially created to simulate the flow inside a cyclone in the work of Souza (2003). This software is continuously under development at MFLab and it was already widely validate by different students. A briefly history of the software present cases for the analysis of the influence of the filtering medium on the behaviour of the filtering hydrocyclone Souza et al. (2000), presenting preliminary results of LES simulations of a hydrocyclone Souza and Neto (2004), analysing sub-grid modelling effects in the simulation of single-phase turbulent flow in an industrial cyclone separator Salvo et al. (2012), using LES to solve the gas–particle flow in cyclone separators de Souza et al. (2012), testing the four-way coupling for the gas-particle flow in a diffuser de Souza et al. (2014), testing the effects of the gas outlet duct length and shape on the performance of cyclone separators de Souza et al. (2015a), studying the formation of vortex breakdown in conical–cylindrical cavities de Moro Martins et al. (2014), investigating erosion due to particles in elbows by means of numerical simulations Pereira et al. (2014), investigate gas-solid turbulence modulation in Eulerian-Lagrange simulations Utzig et al. (2015), investigating mass loading effects on elbow erosion Duarte et al. (2015), simulation of the performance of small cyclone separators de Souza et al. (2015b), simulating a twisted tape insert for reducing bend erosion Dos Santos et al. (2016), simulating a vortex chamber for reducing elbow erosion Duarte et al. (2016), propose innovative geometries for pipe wall erosion reduction Duarte and de Souza (2017), testing the role of inter-particle collisions on elbow erosion Duarte et al. (2017), testing the effects of density interpolation schemes for the VOF scheme Fontes et al. (2018a), improvement in a hybrid model applied to LJIC Fontes et al. (2019), testing geometries for reducing elbow erosion Duarte et al. (2020b), new turbulence closure models validations on bluff bodies Duarte et al. (2020a), dynamic mesh approaches for eroded shape predictions Duarte and de Souza (2021), and drag reduction by micro-bubbles Velasco et al. (2022), optimisation of tube shapes against erosion Santos et al. (2022). During the development of this thesis, the implementation of the EWF for the liquid film simulations was carried out. As observed many papers were published for particles simulated as Lagrangian phases. Many algorithms used to compute particles as discrete phase were reused for the simulation of droplets.

In this chapter the numerical procedure is explained for the VOF simulations and CONVERGE CFD software in Subsection 5.1. The numerical procedure for the EWF simulations is presented in subsection 5.2. The results and discussion of the numerical simulations are presented in Chapter 6.

5.1 VOF simulations

For the numerical simulations, three cases were selected among the physical experiments to be reproduced using VOF method. These cases were selected to cover three different regions of the graph presented in Figure 4.53. The first case with a low Scd, in a region close to the partial deposition, called Case 1. The second case in an intermediate Scd, in a region where a change in Scd proportionally changes the non dimensional pool size, called Case 2. The third case in a region that a small increment on Scd causes a high change on the non dimensional pool size, called Case 3.

A parallelepiped surface mesh with 6 mm width, 10 mm length, and 16 mm height was created in Convergent Science Inc.'s CONVERGE^{TM} CFD software, as represented in Figure 5.1. This surface corresponds to the image area of the experiment. The three spheres inside the domain represent the region where the droplets were initialised, with their velocity magnitude and direction corresponding to physical experiments. Incoming droplets, with the same velocity and diameter, enter the domain in the top boundary condition. The simulations run until water flows out of the computational domain at the bottom boundary condition (not represented in the image). In this figure, the grey triangles represent the wall boundary conditions, in which the droplets are colliding.

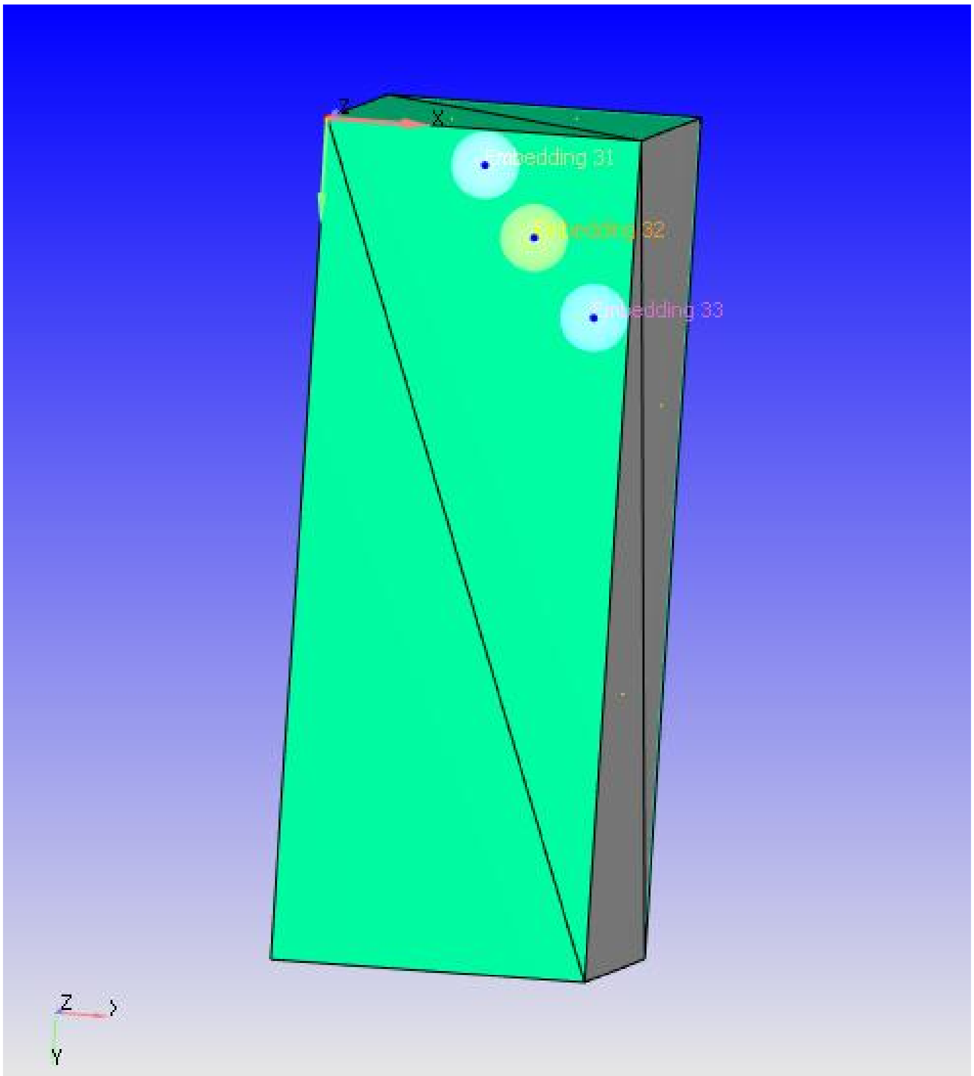

Figure 5.1: Surface mesh representing the computational domain. The surface mesh is used to generate a Cartesian mesh by means of the cut cell technique.

The surface mesh illustrated in Figure 5.1 was used to generate a structured Cartesian mesh for the simulations. Two techniques were used to locally refine the mesh. The first technique was used to refine the wall region, the inlet boundary condition, and the regions where droplets were initialised. These embedded regions refine the mesh by a factor of 2^n. For the simulations, n was considered 4. The embedded regions for the droplets were used only at the beginning of the simulations.

To keep track of the interface of liquid and gas, a second technique was used, namely Adaptive Mesh Refinement (AMR). This technique was used to track cells with values between 0 and 1 for α and locally refine the mesh by the same factor of 4 used for the embedded regions.

The base size for the cells in the Cartesian mesh was considered 0.4 mm. In both techniques, in the regions chosen to be refined by the criterion of 2^n, the mesh base size becomes 0.01875 mm. The time step is also variable according to predefined values. The minimum time step value was set to 10^{-7} and it is corrected for each time step automatically according to the CFL value. Gravity was set to $9.81 m/s^2$ in the positive y direction.

Figure 5.2 illustrates the mesh generated from the surface mesh. As observed in this figure, the mesh was initially refined at the inlet boundary, where the droplets are issuing, and at the wall where the droplets will impinge. In this figure, the initial droplets are illustrated inside the domain, as well as an incoming droplet issuing from the boundary condition.

For the simulated cases, the droplets have a diameter of 0.645 mm. To achieve different momentum parameters, the velocity magnitude was kept constant, but the direction was changed. In the simulations, the value of the void fraction was defined as one for the gas phase and zero for the liquid. The air phase was considered quiescent for initialisation. The liquid and gas properties used for the simulations are presented in Table 4.1. A contact angle of 101.5° was used in the liquid-wall model, as calculated using the experimental setup. The HRIC and PLIC schemes were used and their results are discussed on Chapter 6.

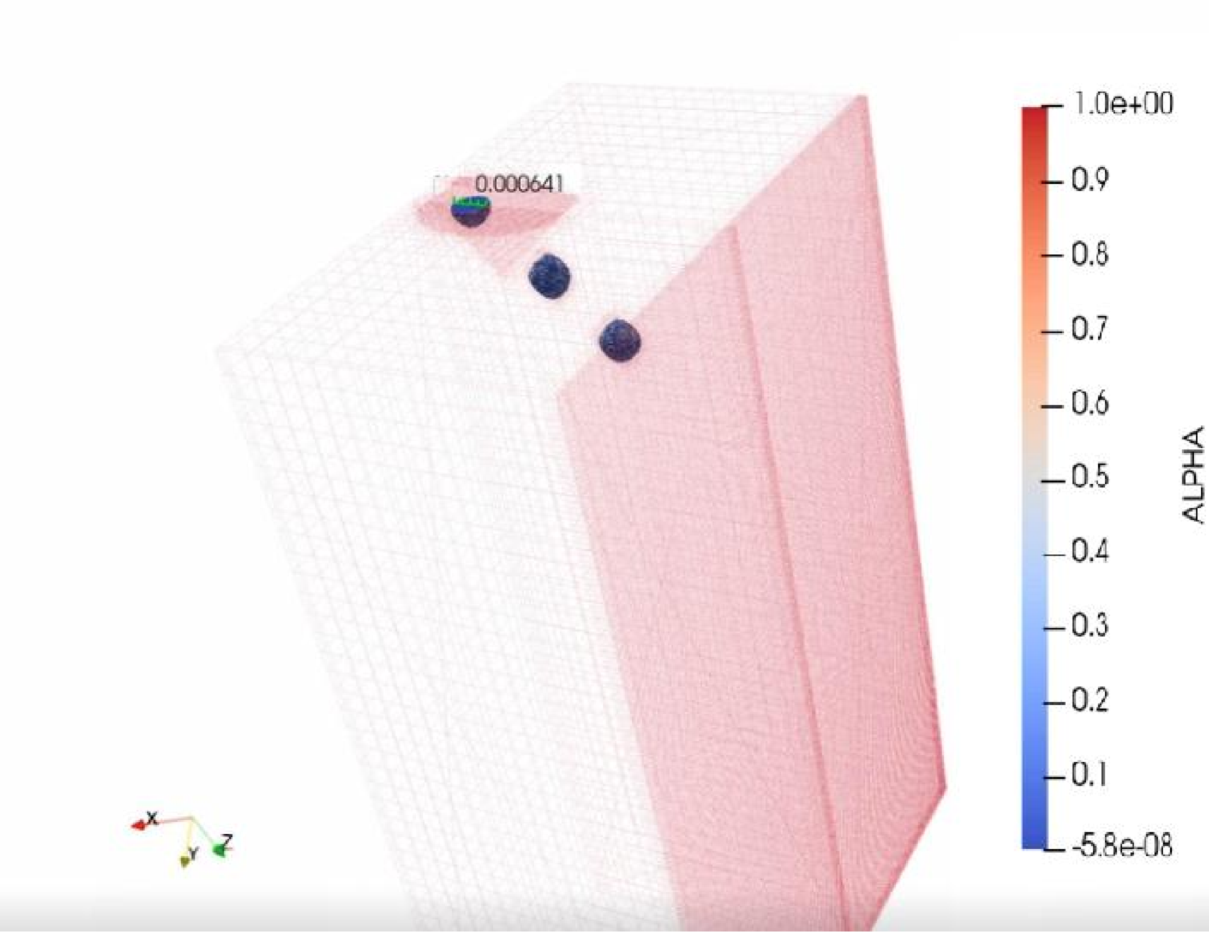

Figure 5.2: Initial setup illustrating the mesh with the droplets inside the domain. As only half of the droplets are simulated, the computational domain was mirrored to illustrate complete droplets.

The initial embedded regions for droplets are illustrated in Figure 5.3. To run the simulations faster, the wall refinement was kept, but the initial droplets refinement was removed after a few time steps. Further refinement for the droplets regions was performed by the AMR as the droplets move inside the computational domain, as represented in Figure 5.4. Note that inside the droplet the mesh is not as refined as at the interface between fluids. As observed, the refined region is also beyond the droplet interface boundaries. This is happening because the AMR has also been set for velocity, as represented in Figure 5.5.

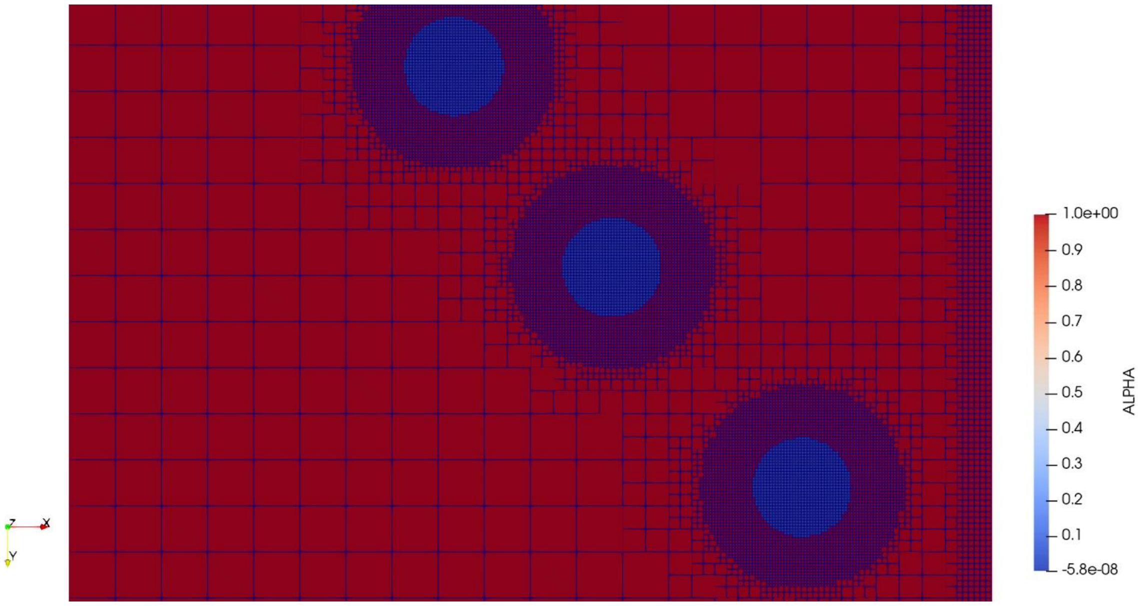

Figure 5.3: Embedded regions refined at initial stages of the simulation. This mesh refinement technique was used to better represent the droplets initiated inside the computational domain.

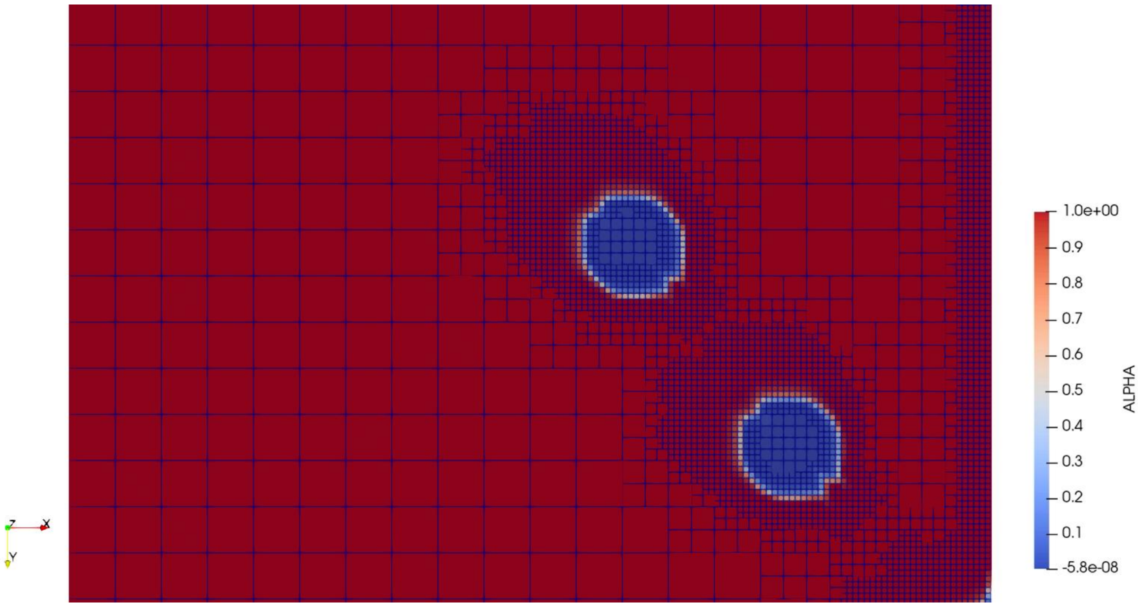

Figure 5.4: Adaptive mesh refinement illustrating the refinement of the mesh around the droplet. This technique was used to refine regions with variations in α to better track the interface between fluids.

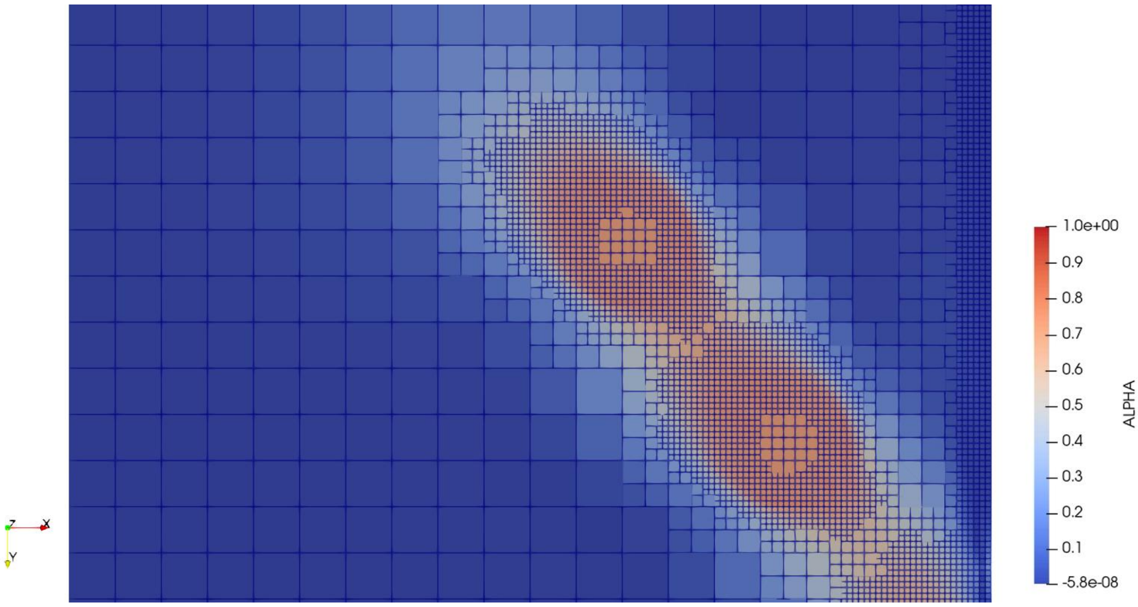

Figure 5.5: Adaptive mesh refinement for velocity. This technique was used to refine regions with variations in velocity to better represent the momentum exchange at the fluids interface.

The droplets inside the domain were set with an initial velocity and the air around them was quiescent.

For the simulations, the adaptive time step was used. The variations were dependent on the CFL number and had a large difference for HRIC and PLIC simulations. For the HRIC scheme, the simulations were run with a time step of approximately 5.10^{-6}, while the simulations using PLIC scheme were run with a predefined minimum time step of 1.10^{-7}, which means that it would require even smaller time steps. These observations are opposed to the results observed for flows aligned with the mesh presented by (de Lima et al., 2020).

The gas flow was considered as incompressible. The maximum number of PISO iterations per time step is set to 20 with tolerance of 10^{-5}. The convective flux scheme used was the flux blending, which is a blend of second-order upwind and reconstructed central difference spatial discretisation schemes. For turbulence closure modelling, the $RNG\ k-\epsilon$ model was used.

5.2 EWF simulations

For the EWF simulations three different cases were run. The first case is the droplet spreading over a surface. The physical experimentation to validate this case was published by Diez et al. (1994), in which he developed an analytical solution, that was validated against experimental data. The second case was published by Shedd et al. (2009a) and consists of a cross flow of a liquid jet in an air stream. In this case, the jet breaks up in small droplets and hits an opposite wall forming liquid film. For these cases, the liquid film is computed using the EWF method, which is a two-dimensional method to predict thin liquid film formation. The third case consists of the same case as the second with a different liquid jet velocity. The cases are described in detail throughout this section.

The first simulation was run to test the EWF method and the capillary effects. The same test case was also simulated by different authors such as Diez et al. (1994) and Baleta et al. (2015). The following paragraphs will briefly explain the case used for numerical validation of the first tested case.

In his work, Diez et al. (1994) developed an analytical solution for the spreading of a droplet on a rigid flat plate, as represented in Figure 5.6 with the main parameters. The droplet spreads spontaneously as it has a positive value for the spreading parameter. The author compared the results of the developed analytical solution with experimental data as represented in Figure 5.7. The results are normalised. The height of the film (h) is normalised by the maximum height (h_f). The radius of the droplet (r) is normalised by the maximum radius (r_f). In Figure 5.7 the solid line represents the theoretical profile. The experimental results are represented by the markers for different initial volumes, viscosity, initial height and initial radius. The squares represent a droplet of initial volume of 0.12 mm^3, kinematic viscosity of 10.3 cm^2/s, initial radius of x_f 1.4 mm and height of 38 μm. The triangles represent a droplet of initial volume of 4.04 mm^3, kinematic viscosity of 1.0 cm^2/s, initial radius of x_f 4.67 mm and height of 103

μm. The crosses represent a droplet of initial volume of 0.05 mm^3, kinematic viscosity of 0.1 cm^2/s, initial radius of x_f 1.2 mm and height of 12.7 μm. One of the main observation is that the results are not dependent on time for the normalised variables.

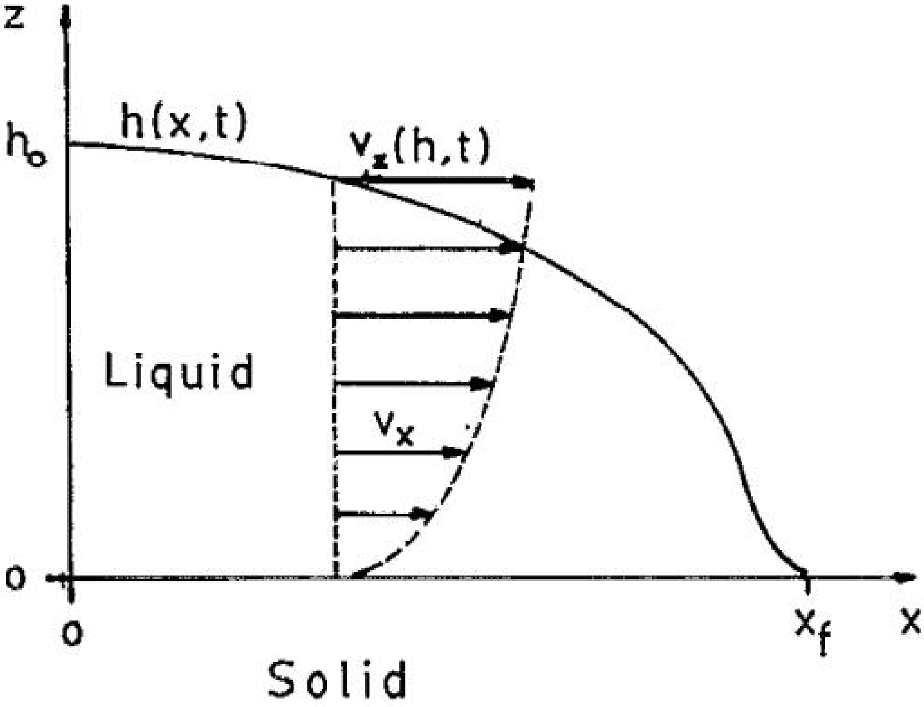

Figure 5.6: Representation of droplet spreading by (Diez et al., 1994). The main parameters used to develop an analytical solution for the spreading of a viscous droplet are presented.

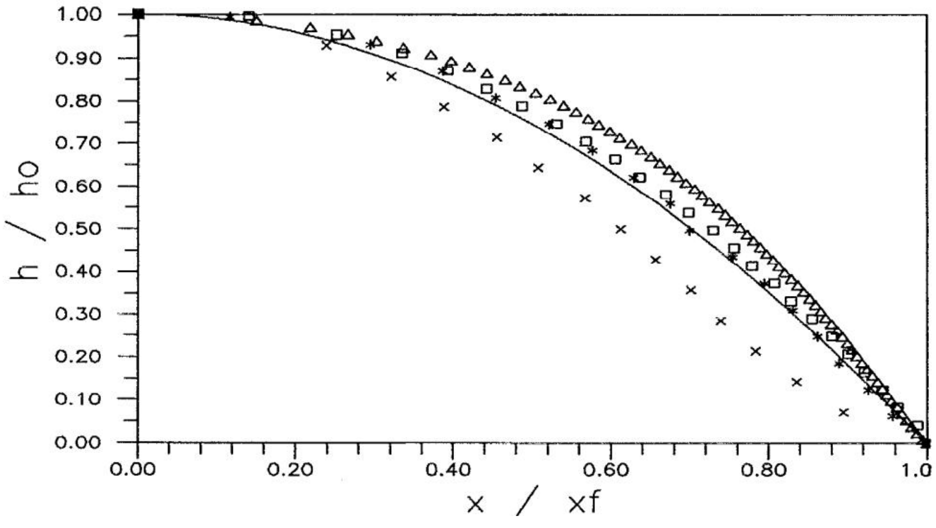

Figure 5.7: Results for the droplet spreading physical experimentation presented by (Diez et al., 1994). The solid line represents the theoretical profile. The experimental results are represented by the markers for different initial volumes, viscosity, initial height and initial radius.

Among the cases presented by Diez et al. (1994), the case of a droplet with 0.08 mm maximum height, a volume of 0.12 mm^3, and a paraboloid shape was chosen to be analysed.

The computational domain for the first case with its main dimension is represented in Figure 5.8. The domain has dimensions of: length 5 mm, width 5 mm, and height 0.1 mm.

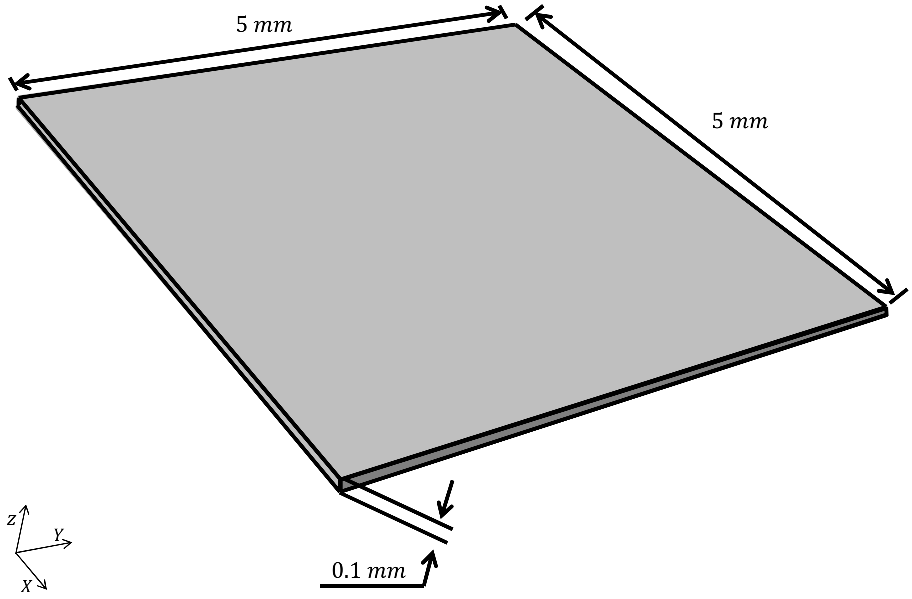

Figure 5.8: Computational domain for droplet spreading. The main dimensions are presented.

The mesh for the first test is represented in Figure 5.9. The mesh contains 20000 elements (100x100x2) in an unstructured mesh.

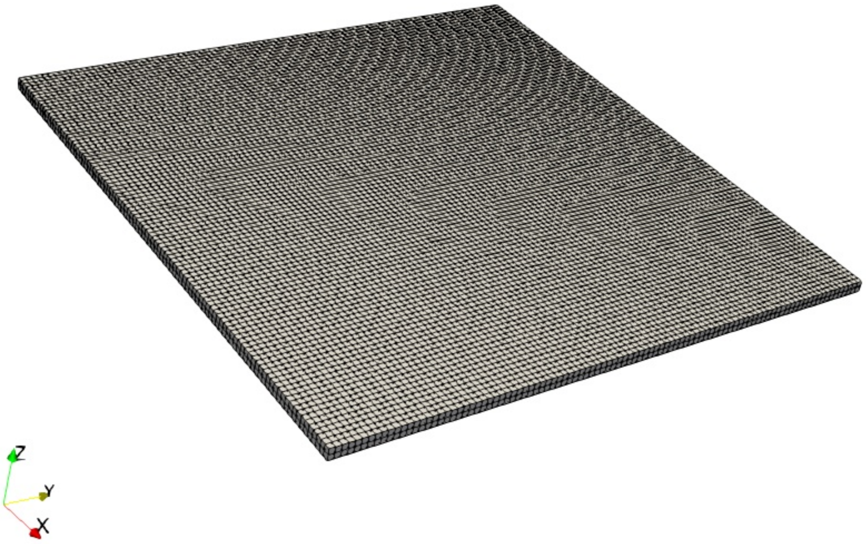

Figure 5.9: Mesh used for droplet spreading case. This unstructured mesh contains 20000 elements.

The boundary conditions for the droplet spreading case are represented in Figure 5.10. The wall film condition was set at the bottom of the computational domain. The other boundary conditions were set as outlet with absolute pressure equals to zero.

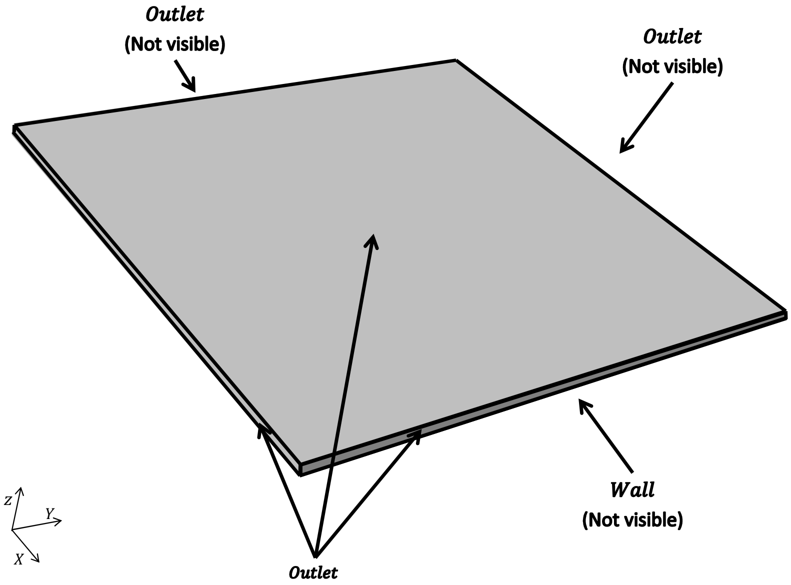

Figure 5.10: Boundary conditions for droplet spreading case.

The simulation starts with a droplet at the centre of the domain. The initial condition for the thickness of the droplet is represented in Figure 5.11. An important reminder is that for this model the droplet is two dimensional. The velocity was set to zero in all the domain.

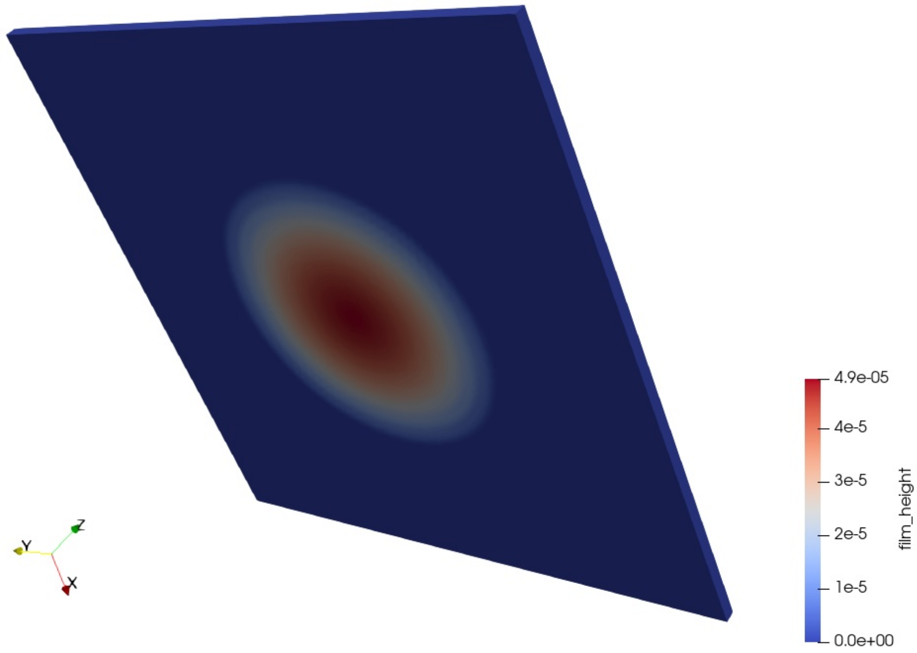

Figure 5.11: Initial conditions for droplet spreading test case of the EWF model. The coloured region represents a paraboloid shaped droplet with its maximum height at the centre (coloured by red). This initial condition is set at the wall.

For the second and third cases used to validate the EWF method, the experiments of Shedd et al. (2009a) were used. The experiments consist of a liquid jet that interacts with a cross flow of air, as represented on Figure 5.12. The brown section is the air flow entrance. A liquid is then injected into the system as illustrated by the region indicated as Injector.

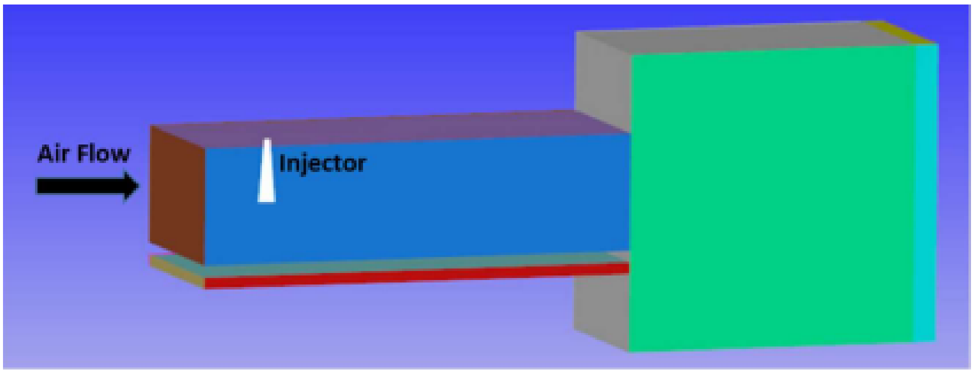

Figure 5.12: Computational domain for the jet in cross flow case. In brown is the air entrance and in white the liquid injection as in the work of (Drennan et al., 2019)

The main dimensions of the test bench are illustrated in Figure 5.13. The test section is made of polycarbonate, which facilitate optical access. There are two air entrances, a larger one, where the air flow velocity is represented by U_1, called main way, and a smaller with velocity U_2. The light blue region represented in Figure 5.13 is the liquid issuing out from the nozzle, interacting with the main air flow, impinging on the surface, forming a thin liquid film, and finally interacting with the secondary flow.

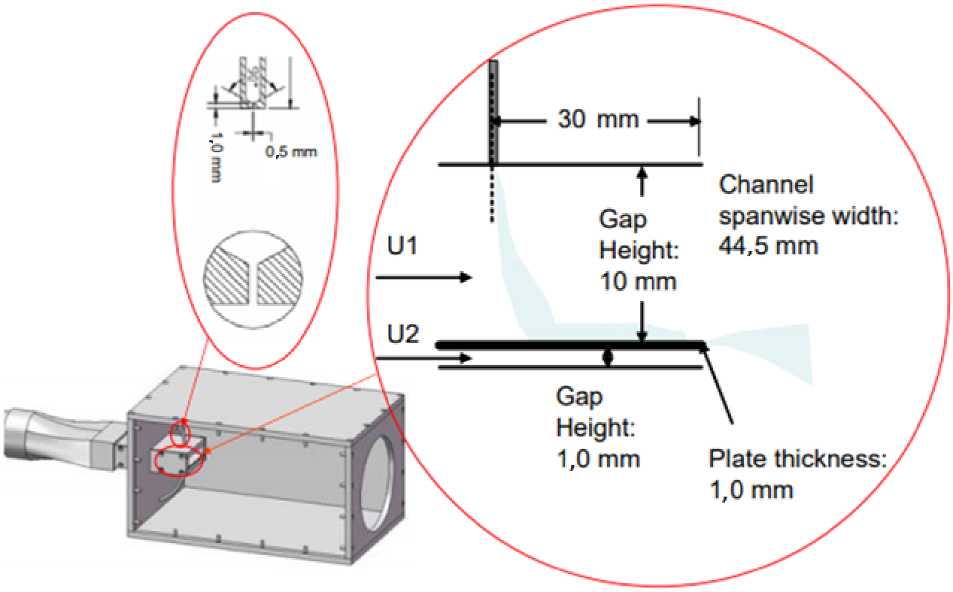

Figure 5.13: Physical experimentation setup for the liquid jet in cross flow. The main dimensions are highlighted and were used for building the numerical simulations setup. The experiment was carried out by (Shedd et al., 2009a)

Figure 5.14 represents the liquid jet dynamics in the system, which is very similar to the injection of fuel in air-blast atomisers. After liquid injection, it is subjected to a cross flow of air. This interaction causes this liquid to undergo a first break-up process as well as bends the liquid jet in the flow direction. The jet and the formed droplets collides with the wall forming a liquid film on the surface. This liquid film flows in the direction of the airflow until it goes out of the plate and interacts with the secondary air-stream, undergoing a film breaking process. The interaction with the secondary air flow will not be considered in the present thesis.

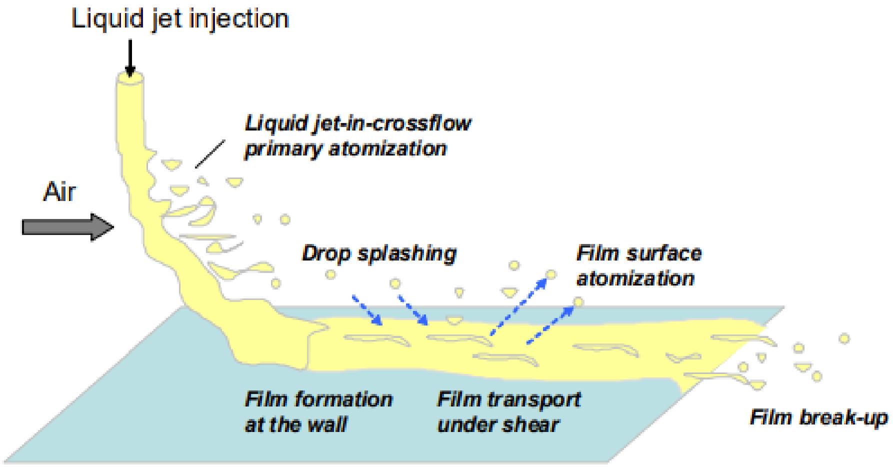

Figure 5.14: Physics of the jet and film formation. This sketch was presented by (Shedd et al., 2009a) and illustrates the phenomena that involves the interaction between the cross flow of air and the liquid jet.

The computational domain for the second and third cases is represented in Figure 5.15 with its main dimensions. The nozzle is represented by the blue cylinder, which is $6.34\ mm$ away from the inlet and has a $0.5\ mm$ diameter hole. The coordinate system centre is represented by the dot in the centre of the nozzle. As the focus of this work is on the liquid film formation only one air inlet was considered. The effects of the secondary air entrance were then unconsidered and the geometry removed from the computational domain. As only Lagrangian droplets are considered for this case, the geometry part of the nozzle entrance was not considered.

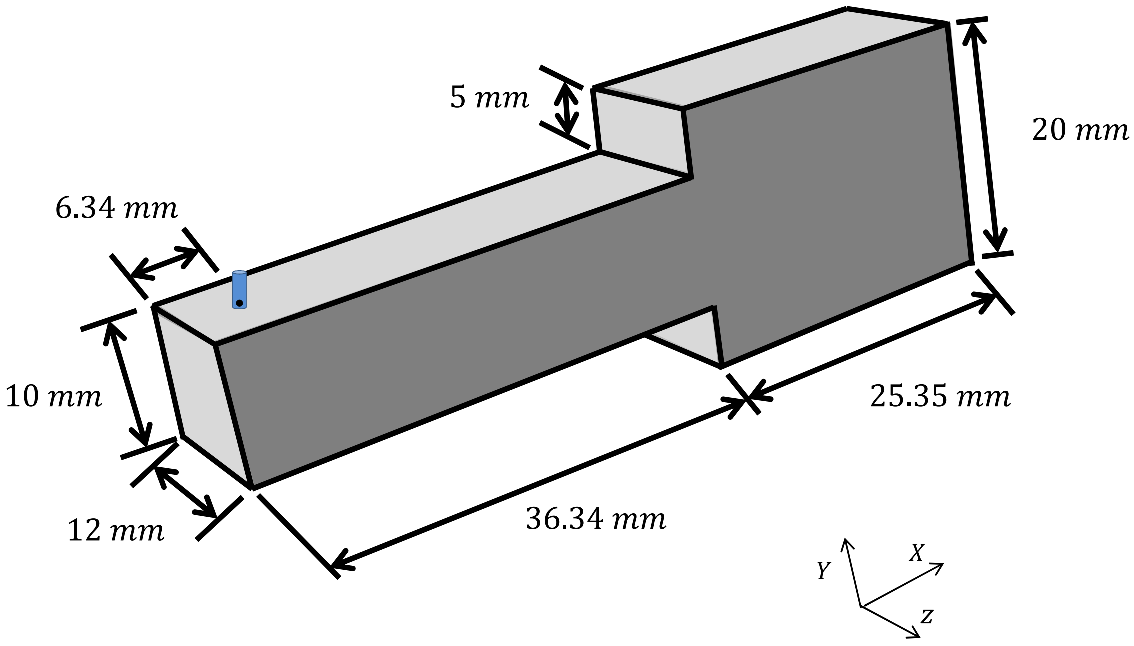

Figure 5.15: Computational domain dimensions for cross-flow case. The main dimensions are presented. The blue cylinder represents the region in which the jet enters the experimental chamber.

The mesh for this case is represented in Figure 5.16. This mesh has a total number of nodes of 662240 and 637767 elements. For its generation the software ICEM-ANSYS was used. Near wall regions were refined to capture the physics of wall effects. Using empirical data, a value of $y^+ = 1$ was chosen to be used on the mesh building process. More details are found in White (1962).

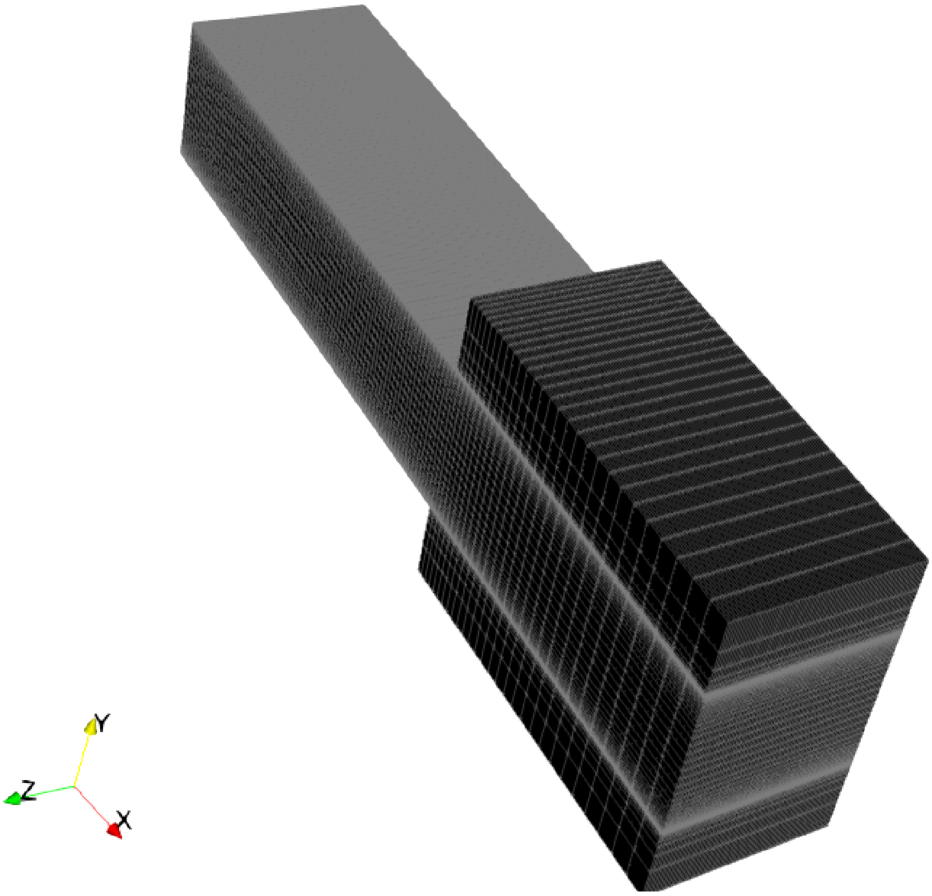

Figure 5.16: Mesh used for cross-flow case. This unstructured mesh contains 637767 elements.

To evaluate grid convergence, the concept of Grid Convergence Index (GCI) was applied. This test was applied to evaluate three different grids, namely fine, medium, and coarse mesh. The simulations were run without the droplets in the domain to verify the influence of the mesh on the air flow.

According to (ROACHE, 1994), the GCI measures the distance between the simulation results and the asymptotic numerical value. The grid convergence was calculated according to Roache (1994, 1997, 1998) and the results are presented in Chapter 6.

The boundary conditions for the second and third case are represented in Figure 5.17 according to the description of Chapter 3.

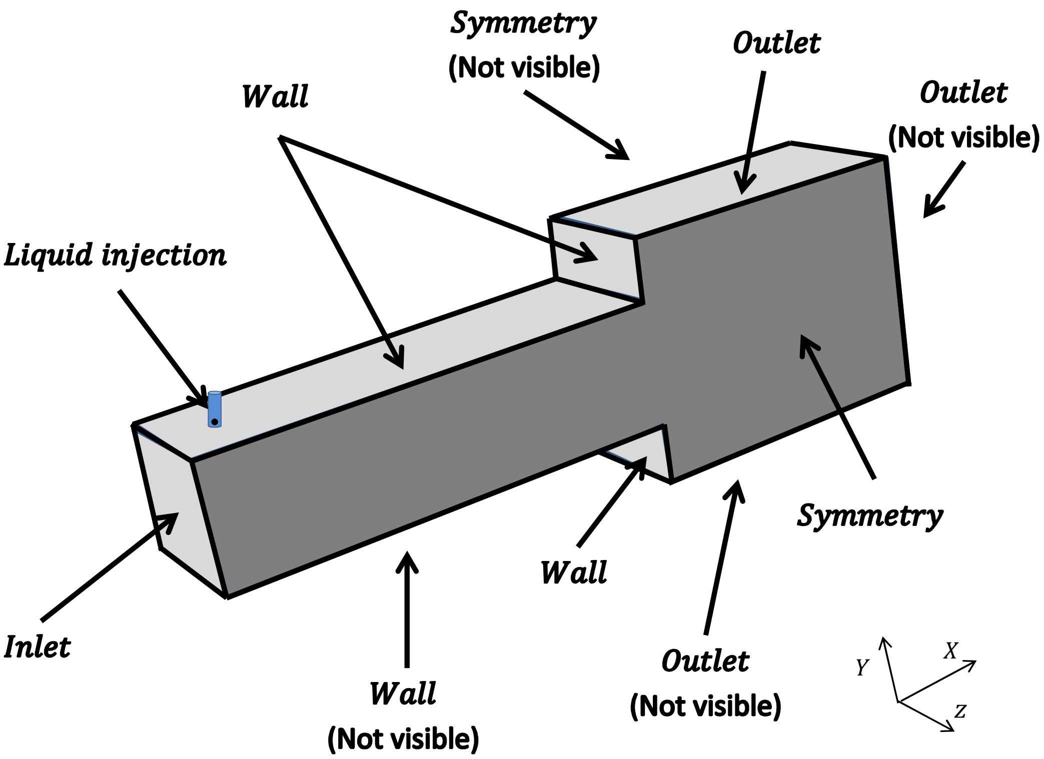

Figure 5.17: Boundary conditions for cross-flow case. The liquid injection region is marked in blue.

For these cases, parcels containing droplets with the same radius and velocity are injected in the computational domain. As mentioned before, two cases were tested. The difference between them is only the velocity of liquid injection and the mass flow. The first case considered an injection of mineral spirits with 12.7 m/s (case 1) and the second case with 17 m/s (case 2). For the Lagrangian droplets an initial radius of 0.5 mm was considered, which is the nozzle diameter.

For the inlet boundary condition air is injected at 81 m/s and was considered as a fully developed turbulent inlet profile. In the inlet boundary condition the condition of escape is considered for the droplets. As the inlet boundary condition was truncated, the velocity profile was predicted considering a fully developed boundary layer on a plate. The equations for prediction of the velocity profile are presented in Equation 5.1. The equation to predict the turbulent boundary layer thickness is presented in Equation 5.2.

$$\begin{aligned} u = u_\infty \left(\frac{d_w}{\delta_T}\right)^{1/7}, &\quad \text{if } \delta_T > d_w \\ u = u_\infty, &\quad \text{if } \delta_T < d_w \end{aligned} \tag{5.1}$$

in which d_w is the distance to the nearest wall, u_∞ is the characteristic flow velocity, and δ_T is the turbulent boundary layer thickness at the air inlet.

$$\delta_T = 0.37 \left(\frac{\nu}{u_\infty} \right)^{0.2} L_T^{0.8}, \tag{5.2}$$

in which L_T is the distance downstream from the start of the boundary layer.

For the outlet boundary condition it is assumed that the flow is fully developed, therefore, does not undergo further variations in the direction normal to the face of the boundary. In the outlet boundary conditions the condition of escape is considered for the droplets.

For the symmetry boundary condition symmetry was considered. In the symmetry boundary condition the condition of escape is considered for the droplets.

For the wall boundary condition no slip conditions were considered. For the bottom walls film formation was considered, for the top walls only reflection was taken into account.

For initial conditions only air was considered inside the domain. The velocity was set to zero.

The convergence criterion for each iteration was set to 10^{-4} while the divergence criterion was set to 10^{11}. The numerical advective scheme used is the second-order upwind. The second-order central difference scheme is employed for the diffusive terms. The maximum number of SIMPLE iterations per time step is set to 20. The two-way coupling method was set for the coupling of fluid flow and droplets motion. This means that the source terms for momentum due to the droplets will be added to the conservation equations for the Eulerian fluid flow. In this case, the time step for the droplets and the fluid must be the same. The number of parcels generated after secondary break-up was set to 10.

For the droplet spreading case the flow field is not solved, as it will not affect the results. The simulation runs for 80000 time steps of 10^{-5} s.

For the cross flow cases the first simulation is in permanent regime and the droplets are not injected. For that 2000 time steps were run, getting absolute residual source sums in the order of 10^{-3}. The resulting flow field is used as initial conditions on the transient simulation.

For the transient simulation 20000 time steps were run with a time step of $2 \cdot 10^{-6}$ s. After that, the Eulerian flow field is frozen, then the simulation runs just with the droplets. The frozen simulation run for 60000 time steps to get good results for average values.

The air is considered with density of $\rho_g = 1.427\ kg/m^3$, and dynamic viscosity of $\mu_g = 1.7894 \cdot 10^{-5}\ kg/m \cdot s$, at 300 K, as presented by Richards et al. (2016).

The liquid is Mineral Spirits, which has density $\rho_l = 780\ kg/m^3$, and dynamic viscosity $\mu_l = 8.5 \cdot 10^{-4}\ kg/m \cdot s$, at 300 K, as presented by Shedd et al. (2009a).

The surface tension between these phases is $\sigma = 0.024\ N/m$. Shedd et al. (2009a)

Fluid properties are summarised in Table 5.1.

	Density (kg/m^3)	Dynamic viscosity ($kg/m \cdot s$)	Surface tension coefficient (N/m)
Air	1.427	$1.7894 \cdot 10^{-5}$	0.024
Mineral spirits	780	$8.5 \cdot 10^{-4}$	

Table 5.1: Fluids properties at $300\ K$. These properties are used for the EWF simulations.

To analyse the equations presented in Chapter 3 for the EWF method a painstaking study of the parameters that may affect the final results was conducted. The main objects of study are highlighted in the following paragraphs.

Cross-flow simulations are challenging to predict with RANS models, as this process is coupled with the turbulence phenomenon. In order to assess the influence of the turbulence closure model, the first set of tests consisted of using different turbulence closure models, namely k-ϵ, tuned k-ϵ and $k - \omega\ SST$.

After droplet injection on the computational domain, it is subjected to the cross-flow of air and may undergo a break-up process. This break-up generates parcels on the simulations that represents a certain number of droplets. As this approximation is employed, it is necessary to verify how many parcels are necessary to minimise the impact of this approximation. To assess the number of generated child droplets, the second set of tests concerns the number of parcels generated during secondary break-up.

The gas flow can influence in a number of different phenomena that direct impact the behaviour of the liquid film, as example, the gas flow is direct responsible for the break-up of the liquid jet and transport of generated droplets. The gas flow is also relevant to account for the shear stress at the interface between liquid and gas. As no information about the flow condition at the inlet was found, it is important to assess the influence of the boundary layer profile, thus, the third case concerns the length of the plate entrance. This parameter is used to set the boundary conditions for velocity at the inlet as in Equation 5.1 - 5.2.

A sensitive analysis of the terms of the EWF equations was carried out to analyse most relevant parameters, and quantitative verify the impact of them on the simulation results. Therefore, the fourth set of tests concerns the source term for momentum equation.

In the work of Ingle et al. (2014) peaks of liquid film were observed near the edge. This accumulation of liquid was attributed to a back flow of air that slowed down the liquid film. In his work, the liquid film reaches the symmetry boundary condition and only then flow towards the edge. To verify the influence of the distance of the liquid film to the symmetry boundary condition, the fifth set of simulations were carried out with a larger mesh domain.

The third term on the right hand side of Equation 3.46 represents the stress originated by the relative velocity of the gas and the liquid phases. This parameter is expected to have great influence on the simulation results, thus, the sixth set of tests concerns the viscous shear force at the gas-film interface.

The phase coupling is also expected to have a great influence on the results, as it is responsible for slowing down the gas flow. The absence of forces to slow down the gas flow can cause a strong redirection of the liquid jet as well as forcing the break-up process. So, the seventh set of tests concern the coupling between phases.

In this work the liquid jet is injected in the computational domain as a Lagrangian phase. With this approximation the size of the initial droplet was chosen to be the same size as the injector nozzle. To assess the influence of this approximation, the eighth set of tests concern the diameter of the droplet that is injected in the computational domain representing the liquid jet.

The following subsections present the results of each of the set of tests. The main results are illustrated and discussed separately for each of them for Case 1 and Case 2.

6 Numerical Simulations Results and Discussions

This chapter consists of the verification and validation of the numerical simulations. First the VOF results are presented and discussed, then, the EWF model results are presented and discussed in two different sections, one for the droplet spreading case another for the simulation of cross-flow. A comparison of the simulation results from the EWF method was carried out using data found on literature, highlighting the main findings.

For the simulations an Intel®Core^{TM} i7-9700 CPU 3.00 GHz with 16 GiB system memory and eight physical cores was used.

6.1 Volume of Fluid: simulation of droplet collision with wall and film formation

To visualise the computational effort to carry out the simulations, a graphic was generated for an HRIC simulation. This graphic contains the number of cells and memory usage in MB. These results are presented in Figure 6.1. For the sake of brevity, the results are presented only for HRIC because the graph for PLIC behaves similarly. The main difference is that for the same setup, HRIC required more cells than PLIC (in the order of 1.5 M cells for HRIC meanwhile PLIC was in the order of 1.1 M cells) and this fact culminates in a greater memory requirement for the simulations for HRIC (in the order of 9.2 GB for HRIC meanwhile PLIC was in the order of 7.5 GB cells). In addition to the variation in cell number, it is clear from the graphic that simulation requirements and number of cells increase with simulation time. This is caused by the adaptive mesh refinement that acts to generate more cells during film formation and the issuing of new droplets. This behaviour was observed until there was a flow out of the computational domain. At this point, the simulation reaches a number of cells and then oscillates around it. Note that the number of cells increased more than 50%.

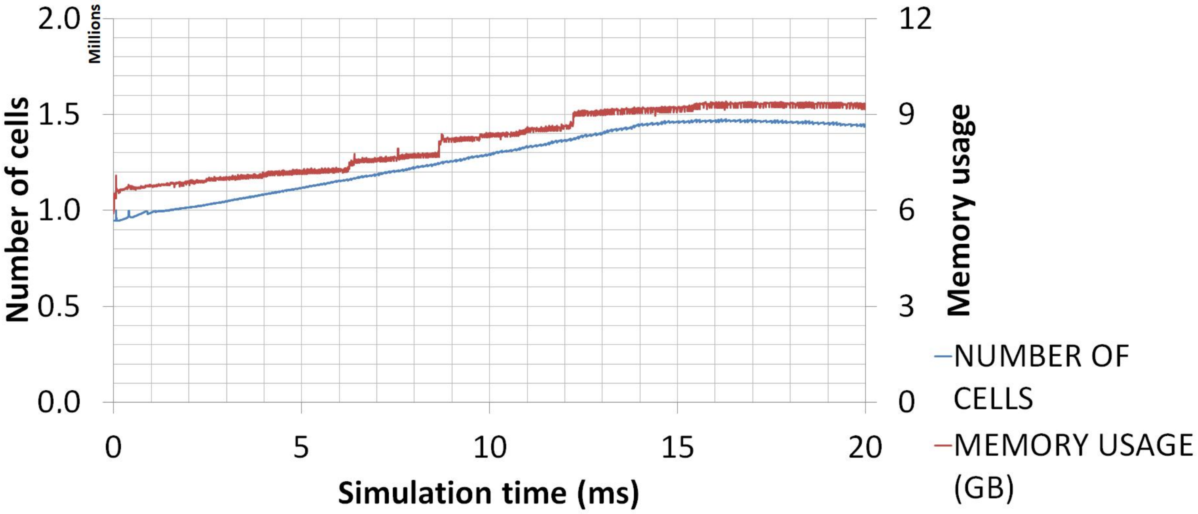

Figure 6.1: Number of cells and memory usage for the VOF simulations using AMR. As the droplets enter the computational domain the number of cells required to simulate the interface increase and so the memory usage.

The simulation time required to run a case for the HRIC scheme was 338299.53 s (approximately 94 hours) to simulate 0.006 s. For the PLIC scheme, 485767.60 s (approximately 135 hours) were necessary to run 0.006 s. As observed, the PLIC simulations needed approximately 43% more time to run the same fraction of second.

For the numerical simulations, three cases were chosen. The case with the smallest Scd is called Case 1, the second smallest Scd is called Case 2, and the case with greatest Scd is called Case 3. For this set of physical and numerical experiments, the droplet size was kept constant and its diameter was $0.645\ mm$. The same procedure was then carried out for the simulation cases, the impact angle was changed and the results are summarised in Figure 6.2 containing the results of the numerical simulations. For the first set of simulations presented in this figure only half of the domain was used to save simulation time, except for the simulation marked with the black square, which was run to test the symmetry boundary condition approximation. The results are qualitative discussed throughout this section.

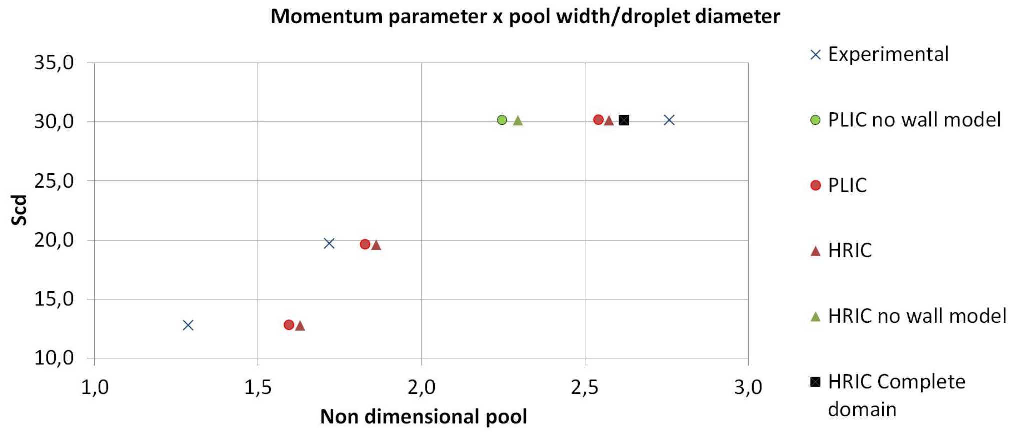

Figure 6.2: Comparison of pool size for numerical and physical experimentation. Good agreement is observed for intermediate Scd values. For high Scd values the importance of the wall model usage is highlighted. These cases were run whit half of the domain to save computational time, except for one HRIC case that was run to test the symmetry boundary condition.

These cases were chosen to cover the range of the physical experimentation that goes from partial deposition (Case 1), going through medium cases in which the Scd parameter has a direct influence on the pool size (Case 2), to cases in which a small variance in Scd parameter generates a high variance on the pool size (Case 3).

From Figure 6.2 it is observed that in Case 1 both schemes presented very similar results for the dimensionless pool size. The difference between the experimental and numerical results is partially explained by the fact that none of the schemes could predict the partial deposition expected in this case. For Case 2, both schemes presented very good agreement with experimental results. It is important to note that in Case 3 both schemes under-predicted the physical experimentation results, which opposes the results found in the other two cases. A test case was run for each of the two methods with the wall model turned off and, as expected, the results deviated even more from the physical experiment.

To analyse the shape of the droplets generated for each scheme, Figure 6.7 was generated for the PLIC scheme and Figure 6.12 for the HRIC scheme. The interface between fluids was considered to be the region with values of α smaller than 0.5. To visualise the interface between the fluids, a sampling line was drawn vertically in the middle of the droplet, as illustrated in Figure 6.3 and plotted in Figure 6.5. A second line was drawn in the direction of the droplet velocity as represented in Figure 6.4 and plotted in Figure 6.6. A similar methodology was carried out to generate Figure 6.12.

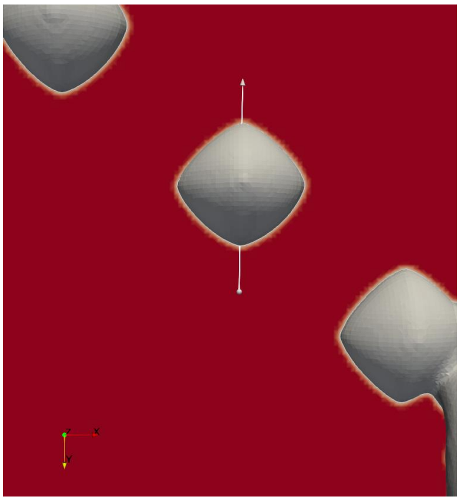

Figure 6.3: Line for tracking PLIC interface (Vertical)

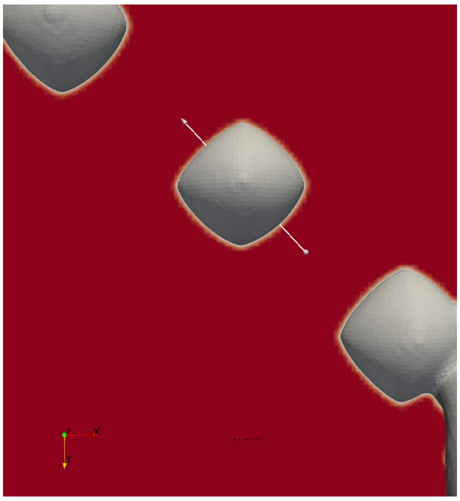

Figure 6.4: Line for tracking PLIC interface (Angled)

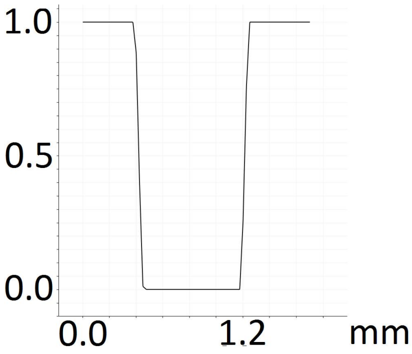

Figure 6.5: Tracked interface for PLIC case (Vertical)

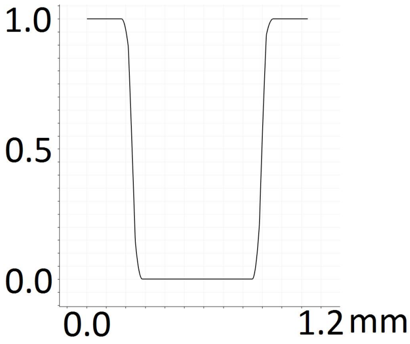

Figure 6.6: Tracked interface for PLIC case (Angled)

Figure 6.7: Droplets for PLIC scheme presenting the interface between fluids. A sharp interface is observed according to the graphs but the droplet was predicted to have a diamond shape.

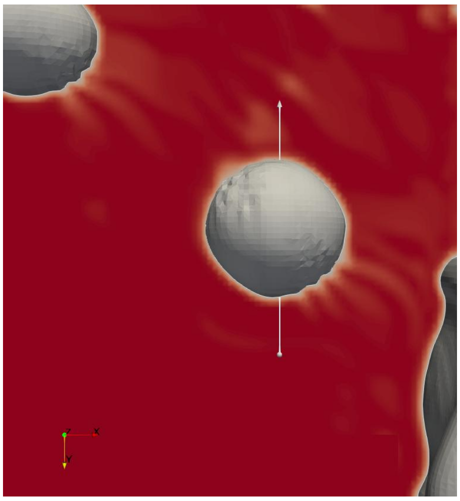

Figure 6.8: Line for tracking HRIC interface (Vertical)

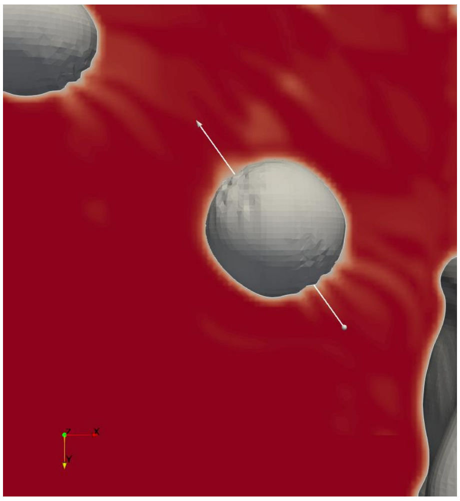

Figure 6.9: Line for tracking HRIC interface (Angled)

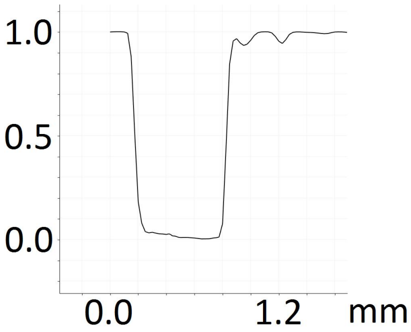

Figure 6.10: Tracked interface for HRIC case (Vertical)

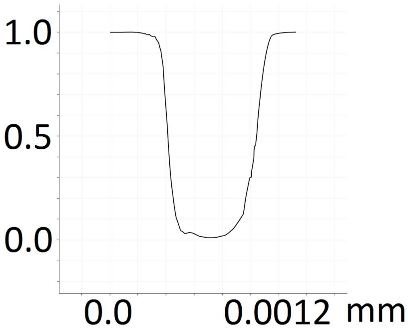

Figure 6.11: Tracked interface for HRIC case (Angled)

Figure 6.12: Droplets for HRIC scheme presenting the interface between fluids. The droplet was predicted to have a spherical shape but the interface has a numerical diffusion.

Note that there is numerical diffusion for the HRIC scheme, as indicated by the interface smearing in Figure 6.8. The AMR algorithm also refines the mesh in this smearing region for the HRIC scheme, which contributes to increasing the number of cells. This effect is also clear in the graph illustrated in figures 6.10 and 6.11, in which the instabilities close to the interface are seen. This effect is caused by the approach used to reconstruct the interface between the fluids in this scheme as presented in the Numerical Model section.

No virtual numerical diffusion is observed in the PLIC scheme as presented in the graphs 6.5 and 6.6. This behaviour is due to the purely geometric interface reconstruction of the scheme. The droplet approached a diamond shape instead of a sphere. This poor prediction on the droplet shape leads to the formation of the pool in a similar way. The pool formation after droplet impingement on the wall is illustrated for Case 3 using PLIC scheme in Figure 6.13 and HRIC in Figure 6.14. In these figures, it is observed that the pool shape of the PLIC scheme became diamond shaped, which is similar to the shape of the impinging droplet. On the other hand, the prediction of the HRIC scheme was more rounded and, therefore, closer to the format captured by the figures of the physical experiment. The figures were reflected along the symmetry boundary condition to improve the visualisation. The symmetry boundary condition is marked by the white line in the middle of the image.

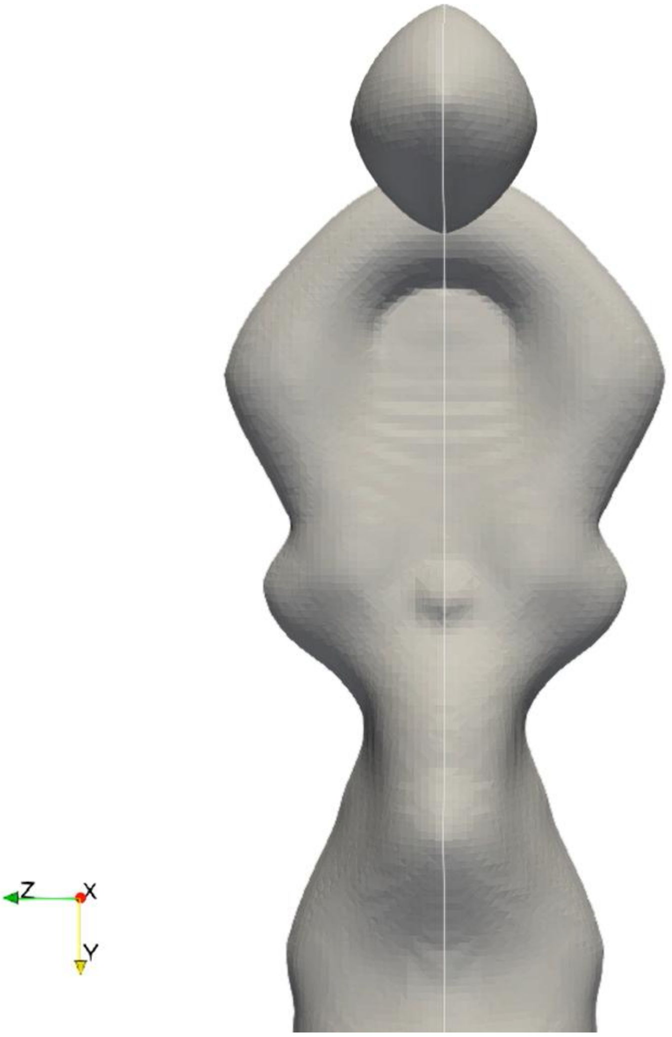

Figure 6.13: Pool shape for PLIC scheme simulation considering half of the domain. The diamond shape of the droplet is also observed in the pool formed by the droplet collision.

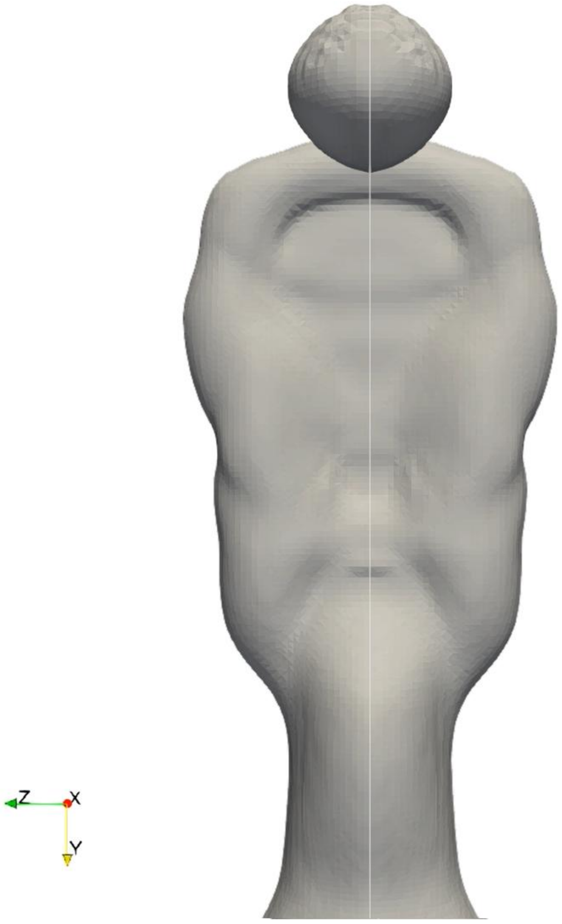

Figure 6.14: Pool shape for HRIC scheme simulation considering half of the domain. The pool shape is more round when compared to the PLIC scheme as the droplet was predicted with an spherical shape.

Simulations were carried out with the complete domain and the results are illustrated in Figure 6.15 for PLIC, and Figure 6.16 for HRIC. The simulations run with the PLIC scheme on the complete domain also presented the diamond pool shape. The pool shape formed by the HRIC was changed to a pool less spread along the y axis and with a slightly wider shape.

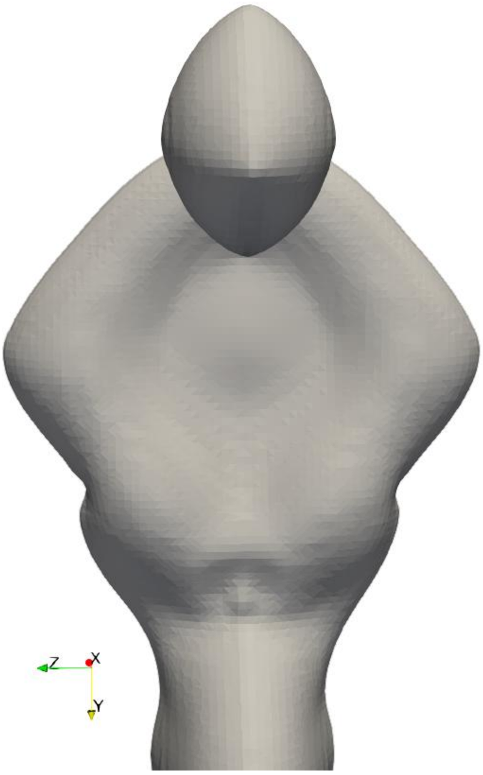

Figure 6.15: Pool shape for PLIC scheme simulation considering the complete domain. The diamond shape of the droplet is also observed in the pool formed by the droplet collision.

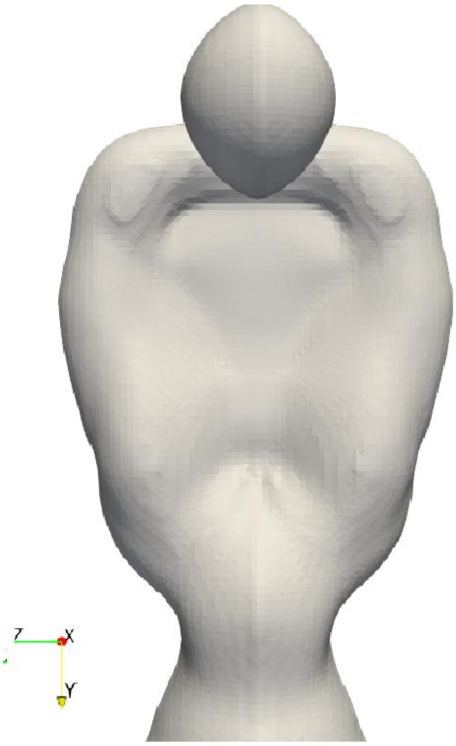

Figure 6.16: Pool shape for HRIC scheme simulation considering the complete domain. The pool shape is more round when compared to the PLIC scheme as the droplet was predicted with an spherical shape.

The HRIC scheme presented a droplet shape closer to the physical experimentation images as well as presenting results closer to the physical experimentation. Considering that, it was chosen to proceed with the liquid film formation analysis.

The results for the simulations to evaluate the wall model are presented on Figure 6.17. The image illustrates the simulations considering the complete domain. On the left of the image, the results for the simulations that considers the wall modelling are illustrated. On the right, the results not considering the wall model are presented. It is observed that the simulation considering the wall model spreads in a wider liquid film when compared to the simulations without the wall model. As presented in Figure 6.2 the simulations considering the wall model predicted values for the non dimensional pool size closer to the physical experimentation.

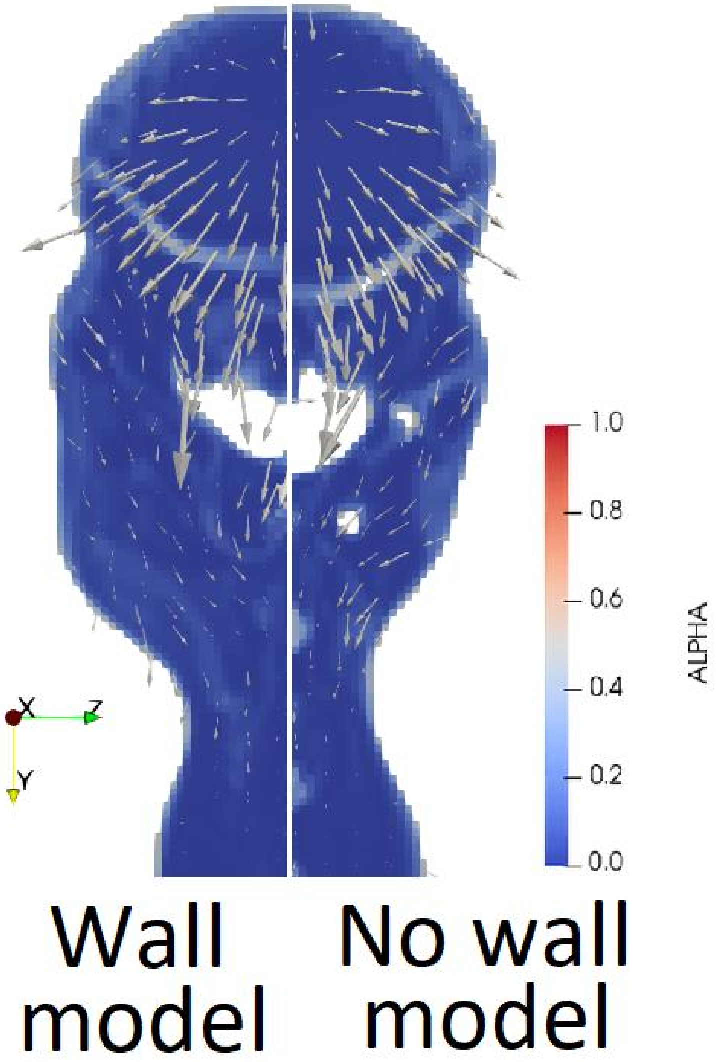

Figure 6.17: Comparison of the simulations using HRIC scheme. The image on the left represents the results for the complete domain considering the wall model and the image on the right the results for the complete domain not considering the wall model. It is observed that the simulations that not consider the wall model did not form a wide liquid film as expected considering the results from physical experimentation.

The results for the simulation considering half of the domain and the complete domain are presented in Figure 6.18. The results for the half domain were mirrored in relation to the white centre-line for a better visualisation. As can be observed in the images, the shape of the pool has changed when the symmetry condition was used and became more spread along this boundary. A comparison with the liquid film shape acquired in the physical experimentation was carried out and presented in Figure 6.19. In this image it is possible to note that the shape resulting from the simulation considering the complete domain is closer to the physical experimentation.

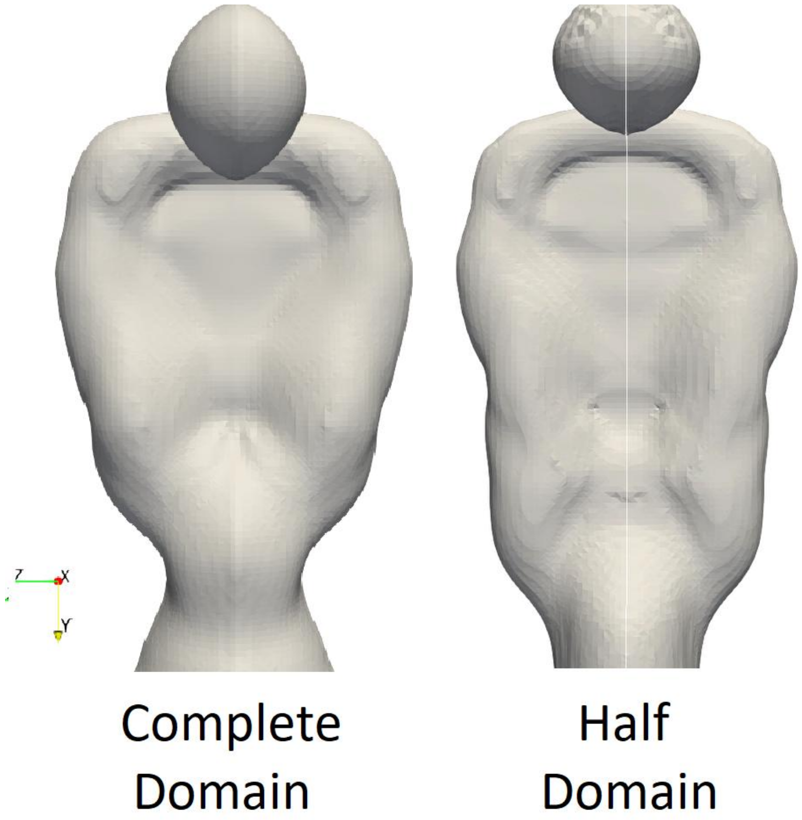

Complete Domain

Half Domain

Figure 6.18: Comparison of the simulations using HRIC scheme. The image on the left represents the results for the complete domain and the image on the right for half of the domain. It is observed that the simulations using half of the domain presented results with more spread liquid film along the symmetry boundary condition.

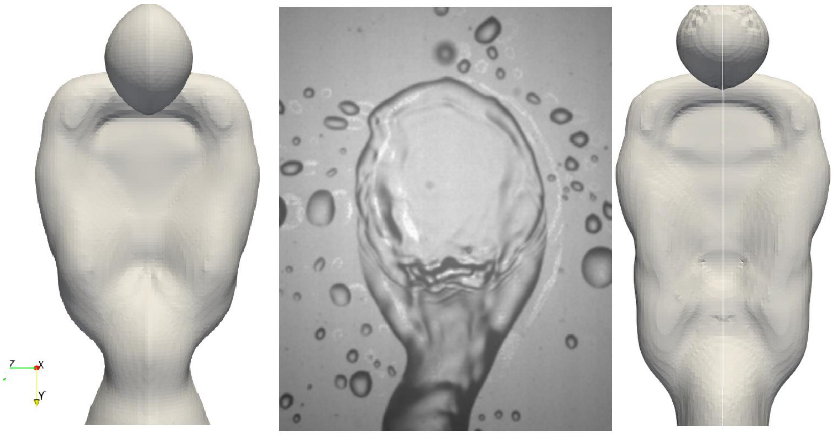

Complete Domain

Physical Experimentation

Half Domain

Figure 6.19: Comparison of the simulation using HRIC scheme and physical experimentation. The image on the left represents the results for the complete domain, in the middle the results for the physical experimentation, and the image on the right for half of the domain. The liquid film generated by the simulation considering the complete domain are closer to the shape of the physical experimentation.

To better understand the difference between the two approaches, Figure 6.20 was generated representing the wet area in blue with the velocity vectors sized by velocity. On the left side of the image the simulation with complete domain is illustrated and on the right side the result considering half of the domain. It is observed that the width of the pools are similar but the results for the half domain presented higher velocities on the y direction. This higher velocity makes the liquid spreads faster on the wall, forming a longer shape than expected and slightly decreases the pool width. To corroborate this fact, Figure 6.21 illustrates the velocity field. As observed higher velocities can be found in the numerical results presented by the simulation considering only half of the domain.

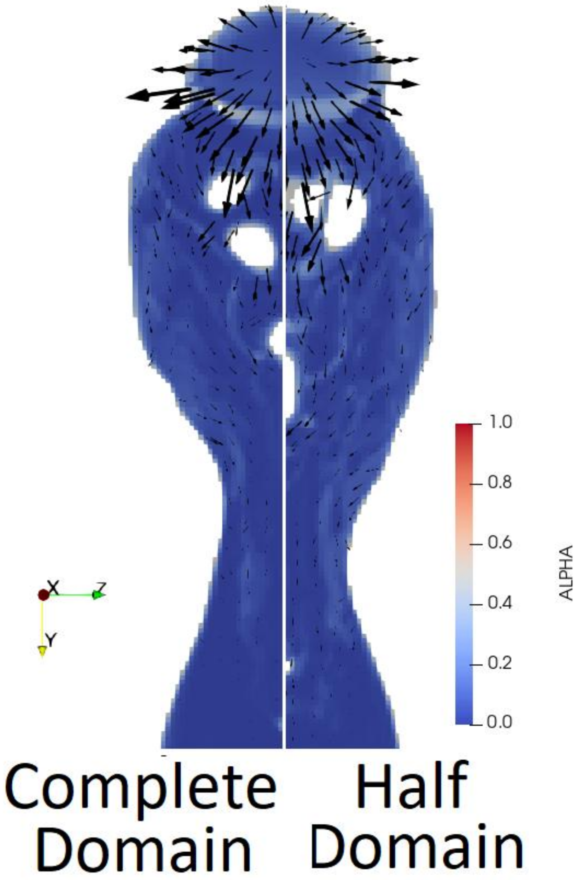

Figure 6.20: Comparison of the simulation using the complete domain and half of the domain for HRIC scheme with velocity vectors. The blue region represents the values of alpha. The image illustrates the fact that the simulations with half domain spreads faster along the y axis. This behaviour makes the pool more stretched in this direction when compared to physical experimentation and the simulations with the complete domain.

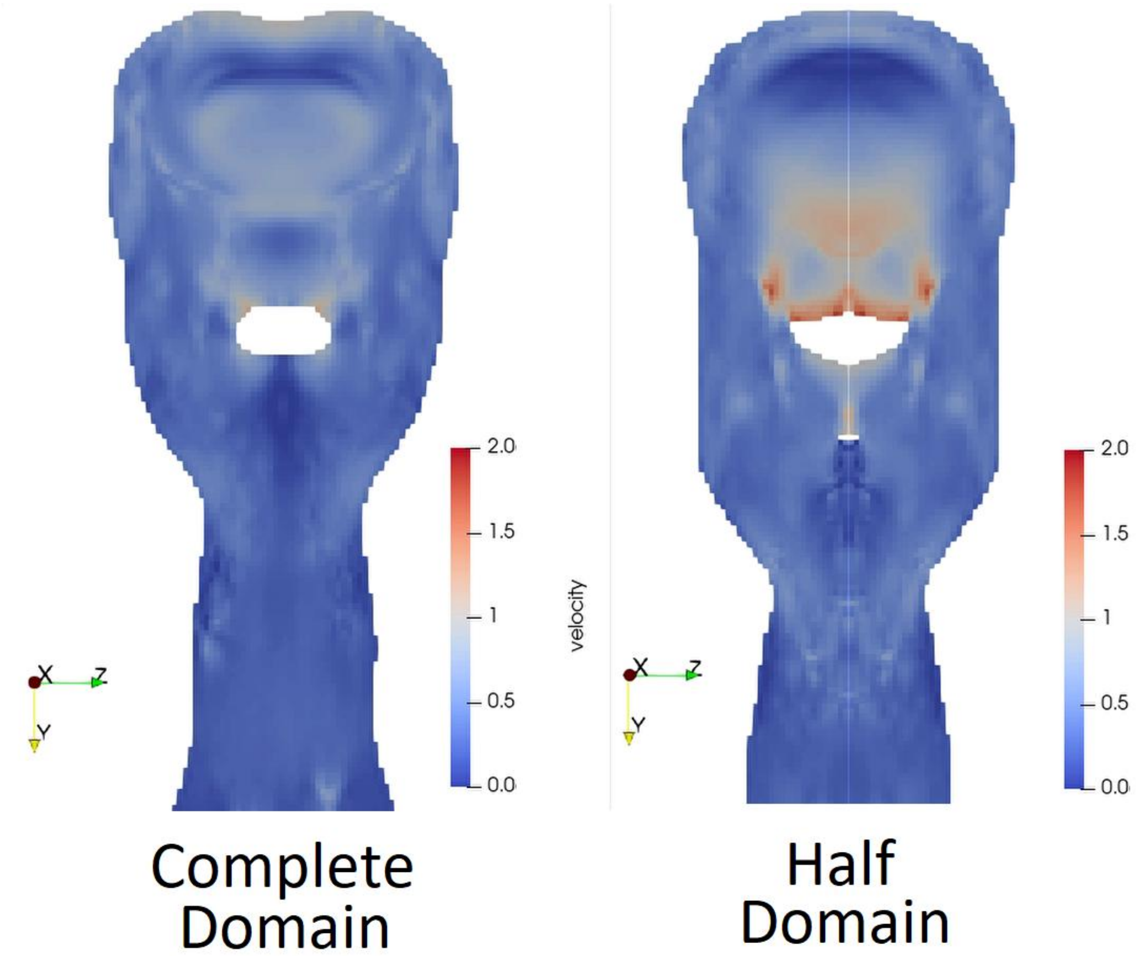

Complete Domain

Half Domain

Figure 6.21: Comparison of the simulation using the complete domain and half of the domain for HRIC scheme with velocity field. The colours represent the velocity field. The image illustrates the fact that the simulations with half domain spreads faster along the y axis. This behaviour makes the pool more stretched in this direction when compared to physical experimentation and the simulations with the complete domain.

To further analyse the spreading of the liquid film, the velocity vectors are plotted on the wall as illustrated in Figure 6.22 for the simulation with the complete domain for the HRIC scheme. In this figures, the blue region represents the wet area on the wall. The vectors are sized by the velocity magnitude. As observed in the sequence of images, the droplet impact is illustrated in Figure 6.22a. In this figure it is possible to note that the velocity magnitude is higher in the droplet impact region and spreads radially. In Figure 6.22b it is possible to observe that the velocity vector is affected by the gravity and change its velocity towards the ground. In Figure 6.22c it is noted that the highest velocity magnitude is pointing in the direction of the gravity, but it is also noted that the velocity vectors in the vicinity of the non wet region are already pointing inwards, which means it is regrouping the liquid and forming the liquid tail. In Figure 6.22d it is observed that the spreading of the pool is almost in the end as the vectors pointing outwards are weak. The vectors on the middle of the pool on the upper limit of the liquid film are stronger in the y direction than the vectors away from the centre-line, these stronger vectors shape the form observed in the upper side of Figure 6.22d.

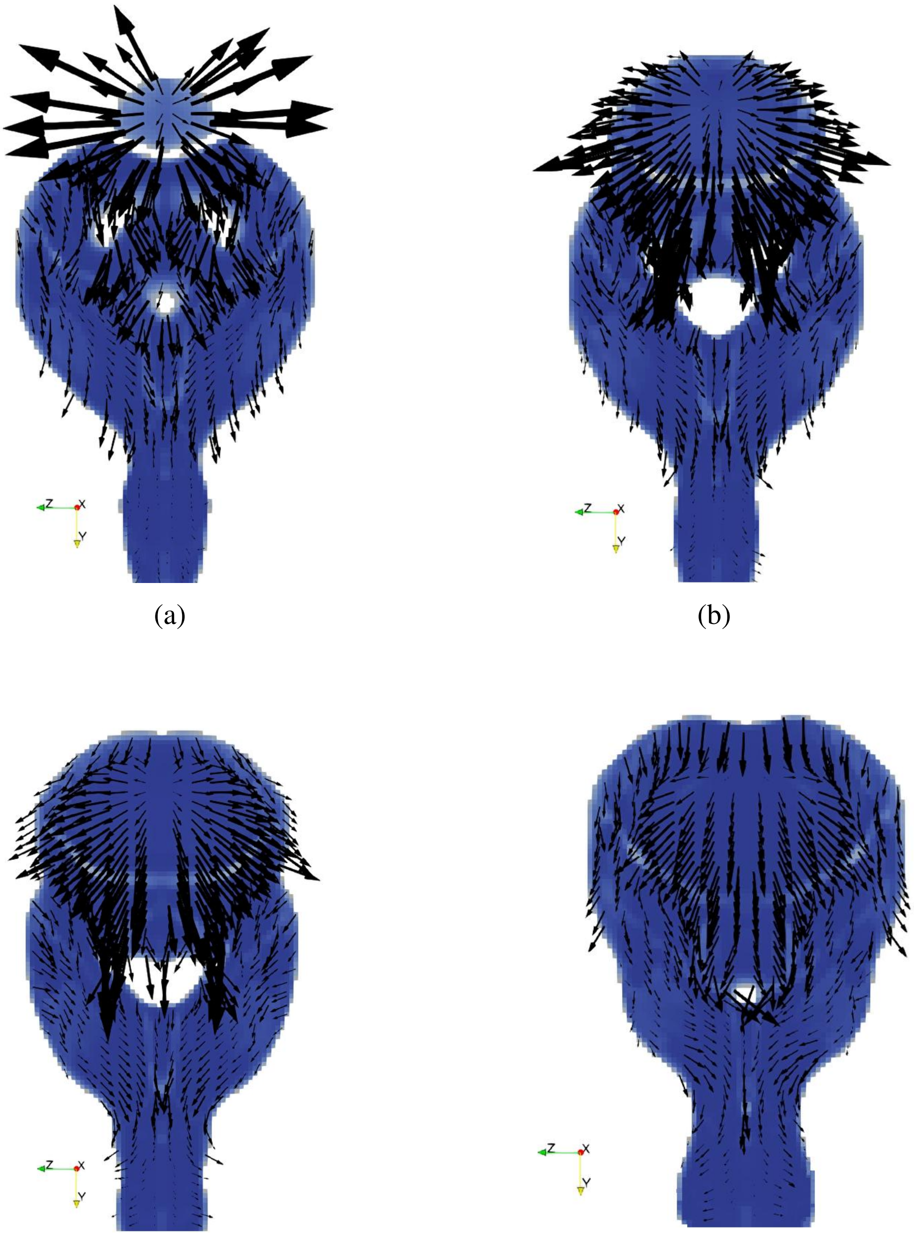

(a) (b)

(c) (d)

Figure 6.22: Droplet collision on wall for the simulation with HRIC scheme. The image represent the sequence of droplets spreading on the wall. Only the wet region is represented. Figure (a) presents a moment just after the droplet collision with the wall. Figure (b) represents the droplet after collision and the start of the spread. Figure (c) represents the droplet already absorbed by the pool and the spreading of the liquid. Figure (d) represents the final stage of the droplet spreading.

To visualise the oscillation in the region of the tail Figure 6.23 illustrates the liquid film from a side view with the corresponding wet area with velocity vectors by its side. On the sequence of images Figure 6.23a illustrates the incoming droplet almost touching the liquid film. Figure 6.23b illustrates the droplet already absorbed by the pool, but the spreading of the droplet did not yet affect the behaviour of the liquid tail. Figure 6.23c illustrates the effects of the rejoining of the mass and momentum of the incoming droplet. Observe that the pool is wider and the velocity vectors are intensified and are pointing to the centre-line. To conserve the mass in that region the film liquid height is increased and forms the shape illustrated by the side view. Figure 6.23d illustrates this increment of height being carried by the effect of gravity, generating the undulation observed by the droplet impingement. In this image it is also observed that the velocity vectors are already aligned with the tail on the direction of gravity. This sequence of images presented a similar behaviour of the physical experimentation results, as observed in Figure 4.51.

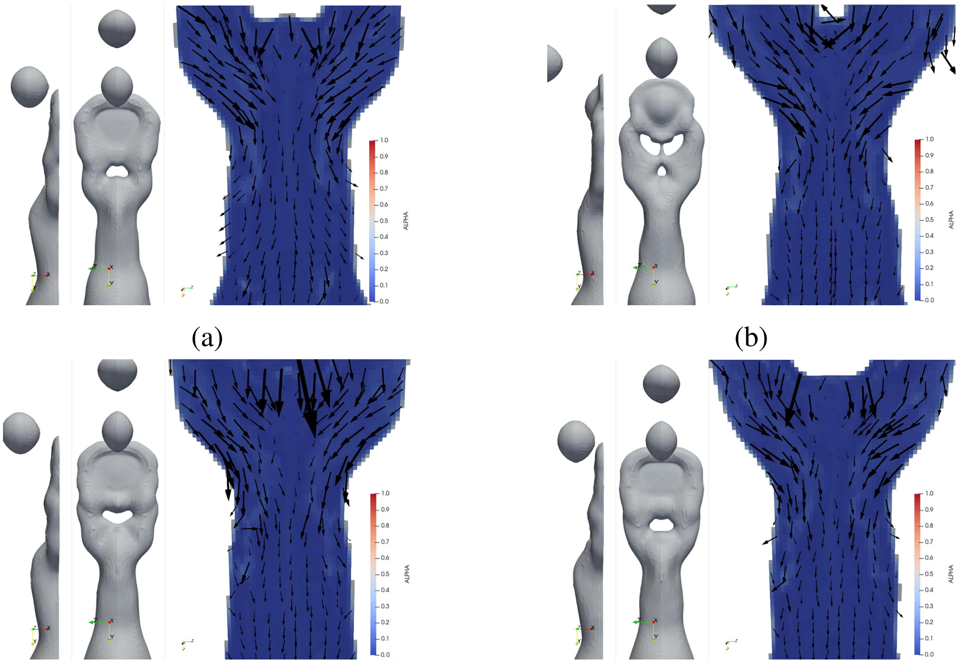

(a) (b)

(c) (d)

Figure 6.23: Side view of droplet collision on wall and the wet area of the tail formation. Velocity vectors are illustrated on the wet area for the visualisation of tail formation. The undulation in the tail is formed by the regrouping of the liquid, forming a local film height higher in the beginning of the tail that is carried by the effect of gravity.

Figure 6.24 illustrates the liquid film represented with the values of alpha on the left side along with velocity vectors. In the middle the velocity field is illustrated. On the right side the wall stress is illustrated. A huge similarity is observed for the velocity distribution and the wall stress. In Figure 6.24a the spreading of the droplet is observed highlighting the regions of maximum velocity and wall stress during the spreading. In Figure 6.24b the velocities on the upper part of the pool can be observed, and how they shape the pool format.

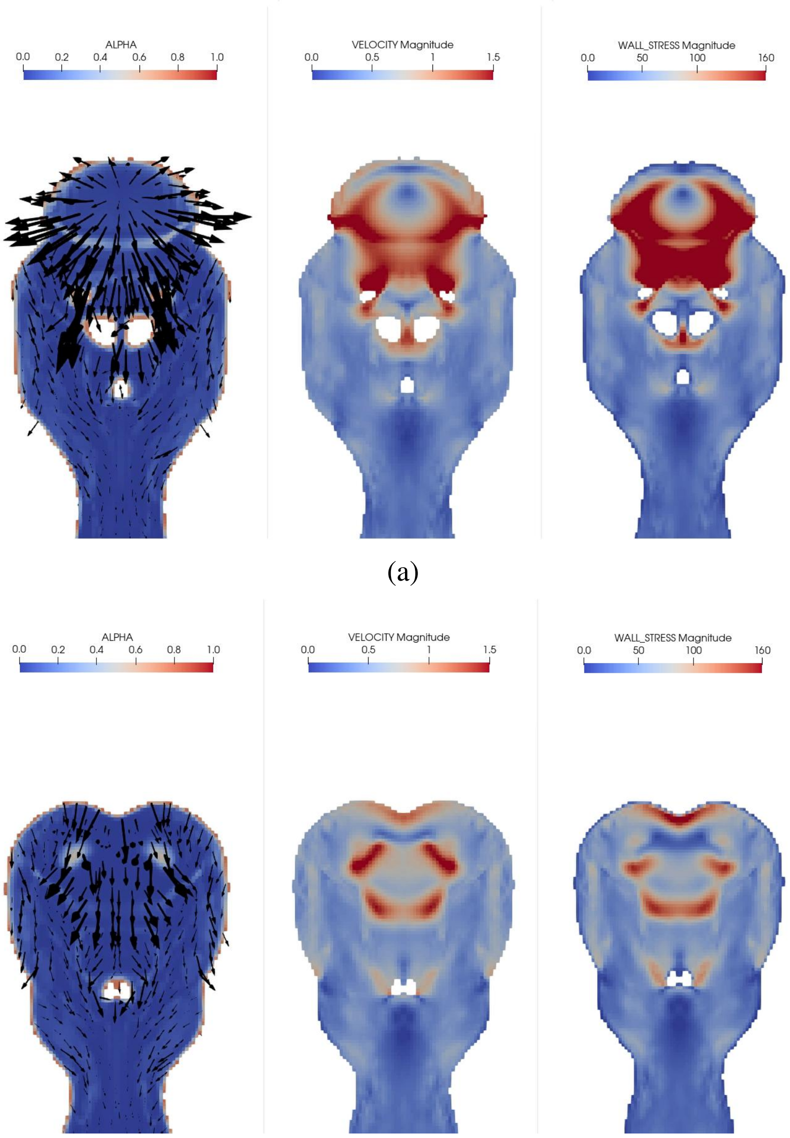

(a)

(b)

Figure 6.24: Liquid film representation along with velocity vectors on the left side. In the middle the velocity field is illustrated. On the right side the wall stress is illustrated. Similarity is observed for the velocity distribution and the wall stress.

6.2 Eulerian wall film formation: simulation of droplet spreading

The results for the height of the liquid film in the droplet spreading case were obtained along the white arrow as represented in Figure 6.25. This data was normalised by the maximum height (h/h_f) and plotted against the normalised radius (r/r_f). h is the local height, h_f is the maximum height, r is the droplet radius, and r_f is the maximum droplet radius.

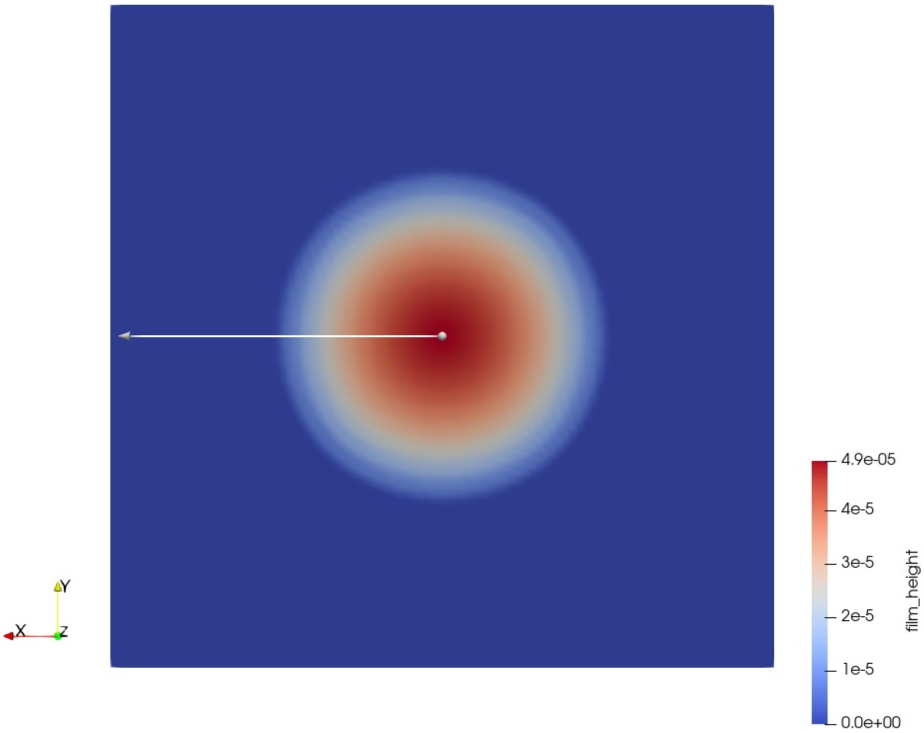

Figure 6.25: Film height of the droplet spreading. The white line that starts at the center of the droplet was used to acquire the film height to compare with the results presented by Diez et al. (1994). The droplet has a paraboloid shape with its maximum height at the centre, presented by the red colour.

The results of the simulations of droplet spreading were validated against Diez et al. (1994) theory, as represented in Figure 6.26. According to his results, the normalised film height is expressed in a function that is not dependent on time. To test this theory, different simulation times were plotted against the analytical data. The time step was set to 10^{-5} s, and the total simulation time was 0.8 s. Data was acquired for 0.1 s (Simulation 0.1 s), 0.2 s (Simulation 0.2 s) and 0.8 s (Simulation 0.8 s).

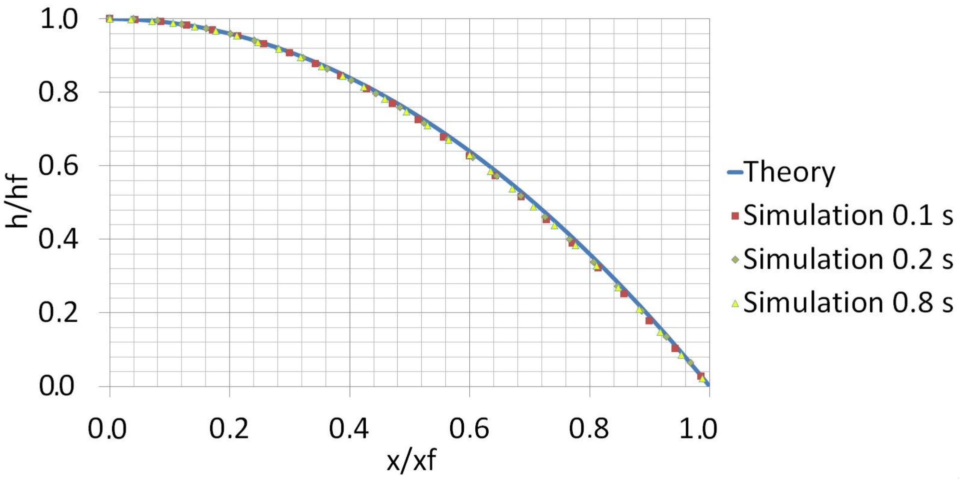

Figure 6.26: Comparison of theory and simulation results for droplet spreading. The line represents the results of the theoretical solution presented by Diez et al. (1994). The dots represents results for the numerical simulations in three different times. Considering the non dimensional numbers presented, the solution is independent of time.

This quantitative comparison was considered a good agreement between simulation and theory. Thus, the simulations and the EWF method implemented were considered validated.

6.3 Eulerian wall film formation: simulation of cross flow

This section concerns the validation of the EWF model for the cross flow case. The simulations run according to the methodology explained in Chapter 5.

To evaluate grid convergence, the concept of Grid Convergence Index (GCI) was applied. This test was applied to evaluate three different grids, namely fine, medium, and coarse mesh. The simulations were run without the droplets in the domain to verify the influence of the mesh on the air flow and the results are presented in Table 6.1.

Table 6.1: Grid independence test based on Grid Convergence Index (GCI) method.

i	N_i	U (m/s)	$\mathrm{GCI}^{\text{fine}}_{i,i+1}$ (%)	R	α
1	662 240	76.648			
			0.059		
2	390 610	76.632		0.661	0.927
			0.090		
3	231 728	76.609			

in which $i = 1$, 2 and 3 denotes the calculations of the fine, medium and coarse mesh respectively. N is the number of elements in the mesh. U is the computed average velocity in x direction. The mean velocity value was calculated in a plane with the normal parallel to the computational domain air flow entrance that contains the point of injection. α is the parameter that evaluates if the solution is in the asymptotic range, the closest to unity the better. R is a ratio that can represent a monotonic convergence if less than unity.

Analysing Table 6.1 it is possible to observe a monotonic convergence. Therefore a mesh with 662 240 elements was used throughout the simulations. Care was taken so that the element size was bigger than the droplets clusters inside the computational domain.

For the simulations in this work the wall temperature was set to a value equal to the droplet temperature. Observing the diagram developed by Kuhnke (2004b) in Figure 3.7 it is concluded that only absorption and splash were possible under these conditions. Throughout the simulations it was found that the non dimensional velocity never exceed the value of 150. Observing the diagram again, it is concluded that the only outcome observed for droplet impingement was complete absorption. The criterion for striping was also never met as the shear stress on the liquid gas interface was low for all cases.

The results for the height of the liquid film in the cross flow case were obtained along the white arrow as represented in Figure 6.27. The beginning of the white arrow represents x coordinate zero, the same x coordinate position of the injector.

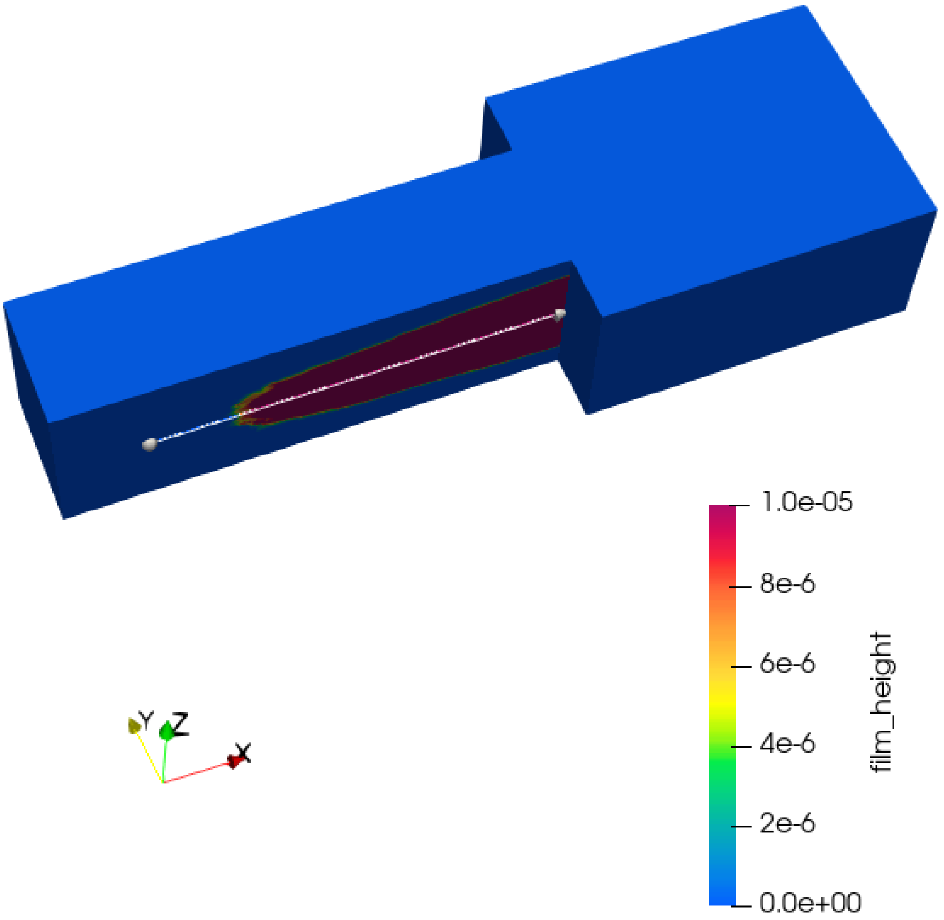

Figure 6.27: Film height of the jet in cross flow case. The white line that starts at the same x position as the jet inlet was used to acquire the liquid film height. This data was used for comparison with the results presented by Arienti et al. (2011).

To have a better idea of the time spent to run each step of the simulations a test was carried out with 2000 time steps of $2 \cdot 10^{-6}$ s. Different methodologies were followed and are highlighted in detail, presenting the times spent for each step, on the following paragraphs.

For a steady state simulation, not considering the Lagrangian phase, the time spent was 15818.95 s (approximately 4.4 hours) with an absolute residual source sum of $1 \cdot 10^{-7}$, requiring 4739 simulation steps. The transient simulations were then started using the final results of the steady state simulation as initial conditions. For this second simulation, the time spent was 98589.09 s (approximately 27.4 hours).

The second set of simulations were run starting from a quiescent environment directly simulating the transient effects and the Lagrangian droplets. This simulation spent 124592.2 s (approximately 34.6 hours). As observed it is already more time than the two cases presented before.

Third set of tests consisted of starting the transient simulation without the droplet injection and then injecting the Lagrangian phase. The simulations considering only the Eulerian phase spent 118210.8 s (approximately 32.8 hours). This was considered a long simulation time, and the test was stopped.

The third set of simulations consisted of the "frozen" Eulerian phase. For this set of simulations the time spent was 719.20 s (approximately 12 minutes).

the presented simulation times, it is concluded that the best approach for simulating the current case is to start from the simulation of the steady state case before running the Lagrangian phase with transient effects. Besides that, the restart files generated for the steady state case can be used in different cases as initial conditions, saving simulation time.

The difference in time for the frozen simulation was highlighted, from hours of simulation to minutes. Figure 6.28 illustrates the benefit of using the "frozen" field for Case 1 using the $k - \omega\ SST$ turbulence closure model. Observe that the film height is smoothed as many more droplets were used to generate the liquid film. For this case 6000 time steps were simulated for the transient simulation, meanwhile the frozen simulation used 200000 time steps.

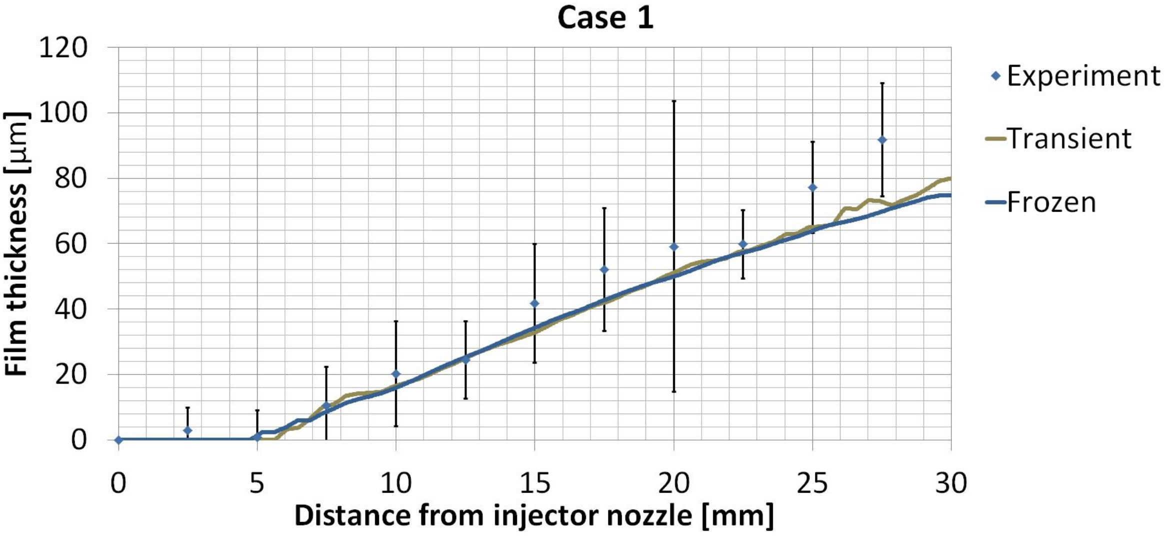

Figure 6.28: Results of averaged liquid film height for Case 1. The dots represent the physical experimentation data from Shedd et al. (2009a). The green line represents the transient simulations and the blue line represents the frozen field simulations. $k - \omega\ SST$ turbulence closure model was used. For the transient simulation 6000 time steps were simulated, meanwhile the frozen simulation used 200000 time steps. Observe that the frozen field was able to generate a smoother curve as more droplets were considered in the simulations.

As observed in Chapter 3, the EWF model depends on several parameters, and different conditions may result in substantial differences in the method behaviour. In order to verify the main influence of these parameters, eight different tests were carried out and the main findings are outlined below and further explained in separated subsections.

6.3.1 Influence of turbulence closure model in the EWF numerical simulations

The first set of tests concern the turbulence closure models. For that, three different models were used, namely k-ϵ, tuned k-ϵ and $k-\omega\ SST$. Considering the simulation time of the frozen field with Lagrangian droplets, the computational time of operation was 5691.99 s for k-ϵ, 9220.53 s for tuned k-ϵ, and 25686.33 s for $k-\omega\ SST$. The number of parcels inside the domain was 20809 for k-ϵ, 22435 for tuned k-ϵ, and 134255 for $k-\omega\ SST$. Comparing the models it is possible to observe that there are more secondary droplets for the $k-\omega\ SST$ model and also a longer time of computational operation. The tuned K-ϵ model required more time for the simulations than the K-ϵ and also had more droplets inside the domain.

The results are represented in Figure 6.29 for Case 1 with a comparison against physical experimentation data. It can be observed from the results that the liquid film height grows progressively towards the edge. The main observations are that the $k-\omega\ SST$ model can better predict the liquid film behaviour, as the k-ϵ and the tuned k-ϵ under-predict the liquid film formation. The differences for the k-ϵ and the tuned k-ϵ are mostly that the liquid film formation starts further from the x coordinate of the jet for tuned k-ϵ. Near the end corner there is another difference, where the results for tuned k-ϵ presented smaller values for the liquid film and even a drop on the film height. The results suggest that the $k-\omega\ SST$ turbulence closure model is more appropriate for this case.

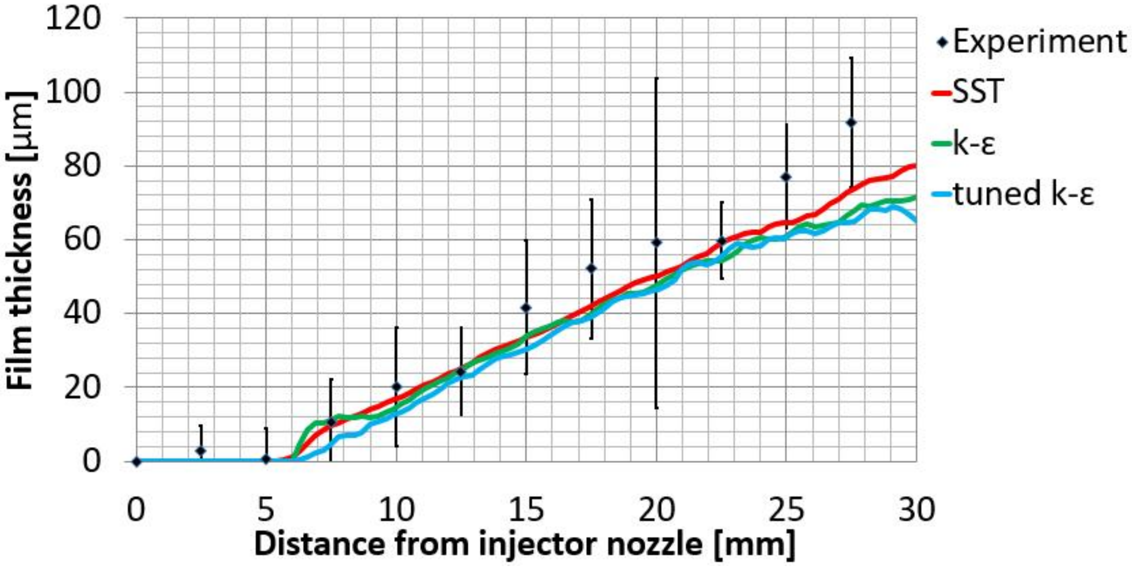

Figure 6.29: Results of averaged liquid film height for Case 1. The dots represent the physical experimentation data from Shedd et al. (2009a) and the lines represents different turbulence closure models used to simulate the Eulerian phase.

For Case 1, images of the liquid film on the wall surface are illustrated in Figure 6.30 for the k-ϵ, in Figure 6.31 for the tuned k-ϵ, and in Figure 6.32 for the $k-\omega\ SST$ model. The scale is represented differently in these figures when compared to Figure 6.27 for better visualisation of the liquid film height. On this images it is observed that the k-ϵ and the tuned k-ϵ behave similar. For the $k-\omega\ SST$ case, the liquid film height presented a different pattern. In this case, higher liquid films are found on the centre of the wall film, while the other two cases presented higher liquid film away from the centre line. For all three cases the liquid film is symmetric in relation to the centre line, which was expected since the simulations are carried out for mean values. These results also indicate that the $k-\omega\ SST$ turbulence model is more suitable for this case, as in the physical experimentation presented by Shedd et al. (2009a) the liquid film decreases in span-wise direction.

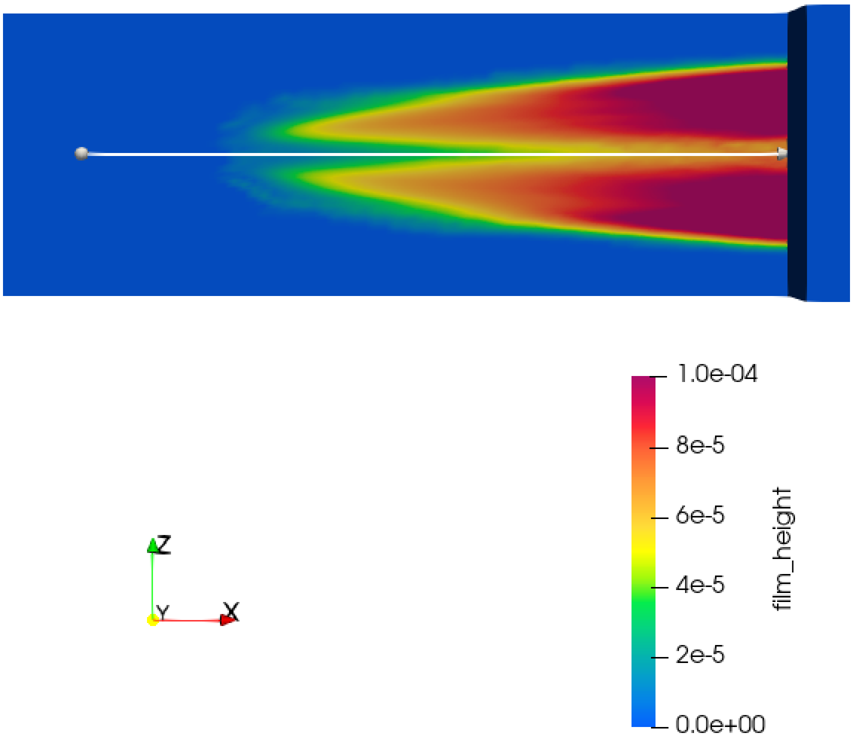

Figure 6.30: Results of averaged liquid film height for Case 1 using k-ϵ turbulence closure model. A symmetric distribution of liquid film is observed as well as peaks away from the centre-line, which were not consistent with the physical experimentation observations.

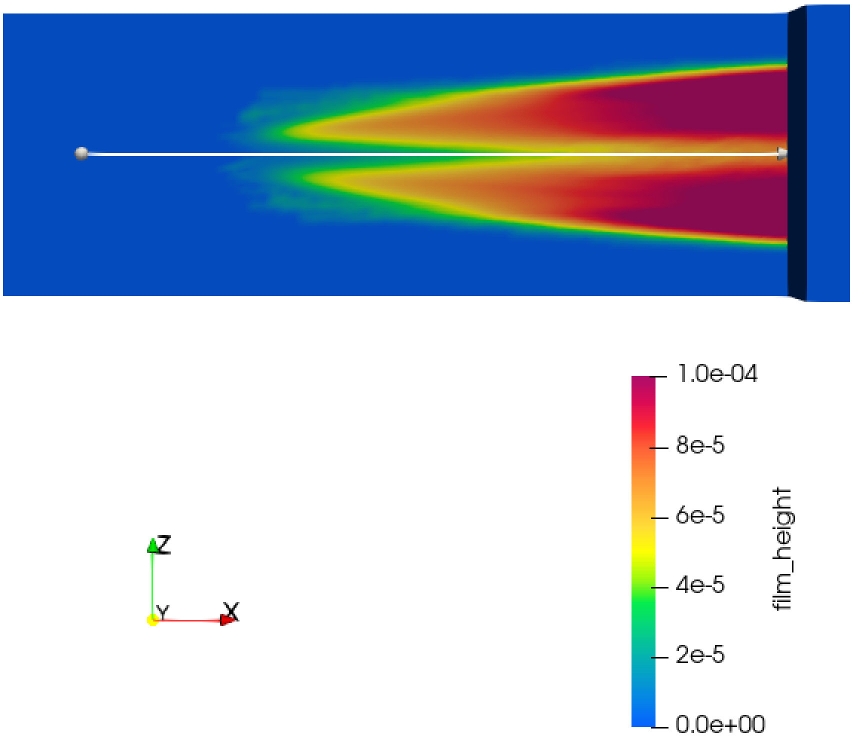

Figure 6.31: Results of averaged liquid film height for Case 1 using tuned k-ϵ turbulence closure model. A symmetric distribution of liquid film is observed as well as peaks away from the centre-line, which were not consistent with the physical experimentation observations.

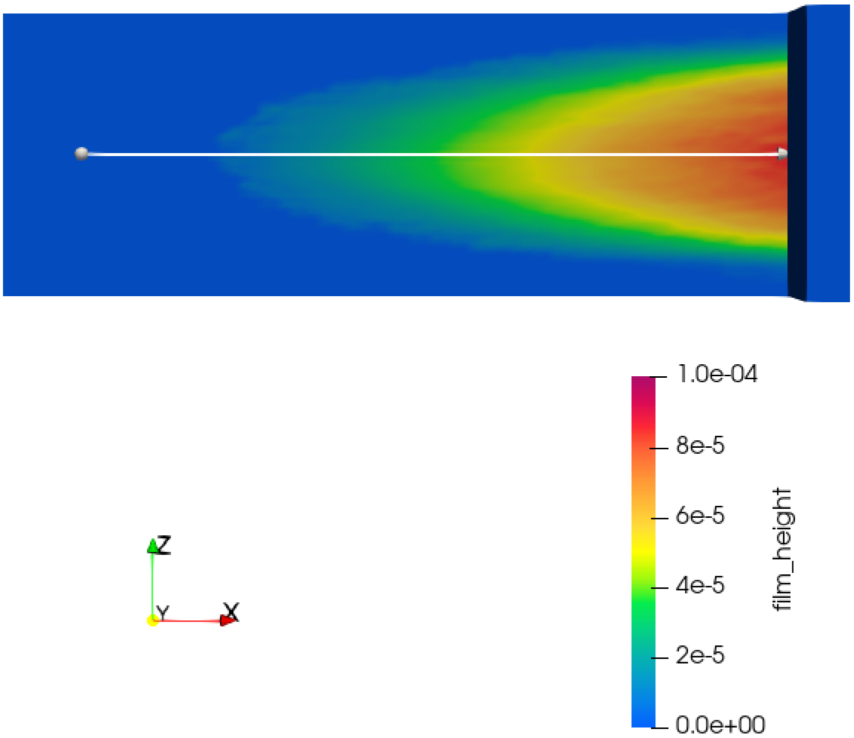

Figure 6.32: Results of averaged liquid film height for Case 1 using $k-\omega\ SST$ turbulence closure model. A symmetric distribution of liquid film is observed as well as a centralised distribution of liquid film. As observed by a less intense red coloured, the liquid film height is smaller for this case.

The main differences observed can be partly explained by the droplets behaviour in each case. The droplets are represented for the different models, being Figure 6.33 for the k-ϵ, Figure 6.34 for tuned k-ϵ, and Figure 6.35 for $k-\omega\ SST$. Velocity is plotted for the Eulerian phase. It is observed for the k-ϵ and tuned k-ϵ that the droplets behaviour are similar. The results for the $k-\omega\ SST$ turbulence closure model presented more droplets at vertical positions along the domain, consequently, more droplets are carried away by the gas phase.

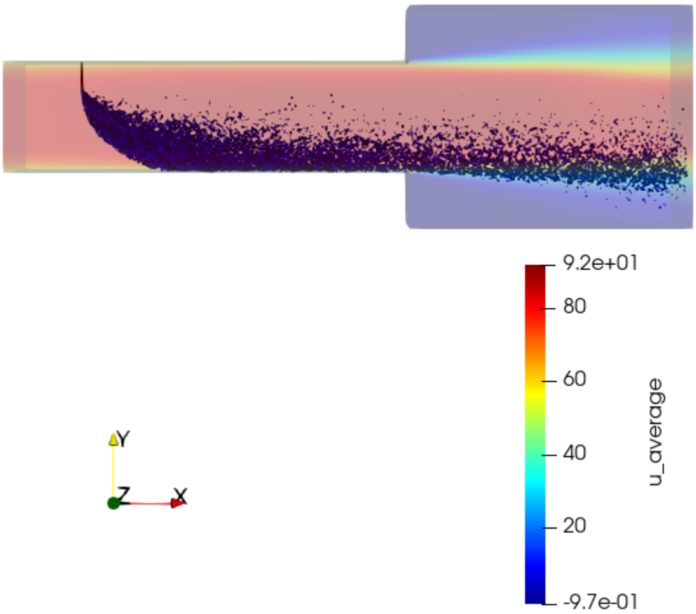

Figure 6.33: Results of droplets distribution inside the domain for Case 1 using k-ϵ turbulence closure model. Less droplets can be observed inside the computational domain, also occupying positions closer to the wall, thus, less droplets are carried by the gas phase.

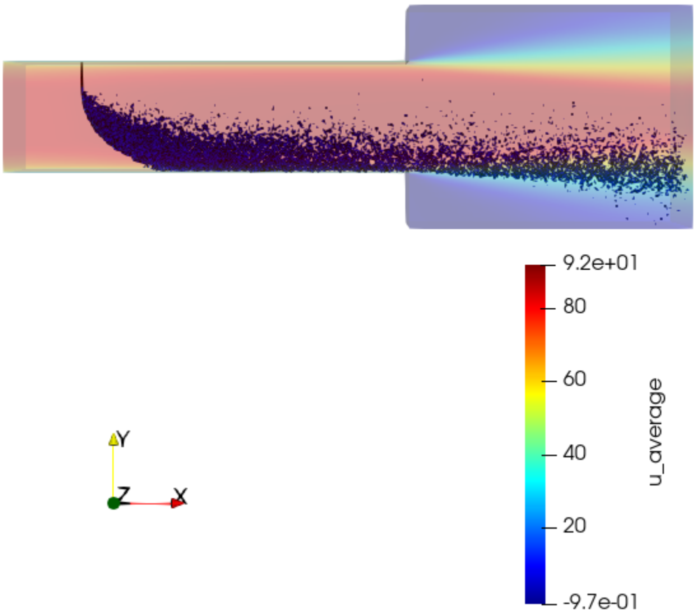

Figure 6.34: Results of droplets distribution inside the domain for Case 1 using tuned k-ϵ turbulence closure model. Less droplets can be observed inside the computational domain, also occupying positions closer to the wall, thus, less droplets are carried by the gas phase.

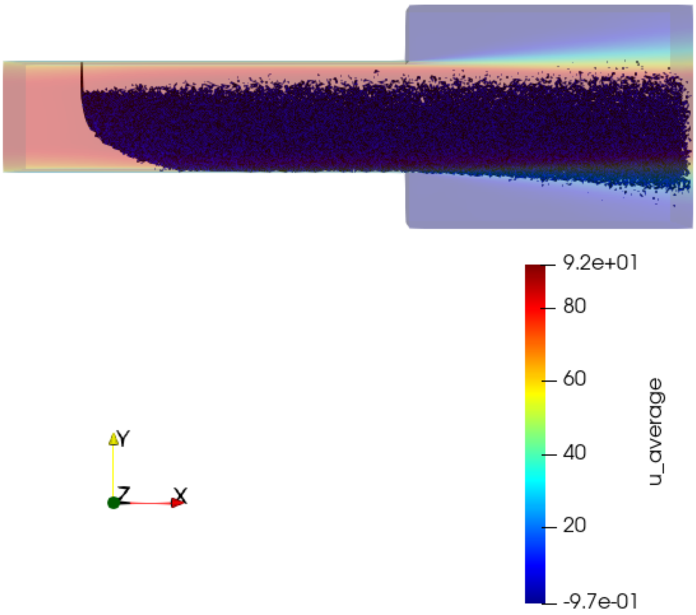

Figure 6.35: Results of droplets distribution inside the domain for Case 1 using $k - \omega\ SST$ turbulence closure model. More droplets can be observed inside the computational domain, also occupying higher positions, thus, more droplets are carried by the gas phase.

The droplets distribution is illustrated in Figure 6.36 for the tuned k-ϵ turbulence closure model and represented with the film height in Figure 6.37 to illustrate the droplet distribution on the liquid film formation. Note that the droplets are coloured by the diameter, and are all represented with the same size. Observing these figures, it becomes clear that the droplets behaviour formed the film liquid shape represented in Figure 6.31. The droplets distribution is represented in Figure 6.38 for the $k - \omega\ SST$ turbulence closure model and represented with the film height in Figure 6.39 to illustrate the droplet distribution on the liquid film formation. It becomes clear from these figures the more evenly distributed concentration of droplets. This distribution generates a liquid film formation with a higher concentration along the centre line of the computational domain as represented in Figure 6.32. This behaviour is different from the other turbulence closure models tested. By analysing the images, it is possible to observe that the droplets prior to the impact on the wall are bigger for k-ϵ than for $k - \omega\ SST$ turbulence closure model, being the latter more disperse over the impacted surface. It is also noted an absence of droplets along the centre line of the computational domain for the k-ϵ results. This behaviour is due to the interaction of the droplets with the air stream, which presented differences for the different turbulence closure models.

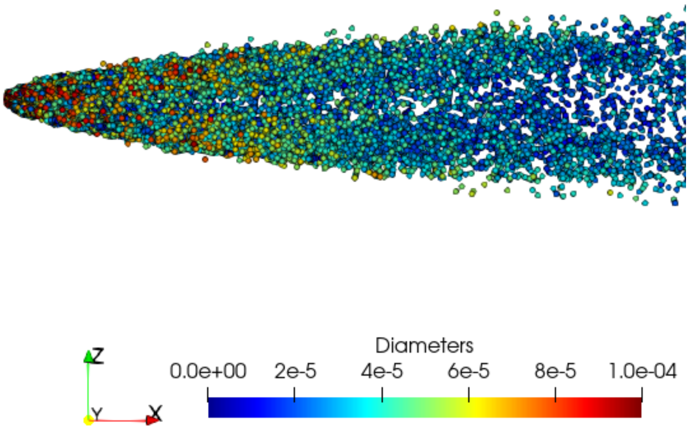

Figure 6.36: Results of droplets distribution inside the domain for Case 1 using k-ϵ turbulence closure model in the bottom view. Droplets are coloured by the size. The bifurcation of the droplets is observed by the absence of droplets in the central region. Bigger droplets were observed in the vicinity of the wall.

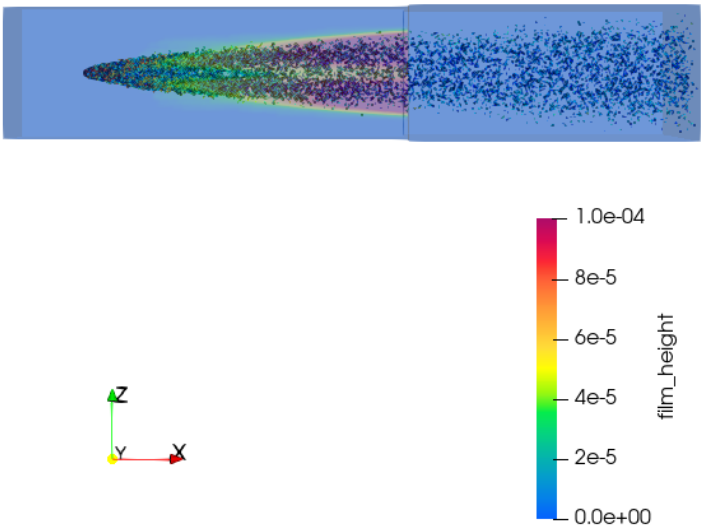

Figure 6.37: Results of droplets distribution and liquid film height inside the domain for Case 1 using k-ϵ turbulence closure model in the bottom view. The bifurcation of the droplets is observed by the absence of droplets in the central region. By illustrating the liquid film height it is possible to observe the influence of the impinging droplets on the liquid film height distribution.

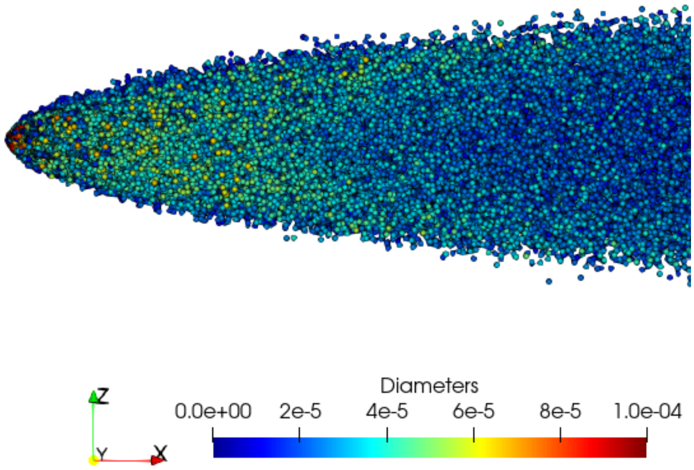

Figure 6.38: Results of droplets distribution inside the domain for Case 1 using $k-\omega\ SST$ turbulence closure model in the bottom view. Droplets are coloured by the size. A more evenly distribution without bifurcation was observed for this case. Smaller droplets are observed in the vicinity of the wall.

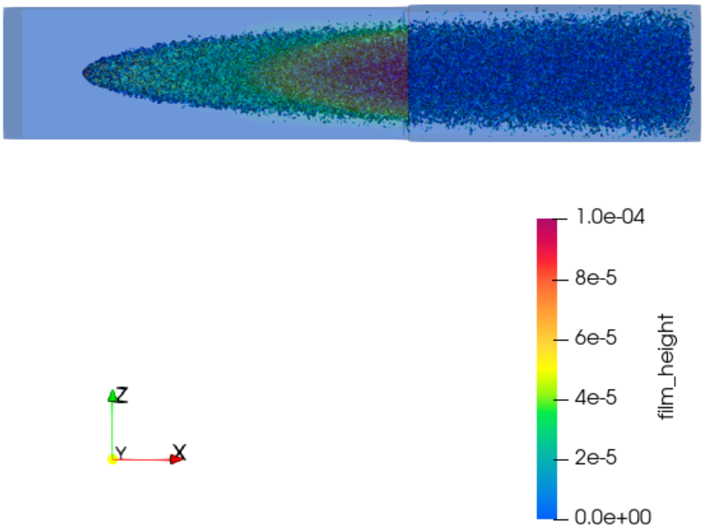

Figure 6.39: Results of droplets distribution and liquid film height inside the domain for Case 1 using $k-\omega\ SST$ turbulence closure model. By illustrating the liquid film height it is possible to observe the influence of the impinging droplets on the liquid film height distribution.

To visualise the impact of the flow field on the droplets distribution Figure 6.40 was generated for the k-ϵ turbulence closure model and Figure 6.41 for the $k-\omega\ SST$. From Figure

6.40 it is possible to note that for the k-ϵ model the gas flow penetrates into the mist of droplets and separates it into two columns. This separation culminates in the shape of the liquid film shape formed at the bottom of the computational domain. A different pattern is observed in Figure 6.41 for the $k - \omega\ SST$ model, in which no bifurcation is observed. On another hand, a much wider zone with low velocity is observed, which marks the presence of droplets, meaning that the area between the Lagrangian and Eulerian phases is expanded. With this expansion, the change of momentum between phases is intensified, and great part of the droplets is carried by the gas flow and do not hit the wall.

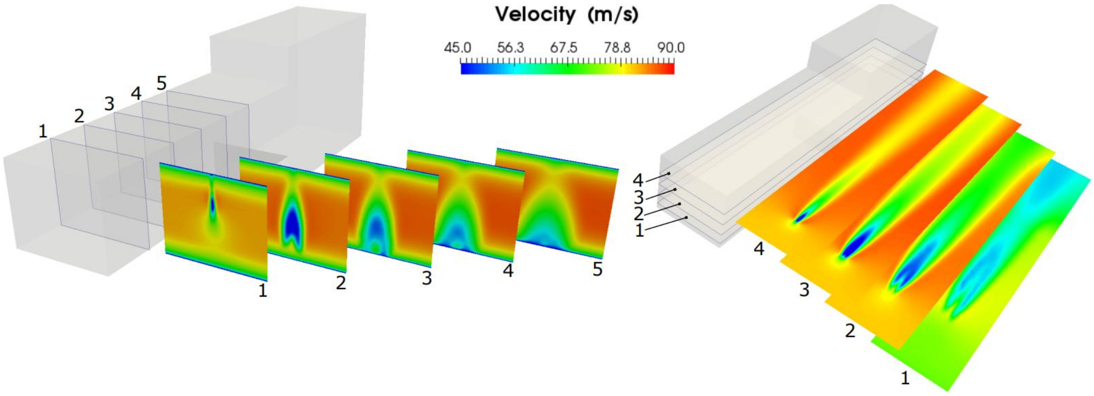

Figure 6.40: Air velocity field for Case 1 for the k-ϵ turbulence closure model. The planes are equally spaced between the injector and the edge for the image on the left and equally spaced between the top and the bottom for the image on the right. The bifurcation pattern is observed as the regions with low velocity represents regions with high concentration of droplets.

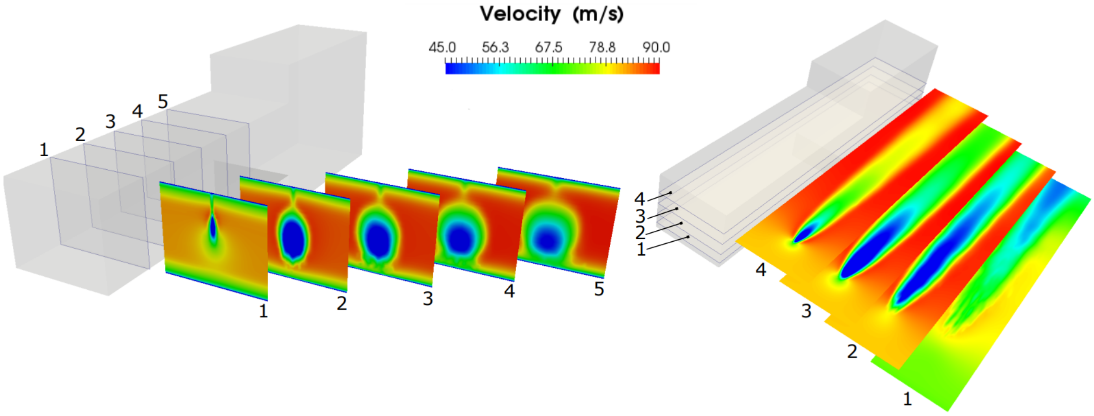

Figure 6.41: Air velocity field for Case 1 for the $k - \omega\ SST$ turbulence closure model. The planes are equally spaced between the injector and the edge for the image on the left and equally spaced between the top and the bottom for the image on the right. No bifurcation is observed. On another hand, a wider region with low velocity is observed.

Concerning the mass source term due to droplet impingement, Figure 6.42 illustrates the results for the k-ϵ model and Figure 6.43 for the $k - \omega\ SST$ model. In Figure 6.42 it is observed that the two columns generated by the penetration of the gas flow into the droplets mist generates two regions with stronger mass source intensity. A fixed scale was set for both figures for better comparison of the results. From the images, it is observed that the source term for mass is stronger for the k-ϵ model. On the other hand, the regions with high source term intensity do not lie on the centre-line.

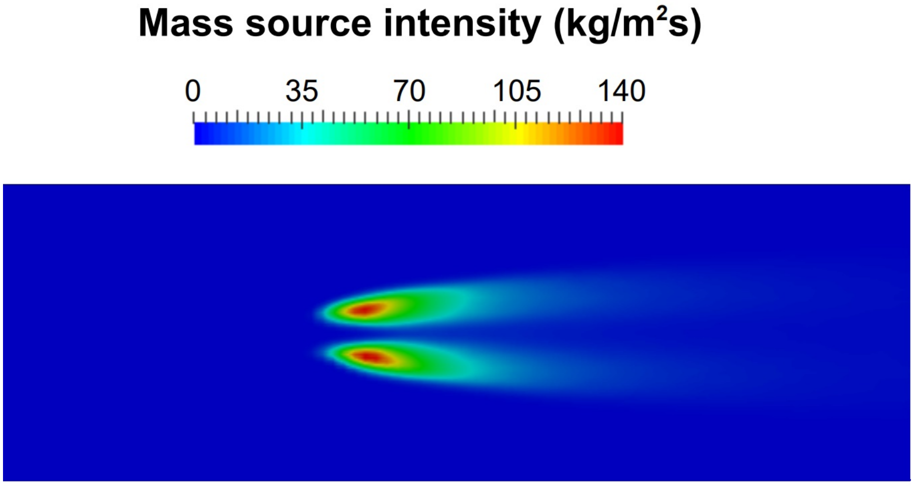

Figure 6.42: Mass source term distribution for Case 1 using tuned k-ϵ turbulence closure model. The image illustrates the stronger mass source intensity in the symmetrical regions away from the centre-line.

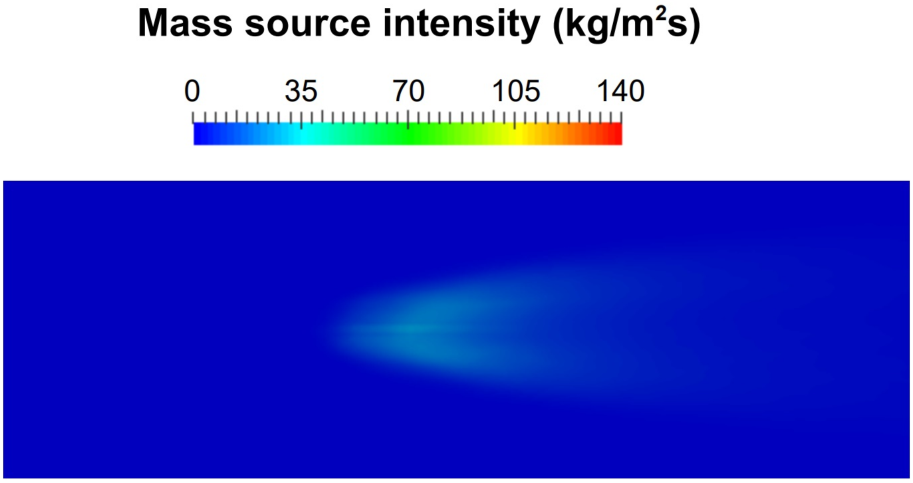

Figure 6.43: Mass source term distribution for Case 1 using $k - \omega\ SST$ turbulence closure model. Although the intensity is smaller than in the simulations using k-ϵ model, the image illustrates the concentration of the mass source over the centre-line.

Concerning the momentum source term due to droplet impingement, Figure 6.44 illustrates the results for the $k - \omega\ SST$ model in span-wise direction and in Figure 6.45 for the stream-wise direction. These results are strongly related to the velocity components as will be confirmed in the following paragraphs. It is interesting to note that the span-wise component of the momentum source is responsible for carrying the liquid film away from the centre-line. Note that the figures were generated with different scales, being the scale Figure 6.44 one order of magnitude smaller than Figure 6.45.

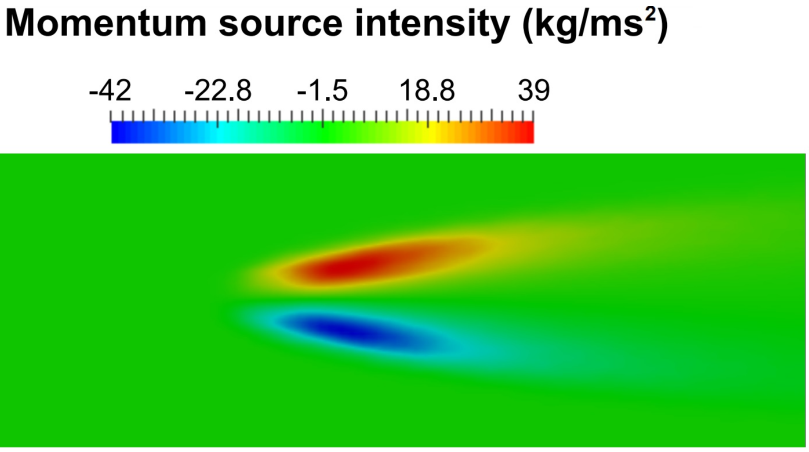

Figure 6.44: Momentum source term distribution in span-wise for Case 1 using $k - \omega\ SST$ turbulence closure model. The image illustrates the momentum source intensity in the symmetrical regions away from the centre-line. The span-wise source term is directly related to the liquid film velocity that spreads the liquid film in the same direction.

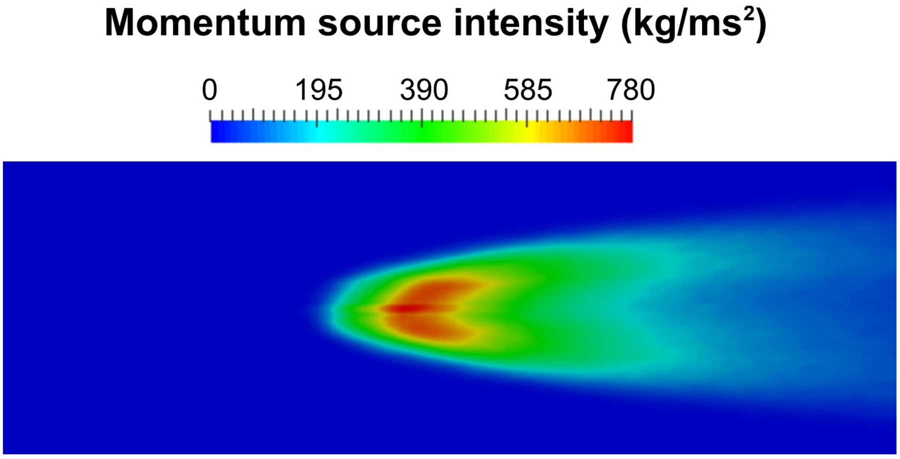

Figure 6.45: Momentum source term distribution in stream-wise direction for Case 1 using $k - \omega\ SST$ turbulence closure model. The image illustrates the concentration of the momentum source intensity over the centre-line. The stream-wise source term is directly related to the liquid film velocity that directs the flow towards the edge.

The results for the film velocity are presented in Figure 6.46 for the k-ϵ model and in Figure 6.47 for the $k - \omega\ SST$ model. These images help on the understanding of the liquid film thickness behaviour and the impact of the mass and momentum sources. Comparing the images it is possible to observe that the $k - \omega\ SST$ model has a lower velocity when compared to the k-ϵ model, and that the pattern of the velocity fields are similar to the observed for the momentum source intensity. It is also observed that the velocity field is weaker in the centre-line region for the k-ϵ turbulence model, presenting values close to null velocity. For the $k - \omega\ SST$ turbulence closure model simulations a slightly bifurcation is observed, however, its modulus is low and the liquid is not spread with high intensity in the span-wise direction. A different observation is made for the k-ϵ turbulence closure model simulations. It presents a high stream-wise velocity, advecting the liquid film towards the edge, causing an accumulation of liquid in that region.

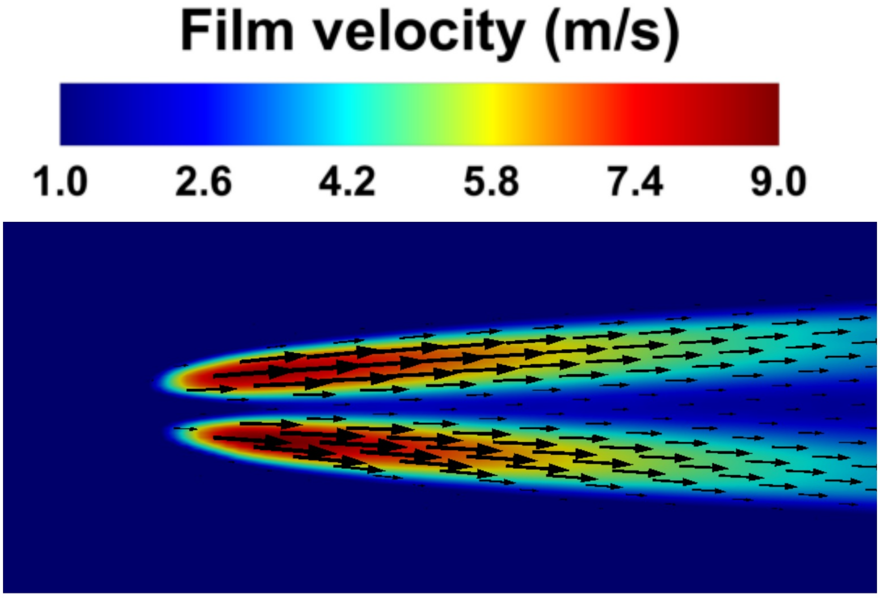

Figure 6.46: Averaged stream-wise film velocity field for Case 1 using k-ϵ turbulence closure model. The image illustrates the symmetrical velocity regions away from the centre-line. It is observed that the velocity along the centre-line is small compared to the regions away from it.

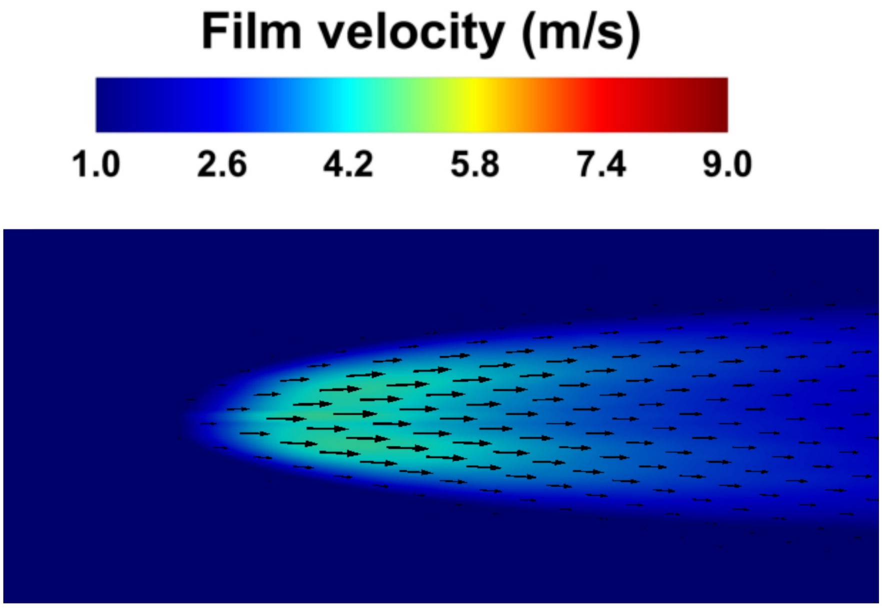

Figure 6.47: Averaged stream-wise film velocity field for Case 1 using $k - \omega\ SST$ turbulence closure model. The velocity field illustrated is weaker than the presented for k-ϵ model, and it is more concentrated over the centre-line.

To understand the role of the liquid jet velocity on the results, an analyses of Case 2 was carried out. Considering the simulation time of the frozen field with droplets, the time of operation was 7380.01 s for k-ϵ, 7316.28 s for tuned k-ϵ, and 23702.26 s for $k - \omega\ SST$. The number of droplets inside the domain was 6898 for k-ϵ, 7055 for tuned k-ϵ, and 121955 for $k - \omega\ SST$. Again, there are more secondary droplets for the $k - \omega\ SST$ case and also a longer time of operation. Comparing to Case 1, there are less droplets inside the domain, this fact is more significant for the k-ϵ models.

The results of film height using different turbulence closure models for Case 2 were acquired along the white line illustrated in Figure 6.27. These results are represented in Figure 6.48 with a comparison against physical experimentation data. It is observed that the liquid film formation for Case 2 is higher than for Case 1. The differences for the k-ϵ and the tuned k-ϵ in these cases are greater when compared to Case 1. The liquid film formation starts further from the injection x coordinate in the k-ϵ results and it also presented smaller results. The behaviour of the simulations after 20 mm started to deviate from the physical experimentation data. An important observation is that the physical experimentation data presented a dip in the film height prior to the edge, in a distance from the injector of approximately 22.5 mm. This behaviour was not predicted by any of the tested models. It is also observed that the deviations from the physical experimentation results were greater for Case 2 when compared to Case 1. As the droplets have a higher velocity when compared to Case 1, they reach the opposing wall in a region closer to the injector.

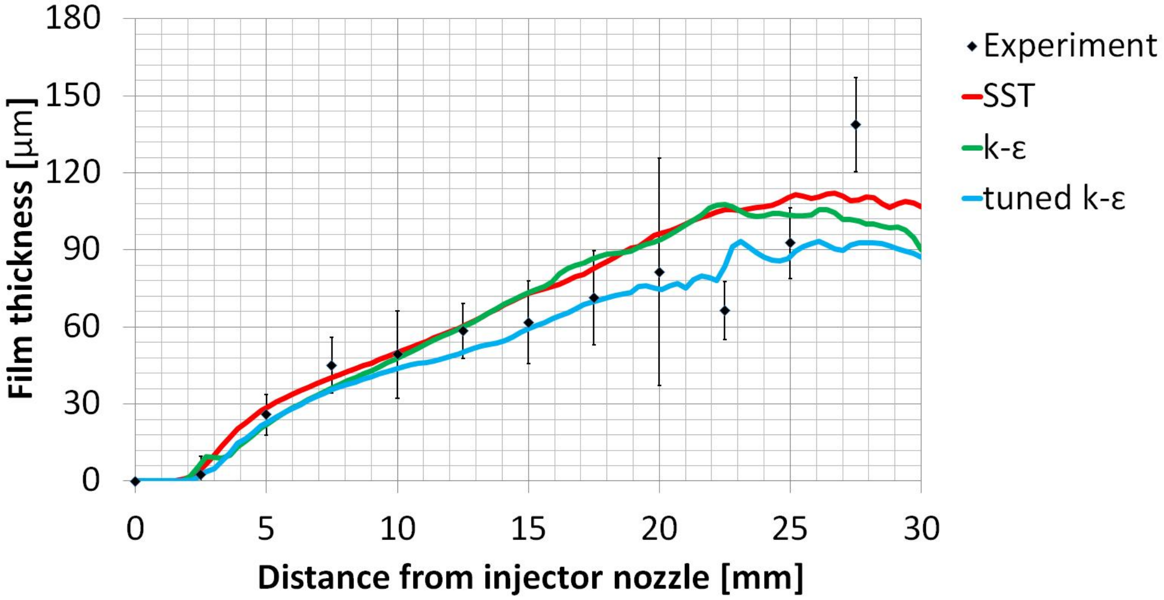

Figure 6.48: Results of averaged liquid film height for Case 2. The dots represent the physical experimentation data from Shedd et al. (2009a) and the lines represents different turbulence closure models used to simulate the Eulerian phase.

For Case 2, images of the liquid film are illustrated in Figure 6.49 for the k-ϵ, in Figure 6.50 for the tuned k-ϵ, and in Figure 6.51 for the $k-\omega\ SST$ model. On this images it is observed that the k-ϵ and the tuned k-ϵ behave similar, as also observed for Case 1. A similar behaviour was found for the $k-\omega\ SST$ case when compared to Case 1. The film liquid height for the $k-\omega\ SST$ model presented a different pattern from the other two models, with higher liquid films at the centre of the wall film. The other two tested models presented higher liquid films away from the centre line.

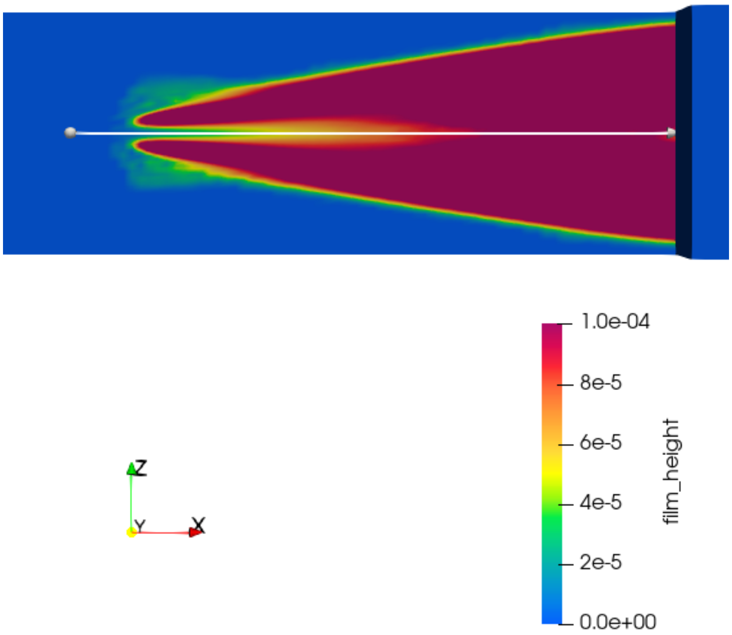

Figure 6.49: Results of averaged liquid film formed for Case 2 using k-ϵ turbulence closure model. The average liquid film height presents a similar shape as Case 1 with symmetry around the centre-line. These results also illustrates the bifurcation pattern observed in other k-ϵ simulations.

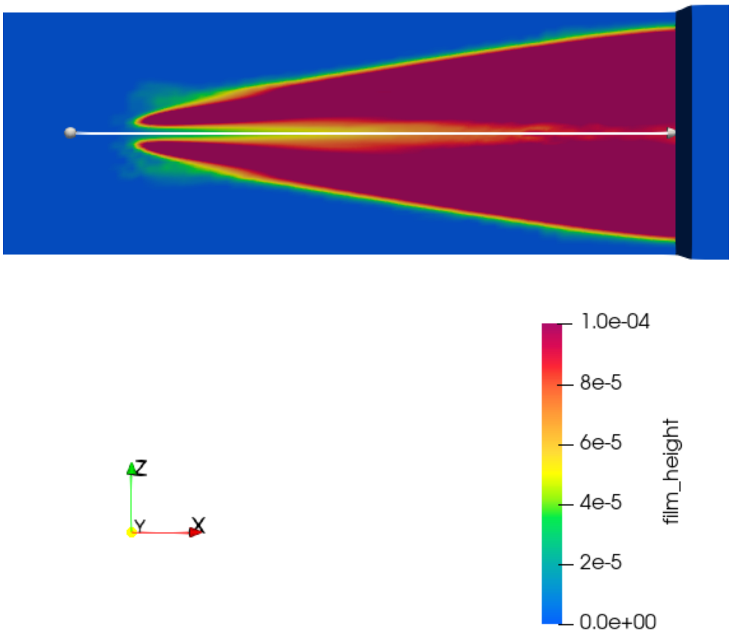

Figure 6.50: Results of averaged liquid film height for Case 2 using tuned k-ϵ turbulence closure model. The average liquid film height presents a similar shape as Case 1 with symmetry around the centre-line. These results also illustrates the bifurcation pattern observed in other k-ϵ simulations.

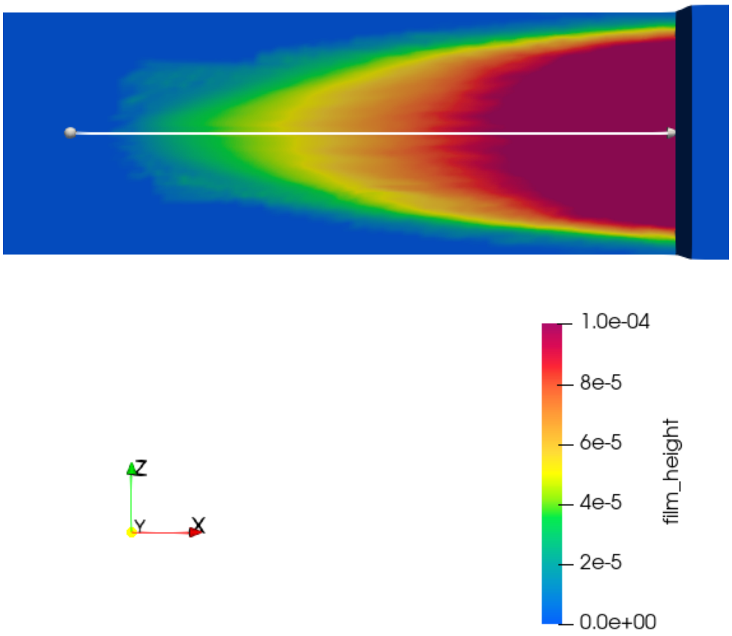

Figure 6.51: Results of averaged liquid film formed for Case 2 using $k-\omega\ SST$ turbulence closure model. The average liquid film height presents a similar shape as Case 1 with symmetry around the centre-line. These results also illustrates the film height concentration over the centre-line observed in Case 1.

A comparison with the work of Drennan et al. (2019) already presents the importance of choosing the right turbulence closure model to simulate the spray wall interaction. In his numerical results a peak was observed away from the centre line as presented in Figure 2.2. These peaks were not observed in the physical experimentation of Shedd et al. (2009a) nor in Figure 6.51 that represents the numerical results using $k-\omega\ SST$ turbulence closure model. It is important to note that in the work of Drennan et al. (2019) the RNG k-ϵ turbulence model was used.

Another important observation of this results is that the back flow of air was not observed nor the accumulation of liquid film near the edge, opposing the results found by Ingle et al. (2014) in Figure 2.1.

The main differences observed for Case 2 can be partly explained by the droplets behaviour in each case. The droplets are represented according for the different models, being Figure 6.52 for the k-ϵ, Figure 6.53 for tuned k-ϵ, and Figure 6.54 for $k-\omega\ SST$. The velocity is plotted for the Eulerian phase. It is observed that for the k-ϵ and tuned k-ϵ that the droplets distribution behaviour are similar. The results for the $k-\omega\ SST$ turbulence closure model presented more droplets at vertical positions along the domain.

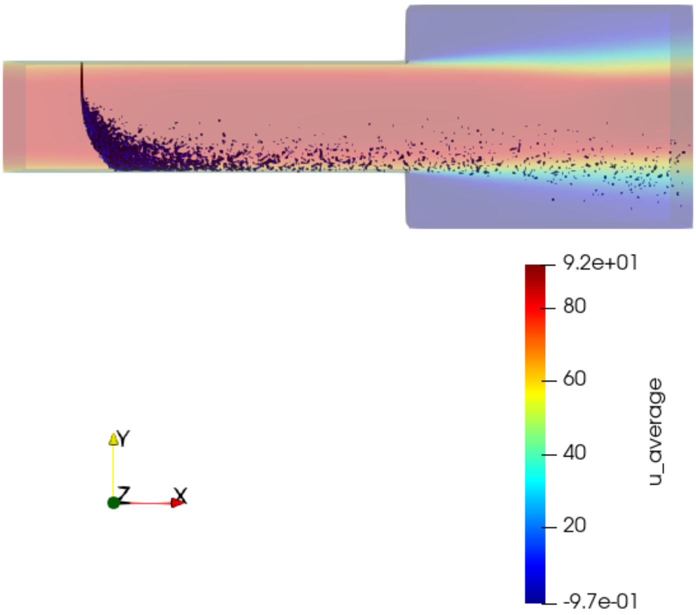

Figure 6.52: Results of droplets distribution inside the domain for Case 2 using k-ϵ turbulence closure model. Less droplets can be observed inside the computational domain, also occupying positions closer to the wall, thus, less droplets are carried by the gas phase.

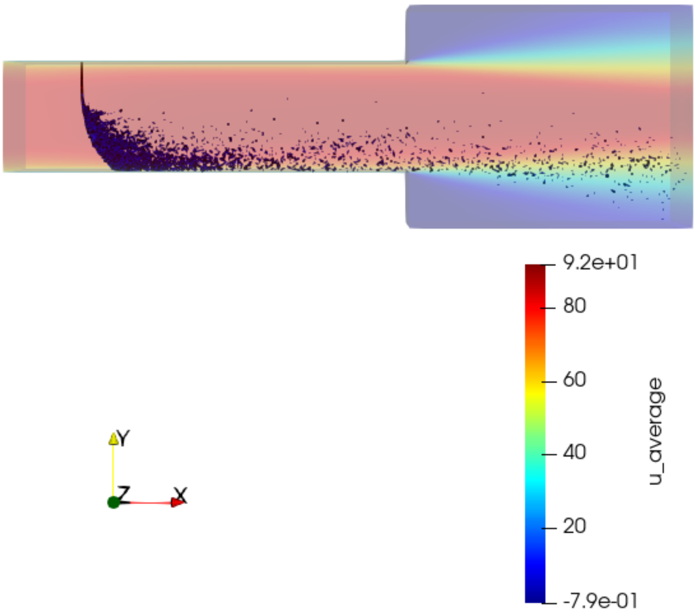

Figure 6.53: Results of droplets distribution inside the domain for Case 2 using tuned k-ϵ turbulence closure model. Less droplets can be observed inside the computational domain, also occupying positions closer to the wall, thus, less droplets are carried by the gas phase.

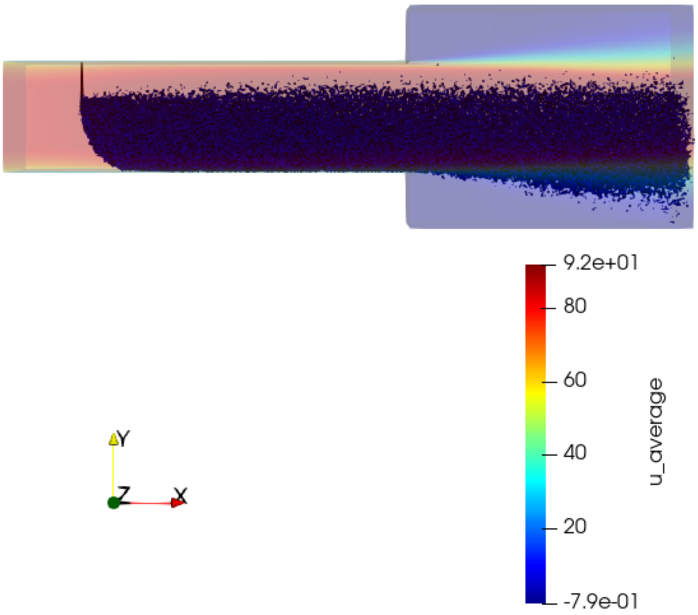

Figure 6.54: Results of droplets distribution inside the domain for Case 2 using $k - \omega\ SST$ turbulence closure model. More droplets can be observed inside the computational domain, also occupying higher positions, thus, more droplets are carried by the gas phase.

The results for Case 2 are very similar to Case 1. For the sake of brevity the images are not illustrated, instead a brief summary is presented. As the droplets have a higher momentum when compared to Case 1, the gas flow has a smaller affect in their trajectory, thus, Case 2 has a higher penetration of the droplets. Hence, more droplets reach the opposing wall forming a higher liquid film.

As the liquid jet increases its velocity, it slows down the gas flow in the centre region of the channel. With a smaller velocity, less droplets are carried out with the gas flow, therefore more droplets impinge on the wall. As more collisions occur, the liquid film height increases.

To verify the influence of the already mentioned parameters on the EWF model, the test cases were carried out using the $k - \omega\ SST$ turbulence closure model. This model was chosen because it presented the best results for liquid film formation.

6.3.2 Influence of number of parcels generated after break-up in the EWF numerical simulations

The second set of simulations test cases were for the number parcels generated during secondary breakup as represented in Figure 6.55 for Case 1 and Figure 6.56 for Case 2. For this test, the number of parcels generated during secondary break-up were changed from 10 to 20 parcels. As it is observed, for Case 1 the models behave very similar and only near the edge the simulation with 10 parcels presented a slight greater height than the simulation with 20 parcels. For Case 2 the differences were also small.

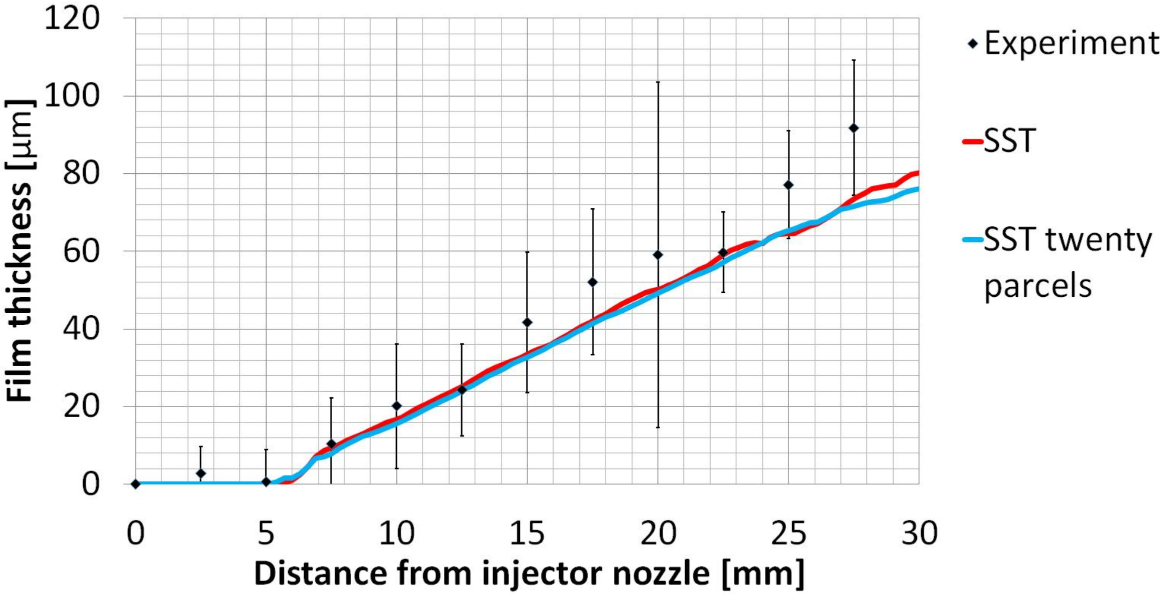

Figure 6.55: Number of parcels generated by secondary break-up test results for liquid film formation for Case 1 using $k-\omega\ SST$ model. The dots represent the physical experimentation data from Shedd et al. (2009a) and the lines represents different number of parcels generated during secondary break-up. The line in red represents 20 parcels generated and in blue 10 parcels. Very similar results were obtained.

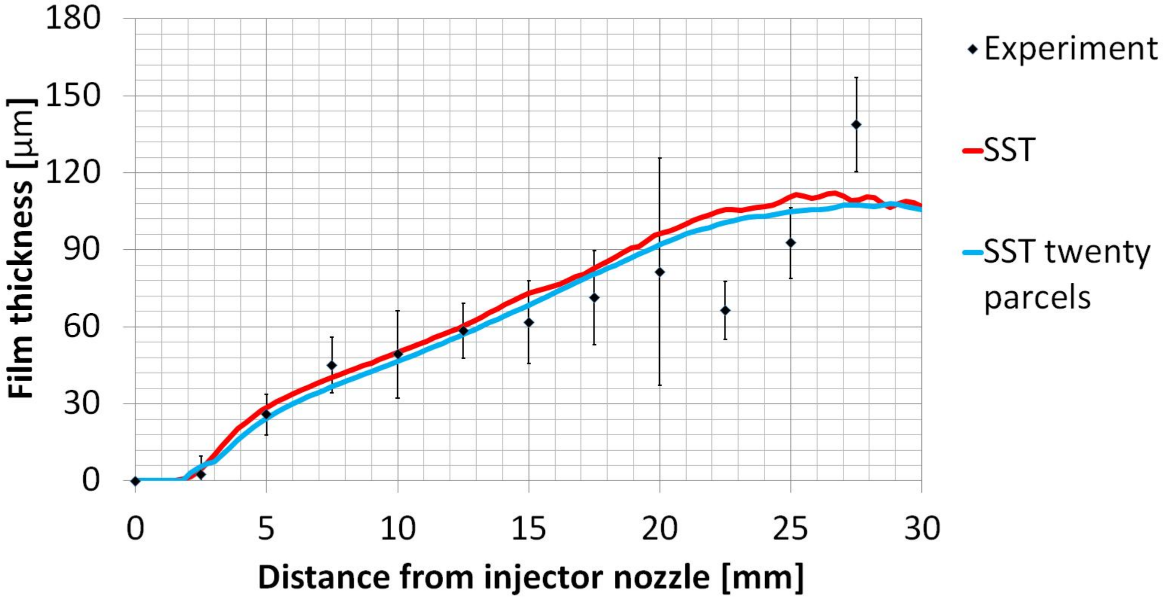

Figure 6.56: Number of parcels generated by secondary break-up test results for film liquid formation for Case 2 using $k - \omega\ SST$ model. The dots represent the physical experimentation data from Shedd et al. (2009a) and the lines represents different number of parcels generated during secondary break-up. The line in red represents 20 parcels generated and in blue 10 parcels. Very similar results were obtained.

6.3.3 Influence of length of the plate entrance in the EWF numerical simulations

The third set of simulations test cases were for the length of the plate entrance, which defines the entrance velocity profile. The results are represented in Figure 6.57 for Case 1 and in Figure 6.58 for Case 2. The simulation was changed from a plate entrance length of of 0.08 m for an entrance of 0.15 m. The case with 0.15 m illustrated better agreement than the case with 0.08 m of entrance length. For Case 1, the simulation with 0.15 m of plate entrance length presented a peak on the initial formation of liquid film, which not happened for the simulation with 0.08 m. For the regions close to the edge, a peak is also observed. For Case 2, an important observation is that the simulation with greater plate entrance length present a higher film liquid across the entire section, as also observed for Case 1.

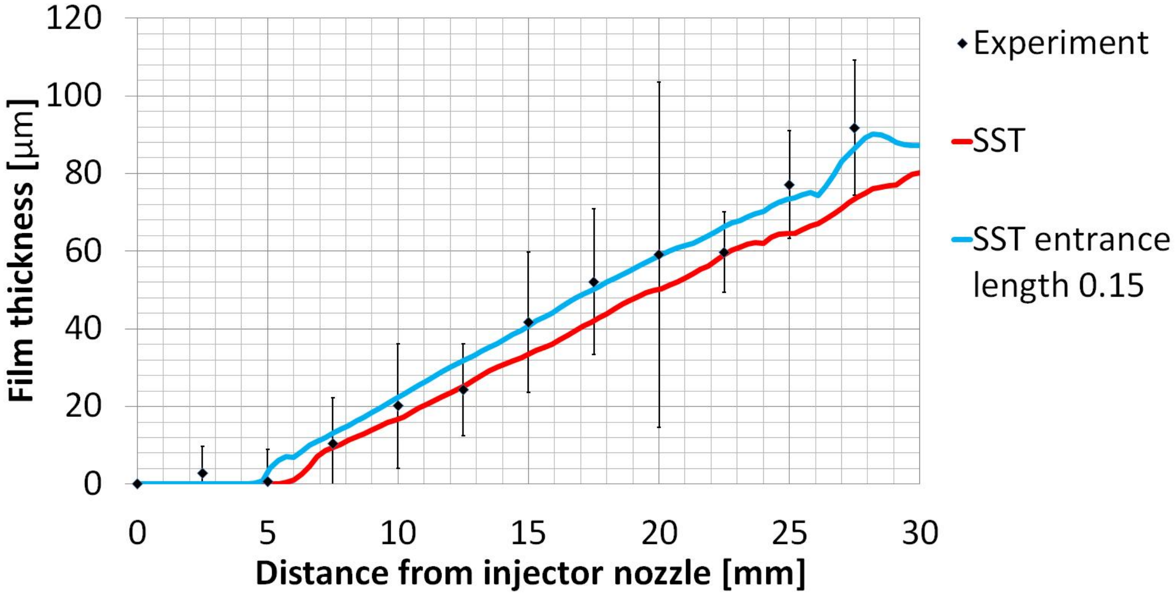

Figure 6.57: Entrance length test results for film liquid formation for Case 1. The dots represent the physical experimentation data from Shedd et al. (2009a) and the lines represents different entrance lengths. The red line represents an equivalence entrance length of 0.15 m and the blue line an equivalent length of 0.08 m. The bigger entrance length presented a greater film height, mostly due to its influence in the gas velocity, and consequently on the liquid film velocity.

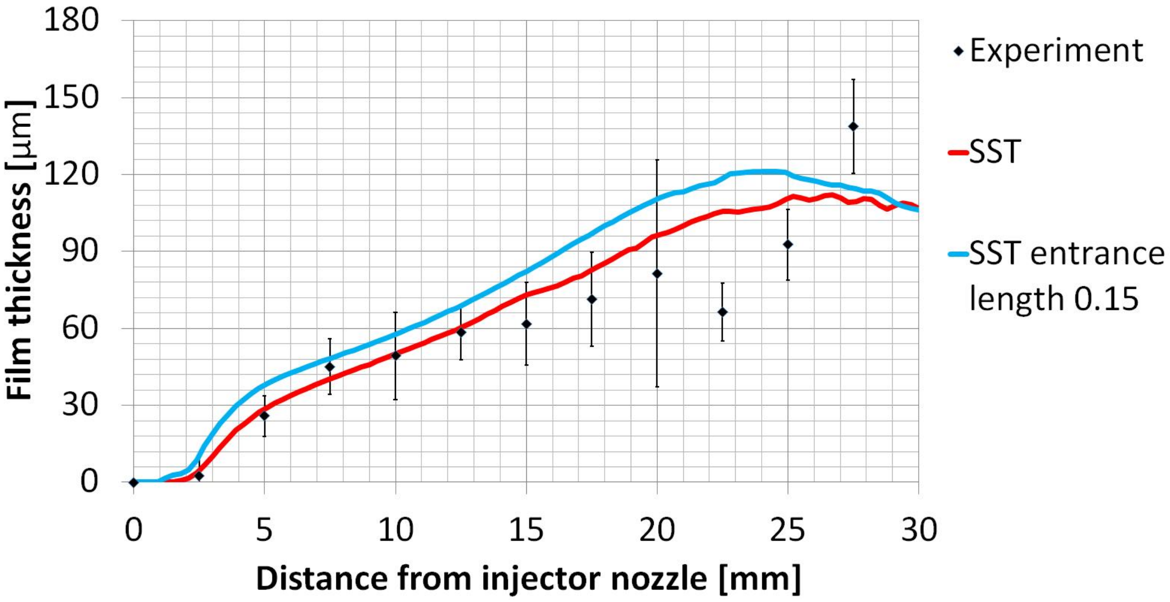

Figure 6.58: Entrance length test results for film liquid formation for Case 2. The dots represent the physical experimentation data from Shedd et al. (2009a) and the lines represents different entrance lengths. The red line represents an equivalence entrance length of 0.15 m and the blue line an equivalent length of 0.08 m. The bigger entrance length presented a greater film height, mostly due to its influence in the gas velocity, and consequently on the liquid film velocity.

This behaviour is due to the fact that with a longer entrance length the gas velocity is lower in the vicinity of the gas-liquid interface. As the gas velocity has an influence on the liquid film velocity by means of the shear force, the liquid film velocity is also slowed down. The stream-wise velocity is also decreased, which in turn decreases the liquid film transport in the same direction. With a smaller advection, the liquid accumulates, forming a higher liquid film along the plate. Figure 6.59 represents the liquid film velocity for the simulation with 80 mm of plate entrance length in Case 1, and Figure 6.60 with plate entrance length of 150 mm for Case 1. Observing the figures for Case 1, it is clearly noted that the liquid film velocity becomes smaller for a longer plate length entrance, observed by a more intense red colour in Figure 6.59. This observations can be extended for Case 2.

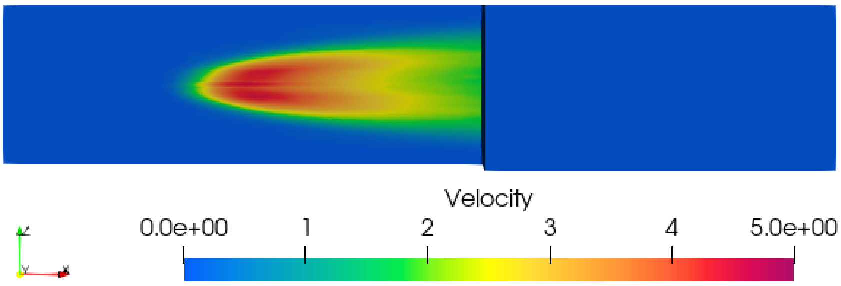

Figure 6.59: Results of averaged velocity for plate length entrance of 0.08 m (Case 1 using $k-\omega\ SST$ model). The image illustrates a more intense red colour, which means a higher velocity of liquid film, spreading the liquid film in a higher intensity manner, thus, generating a smaller liquid film height.

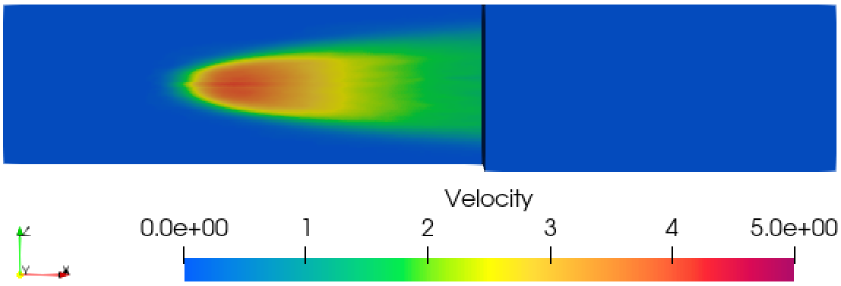

Figure 6.60: Results of averaged velocity for plate length entrance of 0.15 m (Case 1 using $k-\omega\ SST$ model). The image illustrates a less intense red colour, which means a smaller velocity of liquid film, spreading the liquid film in a less intensity manner, thus, generating a higher liquid film height.

6.3.4 Influence of source term for momentum in the EWF numerical simulations

The fourth set of simulation tests were carried out to illustrate the importance of the source term for momentum. The results for the simulation employing $k - \omega \; SST$ model in Case 1 without this source term are represented in blue in Figure 6.61 in comparison with the complete equation in red. From bottom to top the simulation represents the time growth. It is clear that without the source term the mass collected to form the liquid film does not spread as fast as with the source term for momentum. Although the liquid film is also transported by other forces such as pressure gradient, the liquid mass accumulates in the region where the droplets first impinge on the wall. For the simulations the film thickness do not converge, this effect highlights that the source term for momentum has a major role in the simulations.

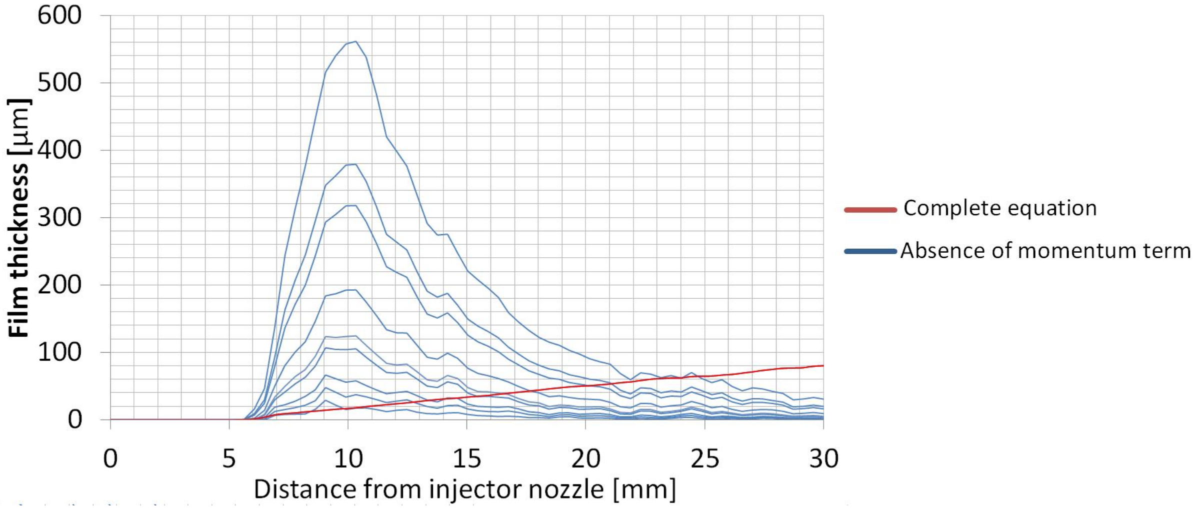

Figure 6.61: Results for the tests of source term for momentum for film liquid formation for Case 1 using $k - \omega \; SST$ model. The red line represents the simulation running with the complete model and the blue lines represent the model disregarding the momentum source term for droplet absorption. The lines from bottom to top represent ascendant time. It is observed that there is an accumulation of liquid film in the impacting region as the simulation time grows. The simulations did not converge for this case.

6.3.5 Influence of the width of the domain in the EWF numerical simulations

The fifth set of simulation tests were carried out with a larger mesh as presented in Figure 6.62. The results for film height on Case 1 are presented in Figure 6.63 in comparison with the results for the first mesh used and the experimental data. The results for film height distribution are illustrated in Figure 6.64. The differences are not very expressive, but around 25 mm, which is a region of large liquid film, a difference of 6 μm is found for the film height. Both of the simulations are inside the range of the experimental data being the larger mesh closer to the average of experimental data.

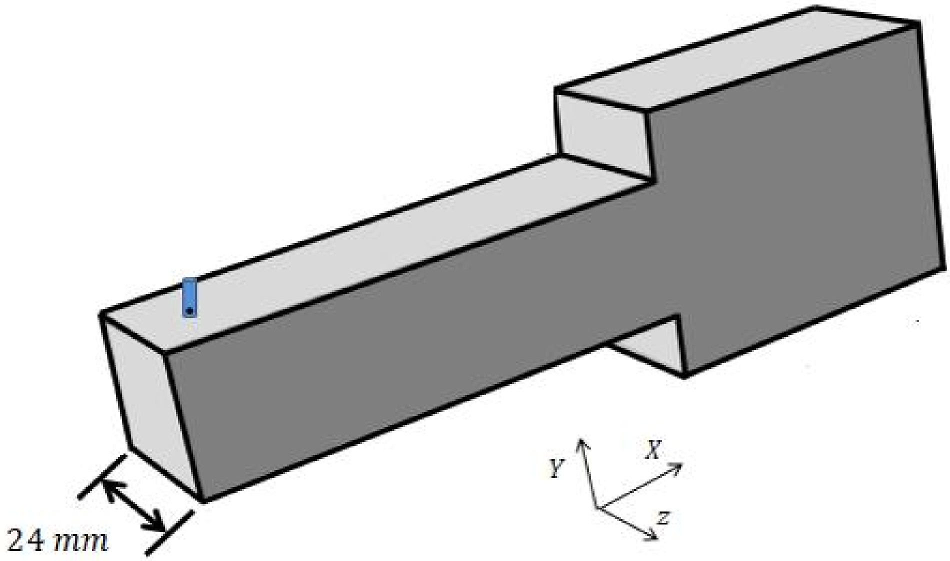

Figure 6.62: Larger computational domain for stability test (twice the width). This computational domain is used to run cross flow simulations with $k-\omega\ SST$ turbulence closure model.

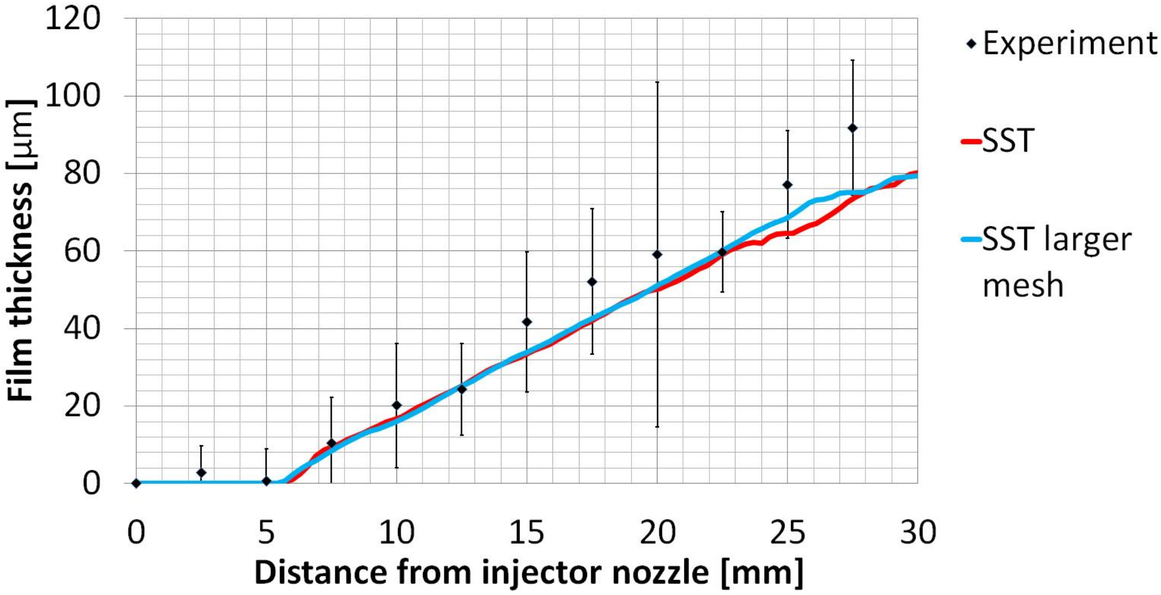

Figure 6.63: Larger mesh test results for film liquid formation for Case 1 using $k-\omega\ SST$ model. The dots represent the physical experimentation data from Shedd et al. (2009a), the red line represents the computational domain with 12 mm width, and the blue line with 24 mm width. The results presented similar behaviour.

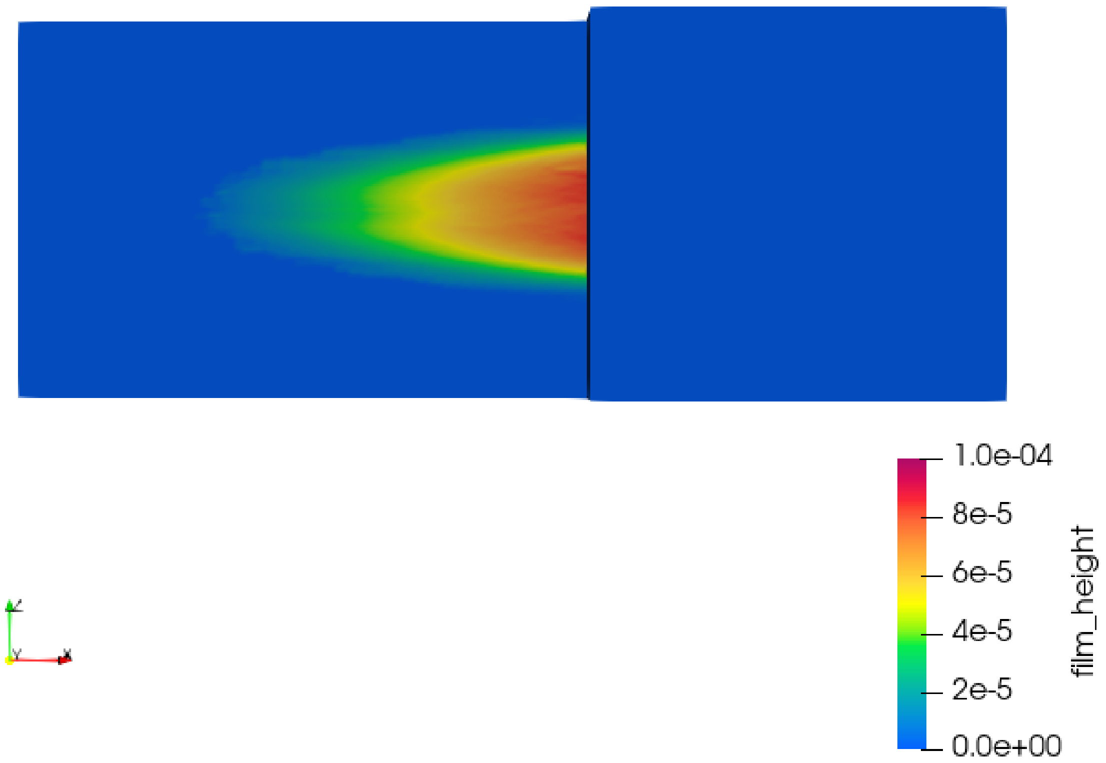

Figure 6.64: Results of averaged liquid film formed for Case 1 using $k - \omega\ SST$ turbulence closure model for the larger mesh stability test. Considering the region near the liquid film formation, the results presented similar behaviour as in the smaller computational domain.

The results for film height for Case 2 using the larger mesh are presented in Figure 6.65 in comparison with the results for the first mesh used and the experimental data. The results for film height distribution are illustrated in Figure 6.66 for the larger mesh. The differences are most expressive between 15 mm and 22 mm. The greatest difference found was of 8 μm for the film height. Both of the simulations are inside the range of the experimental data being the larger mesh closer to the average of experimental data. None of the tested cases could predict the dip o film height.

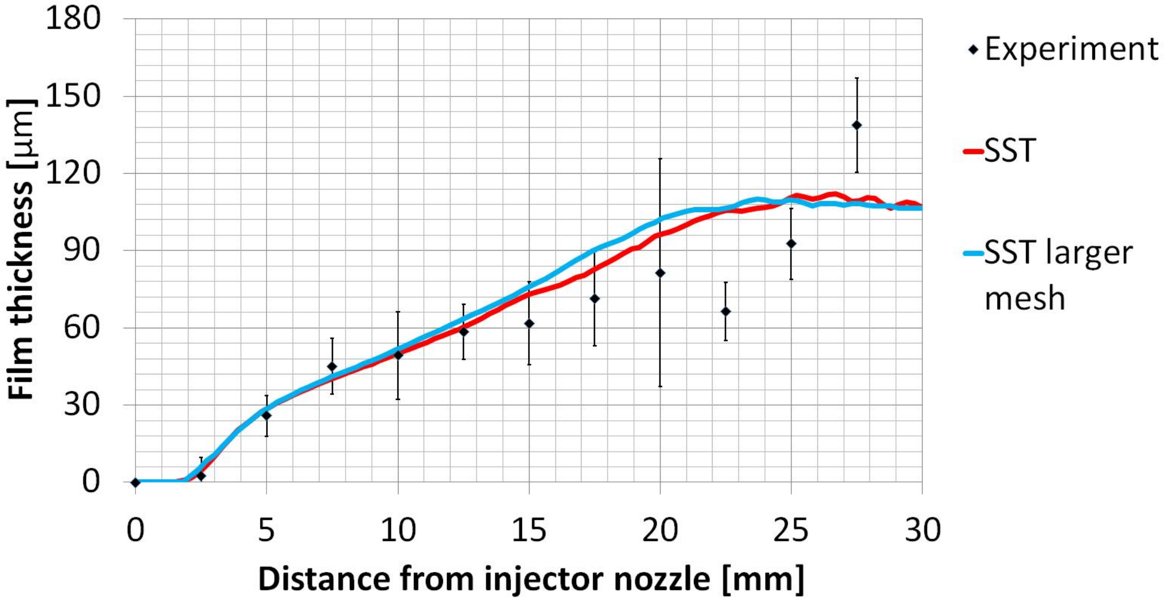

Figure 6.65: Larger mesh test results for film liquid formation for Case 2 using $k-\omega\ SST$ model. The dots represent the physical experimentation data from Shedd et al. (2009a), the red line represents the computational domain with 12 mm width, and the blue line with 24 mm width. The results presented similar behaviour.

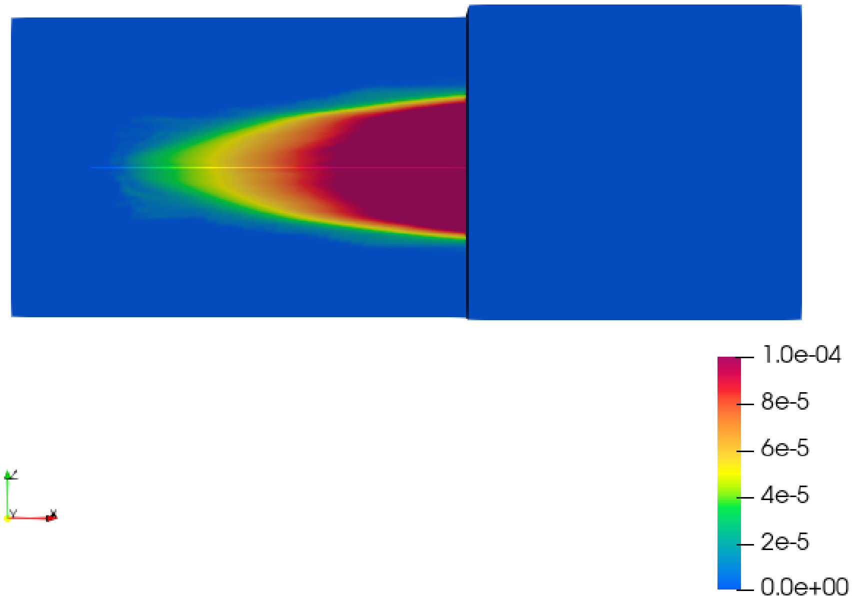

Figure 6.66: Results of averaged liquid film formed for Case 2 using $k-\omega\ SST$ turbulence closure model for the larger mesh stability test. Considering the region near the liquid film formation, the results presented similar behaviour as in the smaller computational domain

6.3.6 Influence of viscous shear force in the EWF numerical simulations

The sixth set of tests evaluates the viscous shear force, i.e. the role of the third term of the momentum conservation equation (Equation 3.46). For this case, the complete equations are analysed before disregarding the viscous forces. The main results are presented in Figure 6.67 for the $k-\omega\ SST$ model in the span-wise direction for Case 1, in Figure 6.68 for the $k-\omega\ SST$ model stream-wise direction for Case 1, Figure 6.67 for the $k-\omega\ SST$ model in the span-wise direction for Case 2, and in Figure 6.68 for the $k-\omega\ SST$ model stream-wise direction for Case 2. In the figures, the x and z components of the viscous shear vector field are illustrated. What stood out from these images is the fact that the viscous force is negative on the liquid film flow, which means that the gas flow in the region is slower than the liquid film. With that, the gas flow acts as a damping for the liquid, preventing it from spreading faster. As expected the viscous shear force is more intense for Case 2.

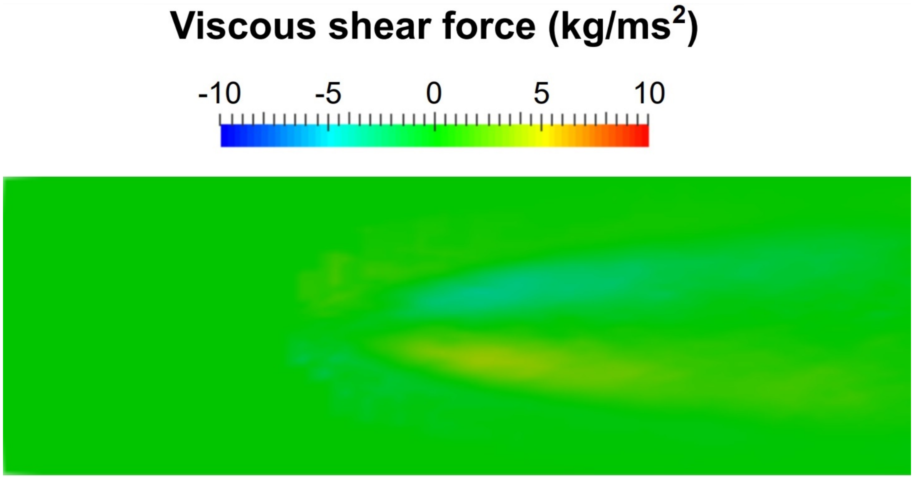

Figure 6.67: Viscous shear force distribution at the gas-liquid interface by employing the $k-\omega\ SST$ model in Case 1 in span-wise direction. The span-wise component was found to be in the direction of the centre-line, contributing for keeping the liquid film from spreading.

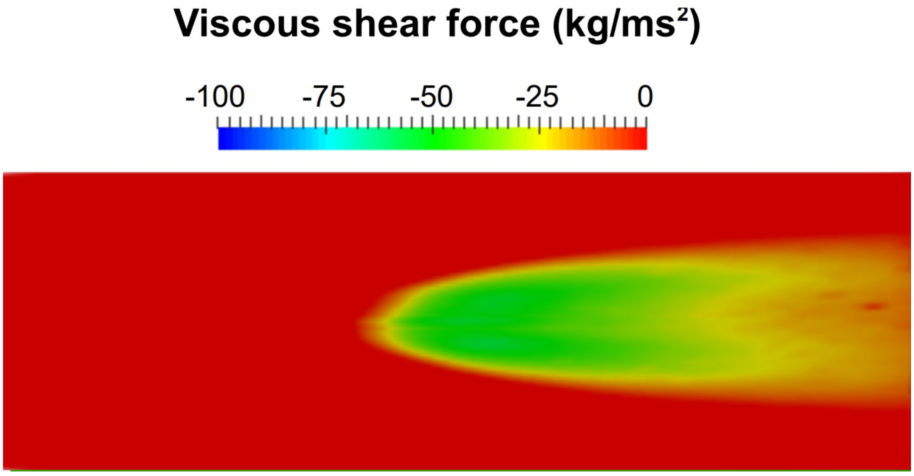

Figure 6.68: Viscous shear force distribution at the gas-liquid interface by employing the $k - \omega\ SST$ model in Case 1 in stream-wise direction. The stream-wise component was found to be negative, contributing for keeping the liquid film from spreading.

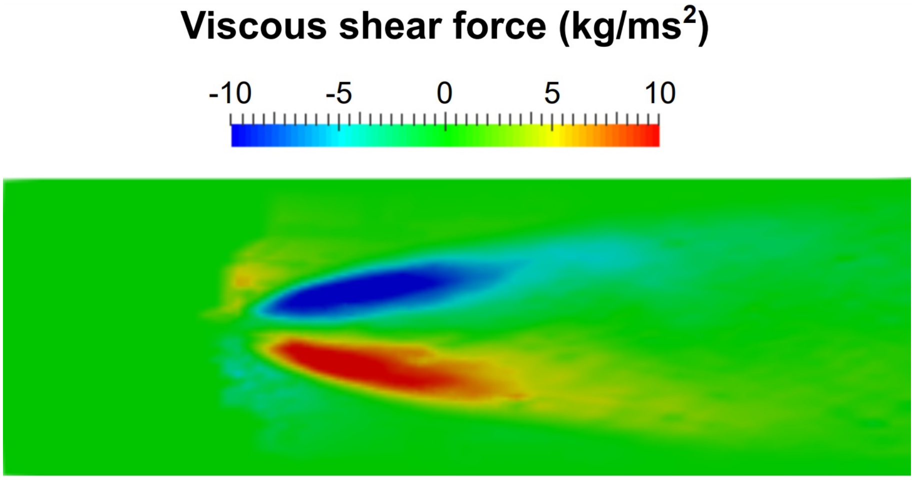

Figure 6.69: Viscous shear force distribution at the gas-liquid interface by employing the $k - \omega\ SST$ model in Case 2 in span-wise direction. The span-wise component was found to be in the direction of the centre-line, contributing for keeping the liquid film from spreading.

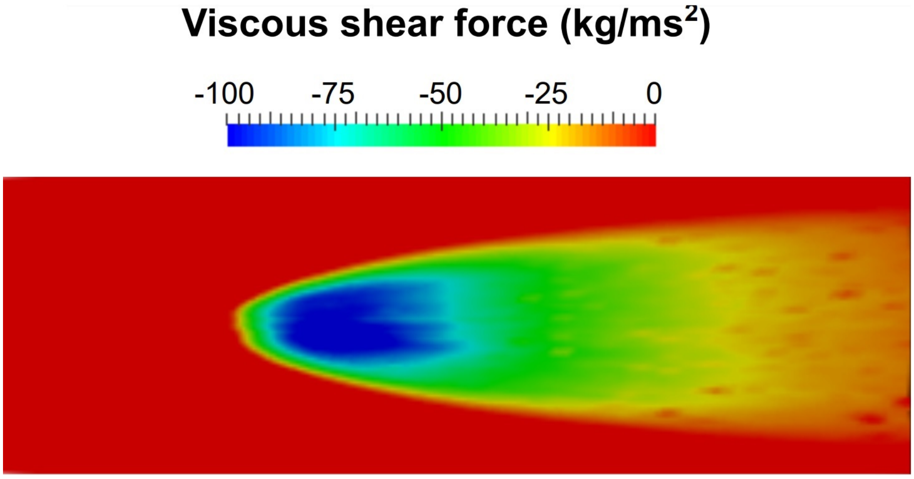

Figure 6.70: Viscous shear force distribution at the gas-liquid interface by employing the $k - \omega\ SST$ model in Case 2 in stream-wise direction. The stream-wise component was found to be negative, contributing for keeping the liquid film from spreading.

With the absence of the shear force, the liquid film tends to spread more rapidly, and so the height on the centre-line is smaller when compared with the simulations considering the shear stress. This comparison is illustrated in Figure 6.71 for the $k - \omega\ SST$ model in Case 1 and Figure 6.72 for the $k - \omega\ SST$ model in Case 2. As observed, in Case 2 the role of the shear stress is more important on preserving the film height when compared to Case 1. The role of the shear stress gradually increases along the centre-line in the direction of the edge. The difference is higher in Case 2.

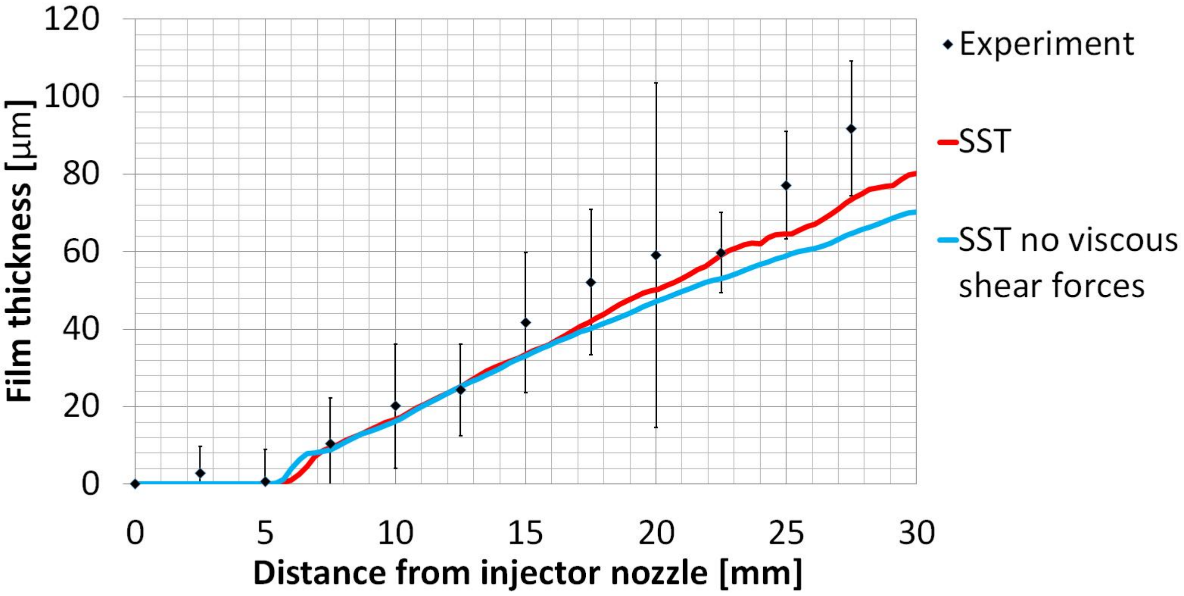

Figure 6.71: Effect of the shear stress at the gas-liquid interface for Cases 1 employing $k - \omega \ SST$ model. The results illustrates the relative importance of the shear stress on film momentum equation. In red is the results for the equations without the viscous shear forces, in blue is the results for the complete equations, and the dots are results from physical experimentation from Shedd et al. (2009a). It is observed that the shear stress helps preserve the film thickness at the centre-line.

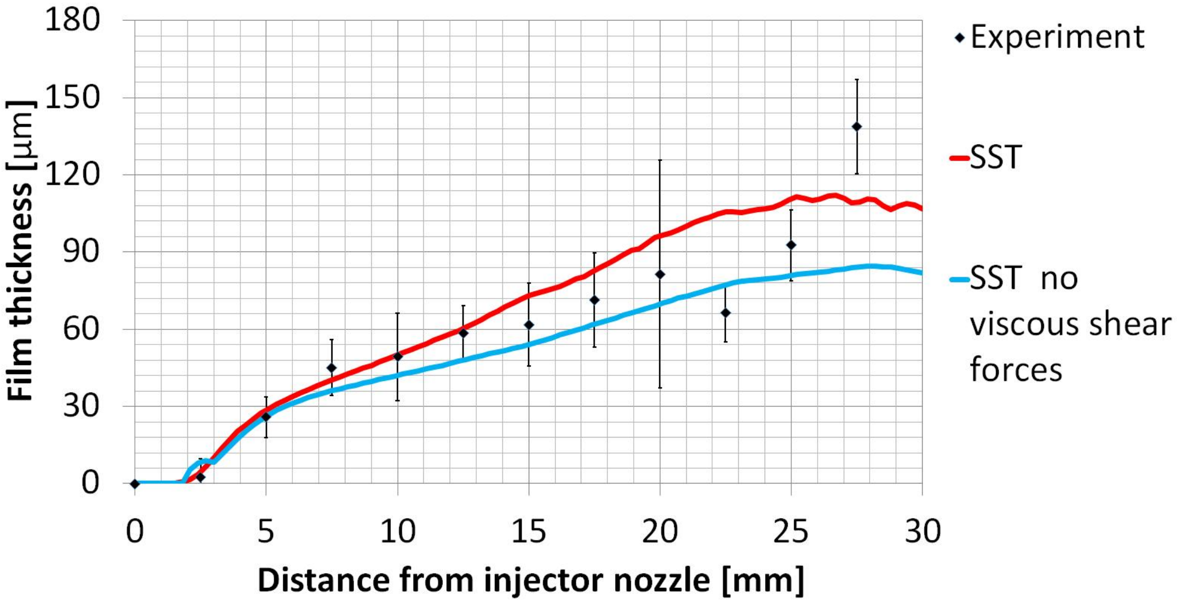

Figure 6.72: Effect of the shear stress at the gas-liquid interface for Cases 2 employing $k - \omega \ SST$ model. The results illustrates the relative importance of the shear stress on film momentum equation. In red is the results for the equations without the viscous shear forces, in blue is the results for the complete equations, and the dots are results from physical experimentation from Shedd et al. (2009a). It is observed that the shear stress helps preserve the film thickness at the centre-line. The impact of the shear stress is greater in Case 2 than in Case1.

6.3.7 Influence of phase coupling in the EWF numerical simulations

The seventh set of tests concerns the coupling between liquid and gas phases. In the one-way coupling the fluid affects the droplets, but the force that the droplets exert in the gas flow is not considered. As can be seen in Figure 6.73, which represents a simulation ran using the one-way coupling method for Case 1, no film is generated with this approach, as the droplets do not impinge on the opposing wall. A similar behaviour was observed in Case 2, thus the image is not presented. By means of the analysed image it was concluded that two-way coupling is fundamental for the phenomena in analyses.

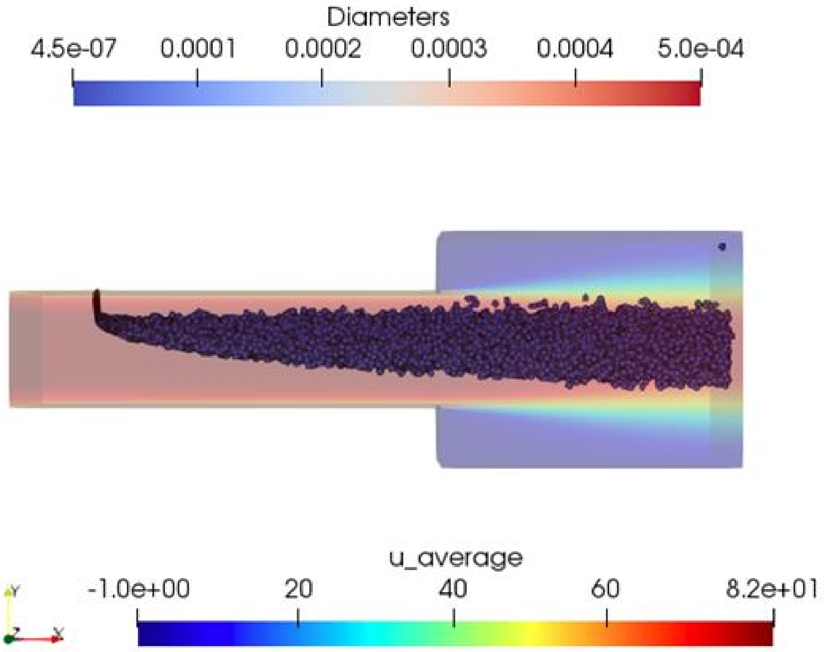

Figure 6.73: One-way coupling results using $k - \omega\ SST$ model for Case 1. No droplet impinges on the opposing wall, meaning that no liquid film was observed. This approach is not suitable for this case.

6.3.8 Influence of the size of the injected parcel in the EWF numerical simulations

The eighth set of simulations test cases were for the droplet size injected in the domain as represented in Figure 6.74 for Case 1 and Figure 6.75 for Case 2. For these tests, the droplet size was set as 0.25 mm instead of 0.5 mm. For Case 1, the test with half of the droplet size presented numerical results fitting better inside the experimental limits. The behaviour changed in the beginning of the liquid film formation, where the simulation with 0.25 mm of initial droplet size had a peak on the value of liquid film height. For Case 2, the behaviour of both simulations were similar. The region close to the edge of the wall film of the case with droplet size of 0.25 mm presented a greater liquid film height, which was closer to the experiment. In general, the results were very similar for the size of the injected droplet.

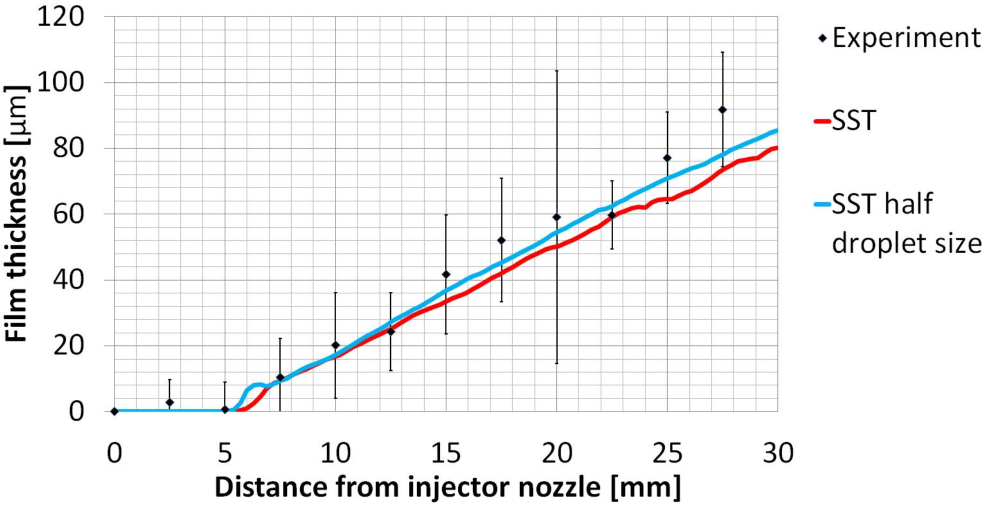

Figure 6.74: Droplet size test results for liquid film formation for Case 1 using $k-\omega\ SST$ model. The dots represent the physical experimentation data from Shedd et al. (2009a) and the lines represents different droplet sizes used to initialise the jet as Lagrangian phase. Red stands for 0.5 mm and blue for 0.25 mm. The results presented were very similar.

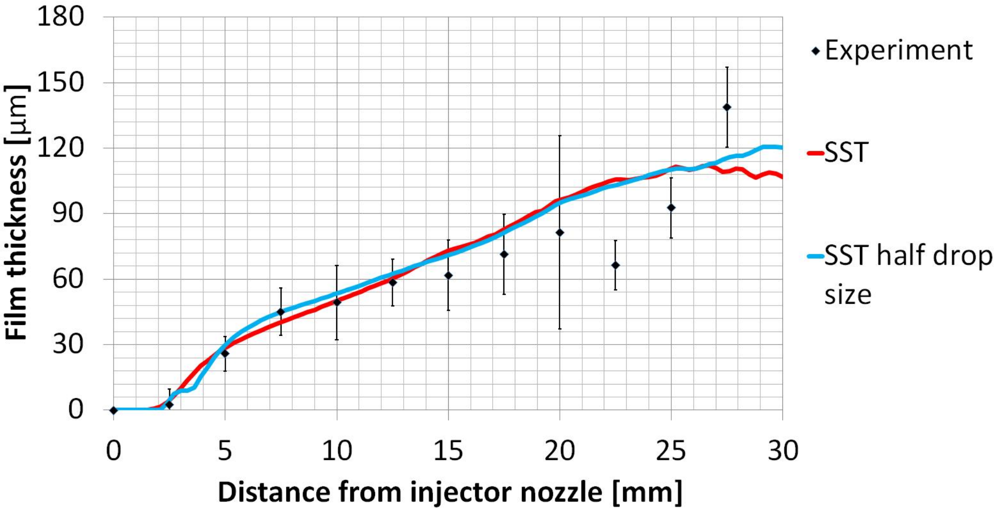

Figure 6.75: Droplet size test results for liquid film formation for Case 2 using $k-\omega\ SST$ model. The dots represent the physical experimentation data from Shedd et al. (2009a) and the lines represents different droplet sizes used to initialise the jet as Lagrangian phase. Red stands for 0.5 mm and blue for 0.25 mm. The results presented were very similar. The dip in liquid film height was not captured by any of the simulations.

7 Final Remarks

This chapter presents the main conclusions and suggestions for future works in two separate subsections. First the main conclusions are presented for the physical experimentation results, then for the VOF numerical results, and for the EWF numerical modelling. A subsection integrating the main conclusions for the different results obtained in the present work is presented. Then, the suggested future works are presented.

7.1 Conclusions

In former works the PLIC scheme outperformed the HRIC scheme in both accuracy of the results and simulation time as presented by de Lima et al. (2020). In that work the numerical simulation setup was based on the experiments of Oguz and Prosperetti (1990), which consisted in a droplet vertically impinging on a pool. To complete the analysis presented in that manuscript new physical experimentation was needed. The alignment of the flow has a direct impact on the results, then the new experimental test rig was design to miss-align the flow with the Cartesian mesh. Also, the experimentation developed was design so that the droplets impinge on a plate that was aligned with gravity. The droplets impinge on the wall at different impact angles and velocities to verify the influence of different parameters on the outcomes of the impact. These results were not found in previous works presented on the literature and the main findings are summarised as follows:

· Important observations were found in the experimental results. A correlation was found for the Scd and a non-dimensional pool size for different droplet sizes and impact angle.

· Regions where partial deposition was most likely to occur were found by means of physical experiments.

· A script was generated using Fiji and it is available for other users for modification and free use.

Using the new set of experiments the numerical setup for the VOF test cases could be assembled. For the simulations, the Volume of Fluid (VOF) method was used with two different schemes for the advection term of the VOF transport equations, namely, High-Resolution Interface Capturing (HRIC) and Piecewise-Linear Interface Calculation (PLIC). The simulations presented good agreement with experimental observations and were considered validated. The results were a further analysis of previous studies and the new findings are summarised as follows:

· The PLIC scheme can only be used in cases of flows considered incompressible as well as cases in which the energy and turbulence equations are not solved. The HRIC scheme does not have these limitations.

· As the PLIC scheme is a geometrical scheme, it can maintain a sharper interface than the HRIC scheme.

· For algebraic schemes, some numerical diffusion is expected due to the numerical approximation of the interface reconstruction as observed in the numerical results.

· The PLIC scheme was not able to predict the round shape of the droplets in a Cartesian mesh with an unaligned flow. This has a direct impact in the prediction of pool formation, which follows the shape of the droplet.

· For the cases presented, the PLIC scheme required a smaller time step. These results are opposed to the results presented in previous works for flows aligned with the Cartesian mesh.

Using the physical experiments of Shedd et al. (2009b) a numerical setup to simulate thin liquid film on a flat plate in a liquid jet in air cross-flow was built. The experiments involved several parameters which makes it a very complex phenomena with plenty of unanswered questions. With the implementation of the EWF method many opened questions were properly addressed in this work. Many parameters of the equations involving the studied phenomena were analysed to verify the influence of each one in the numerical results. These analysis are a great step to further the knowledge into the referred phenomenon, and the main findings of the EWF methodology in this work are summarised as:

· The EWF approximation for thin liquid films proved to be an accurate tool and did not require much time to simulate wall film formation in three dimensional meshes with a two-dimensional approach.

· Three different turbulence closure models were tested. The $k - \varepsilon$, the tuned $k - \varepsilon$ and the $k - \omega\ SST$ models. In general the $k - \omega\ SST$ model presented better results in the current numerical simulations.

· Although none of the results could predict the dip presented in the physical experimentation in case 2, numerical results were validated against physical experimentation, presenting good agreement.

· The momentum source term was proven to be the most important in the equations implemented for the simulations. Without this term the simulations did not converge.

· The influence of the two way coupling was highlighted by the fact that without it, the droplets were not able to reach the opposite wall.

· An interesting observation was that the shear forces act in holding the liquid film.

7.1.1 General conclusions

The main purpose of the current thesis was to analyse the most modern techniques to predict film formation behaviour. An extensive overview of different methodologies was presented. With the lack of results available on the literature to validate the methods, a physical test rig was designed. The results found were used to improve the algorithm used for the VOF calculations. To validate the EWF modelling, results available on the literature were used.

Each of the evaluated techniques have their importance in engineering tasks. As the VOF methodologies require more computational time than the EWF approaches, they are used to solve cases that involves smaller computational domains as well as deepen the knowledge in phenomena involving multi phase flows. The numerical results of these type of simulations can even be used to further develop numerical tools such as the EWF techniques.

As the EWF method requires less computational time for the simulations than the VOF method, it can be used to solve more realistic engineering tasks. As an example, the flow inside a turbine combustion chamber can be predicted by these modelling, helping on a faster optimisation of the design.

Currently under development there are also hybrid approaches. Those approaches combine the best of each technique. Regions of the flow in which the VOF technique is required are modelled as such. Regions in which this technique becomes unfeasible due to simulation time or mesh refinement, such as break-up of the liquid jet, the liquid portion of the VOF is then converted into Lagrangian clusters of droplets, which can be further converted in liquid film on the EWF method.

Although further evaluation is still required in order to cover a broader range of cases and a wider variety of numerical approaches, an important step was taken in the present work towards a better understanding of liquid film dynamics and improvement on numerical techniques.

7.2 Future works

During the development of this work, and based on the experience gained, some points were identified in which continued research can bring good development to science and engineering. These points are summarised below:

· Physical experimentation with controlled temperature and vibration are needed to further develop the experimental results.

· Some improvements need to be made to the model so that it can correctly reproduce the striping outcome for wall collision in VOF simulations.

· The Inlaid mesh currently under development requires adjustments to allow PLIC scheme simulations to run.

· Sharpening equations can be coupled with HRIC scheme to suppress numerical diffusion.

· New physical experimentation is needed to further investigate the dip in case 2 for EWF modelling. With this new data the model can be adjusted and correctly predict the thin liquid film formation.

· The interaction with the secondary flow needs to be implemented and validated. This step is important in order to consider break-up of liquid films on the numerical simulations.

REFERENCES

Akop, M.Z., Zama, Y., Furuhata, T., Arai, M., 2013a. Characteristics of adhesion of diesel fuel on impingement disk wall. part 1: effect of impingement area and inclination angle of disk. Atomization and Sprays 23.

Akop, M.Z., Zama, Y., Furuhata, T., Arai, M., 2013b. Experimental investigations on adhered fuel and impinging diesel spray normal to a wall. Atomization and Sprays 23.

Akop, M.Z., Zama, Y., Furuhata, T., Arai, M., 2014a. Characteristics of adhesion diesel fuel on an impingement disk wall part 2: Droplet weber number and adhered fuel mass. Atomization and Sprays 24.

Akop, M.Z., Zama, Y., Furuhata, T., Arai, M., 2014b. Characteristics of adhesion diesel fuel on an impingement disk wall. part 3: ambient pressure effect. Atomization and Sprays 24.

Al-Roub, M., Farrell, P.V., Senda, J., 1996. Near wall interaction in spray impingement. SAE transactions , 1304–1318.

Andreassi, L., Ubertini, S., Allocca, L., 2007. Experimental and numerical analysis of high pressure diesel spray–wall interaction. International journal of multiphase flow 33, 742–765.

Arienti, M., Madabhushi, R., Van Slooten, P., Soteriou, M., 2006. Aerodynamic blockage effect on the spray characteristics of a liquid jet atomized by crossflowing air, in: Turbo Expo: Power for Land, Sea, and Air, pp. 467–476.

Arienti, M., Soteriou, M., 2007. Dynamics of pulsed jet in crossflow, in: Turbo Expo: Power for Land, Sea, and Air, pp. 629–640.

Arienti, M., Wang, L., Corn, M., Li, X., Soteriou, M., Shedd, T., Herrmann, M., 2011. Modeling wall film formation and breakup using an integrated interface-tracking/discrete-phase approach. Journal of Engineering for Gas Turbines and Power 133.

Asgari, B., Amani, E., 2021. An improved spray-wall interaction model for eulerian-lagrangian simulation of liquid sprays. International Journal of Multiphase Flow 134, 103487.

Bai, C., Gosman, A., 1995. Development of methodology for spray impingement simulation. SAE transactions , 550–568.

Bai, C., Gosman, A., 1996. Mathematical modelling of wall films formed by impinging sprays. SAE transactions , 782–796.

Baleta, J., Vujanović, M., Pachler, K., Duić, N., 2015. Numerical modeling of urea water based selective catalytic reduction for mitigation of nox from transport sector. Journal of Cleaner Production 88, 280–288.

Baumgarten, C., 2006. Mixture formation in internal combustion engines. Springer Science & Business Media.

Boussinesq, J., 1877. Essai sur la théorie des eaux courantes. Impr. nationale.

Bussmann, M., Chandra, S., Mostaghimi, J., 2000. Modeling the splash of a droplet impacting a solid surface. Physics of fluids 12, 3121–3132.

Chaussonnet, G., Riber, E., Vermorel, O., Cuenot, B., Gepperth, S., Koch, R., 2013. Large eddy simulation of a prefilming airblast atomizer. ILASS .

Chen, B., Li, J., Mao, F., Tian, R., 2019. Numerical study on the characteristics of single wetted flat wire with single droplet impact under the disturbance of airflow. Nuclear Engineering and Design 345, 74–84.

Dahms, R.N., Oefelein, J.C., 2016. The significance of drop non-sphericity in sprays. International Journal of Multiphase Flow 86, 67–85.

Diez, J., Gratton, R., Thomas, L., Marino, B., 1994. Laplace pressure driven drop spreading. Physics of Fluids 6, 24–33.

Dos Santos, V.F., de Souza, F.J., Duarte, C.A.R., 2016. Reducing bend erosion with a twisted tape insert. Powder Technology 301, 889–910.

Drennan, S.A., Kumar, G., Akin, B., 2019. Fundamental pre-filming atomizer performance predictions with autonomous meshing, in: AIAA Scitech 2019 Forum, p. 1736.

Duarte, C.A.R., Duarte, L.E.R., de Lima, B.S., de Souza, F.J., 2020a. Performance of an optimized k- turbulence model for flows around bluff bodies. Mechanics Research Communications 105, 103518.

Duarte, C.A.R., de Souza, F.J., 2017. Innovative pipe wall design to mitigate elbow erosion: A cfd analysis. Wear 380, 176–190.

Duarte, C.A.R., de Souza, F.J., 2021. Dynamic mesh approaches for eroded shape predictions. Wear 484, 203438.

Duarte, C.A.R., de Souza, F.J., dos Santos, V.F., 2015. Numerical investigation of mass loading effects on elbow erosion. Powder Technology 283, 593–606.

Duarte, C.A.R., de Souza, F.J., dos Santos, V.F., 2016. Mitigating elbow erosion with a vortex chamber. Powder Technology 288, 6–25.

Duarte, C.A.R., de Souza, F.J., de Vasconcelos Salvo, R., dos Santos, V.F., 2017. The role of inter-particle collisions on elbow erosion. International journal of multiphase flow 89, 1–22.

Duarte, C.A.R., de Souza, F.J., Venturi, D.N., Sommerfeld, M., 2020b. A numerical assessment of two geometries for reducing elbow erosion. Particuology 49, 117–133.

Ebner, J., Schober, P., Schafer, O., Koch, R., Wittig, S., 2004. Modelling of shear-driven liquid wall films: effect of accelerated air flow on the film flow propagation. Progress in Computational Fluid Dynamics, an International Journal 4, 183–190.

Ferrão, I., Barata, J.M., Silva, A., 2019. A study of a single droplet impinging onto a sloped surface: Jet-fuel and biofuel mixtures, in: ILASS 2019-29th European Conference on Liquid Atomization and Spray Systems.

Ferziger, J.H., Perić, M., 2002. Computational methods for fluid dynamics. volume 3. Springer.

Finotello, G., 2019. Droplet collision dynamics in a spray dryer: experiments and simulations .

Fontes, D.H., Duarte, C.A.R., de Souza, F.J., 2018a. Numerical simulation of a water droplet splash: Effects of density interpolation schemes. Mechanics Research Communications 90, 18–25.

Fontes, D.H., Vilela, V., de Souza Meira, L., de Souza, F.J., 2019. Improved hybrid model applied to liquid jet in crossflow. International Journal of Multiphase Flow 114, 98–114.

Fontes, D.H., et al., 2018b. Estudo numérico de jato líquido em escoamento cruzado usando uma abordagem híbrida .

Foucart, H., Habchi, C., Le Coz, J., Baritaud, T., 1998. Development of a three dimensional model of wall fuel liquid film for internal combustion engines. SAE transactions , 60–73.

FREIRE, A., ILHA, A., COLAÇO, M., 2006. Simulação numérica de escoamentos complexos–turbulência. 5ª ESCOLA DE PRIMAVERA EM TRANSIÇÃO E TURBULÊNCIA , 405–466.

Haselbacher, A., Najjar, F.M., Ferry, J.P., 2007. An efficient and robust particle-localization algorithm for unstructured grids. Journal of Computational Physics 225, 2198–2213.

Herrmann, M., 2008. A balanced force refined level set grid method for two-phase flows on unstructured flow solver grids. Journal of computational physics 227, 2674–2706.

Heywood, J.B., 1988. Internal combustion engine fundamentals .

Himmelsbach, J., Noll, B., Wittig, S., 1994. Experimental and numerical studies of evaporating wavy fuel films in turbulent air flow. International journal of heat and mass transfer 37, 1217–1226.

Ingle, R., Yadav, R., Punekar, H., Cao, J., 2014. Modeling of particle wall interaction and film transport using eulerian wall film model, in: ASME 2014 Gas Turbine India Conference, American Society of Mechanical Engineers Digital Collection.

Issa, R.I., 1986. Solution of the implicitly discretised fluid flow equations by operator-splitting. Journal of computational physics 62, 40–65.

Keshavarzi, G., Yeoh, G.H., Barber, T., 2013. Comparison of the vof and clsvof methods in interface capturing of a rising bubble. The Journal of Computational Multiphase Flows 5, 43–55.

Kiura, T., Shedd, T.A., Blaser, B.C., 2009. Investigation of spray evaporation and numerical model applied for fuel-injection small engines. SAE International Journal of Engines 1, 1402–1409.

Kuhnke, D., 2004a. Spray/wall interaction modelling by dimensionless data analysis. Shaker.

Kuhnke, D., 2004b. Spray/Wall-interaction Modelling by Dimensionless Data Analysis. Ph.D. thesis. Darmstadt University of Technology. Darmstadt.

Lesieur, M., 2008. Introduction to turbulence in fluid mechanics. Turbulence in Fluids: Fourth Revised and Enlarged Edition , 1–23.

Li, L., Green, S.I., Davy, M.H., Eadie, D.T., 2010a. Viscoelastic air-blast sprays in a cross-flow. part 1: Penetration and dispersion. Atomization and Sprays 20.

Li, L., Green, S.I., Davy, M.H., Eadie, D.T., 2010b. Viscoelastic air-blast sprays in a cross-flow. part 2: droplet velocities. Atomization and Sprays 20.

Li, R., Ninokata, H., Mori, M., 2011. A numerical study of impact force caused by liquid droplet impingement onto a rigid wall. Progress in Nuclear Energy 53, 881–885.

de Lima, B.S., de Souza Meira, L., de Souza, F.J., 2020. Numerical simulation of a water droplet splash: Comparison between plic and hric schemes for the vof transport equation. European Journal of Mechanics-B/Fluids 84, 63–70.

Luo, H., 2021. Experimental investigations on fuel spray and impingement for gasoline direct injection engines. Internal Combustion Engine Technology and Applications of Biodiesel Fuel , 25.

Luo, H., Uchitomi, S., Nishida, K., Ogata, Y., Zhang, W., Fujikawa, T., 2017. Experimental investigation on fuel film formation by spray impingement on flat walls with different surface roughness. Atomization and Sprays 27.

Malgarinos, I., Nikolopoulos, N., Gavaises, M., 2015. Coupling a local adaptive grid refinement technique with an interface sharpening scheme for the simulation of two-phase flow and free-surface flows using vof methodology. Journal of Computational Physics 300, 732–753.

Malgarinos, I., Nikolopoulos, N., Marengo, M., Antonini, C., Gavaises, M., 2014. Vof simulations of the contact angle dynamics during the drop spreading: Standard models and a new wetting force model. Advances in colloid and interface science 212, 1–20.

Mao, T., Kuhn, D.C., Tran, H., 1997. Spread and rebound of liquid droplets upon impact on flat surfaces. AIChE Journal 43, 2169–2179.

Maroteaux, F., Llory, D., Le Coz, J., Habchi, C., 2002. Liquid film atomization on wall edges—separation criterion and droplets formation model. J. Fluids Eng. 124, 565–575.

Mathews, W., Lee, C.F., Peters, J.E., 2003. Experimental investigations of spray/wall impingement. Atomization and Sprays 13.

Mawarsih, E., Budiana, E.P., Deendarlianto, Indarto, Kamal, S., 2020. Numerical simulation of single droplet phenomenon using method finite difference and front-tracking, in: AIP Conference Proceedings, AIP Publishing LLC. p. 020016.

Meingast, U., Staudt, M., Reichelt, L., Renz, U., Sommerhoff, F.A., 2000. Analysis of spray/wall interaction under diesel engine conditions. SAE transactions , 299–312.

Menter, F.R., Kuntz, M., Langtry, R., 2003. Ten Years of Industrial Experience with the SST Turbulence Model. Turbulence Heat and Mass Transfer 4 4, 625–632. URL: `http://cfd.mace.manchester.ac.uk/flomania/pds{_}papers/file{_}pds-1068134610Menter-SST-paper.pdf`, doi:`10.4028/www.scientific.net/AMR.576.60`.

Moita, A., Moreira, A., 2007. Drop impacts onto cold and heated rigid surfaces: morphological comparisons, disintegration limits and secondary atomization. International journal of heat and fluid flow 28, 735–752.

Moreira, A., Moita, A., Panao, M., 2010. Advances and challenges in explaining fuel spray impingement: How much of single droplet impact research is useful? Progress in energy and combustion science 36, 554–580.

de Moro Martins, D.A., de Souza, F.J., de Vasconcelos Salvo, R., 2014. Formation of vortex breakdown in conical–cylindrical cavities. International journal of heat and fluid flow 48, 52–68.

Morton, D., Rudman, M., Jong-Leng, L., 2000. An investigation of the flow regimes resulting from splashing drops. Physics of Fluids 12, 747–763.

Mundo, C., Sommerfeld, M., Tropea, C., 1995. Droplet-wall collisions: experimental studies of the deformation and breakup process. International journal of multiphase flow 21, 151–173.

Nikolopoulos, N., Theodorakakos, A., Bergeles, G., 2005. Normal impingement of a droplet onto a wall film: a numerical investigation. International Journal of Heat and Fluid Flow 26, 119–132.

Nikolopoulos, N., Theodorakakos, A., Bergeles, G., 2007. Three-dimensional numerical investigation of a droplet impinging normally onto a wall film. Journal of computational physics 225, 322–341.

Nourgaliev, R., Wiri, S., Dinh, N., Theofanous, T., 2005. On improving mass conservation of level set by reducing spatial discretization errors. International journal of multiphase flow 31, 1329–1336.

Oguz, H.N., Prosperetti, A., 1990. Bubble entrainment by the impact of drops on liquid surfaces. Journal of Fluid Mechanics 219, 143–179.

Okawa, T., Shiraishi, T., Mori, T., 2008. Effect of impingement angle on the outcome of single water drop impact onto a plane water surface. Experiments in Fluids 44, 331–339.

O'rourke, P., Amsden, A., 1996. A particle numerical model for wall film dynamics in port-injected engines. SAE transactions , 2000–2013.

Panão, M.R.O., Moreira, A.L., 2005. Experimental characterization of an intermittent gasoline spray impinging under cross-flow conditions. Atomization and Sprays 15.

Pasandideh-Fard, M., Bhola, R., Chandra, S., Mostaghimi, J., 1998. Deposition of tin droplets on a steel plate: simulations and experiments. International Journal of Heat and Mass Transfer 41, 2929–2945.

Pereira, G.C., de Souza, F.J., de Moro Martins, D.A., 2014. Numerical prediction of the erosion due to particles in elbows. Powder Technology 261, 105–117.

Pivello, M.R., Villar, M.M., Serfaty, R., Roma, A.M., Silveira-Neto, A.d., 2014. A fully adaptive front tracking method for the simulation of two phase flows. International Journal of Multiphase Flow 58, 72–82.

Ray, J., Lefantzi, S., Arunajatesan, S., Dechant, L., 2014. Tuning a RANS ke model for jet-in-crossflow simulations. Technical Report. Sandia National Lab.(SNL-CA), Livermore, CA

(United States); Sandia National . . . .

Reitz, R.D., 1987. Modeling atomization processes in high-pressure vaporizing sprays. Atomisation Spray Technology 3, 309–337.

Richards, K., Senecal, P.K., Pomraning, E., 2016. Converge v2. 3 manual. Convergent Science, Inc., Madison, WI .

Rider, W., Kothe, D., 1995. Stretching and tearing interface tracking methods, in: 12th Computational Fluid Dynamics Conference, p. 1717.

Rioboo, R., Tropea, C., Marengo, M., 2001. Outcomes from a drop impact on solid surfaces. Atomization and sprays 11.

Roache, P.J., 1994. Perspective: A method for uniform reporting of grid refinement studies. Journal of Fluids Engineering 116, 405–413. doi:`https://doi.org/10.1115/1.2910291`.

Roache, P.J., 1997. Quantification of uncertainty in computational fluid dynamics. Annual Review of Fluid Mechanics 29, 123–160. doi:`https://doi.org/10.1146/annurev.fluid.29.1.123`.

Roache, P.J., 1998. Verification of codes and calculations. AIAA journal 36, 696–702. doi:`https://doi.org/10.2514/2.457`.

Salvo, R., Souza, F., Martins, D., 2012. Analysis of sub-grid modeling effects in the simulation of the single-phase turbulent flow in an industrial cyclone separator. Revista de Engenharia Térmica 11, 44–52.

Samenfink, W., Elsäßer, A., Dullenkopf, K., Wittig, S., 1999. Droplet interaction with shear-driven liquid films: analysis of deposition and secondary droplet characteristics. International journal of heat and fluid flow 20, 462–469.

Santos, J.G.d.F., de Souza, F.J., de Lima, B.S., 2022. Shape optimization of pipeline components. The Canadian Journal of Chemical Engineering .

Shedd, T., Corn, M., Cohen, J., Arienti, M., Soteriou, M., 2009a. Liquid film formation by an impinging jet in a high-velocity air stream, in: 47th AIAA Aerospace Sciences Meeting including The New Horizons Forum and Aerospace Exposition, p. 998.

Shedd, T., Newell, T., 1997. An automated optical liquid film thickness measurement method, Air Conditioning and Refrigeration Center, University of Illinois, Urbana-Champaign, USA. Technical Report. ACRC TR-134.

Shedd, T.A., Corn, M.L., Arienti, M., Soteriou, M.C., 2009b. Liquid Jet Breakup by an Impinging Air Jet, in: 47th AIAA Aerospace Sciences Meeting including the New Horizons Forum and Aerospace Exposition, p. 998.

Shim, Y.S., Choi, G.M., Kim, D.J., 2008. Numerical and experimental study on hollow-cone fuel spray of highpressure swirl injector under high ambient pressure condition. Journal of Mechanical Science and Technology 22, 320–329.

Si, X.A., Sami, M., Xi, J., 2021. Liquid film translocation significantly enhances nasal spray delivery to olfactory region: a numerical simulation study. Pharmaceutics 13, 903.

Sommerfeld, M., 2001. Validation of a stochastic lagrangian modelling approach for inter-particle collisions in homogeneous isotropic turbulence. International Journal of Multiphase Flow 27, 1829–1858.

Sotoudeh, F., Kamali, R., Mousavi, S.M., Karimi, N., Lee, B.J., Khojasteh, D., 2021. Understanding droplet collision with superhydrophobic-hydrophobic–hydrophilic hybrid surfaces. Colloids and Surfaces A: Physicochemical and Engineering Aspects 614, 126140.

Souza, F., 2003. Simulação de Grandes-Escalas de Escoamentos em um Hidrociclone. Ph.D. thesis. Tese de Doutorado, Universidade Federal de Uberlândia.

Souza, F., Neto, A.S., 2004. Preliminary results of large eddy simulations of a hydrocyclone. Revista de Engenharia Térmica 3, 168–173.

Souza, F., Vieira, L., Damasceno, J., Barrozo, M., 2000. Analysis of the influence of the filtering medium on the behaviour of the filtering hydrocyclone. Powder Technology 107, 259–267.

de Souza, F.J., Silva, A.L., Utzig, J., 2014. Four-way coupled simulations of the gas–particle flow in a diffuser. Powder technology 253, 496–508.

de Souza, F.J., de Vasconcelos Salvo, R., de Moro Martins, D., 2015a. Effects of the gas outlet duct length and shape on the performance of cyclone separators. Separation and Purification Technology 142, 90–100.

de Souza, F.J., de Vasconcelos Salvo, R., de Moro Martins, D., 2015b. Simulation of the performance of small cyclone separators through the use of post cyclones (poc) and annular overflow ducts. Separation and Purification Technology 142, 71–82.

de Souza, F.J., de Vasconcelos Salvo, R., de Moro Martins, D.A., 2012. Large eddy simulation of the gas–particle flow in cyclone separators. Separation and Purification Technology 94, 61–70.

Stalder, A., Kulik, G., Sage, D., Barbieri, L., Hoffmann, P., 2006. A snake-based approach to accurate determination of both contact points and contact angles. Colloids And Surfaces A: Physicochemical And Engineering Aspects 286, 92–103.

Stanton, D.W., Rutland, C.J., 1996. Modeling fuel film formation and wall interaction in diesel engines. SAE transactions , 808–824.

Stanton, D.W., Rutland, C.J., 1998. Multi-dimensional modeling of thin liquid films and spray-wall interactions resulting from impinging sprays. International Journal of Heat and Mass Transfer 41, 3037–3054.

Stevenin, C., Vallet, A., Tomas, S., Amielh, M., Anselmet, F., 2016. Eulerian atomization modeling of a pressure-atomized spray for sprinkler irrigation. International Journal of Heat and Fluid Flow 57, 142–149.

Tanner, F.X., 1997. Liquid jet atomization and droplet breakup modeling of non-evaporating diesel fuel sprays. SAE transactions , 127–140.

Thoroddsen, S., Sakakibara, J., 1998. Evolution of the fingering pattern of an impacting drop. Physics of fluids 10, 1359–1374.

Utzig, J., Guerra, H.P., Decker, R.K., et al., 2015. Gas-solid turbulence modulation: Wavelet mra and euler/lagrange simulations. CHEMICAL ENGINEERING 43.

Velasco, L.J., Venturi, D.N., Fontes, D.H., de Souza, F.J., 2022. Numerical simulation of drag reduction by microbubbles in a vertical channel. European Journal of Mechanics-B/Fluids 92, 215–225.

Versteeg, H.K., Malalasekera, W., 2007. An introduction to computational fluid dynamics: the finite volume method. Pearson education.

White, F.M., 1962. Mecânica dos fluidos. McGraw Hill Brasil.

Wilcox, D.C., 1988. Multiscale model for turbulent flows. AIAA journal 26, 1311–1320.

Xiao, D., Li, X., Hung, D.L., Xu, M., 2019. Characteristics of impinging spray and corresponding fuel film under different injection and ambient pressure. Technical Report. SAE Technical Paper.

Yokoi, K., Vadillo, D., Hinch, J., Hutchings, I., 2009. Numerical studies of the influence of the dynamic contact angle on a droplet impacting on a dry surface. Physics of Fluids 21, 072102.

Yu, X., Shang, B., Xie, B., Huang, M., Luo, X., 2015. Spreading behaviors of silicone droplet impact on flat solid surface: Experiments and vof simulations, in: 2015 16th International Conference on Electronic Packaging Technology (ICEPT), IEEE. pp. 1058–1061.

Zhang, Y., Jia, M., Liu, H., Xie, M., 2016. Development of an improved liquid film model for spray/wall interaction under engine-relevant conditions. International Journal of Multiphase Flow 79, 74–87.

Zhao, L., Ahuja, N., Zhu, X., Zhao, Z., Lee, S.Y., 2018. Splashing criterion and topological features of a single droplet impinging on the flat plate. Technical Report.

Appendix A

```
/*
This script calculates the average of the film height profile and the angle of impact of droplets in a chosen folder.
Make sure to change the values of fps and pixel size in the section Input variables. Also change the tunning variables if necessary.
Make sure that there are in the chosen folder the following files: "zbackground.bmp" and "zstandard.bmp". This files are used to calculate the reflection of the plate.
Considering the alphabetical order your sequence of images should come before "zbackground.bmp" and "zstandard.bmp".
It must not contain any other files. After printing results as txt files you need to remove it from the folder in order to run the script again.
Pay attention on setting the values of brightness and colour as well as threshold.
*/
//Variables for printing and saving files
dir1=getDirectory("Choose a Directory");
printingWindows=true;        //Print results to new windows on Fiji
if (printingWindows) {
  closeResultsDroplet=true;    //Close results of droplets window (only make it true if printingWindows is true)
  closeResultsFilm=true;       //Close results of film windows (only make it true if printingWindows is true)
  closeTestResults=true;       //Close results window for testing (only make it true if printingWindows is true)
  printingTxt=true;        //Print results to txt files (only make it true if printingWindows is true)
}
closePictures=true;          //Close working pictures
printAverageImage=true;        //Print the average image for film thickness
closeAveragePictures=true;       //Close average images
set_batch=true;            //Setting batch makes the script run faster by not opening the images
set_Threshold=false;         //Set values threshold according to fine tuning parameters
set_BrightnessAndColour=false;     //Set values for brightness and colour according to fine tuning parameters
//End of setting variables for printing
setBatchMode(false);
if (set_batch) {
  setBatchMode(true);
}
//Cleaning outputs
run("Clear Results");
print("\\Clear");
if (isOpen("Log")) {
```

```
  selectWindow("Log");
  run("Close");
}
if (isOpen("Results")) {
  selectWindow("Results");
  run("Close");
}
if (isOpen("Droplet_average")) {
    selectWindow("Droplet_average");
    run("Close");
  }
if (isOpen("TESTS")) {
  selectWindow("TESTS");
  run("Close");
}
if (isOpen("Results_film_liquid_height")) {
  selectWindow("Results_film_liquid_height");
  run("Close");
}
//Creating windows on Fiji
if(printingWindows){
  title1 = "Results_impacted";
  title2 = "["+title1+"]";
  f1=title2;
  run("New... ", "name="+title2+" type=Table");
  print(f1, "\\Headings:X_[mm]\tY_[mm]\tArea_[mm2]\tWidth_[mm]\tHeight_[mm]\tCirc\tAR\tRound\tSolidity\tDrop_ID\tVx_[mm/s]\tVy_[mm/s]\tImpact_Angle_[degrees]");
  title3 = "Results_film_liquid_height";
  title4 = "["+title3+"]";
  f2=title4;
  run("New... ", "name="+title4+" type=Table");
  print(f2, "\\Headings:Distance_along_wall_[mm]\tFilm_Height_[mm]");
  title7 = "Droplet_average";
  title8 = "["+title7+"]";
  f4=title8;
  run("New... ", "name="+title8+" type=Table");
  print(f4, "\\Headings:X_[mm]\tY_[mm]\tArea_[mm2]\tWidth_[mm]\tHeight_[mm]\tCirc\tAR\tRound\tSolidity\tNumber_of_collisions\tVx_[mm/s]\tVy_[mm/s]\tV_Mag_[m/s]\tImpact_Angle_[degrees]\tReynolds\tWeber\th_max_[mm]\th_max/d_0\tLaplace\tS_cd\th_average_[m]\tK");
  title5 = "TESTS";
  title6 = "["+title5+"]";
  f3=title6;
  run("New... ", "name="+title6+" type=Table");
}
```

```
//Input variables (change for your case)
fps=10000;                  //frames per second [1/s]
pixelSize=14/835;             //size of each pixel [mm/pixel]
viscosity_l=8.9/10000;          //viscosity of the droplet [P a  s]
density_l=997;              //density of the droplet [kg/m3]
surface_tension=0.07275;        //surface tension liquid-gas [N/m]
//Fine tune parameters
countourRectangleSize=10;         //Variable used to check around the
    droplet for collision
percentageOfPictureToCheck=60;      //Variable to check for droplets on
    each of the images
distanceNewOrCollision=25;          //Variable used to check for new
    droplets and collision
AdjustMinimumMeanSquareError=1/1000;    //Variable used to adjust the
    minimum mean square error approximation for impact angle
AdjustMinimumMeanSquareError2=5;        //Variable used to adjust the
    minimum mean square error approximation for impact angle
lvt=10;                 //Lower value for threshold
gvt=99;                 //Greater value for theshold
lvcb=0;                 //Lower value to adjust brightness and contrast of
    list images
gvcb=80;                //Greater value to adjust brightness and contrast
    of list images
// Combining zbackground and image then making binary and fililing holes
list1 = getFileList(dir1);
if (File.exists(dir1 + "zbackground.bmp") && File.exists(dir1 + "zstandard.
    bmp") && !File.exists(dir1 + "average.bmp")) { //Check if zbackground
    and zstandard are on the working folder and if there is the average file
open(dir1 + "zbackground.bmp");
open(dir1 + "zstandard.bmp");
imageCalculator("Difference create", "zbackground.bmp","zstandard.bmp");
if (isOpen("Result of zbackground.bmp")) {

  selectWindow("Result of zbackground.bmp");
}
if (set_BrightnessAndColour) {
  setMinAndMax(lvcb, gvcb);
  run("Apply LUT");
}
if (set_Threshold) {
  setAutoThreshold("Default");
  run("Threshold...");
  setThreshold(lvt, gvt);
}
run("Convert to Mask");
if (isOpen("Threshold")){
  selectWindow("Threshold");
```

```
  run("Close");
}
run("Make Binary");
run("Fill Holes");
if (isOpen("zbackground.bmp")) {
  selectWindow("zbackground.bmp");
  run("Close");
}
if (isOpen("zstandard.bmp")) {
  selectWindow("zstandard.bmp");
  run("Close");
}
if (isOpen("Result of zbackground.bmp")) {

  selectWindow("Result of zbackground.bmp");
}
width = getWidth;
height = getHeight;
// Find the edge of the images cutting and rotating
//Finding nearest droplet and its reflection
makeRectangle(0, 0, width, height);
run("Set Measurements...", "area centroid bounding redirect=None decimal=3"
    );
run("Analyze Particles...", "size=80-Infinity show=Nothing display exclude
    clear");
n=nResults;
x1=x2=getResult ("X", 0);
y1=y2=getResult ("Y", 0);
//the higher value of y is stored on y1
for (i = 0; i < n; i++) {
  newy = getResult ("Y", i);
  if (y1 < newy) {
    y1=newy;
    x1= getResult ("X", i);
  }
}
//the second higher value of y is stored on y2
for (i = 0; i < n; i++) {
  newy = getResult ("Y", i);
  if (y2 < newy) {
    if (y2 < y1 - 1) {
      y2=newy;
      x2= getResult ("X", i);
    }
  }
}
//Finding the vector normal to the midle point of the droplets
```

```
dx = (x1 - x2)/2;
dy = (y1 - y2)/2 ;
Xmid = x2 + dx;
Ymid = y2 + dy;
k = -(x2-x1)/(y2-y1);
Y_0 = k*(0-Xmid)+Ymid;
X_0 = Xmid -Ymid/k;
teta=(acos((X_0)/(sqrt(X_0*X_0+Y_0*Y_0)))*(180/PI)-90);
if (isOpen("Result of zbackground.bmp")) {
  selectWindow("Result of zbackground.bmp");
  run("Close");
}
if (teta>0 || teta<0 || teta==0) {        //If teta is not numeric you may consider refining the fine tuning variables
//Working with the list of images
setOption("ExpandableArrays", true);
DistanceEdge_mean= newArray();
y_mean= newArray();
droplet_average=newArray(0,0,0,0,0,0,0,0,0,0,0,0,0,0);
lenghtlist=list1.length;
drop_count=0;
xDropletOld = newArray(0,0,0);
yDropletOld = newArray(0,0,0);
dropletnew = newArray(0,0,0,0,0,0,0,0,0,0,0,0,0,0);
dropletold = newArray(0,0,0,0,0,0,0,0,0,0,0,0,0,0);
h_max=0;
for (y_Pos = 0; y_Pos < height+200; y_Pos++) {
  DistanceEdge_mean[y_Pos]=0;
}
for (i = 0; i < lenghtlist-2; i++) {  //Working on all the images
  open(dir1+list1[i]);
  if(printingWindows){
    print(f3,list1[i]);     //print current picture on TESTS window
  }
  // Combining zbackground and image then making binary and fililing holes
  open(dir1 + "zbackground.bmp");
  imageCalculator("Difference", list1[i],"zbackground.bmp");
  if (isOpen("zbackground.bmp")) {
    selectWindow("zbackground.bmp");
    run("Close");
  }
  if (isOpen(list1[i])) {
    selectWindow(list1[i]);
  }
  if (set_BrightnessAndColour) {
    setMinAndMax(lvcb, gvcb);
    run("Apply LUT");
```

```
}
if (set_Threshold) {
  setAutoThreshold("Default");
  run("Threshold...");
  setThreshold(lvt, gvt);
}
run("Convert to Mask");
if (isOpen(list1[i])) {
  selectWindow(list1[i]);
}
run("Make Binary");
run("Fill Holes");
//Rotating image according to "Finding the vector normal to the midle
 point of the droplets" section
//print(f3,teta);
run("Rotate... ", "angle=teta grid=1 interpolation=None");
newx=X_0+height/k;
width = getWidth;
height = getHeight;
makePolygon(newx,0, width,0, width,height, newx,height);
run("Clear Outside");
run("Crop");
run("Make Binary");
//After rotating and croping the values of height and width are updated
width = getWidth;
height = getHeight;
//Calculating the average of film thickness along the wall over all
 images
for (y_Pos = 0; y_Pos < height; y_Pos++) {
  makeLine(0, y_Pos, width, y_Pos);
  run("Clear Results");
  profile = getProfile();
  for (j_edge=1; j_edge<profile.length; j_edge++){
    if(profile[j_edge]<=profile[j_edge-1]*0.8){
      DistanceEdge=j_edge-1;
      j_edge=profile.length;
    }
  }
  DistanceEdge_mean[y_Pos]=DistanceEdge_mean[y_Pos]*((i)/(i+1))+
 DistanceEdge/(i+1); //Equation for average
  if (DistanceEdge_mean[y_Pos]>h_max) {
    h_max=DistanceEdge_mean[y_Pos];
  }
}
//Finding velocity and angle of impact for droplets and saving droplets
//Finding the droplets inside the domain
setTool("rectangle");
```

```
makeRectangle(0, 0, width, height*percentageOfPictureToCheck/100);
run("Set Measurements...", "area centroid bounding redirect=None decimal=3");
run("Analyze Particles...", "size=80-Infinity show=Nothing display exclude clear");
numDrop=nResults;                                   //number of droplets inside the domain
setTool("rectangle");
makeRectangle(0, 0, width, height*percentageOfPictureToCheck/100);
run("Set Measurements...", "area centroid bounding shape redirect=None decimal=3");
run("Analyze Particles...", "size=80-Infinity show=Nothing display exclude clear");
if (nResults>0) {                                   //Only run droplet script if there are droplets
  //The highest value of y is stored on y1, and for x in x1
  x1=getResult ("X", 0);
  y1=getResult ("Y", 0);
  dropletold[0]=dropletnew[0];
  dropletold[1]=dropletnew[1];
  dropletold[2]=dropletnew[2];
  dropletold[3]=dropletnew[3];
  dropletold[4]=dropletnew[4];
  dropletold[5]=dropletnew[5];
  dropletold[6]=dropletnew[6];
  dropletold[7]=dropletnew[7];
  dropletold[8]=dropletnew[8];
  dropletold[9]=dropletnew[9];
  dropletnew[0]=getResult ("X", 0);
  dropletnew[1]=getResult ("Y", 0);
  dropletnew[2]=getResult ("Area", 0);
  dropletnew[3]=getResult ("Width", 0);
  dropletnew[4]=getResult ("Height", 0);
  dropletnew[5]=getResult ("Circ.", 0);
  dropletnew[6]=getResult ("AR", 0);
  dropletnew[7]=getResult ("Round", 0);
  dropletnew[8]=getResult ("Solidity", 0);
  dropletnew[9]=i;
  //Finding the droplet which is closest to the wall
  print("\\Clear");
  for (j = 0; j < numDrop; j++) {
    newx = getResult ("X", j);
    newy = getResult ("Y", j);
    if (x1 > newx) {
      x1=newx;
      y1=newy;
      dropletnew[0]=getResult ("X", j);
```

```
      dropletnew[1]=getResult ("Y", j);
      dropletnew[2]=getResult ("Area", j);
      dropletnew[3]=getResult ("Width", j);
      dropletnew[4]=getResult ("Height", j);
      dropletnew[5]=getResult ("Circ.", j);
      dropletnew[6]=getResult ("AR", j);
      dropletnew[7]=getResult ("Round", j);
      dropletnew[8]=getResult ("Solidity", j);
    dropletnew[9]=i; //ID
  }
 }
xDropletOld[0]=xDropletOld[1];
xDropletOld[1]=xDropletOld[2];
xDropletOld[2]=x1;
yDropletOld[0]=yDropletOld[1];
yDropletOld[1]=yDropletOld[2];
yDropletOld[2]=y1;
//Calculating velocity
if (yDropletOld[0] != 0 && yDropletOld[1] != 0) {         //Checking if
 it is not in the first two images
  dropletnew[10]=(xDropletOld[1]-xDropletOld[0])*fps;     //Vx [pixels
per second]
  dropletnew[11]=(yDropletOld[1]-yDropletOld[0])*fps;     //Vy [pixels
per second]
}
Vx=dropletnew[10];                                  //Velocity in
pixels per second
Vy=dropletnew[11];                              //Velocity in pixels
per second
//Calculating the impact angle
angleOfVelocity=(atan(Vx/Vy));                  //Angle in radians
dropletnew[12]=angleOfVelocity*180/PI;                      //Impact
angle in degrees
if (yDropletOld[0] != 0 && yDropletOld[1] != 0) {         //Checking if
 it is not in the first two images
  if (xDropletOld[2] > xDropletOld[1]) {            //Condition for
collision is if the last droplet detected has a lower x than last image
    if (isOpen(list1[i-1])) {
      selectWindow(list1[i-1]);             //Select one image before
the impact
    }
    if (dropletnew[12]<0) {
      if(printingWindows){
        print(f1, dropletold[0]*pixelSize+"\t"+dropletold[1]*pixelSize+
"\t"+dropletold[2]*pixelSize*pixelSize+"\t"+dropletold[3]*pixelSize+"\t"
+dropletold[4]*pixelSize+"\t"+dropletold[5]+"\t"+dropletold[6]+"\t"+
```

```
dropletold[7]+"\t"+dropletold[8]+"\t"+dropletold[9]+"\t"+dropletnew[10]*pixelSize+"\t"+dropletnew[11]*pixelSize+"\t"+dropletnew[12]);
          }
          //Calculating average parameters for droplet (makes no sense for ID)
          droplet_average[0]=droplet_average[0]*(drop_count/(drop_count+1))+(dropletold[0]/(drop_count+1));
            droplet_average[1]=droplet_average[1]*(drop_count/(drop_count+1))+(dropletold[1]/(drop_count+1));
            droplet_average[2]=droplet_average[2]*(drop_count/(drop_count+1))+(dropletold[2]/(drop_count+1));
            droplet_average[3]=droplet_average[3]*(drop_count/(drop_count+1))+(dropletold[3]/(drop_count+1));
            droplet_average[4]=droplet_average[4]*(drop_count/(drop_count+1))+(dropletold[4]/(drop_count+1));
            droplet_average[5]=droplet_average[5]*(drop_count/(drop_count+1))+(dropletold[5]/(drop_count+1));
            droplet_average[6]=droplet_average[6]*(drop_count/(drop_count+1))+(dropletold[6]/(drop_count+1));
            droplet_average[7]=droplet_average[7]*(drop_count/(drop_count+1))+(dropletold[7]/(drop_count+1));
            droplet_average[8]=droplet_average[8]*(drop_count/(drop_count+1))+(dropletold[8]/(drop_count+1));
          droplet_average[10]=droplet_average[10]*(drop_count/(drop_count+1))+(dropletnew[10]/(drop_count+1));
          droplet_average[11]=droplet_average[11]*(drop_count/(drop_count+1))+(dropletnew[11]/(drop_count+1));
          droplet_average[12]=droplet_average[12]*(drop_count/(drop_count+1))+(dropletnew[12]/(drop_count+1));
          drop_count++;
          droplet_average[9]=drop_count;     //instead of ID store drop_count
        }
      }
    }
  }
  if(closePictures){
    if (i-1>0){
      if (isOpen(list1[i-2])) {
        selectWindow(list1[i-2]);
        run("Close");
      }
    }
  }
}
if(closePictures){
  if (isOpen(list1[i-1])) {
```

```
    selectWindow(list1[i-1]);
    run("Close");
  }
  if (isOpen(list1[i-2])) {
    selectWindow(list1[i-2]);
    run("Close");
  }
}
if (set_batch) {
  setBatchMode(false);
}
if(printingWindows){
  if (isOpen("Droplet_average")) {
    selectWindow("Droplet_average");
    V_mag=(sqrt((droplet_average[10]*pixelSize*droplet_average[10]*pixelSize)+(droplet_average[11]*pixelSize*droplet_average[11]*pixelSize)))/1000;
    D_average=(droplet_average[3]*pixelSize+droplet_average[4]*pixelSize)/2000;
    count_h=0;
    h_average=0;
    for (y_Pos = 0; y_Pos < height - 20; y_Pos++) {
      if (DistanceEdge_mean[y_Pos]>0) {
        h_average=h_average+DistanceEdge_mean[y_Pos];
        count_h++;
      }
    }
    h_average=h_average*pixelSize/(count_h*1000);
    droplet_average[13]=(V_mag*D_average*density_l)/viscosity_l;                    //Reynolds
    droplet_average[14]=(V_mag*V_mag*D_average*density_l)/surface_tension;                  //Weber
    droplet_average[15]=h_max;                       //h_max
    droplet_average[16]=h_max/D_average;                   //h_max/d_0
    droplet_average[17]=density_l*surface_tension*D_average/(viscosity_l*viscosity_l);                    //Laplace
    droplet_average[18]=(1/24)*(droplet_average[13]*Math.pow(droplet_average[17],-0.4189));                  //Scd
    droplet_average[19]=h_average;                   //h_average
    droplet_average[20]=Math.pow(droplet_average[14],0.5)*Math.pow(droplet_average[13],0.25);                  //K
    print(f4, droplet_average[0]*pixelSize+"\t"+droplet_average[1]*pixelSize+"\t"+droplet_average[2]*pixelSize*pixelSize+"\t"+droplet_average[3]*pixelSize+"\t"+droplet_average[4]*pixelSize+"\t"+
```

```
   droplet_average[5]+"\t"+droplet_average[6]+"\t"+droplet_average[7]+"\t"+
   droplet_average[8]+"\t"+droplet_average[9]+"\t"+droplet_average[10]*
   pixelSize+"\t"+droplet_average[11]*pixelSize+"\t"+(sqrt((droplet_average
   [10]*pixelSize*droplet_average[10]*pixelSize)+(droplet_average[11]*
   pixelSize*droplet_average[11]*pixelSize)))/1000+"\t"+droplet_average
   [12]+"\t"+droplet_average[13]+"\t"+droplet_average[14]+"\t"+
   droplet_average[15]+"\t"+droplet_average[16]+"\t"+droplet_average[16]+"\
   t"+droplet_average[17]+"\t"+droplet_average[18]+"\t"+droplet_average
   [19]+"\t"+droplet_average[20]);
  }
}
if(printingWindows){
  if (isOpen("Results_film_liquid_height")) {
    selectWindow("Results_film_liquid_height");
    for (y_Pos = 0; y_Pos < height - 20; y_Pos++) {
      print(f2, y_Pos*pixelSize+"\t"+DistanceEdge_mean[y_Pos]*pixelSize);
    }
  }
}
if (set_batch) {
  setBatchMode(true);
}
if (printingTxt) {
  if (isOpen("Results_impacted")) {
    selectWindow("Results_impacted");
    saveAs("results",dir1+title1+".txt");
  }
  if (isOpen("Results_film_liquid_height")) {
    selectWindow("Results_film_liquid_height");
    saveAs("results",dir1+title3+".txt");
  }
  if (isOpen("Droplet_average")) {
    selectWindow("Droplet_average");
    saveAs("results",dir1+title7+".txt");
  }
}
if (isOpen("Log")) {
  selectWindow("Log");
  run("Close");
}
if (isOpen("Results")) {
  selectWindow("Results");
  run("Close");
}
if (closeResultsDroplet) {
  if (isOpen("Results_impacted")) {
    selectWindow("Results_impacted");
```

```
    run("Close");
  }
}
if (closeResultsFilm) {
  if (isOpen("Results_film_liquid_height")) {
    selectWindow("Results_film_liquid_height");
    run("Close");
  }
}
if (closeTestResults) {
  if (isOpen("TESTS")) {
    selectWindow("TESTS");
    run("Close");
  }
}
if (closeResultsDroplet) {
  if (isOpen("Droplet_average")) {
    selectWindow("Droplet_average");
    run("Close");
  }
}
if (printAverageImage) {
  open(dir1 + "zbackground.bmp");
  imageCalculator("Subtract create", "zbackground.bmp","zbackground.bmp");

  if (isOpen("zbackground.bmp")) {
    selectWindow("zbackground.bmp");
    run("Close");
  }
  if (isOpen("Result of zbackground.bmp")) {
    selectWindow("Result of zbackground.bmp");
  }
  width = getWidth;
  height = getHeight;
  for (y_Pos = 0; y_Pos < height+20; y_Pos++) {
      if (DistanceEdge_mean[y_Pos]==0) {

      }else {
        makeLine(0, y_Pos, DistanceEdge_mean[y_Pos], y_Pos);
        run("Draw");
      }
  }
  makeRectangle(0, 0, width, height-50);
  run("Duplicate...", " ");
  saveAs("BMP", dir1 + "average.bmp");
  if (isOpen("Result of zbackground.bmp")) {
    selectWindow("Result of zbackground.bmp");
```

```
    run("Close");
  }
}
if (closeAveragePictures) {
  selectWindow("average.bmp");
  run("Close");
}
if (isOpen("Threshold")) {
  selectWindow("Threshold");
  run("Close");
}
//
   //////////////////////////////////////////////////////////////////////////

//Error condition for non numerical teta
}else{
  if (isOpen("Warning")) {
    selectWindow("Warning");
    titleteta = "Warning";
    titleteta2 = "["+titleteta+"]";
    fteta=titleteta2;
    print(fteta, dir1);
  }else{
    titleteta = "Warning";
    titleteta2 = "["+titleteta+"]";
    fteta=titleteta2;
    run("New... ", "name="+titleteta2+" type=Table");
    print(fteta, "\\Headings:Warning!!!");
    print(fteta, "Non numerical value for rotating the images");
    print(fteta, "Consider changing the fine tuning variables");
    print(fteta, "This problem may occur when droplets cannot be identified
   ");
    print(fteta, "List of error folders");
    print(fteta, dir1);
  }
  if (closeResultsDroplet) {
    if (isOpen("Results_impacted")) {
      selectWindow("Results_impacted");
      run("Close");
    }
  }
  if (closeResultsFilm) {
    if (isOpen("Results_profile")) {
      selectWindow("Results_profile");
      run("Close");
    }
  }
```

```
}
//
   ///////////////////////////////////////////////////////////////////////////

}else{
  if (isOpen("Warning_files")) {
    selectWindow("Warning_files");
    titlefiles = "Warning_files";
    titlefiles2 = "["+titlefiles+"]";
    ffiles=titlefiles2;
    print(ffiles, dir1);
  }else{
    titlefiles = "Warning_files";
    titlefiles2 = "["+titlefiles+"]";
    ffiles=titlefiles2;
    run("New... ", "name="+titlefiles2+" type=Table");
    print(ffiles, "\\Headings:Warning!!!");
    print(ffiles, "Script did not find the correct images in folder");
    print(ffiles, "Consider checking zbackground and zstandard files");
    selectWindow("Warning_files");
    print(ffiles, dir1);
  }
  if (isOpen("Log")) {
    selectWindow("Log");
    run("Close");
  }
  if (isOpen("Results")) {
    selectWindow("Results");
    run("Close");
  }
  if (closeResultsDroplet) {
    if (isOpen("Results_impacted")) {
      selectWindow("Results_impacted");
      run("Close");
    }
  }
  if (closeResultsFilm) {
    if (isOpen("Results_film_liquid_height")) {
      selectWindow("Results_film_liquid_height");
      run("Close");
    }
  }
  if (closeTestResults) {
    if (isOpen("TESTS")) {
      selectWindow("TESTS");
      run("Close");
    }
```

```
  }
  if (closeResultsDroplet) {
    if (isOpen("Droplet_average")) {
      selectWindow("Droplet_average");
      run("Close");
    }
  }
  if (closeResultsFilm) {
    if (isOpen("Results_profile")) {
      selectWindow("Results_profile");
      run("Close");
    }
  }
}
//////////////////////////////////////////////////////////////////////////////
if (isOpen("Warning")) {
  selectWindow("Warning");
  titleteta = "Warning";
  titleteta2 = "["+titleteta+"]";
  fteta=titleteta2;
  saveAs("results",dir1+titleteta+".txt");
}
if (isOpen("Warning_files")) {
  selectWindow("Warning_files");
  titlefiles = "Warning_files";
  titlefiles2 = "["+titlefiles+"]";
  ffiles=titlefiles2;
  saveAs("results",dir1+titlefiles+".txt");
}
if (isOpen("Log")) {
  selectWindow("Log");
  run("Close");
}
print("The script is finished!");
```

Appendix B

```
/*
This script calculates the average of the film profile in a chosen folder.
Make sure to change the values of fps and pixel size in the section Input variables. Also change the tunning variables if necessary.
Make sure that there are in the chosen folder the following files: "zbackground.bmp" and "zstandard.bmp". This files are used to calculate the reflection of the plate.
Considering the alphabetical order your sequence of images should come before "zbackground.bmp" and "zstandard.bmp".
It must not contain any other files. After printing results as txt files you need to remove it from the folder in order to run the script again.
*/
//Variables for printing and saving files
printingWindows=true;       //Print results to new windows on Fiji
if (printingWindows) {
  closeResultsFilm=true;      //Close results of film windows (only make it true if printingWindows is true)
  closeTestResults=true;      //Close results window for testing (only make it true if printingWindows is true)
  printingTxt=true;       //Print results to txt files (only make it true if printingWindows is true)
}
closePictures=true;          //Close working pictures
closeAveragePictures=true;      //Close average images
fillEmpty=false;           //Fill empty spaces on images (This process is time consuming)
printAverageImage=true;        //Print the average image
printAverageImage2=true;       //Print the average image in the center of image
set_batch=true;            //Setting batch makes the script run faster by not opening the images
//End of setting variables for printing
setBatchMode(false);
if (set_batch) {
  setBatchMode(true);
}
//Cleaning outputs
run("Clear Results");
print("\\Clear");
if (isOpen("Log")) {
  selectWindow("Log");
  run("Close");
}
if (isOpen("Results")) {
  selectWindow("Results");
  run("Close");
```

```
}
//Creating windows on Fiji
if(printingWindows){
  title1 = "Results_profile";
  title2 = "["+title1+"]";
  f1=title2;
  run("New... ", "name="+title2+" type=Table");
  title5 = "TESTS";
  title6 = "["+title5+"]";
  f3=title6;
  run("New... ", "name="+title6+" type=Table");
}
//Input variables (change for your case)
fps=10000;            //frames per second [1/s]
pixelSize=29/734;         //size of each pixel [mm/pixel]
//Fine tune parameters
dropletFiltered=0.3;      //Variable used to filter the splashed droplets
search_pool=250;        //Variable used to look for maximum width of the pool
define_pool=1.6;        //Variable used to define pool width in comparison to upstream flow
average_cut=9;          //Variable used to define the top of the pool
subtract_background=40;     //Variable used to set background rolling
set_threeshold=30;        //Variable used to set threeshold
// Combining zbackground and image then making binary and fililing holes
dir1 = getDirectory("Choose Source Directory ");
list1 = getFileList(dir1);
if (File.exists(dir1 + "zbackground.bmp") && File.exists(dir1 + "zstandard.bmp") && !File.exists(dir1 + "average.bmp")) { //Check if zbackground and zstandard are on the working folder and if there is the average file
//Initializing parameters
setOption("ExpandableArrays", true);
Width_mean= newArray();
DistanceEdge_mean= newArray();
y_mean= newArray();
lenghtlist=list1.length;
open(dir1 + "zbackground.bmp");
width = getWidth;
height = getHeight;
if (isOpen("zbackground.bmp")) {
      selectWindow("zbackground.bmp");
      run("Close");
}
for (y_Pos = 0; y_Pos < height+200; y_Pos++) {
  DistanceEdge_mean[y_Pos]=0;
  Width_mean[y_Pos]=0;
}
```

```
//Finding maximum width location of the pool
open(dir1 + "zbackground.bmp");
open(dir1 + "zstandard.bmp");
imageCalculator("Difference", "zstandard.bmp","zbackground.bmp");
if (isOpen("zbackground.bmp")) {
      selectWindow("zbackground.bmp");
      run("Close");
}
if (isOpen("zstandard.bmp")) {
      selectWindow("zstandard.bmp");
}
run("Subtract Background...", "rolling=subtract_background sliding");
setOption("BlackBackground", true);
setAutoThreshold("Default dark");
run("Threshold...");
setThreshold(set_threeshold, 255);
run("Convert to Mask");
if (isOpen("zstandard.bmp")) {
  selectWindow("zstandard.bmp");
}
run("Make Binary");
run("Fill Holes");
setTool("rectangle");
makeRectangle(0, 0, width, height);
run("Set Measurements...", "area centroid bounding redirect=None decimal=3"
   );
run("Analyze Particles...", "  circularity=dropletFiltered-1.00 show=Masks
   clear");
imageCalculator("Difference", "zstandard.bmp","Mask of "+"zstandard.bmp");
if (isOpen("Mask of "+"zstandard.bmp")) {
  selectWindow("Mask of "+"zstandard.bmp");
  run("Close");
}
if (isOpen("zstandard.bmp")) {
  selectWindow("zstandard.bmp");
}
width = getWidth;
height = getHeight;
Maximum_local_width=0;
count=0;
for (y_Pos = 0; y_Pos < height; y_Pos++) {
  x_low=999999;
  x_high=0;
  makeLine(0, y_Pos, width, y_Pos);
  run("Clear Results");
  profile = getProfile();
  for (j_edge=1; j_edge<profile.length; j_edge++){
```

```
  x=j_edge;
  point_value=profile[j_edge];
  if (point_value>125) {//Detect white
   if (x>x_high) {//Lowest x
    x_high=x;
   }
   if (x<x_low) {
    x_low=x;
   }
  }
 }
 if (x_low>999000) {
  x_low=0;
 }
 Local_width=(x_high-x_low);
 if (Local_width>=Maximum_local_width) {
  Maximum_local_width=Local_width;
  y_maximum_pool=y_Pos;
  x_average_maximum_pool=(x_high+x_low)/2;
 }
 count++;
 if (Local_width<average_cut) {
  Local_width=average_cut;
 }
 if (Maximum_local_width>define_pool*Local_width && Maximum_local_width>average_cut) {
  y_Pos=height;
 }
}
if (isOpen("zstandard.bmp")) {
   selectWindow("zstandard.bmp");
   run("Close");
}
//Working with the list of images
for (i = 0; i < lenghtlist-2; i++) {  //Working on all the images
 open(dir1+list1[i]);
 if(printingWindows){
  print(f3,list1[i]);     //print current picture on TESTS window
 }
 // Combining zbackground and image then making binary and fililing holes
 open(dir1 + "zbackground.bmp");
 imageCalculator("Difference", list1[i],"zbackground.bmp");
 if (isOpen("zbackground.bmp")) {
  selectWindow("zbackground.bmp");
  run("Close");
 }
 if (isOpen(list1[i])) {
```

```
  selectWindow(list1[i]);
}
run("Subtract Background...", "rolling=subtract_background sliding");
setOption("BlackBackground", true);
setAutoThreshold("Default dark");
run("Threshold...");
setThreshold(set_threeshold, 255);
run("Convert to Mask");
if (isOpen(list1[i])) {
  selectWindow(list1[i]);
}
run("Make Binary");
run("Fill Holes");
setTool("rectangle");
makeRectangle(0, 0, width, height);
run("Set Measurements...", "area centroid bounding redirect=None decimal=3");
run("Analyze Particles...", "  circularity=dropletFiltered-1.00 show=Masks clear");
imageCalculator("Difference", list1[i],"Mask of "+list1[i]);
if (isOpen("Mask of "+list1[i])) {
  selectWindow("Mask of "+list1[i]);
  run("Close");
}
if (isOpen(list1[i])) {
  selectWindow(list1[i]);
}
width = getWidth;
height = getHeight;
for (y_Pos = 0; y_Pos < height; y_Pos++) {
  x_low=999999;
  x_high=0;
  makeLine(0, y_Pos, width, y_Pos);
  run("Clear Results");
  profile = getProfile();
  for (j_edge=1; j_edge<profile.length; j_edge++){
    x=j_edge;
    point_value=profile[j_edge];
    if (point_value>125) {//Detect white
      if (x>x_high) {//Lowest x
        x_high=x;
      }
      if (x<x_low) {
        x_low=x;
      }
    }
    if (x_low!=999999 && x_high!=0) { //white points detected
```

```
        if(fillEmpty){
          makeLine(x_low, y_Pos, x_high,y_Pos);
          run("Draw");
        }
      }
    }
    if (x_low>999000) {
      x_low=0;
    }
    Width_mean[y_Pos]=Width_mean[y_Pos]*((i)/(i+1))+(x_high-x_low)/(i+1);     //Equation for average
    DistanceEdge_mean[y_Pos]=DistanceEdge_mean[y_Pos]*((i)/(i+1))+x_low/(i+1);    //Equation for average
  }
  if(closePictures){
    if (i-1>0) {
      if (isOpen(list1[i-2])) {
        selectWindow(list1[i-2]);
        run("Close");
      }
    }
  }
}
for (y_Pos = 0; y_Pos < height - 20; y_Pos++) {
  if (Width_mean[y_Pos]<average_cut) {
    Width_mean[y_Pos]=0;
    DistanceEdge_mean[y_Pos]=0;
  }
}
if (set_batch) {
  setBatchMode(false);
}
if(printingWindows){
  count=0;
  maximum_pool_width=Width_mean[y_maximum_pool];
  if (isOpen("Results_profile")) {
    selectWindow("Results_profile");
    print(f1, "\\Headings: \t \t ");
    print(f1,"Maximum_pool_location:"+"\t"+y_maximum_pool*pixelSize+"\t"+"[mm]");
    print(f1,"Maximum_width:"+"\t"+maximum_pool_width*pixelSize+"\t"+"[mm]");
    print(f1,"Y_[mm]\tX_left[mm]\tWidth_[mm]");
    for (y_Pos = 0; y_Pos < height - 20; y_Pos++) {
      if (y_Pos < y_maximum_pool && Width_mean[y_Pos]>average_cut) {
        DistanceEdge_mean[y_Pos]= x_average_maximum_pool-Width_mean[y_Pos]/2;
```

```
      }
      print(f1, y_Pos*pixelSize+"\t"+DistanceEdge_mean[y_Pos]*pixelSize+"\t"+Width_mean[y_Pos]*pixelSize);
    }
  }
}
if (set_batch) {
  setBatchMode(true);
}
if(closePictures){
  if (isOpen(list1[i-1])) {
    selectWindow(list1[i-1]);
    run("Close");
  }
  if (isOpen(list1[i-2])) {
    selectWindow(list1[i-2]);
    run("Close");
  }
}
if (printingTxt) {
  if (isOpen("Results_profile")) {
    selectWindow("Results_profile");
    saveAs("results",dir1+title1+".txt");
  }
}
if (isOpen("Log")) {
  if (isOpen("Log")) {
    selectWindow("Log");
    run("Close");
  }
}
if (isOpen("Results")) {
  if (isOpen("Results")) {
    selectWindow("Results");
    run("Close");
  }
}
if (printAverageImage) {
  open(dir1 + "zbackground.bmp");
  imageCalculator("Subtract create", "zbackground.bmp","zbackground.bmp");
  if (isOpen("zbackground.bmp")) {
    selectWindow("zbackground.bmp");
    run("Close");
  }
  if (isOpen("Result of zbackground.bmp")) {
    selectWindow("Result of zbackground.bmp");
  }
```

```
  width = getWidth;
  height = getHeight;
  for (y_Pos = 0; y_Pos < height; y_Pos++) {
    if (y_Pos < y_maximum_pool && Width_mean[y_Pos]>average_cut) {
      DistanceEdge_mean[y_Pos]= x_average_maximum_pool-Width_mean[y_Pos]/2;
    }
    if (DistanceEdge_mean[y_Pos]!=0) {
      makeLine(DistanceEdge_mean[y_Pos], y_Pos, Width_mean[y_Pos] + DistanceEdge_mean[y_Pos], y_Pos);
      run("Draw");
    }
  }
  saveAs("BMP", dir1 + "average.bmp");
}
if (printAverageImage2) {
  open(dir1 + "zbackground.bmp");
  imageCalculator("Subtract create", "zbackground.bmp","zbackground.bmp");
  if (isOpen("zbackground.bmp")) {
    selectWindow("zbackground.bmp");
    run("Close");
  }
  if (isOpen("Result of zbackground.bmp")) {
    selectWindow("Result of zbackground.bmp");
  }
  width = getWidth;
  height = getHeight;
  for (y_Pos = 0; y_Pos < height; y_Pos++) {
    if (DistanceEdge_mean[y_Pos]!=0) {
      makeLine((width-Width_mean[y_Pos])/2, y_Pos, (width+Width_mean[y_Pos])/2, y_Pos);
      run("Draw");
    }
  }
  saveAs("BMP", dir1 + "averageTwo.bmp");
}
if (closeAveragePictures) {
  if (isOpen("average.bmp")) {
    selectWindow("average.bmp");
    run("Close");
  }
  if (isOpen("averageTwo.bmp")) {
    selectWindow("averageTwo.bmp");
    run("Close");
  }
}
if (closeResultsFilm) {
  if (isOpen("Results_profile")) {
```

```
    selectWindow("Results_profile");
    run("Close");
  }
}
if (closeTestResults) {
  if (isOpen("TESTS")) {
    selectWindow("TESTS");
    run("Close");
  }
}
if (isOpen("Threshold")) {
  selectWindow("Threshold");
  run("Close");
}
//
   ///////////////////////////////////////////////////////////////////////////

}else{
  if (isOpen("Warning_files")) {
    selectWindow("Warning_files");
    titlefiles = "Warning_files";
    titlefiles2 = "["+titlefiles+"]";
    ffiles=titlefiles2;
    print(ffiles, dir1);
  }else{
    titlefiles = "Warning_files";
    titlefiles2 = "["+titlefiles+"]";
    ffiles=titlefiles2;
    run("New... ", "name="+titlefiles2+" type=Table");
    print(ffiles, "\\Headings:Warning!!!");
    print(ffiles, "Script did not find the correct images in folder");
    print(ffiles, "Consider checking zbackground and zstandard files");
    selectWindow("Warning_files");
    print(ffiles, dir1);
  }
  if (isOpen("Log")) {
    selectWindow("Log");
    run("Close");
  }
  if (isOpen("Results")) {
    selectWindow("Results");
    run("Close");
  }
  if (closeTestResults) {
    if (isOpen("TESTS")) {
      selectWindow("TESTS");
      run("Close");
```

```
    }
  }
  if (closeResultsFilm) {
    if (isOpen("Results_profile")) {
      selectWindow("Results_profile");
      run("Close");
    }
  }
}
/////////////////////////////////////////////////////////////////////////////
print("The script is finished!");
```